

# Superconducting Microwave Resonator Arrays for Submillimeter/Far-Infrared Imaging

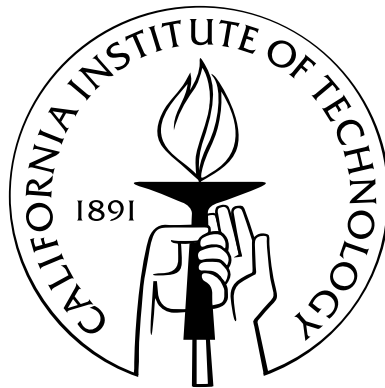
Thesis by

Omid Noroozian

In Partial Fulfillment of the Requirements

for the Degree of

Doctor of Philosophy



California Institute of Technology

Pasadena, California

2012

(Defended April 18, 2012)



*Dedicated to my family*

# Acknowledgments

It has been a truly wonderful experience to have worked at the submillimeter astronomy research group at Caltech. During the past 5.5 years I have been very fortunate to learn from some of the best scientists and engineers in the field of superconducting photon detectors. My journey has been one of both professional and personal enlightenment - one which has deepened my appreciation for the beauty of science and the methodology that has been behind mankind's greatest discoveries. This journey would not have been possible without the support, guidance, and encouragement from my advisor, Professor Jonas Zmuidzinas. I would like to express my deepest gratitude for the opportunity he gave me to explore my curiosity with freedom, whatever or wherever it was, his patience in teaching me the intricate details of scientific inquiry, and for being a guide to both my professional and personal life. It has been a great pleasure to work with him.

I have had the privilege to work with and learn from many colleagues whose help and support have been paramount to the completion of this thesis. I would especially like to thank Dr. Peter Day for helping me with measurements, for using his laboratory at JPL, and for his guidance and creative insight. The beautiful devices in this work were all fabricated by Dr. Henry Leduc at JPL for which I am very thankful. I would also like to extend my special thanks to Dr. Byeong Ho Eom for assisting me with many experiments at JPL. To Professor Sunil Golwala, I would like to express my gratitude for all his help with my thesis work and proposals, creative flashes of ideas, and support for my professional development. A special thank you goes to Dr. Jiansong Gao who has been a close colleague, a friend, and was a wonderful office mate from whom I learned some of the most elaborate details of our work. I would

also like to extend special thanks to Ran Duan for being a great companion and office mate, and for being there whenever I needed help.

I am indebted to all my current and former colleagues at the submillimeter astronomy group at Caltech, including Anastasios Vayonakis, Dr. David Moore, Nicole Czakon, Dr. Matt Hollister, Dr. Tom Downs, Dr. Loren Swenson, Dr. Chris McKenney, Professor Ben Mazin, Dr. James Schlaerth, Dr. Jack Sayers, Dr. Matthew Sumner, Dr. Roger O'Brient, and Dr. Jacob Kooi, for their support, for their insightful discussions, and for providing a stimulating and fun group environment.

I would like to express my gratitude to my former advisor at Delft University of Technology in the Netherlands, Professor Teun Klapwijk, for introducing me to the field of superconducting photon detectors, and for being a role model for many aspects of my professional career.

Apart from academic life, my time in Pasadena and Los Angeles has been enriched by many valuable friendships. I would especially like to thank Pedram Khalili for his unconditional friendship and support. He has been like a brother to me. I am also grateful to my friends Ali Ayazi, Shahin Ayazi, Mohsen Mollazadeh, Ali Sajjadi, Sara Haghayegh, Lillian Zeinalzadegan, Niloufar Safaei Nili, Younes Nouri, Raquel Monje, Aaron Noell, Tom Bell, Christos Santis, Kaveh Pahlevan, Pablo Henonin, Matt Shaw, Nuria Llombart, Juan Bueno, Ali Vakili, Sormeh Shadbakht, and many others for bringing fun and joy to my life. I have many wonderful memories from our adventures and trips.

Most important of all, this thesis is dedicated to my family. I owe my deepest gratitude to them. To my father, Ebrahim, who has been the source of my encouragement and inspiration for studying science as far back in time as I can remember; to my mother, Truus, whose unconditional love, support, and encouragement for my decisions gave me the strength and boldness to pursue my ambitions in life; to my brother, Arman, and his fiancée, Saman, whose support, encouragement, and humor kept me going; to my dearest wife, Azadeh, for her love, support, encouragement, and patience during the final stages of my thesis; and to my wife's parents, Elaheh and Farhad, for their understanding and support - thank you!

# Abstract

Superconducting microwave resonators have the potential to revolutionize submillimeter and far-infrared astronomy, and with it our understanding of the universe. The field of low-temperature detector technology has reached a point where extremely sensitive devices like transition-edge sensors are now capable of detecting radiation limited by the background noise of the universe. However, the size of these detector arrays are limited to only a few thousand pixels. This is because of the cost and complexity of fabricating large-scale arrays of these detectors that can reach up to 10 lithographic levels on chip, and the complicated SQUID-based multiplexing circuitry and wiring for readout of each detector. In order to make substantial progress, next-generation ground-based telescopes such as CCAT or future space telescopes require focal planes with large-scale detector arrays of  $10^4$ – $10^6$  pixels. Arrays using microwave kinetic inductance detectors (MKID) are a potential solution. These arrays can be easily made with a single layer of superconducting metal film deposited on a silicon substrate and patterned using conventional optical lithography. Furthermore, MKIDs are inherently multiplexable in the frequency domain, allowing  $\sim 10^3$  detectors to be read out using a single coaxial transmission line and cryogenic amplifier, drastically reducing cost and complexity.

An MKID uses the change in the microwave surface impedance of a superconducting thin-film microresonator to detect photons. Absorption of photons in the superconductor breaks Cooper pairs into quasiparticles, changing the complex surface impedance, which results in a perturbation of resonator frequency and quality factor. For excitation and readout, the resonator is weakly coupled to a transmission line. The complex amplitude of a microwave probe signal tuned on-resonance and

transmitted on the feedline past the resonator is perturbed as photons are absorbed in the superconductor. The perturbation can be detected using a cryogenic amplifier and subsequent homodyne mixing at room temperature. In an array of MKIDs, all the resonators are coupled to a shared feedline and are tuned to slightly different frequencies. They can be read out simultaneously using a comb of frequencies generated and measured using digital techniques.

This thesis documents an effort to demonstrate the basic operation of  $\sim 256$  pixel arrays of lumped-element MKIDs made from superconducting  $\text{TiN}_x$  on silicon. The resonators are designed and simulated for optimum operation. Various properties of the resonators and arrays are measured and compared to theoretical expectations. A particularly exciting observation is the extremely high quality factors ( $\sim 3 \times 10^7$ ) of our  $\text{TiN}_x$  resonators which is essential for ultra-high sensitivity. The arrays are tightly packed both in space and in frequency which is desirable for larger full-size arrays. However, this can cause a serious problem in terms of microwave crosstalk between neighboring pixels. We show that by properly designing the resonator geometry, crosstalk can be eliminated; this is supported by our measurement results. We also tackle the problem of excess frequency noise in MKIDs. Intrinsic noise in the form of an excess resonance frequency jitter exists in planar superconducting resonators that are made on dielectric substrates. We conclusively show that this noise is due to fluctuations of the resonator capacitance. In turn, the capacitance fluctuations are thought to be driven by two-level system (TLS) fluctuators in a thin layer on the surface of the device. With a modified resonator design we demonstrate with measurements that this noise can be substantially reduced. An optimized version of this resonator was designed for the multiwavelength submillimeter kinetic inductance camera (MUSIC) instrument for the Caltech Submillimeter Observatory.

# Contents

<b>Acknowledgments</b>	<b>iv</b>
<b>Abstract</b>	<b>vi</b>
<b>1 Introduction</b>	<b>1</b>
1.1 Scientific motivation . . . . .	1
1.1.1 Submillimeter/far-IR astronomy . . . . .	1
1.1.2 Detector technology . . . . .	3
1.2 Microwave kinetic inductance detectors . . . . .	6
<b>2 Principles of kinetic inductance detectors</b>	<b>9</b>
2.1 Principle of detection . . . . .	9
2.1.1 Surface impedance and complex conductivity of superconductors	9
2.1.2 Quasiparticle lifetime . . . . .	13
2.2 Resonator circuit . . . . .	16
2.3 Resonator response . . . . .	21
2.4 Resonator sensitivity . . . . .	24
2.4.1 Photon noise limited condition . . . . .	26
<b>3 Two-level system (TLS) noise reduction for MKIDs</b>	<b>28</b>
3.1 Introduction to two-level systems . . . . .	29
3.2 Resonator loss from TLS . . . . .	30
3.3 Resonator frequency noise from TLS . . . . .	33
3.4 A microwave resonator design for reduced TLS noise . . . . .	35

3.4.1	Device details . . . . .	37
3.4.2	Some design considerations . . . . .	40
3.5	Measurements . . . . .	41
3.5.1	Low-temperature resonance frequencies and quality factors . .	41
3.5.2	Temperature sweep . . . . .	43
3.5.3	Noise measurement technique and data analysis . . . . .	48
3.5.4	Noise results and discussion . . . . .	50
3.5.5	Dark NEP . . . . .	54
3.6	IDC resonators for the multiwavelength submillimeter kinetic inductance camera (MUSIC) . . . . .	56
3.7	Chapter summary . . . . .	58
<b>4</b>	<b>Submillimeter/far-infrared imaging arrays using <math>\text{TiN}_x</math> MKIDs</b>	<b>59</b>
4.1	MKID resonator types . . . . .	60
4.2	Lumped-element kinetic inductance detectors . . . . .	65
4.2.1	Radiation coupling method . . . . .	65
4.2.2	Analytical approximations for capacitance and inductance . .	68
4.3	Approximate analytical design of a lumped-element resonator . . . .	70
4.3.1	Inductor meander . . . . .	71
4.3.2	Interdigitated capacitor . . . . .	72
4.3.3	Resonance frequency . . . . .	73
4.3.4	Coupling quality factor and feedline . . . . .	73
4.3.5	Electromagnetic simulations . . . . .	76
4.4	Resonator and array designs . . . . .	79
4.4.1	Design A (“meander”) . . . . .	79
4.4.2	Design B (“spiral”) . . . . .	82
4.4.3	Fabrication method . . . . .	87
4.5	Measurements . . . . .	87
4.5.1	Setup . . . . .	87
4.5.2	Design A measurements . . . . .	88

4.5.2.1	Film $T_c$ measurement . . . . .	88
4.5.2.2	Low-temperature resonance frequencies and quality factors . . . . .	88
4.5.2.3	Bath temperature sweep . . . . .	89
4.5.2.4	Black-body response . . . . .	93
4.5.3	Design B measurements . . . . .	94
4.5.3.1	Film $T_c$ measurement . . . . .	94
4.5.3.2	Low-temperature resonance frequencies and quality factors . . . . .	95
4.5.3.3	Bath temperature sweep . . . . .	96
4.5.3.4	Black-body response . . . . .	96
4.6	Material-dependent sensitivity in MKIDs . . . . .	104
4.6.1	TiN <sub>x</sub> film fabrication . . . . .	105
4.6.2	Film properties and advantages of TiN <sub>x</sub> resonators . . . . .	106
4.7	Chapter summary . . . . .	109
<b>5</b>	<b>Crosstalk reduction for superconducting microwave resonator arrays</b>	<b>111</b>
5.1	Coupled resonators model . . . . .	112
5.2	Calculation of coupling elements from $\delta f_{\text{split}}$ . . . . .	116
5.3	Simulation of coupled pixels . . . . .	119
5.4	Full array circuit model and simulation . . . . .	122
5.4.1	Array eigenfrequencies . . . . .	124
5.4.2	Array eigenvectors . . . . .	128
5.4.3	Array eigenfrequency quality factors . . . . .	132
5.5	Pixel crosstalk . . . . .	137
5.5.1	Crosstalk simulation . . . . .	139
5.6	Measurements . . . . .	142
5.6.1	Measurement setup . . . . .	143
5.6.2	Frequency . . . . .	143

5.6.3	Quality factor . . . . .	147
5.6.4	Crosstalk . . . . .	150
<b>A</b>	<b>Resonator circuit transmission <math>S_{21}</math></b>	<b>154</b>
	<b>Bibliography</b>	<b>161</b>

# Chapter 1

## Introduction

### 1.1 Scientific motivation

#### 1.1.1 Submillimeter/far-IR astronomy

The submillimeter and far-infrared electromagnetic bands can be defined loosely as wavelengths from 1 mm to 300  $\mu\text{m}$  and from 300  $\mu\text{m}$  to 30  $\mu\text{m}$ . They are one of the most important yet least unexplored regions of the electromagnetic spectrum for astronomy. Results from the NASA Cosmic Background Explorer (COBE) have indicated that half of the luminosity of the universe and 98% of the photons emitted since the Big Bang are now observable in the submillimeter and far-IR range [1]. This means that a huge wealth of scientific information is contained in this region. Yet, it is one of the least explored fields in astronomy mainly due to the technological difficulty of building sensitive instruments and detectors in this range.

Star and planetary formation processes happen deep inside interstellar gas and dust clouds. These clouds absorb most of the optical and UV light emitted from these stars during their early phases, making it impossible to rely on optical and infrared observations. For example, Fig. 1.1 shows an image of two colliding galaxies which results in a massive burst of star formation. Light from these newly formed

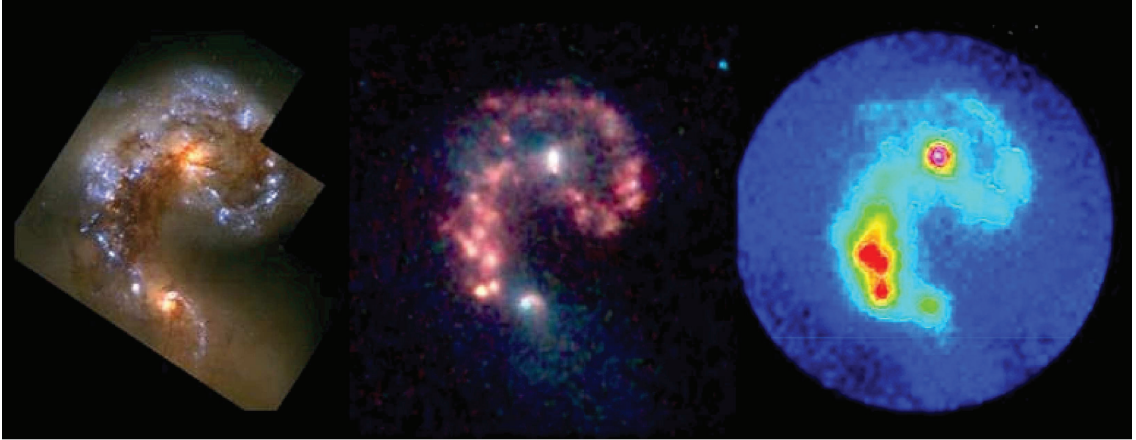


Figure 1.1: NGC 4038/4039 at optical, IR and submm wavelengths. In the Hubble image on the left, light from hot, young stars is visible, as well as dark dust lanes. In the central panel from Spitzer, more sites of star formation become visible. In the right panel, the 350  $\mu\text{m}$  CSO image shows that the bulk of the luminosity derives from star formation invisible at shorter wavelengths. Figure reprinted from [2]

stars is invisible in the optical and infrared bands. However, the absorbed energy in dust clouds is re-emitted at longer wavelengths in the form of submillimeter and far-infrared light. This is one of the reasons why so much of the observed luminosity is in the submm/far-IR. The mechanisms that give rise to far-IR and submillimeter emission are reasonably well understood [1]. The re-emitted light has a modified black-body continuum spectrum which can be used to infer star formation or galactic nuclear activity behind the cloud. There is also important spectral information in this regime. One of the factors in the star-formation process is the cloud cooling mechanism which eventually forms a star. The cooling is due to the rotational spectral line emission of the molecules in the cloud gas [3]. As another example, after the stars have formed, UV emission from massive young stars in our Milky Way galaxy is absorbed in the surrounding molecular dust clouds giving rise to photoelectric heating of the cloud gas which then cools by producing bright  $\text{C}^+$  158  $\mu\text{m}$  line emission [1]. The intensity and line width of such lines gives a wealth of information about the amount and nature of star-forming activity. By resolving these spectral lines even organic molecules that are the building blocks of life have been found in distant dust clouds around protostars where planets form [4]. An overall view of the spectrum of a



for this task. The two main types of detectors used today are bolometric and pair-braking detectors. Bolometric detectors work on the basis of sensing small changes in the temperature of a small superconducting island while pair braking detectors sense the change in the number of quasiparticles that are created when photons break Cooper pairs.

The most sensitive type of bolometric detector today is the transition-edge sensor (TES) [5, 6, 7]. These sensors use the very steep resistive transition from the superconducting state to the normal state. By biasing the detector at the transition, a weak radiation signal can produce a large change in the resistance. For a stable bias point, voltage biasing is used and the current flowing through the resistor is measured by using a superconducting quantum interference device (SQUID) which amplifies the signal. In this technology each pixel needs its own SQUID and readout channel. SQUIDs require a relatively complex fabrication process (up to 10 levels of lithography), and this increases cost, especially for large arrays.

One example of a pair-breaking detector is the superconducting tunnel junction (STJ) detector [8]. These use a superconductor-insulator-superconductor (SIS) junction that has a very thin insulator barrier in between two superconducting contacts. Due to quantum mechanical tunneling a small current exists when the junction is biased with a constant voltage. When photons break Cooper pairs inside the superconductor they create quasiparticles which can tunnel across the barrier and increase the current. A drawback is that since the Cooper pairs can also tunnel – this is the Josephson effect – the pair current must be suppressed using an aligned magnetic field. This can be difficult for large arrays since the magnetic field required can vary for different junctions due to variation in the barrier properties.

Today, submillimeter/far-IR astronomy has reached a point where ground-based detectors have reached background-noise-limited operation where the photon noise from the atmosphere dominates over the intrinsic detector noise. Therefore, to increase the sensitivity of observations for reasonable integration times, large-scale focal

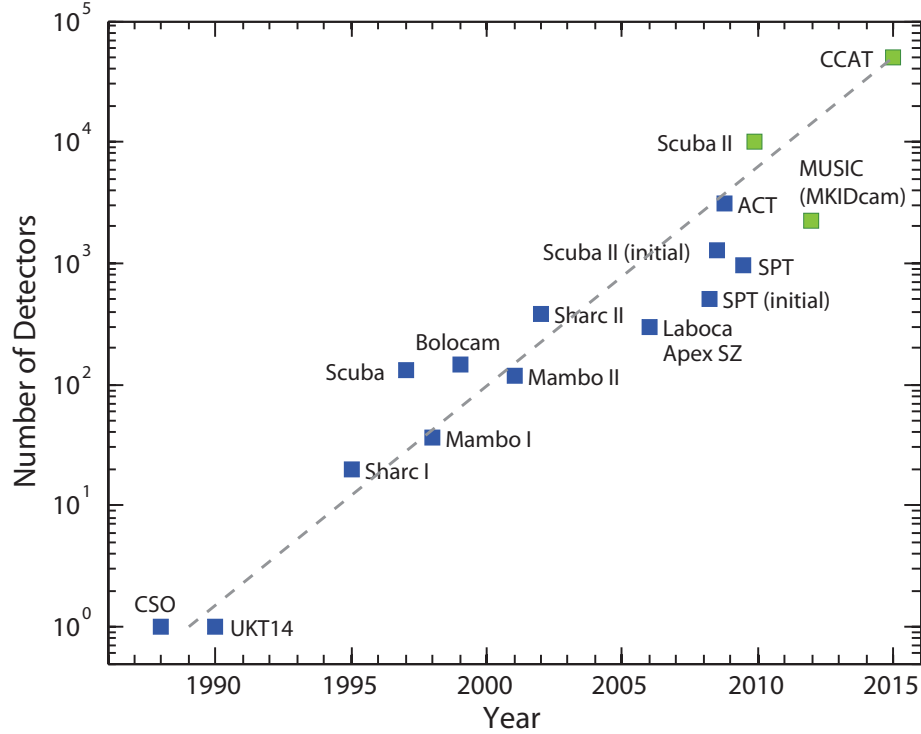


Figure 1.3: The growth of submillimeter detector array size as a function of time has followed an exponential trend over the past two decades, with a growth rate exceeding a factor of 2 every two years. Blue points represent existing (or obsolete) instruments; the green points are projections. MUSIC stands for “multiwavelength submillimeter kinetic inductance camera”. Figure reprinted from [9]

plane arrays with pixels of order  $10^4$ – $10^6$  are required for major progress. Submillimeter and far-IR bolometric arrays have been growing exponentially in a Moore’s law fashion, doubling in size every 20 months [9], and have reached pixel counts as high as  $10^4$  in the SCUBA-2 instrument [10, 11] (see Fig. 1.3). However, further progress has been hampered by complicated and costly fabrication and readout electronics, especially the need for complex cryogenic SQUID-based multiplexing circuits. This has driven the need for simplified alternative detector designs suitable for high packing densities and with lower cost.

## 1.2 Microwave kinetic inductance detectors

Microwave kinetic inductance detectors (MKID) [12, 13] offer a potential solution for large-scale arrays. These arrays can be easily made with a single layer of superconducting metal film deposited on a silicon substrate and patterned using conventional optical lithography. Furthermore, MKIDs are inherently multiplexable in the frequency domain, allowing  $\sim 10^3$  detectors to be read out using a single coaxial transmission line and cryogenic amplifier, and room-temperature electronics, drastically reducing cost and complexity.

MKIDs are a type of pair-breaking detector, in which the absorbed radiation energy breaks Cooper pairs inside a thin superconducting film resulting in a change of the kinetic inductance. The film is cooled to  $T \ll T_c$  and has a superconducting energy gap  $2\Delta \approx 3.52k_B T_c$ . Photons with sufficient energy ( $\nu \geq 2\Delta/h$ ) can break one or more Cooper pairs and create extra quasiparticles as shown in Fig 1.4 (a). These recombine with a time constant  $\tau_{qp} \approx 10^{-6}$ – $10^{-3}$  s depending on the material. During this time, the quasiparticle density increases by a small amount  $\delta n_{qp}$  above its thermal equilibrium value, resulting in a change  $\delta Z_s$  in the surface impedance of the film ( $Z_s = R_s + j\omega L_s$ ). Although  $\delta Z_s$  is quite small, it can be sensitively measured if the film is part of a resonator structure (Fig 1.4 (b)). The resonator is weakly coupled to a transmission line which is used to read out the resonator. Changes in  $L_s$  and  $R_s$  affect the frequency  $f_r$  and quality factor  $Q_r$  of the resonance feature, respectively, changing the amplitude and phase of a microwave probe signal (tuned on the resonance frequency) transmitted through the feedline (Fig 1.4 (c) and (d)). Both of these signals can be read out and are referred to as the frequency direction and dissipation direction signals. A cryogenic SiGe transistor amplifier or a high electron mobility transistor (HEMT) amplifier followed by homodyne mixing at room temperature is used to readout these signals [12]. In an array of MKIDs, all the resonators are coupled to a shared feedline and are tuned to slightly different frequencies. They can be read out simultaneously using a comb of frequencies generated and measured

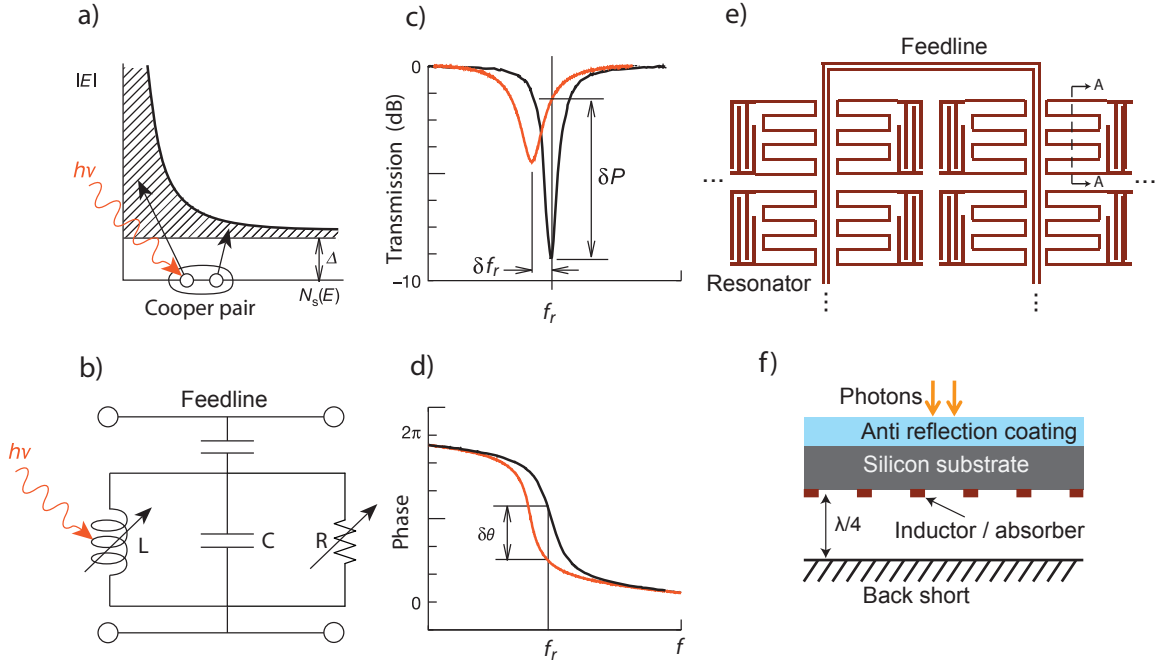


Figure 1.4: Schematic illustration of MKID operation. (a) Photons with energy  $h\nu > 2\Delta$  are absorbed in a superconducting film, breaking Cooper pairs and creating quasiparticle excitations. In this diagram, Cooper pairs are shown at the Fermi level, and the density of states for quasiparticles,  $N_s(E)$ , is plotted as the shaded area as a function of quasiparticle energy  $E$ . (b) The increase in quasiparticle density increases the surface inductance  $L_s$  and the surface resistance  $R_s$  of the film, which is used as part of a microwave resonant circuit. The resonant circuit is depicted schematically as a parallel RLC circuit which is capacitively coupled to a transmission line (feedline). (c) On resonance, the LC circuit loads the through line, producing a dip in its transmission. The quasiparticles produced by the photons increase both  $L_s$  and  $R_s$ , which moves the resonance to lower frequency (due to  $L_s$ ), and makes the dip broader and shallower (due to  $R_s$ ). Both of these effects contribute to changing the transmission amplitude (c) and phase (d) of a microwave probe signal transmitted through the feedline. (e) A  $2 \times 8$  section of the geometry of a close-packed MKID resonator array, with dark regions representing superconducting metallization. (f) Cross-sectional view along A-A in (e) of a resonator showing the illumination mechanism.

using digital techniques [14, 15]. Fig. 1.4 (e) shows a schematic illustration of a section of an MKID array described in chapter 4 and 5 of this thesis. Although the resonators are lumped-element in this case (called lumped-element kinetic inductance detector or LeKID), there are also distributed versions of MKIDs. Fig. 1.4 (f) shows the radiation coupling mechanism to a LeKID. Photons are directly absorbed inside the meandered inductor section.

The fundamental limit to the sensitivity of an MKID is determined by the random generation of quasiparticles by pair-breaking thermal phonons and their subsequent recombination, resulting in generation-recombination noise. Fortunately, this noise is exponentially suppressed at lower temperatures by the Boltzmann factor  $e^{-\Delta/k_B T}$ . However, in practice MKIDs are still limited by other nonfundamental sources of noise, such as amplifier noise and capacitor noise due to two-level system (TLS) fluctuators in amorphous dielectrics. Constant progress in development of lower-noise amplifiers has been very beneficial for MKIDs [16]. TLS noise can be significantly reduced as will be shown in chapter 3 of this thesis, but the remaining noise is still an issue.

MKID arrays are being developed for astronomy at a wide range of wavelengths from millimeter waves to x-rays [17, 18, 19, 20]. Other applications of superconducting resonators are in quantum computation experiments [21, 22, 23], multiplexed readout of transition-edge sensor bolometers [24], and parametric amplifiers [25].

## Chapter 2

# Principles of kinetic inductance detectors

In this chapter we will review the basics of the operation of a microwave kinetic inductance detector (MKID). We will explain the principle of detection going through the chain of signal starting from perturbations to the complex conductivity of a superconductor to the final detection of a voltage. The calculations and the formulae in this chapter will be used later throughout the rest of the thesis.

### 2.1 Principle of detection

#### 2.1.1 Surface impedance and complex conductivity of superconductors

In a superconductor at zero temperature, all the electrons are bound into pairs called Cooper pairs. This happens due to the interaction between the lattice and the electrons which creates a weak attractive force that binds the electrons into pairs. According to BCS theory [26] the pairs have a binding energy of

$$2\Delta_0 \approx 3.52k_B T_c \tag{2.1}$$

where  $T_c$  is the critical temperature above which superconductivity vanishes and  $\Delta_0$  is the energy gap of the superconductor. The binding energy is quite weak, of the order of meV, and thermal energy can easily break the pairs. Thus at a nonzero temperature  $T < T_c$  some of the pairs will be broken into quasi single electrons called quasiparticles. The quasiparticle density per unit volume is given by

$$n_{qp} = 4N_0 \int_{\Delta}^{\infty} \frac{E}{\sqrt{E^2 - \Delta^2}} f(E) dE \quad (2.2)$$

where  $\Delta$  is the nonzero temperature gap and  $f(E) = 1/(1 + e^{E/k_B T})$  is the Fermi-Dirac distribution for the quasiparticles in thermal equilibrium. For  $T \ll T_c$  we have  $\Delta \approx \Delta_0$  and

$$n_{qp} \approx 2N_0 \sqrt{2\pi k_B T \Delta_0} e^{-\frac{\Delta_0}{k_B T}}. \quad (2.3)$$

Here  $N_0$  is the single-spin density of electron states at the Fermi energy, which for aluminum is  $1.72 \times 10^{10} \mu\text{m}^{-3} \text{ eV}^{-1}$  [12]. From Eq. 2.3 we can see that as  $T \rightarrow 0$ ,  $n_{qp} \rightarrow 0$  in an exponential manner. Because of the energy gap, Cooper pairs carrying electrical current cannot easily get excited into a higher energy state which means they cannot scatter like normal electrons. Therefore, superconductors show zero DC resistance below their critical temperature  $T_c$ . However, they do show nonzero resistance and inductance in the case of AC fields. This is because the electromagnetic field can penetrate inside the superconductor over a length of  $\lambda$  (the penetration depth) due to the Meissner effect. When  $T > 0$  the existence of normal electrons (quasiparticles) introduces resistive loss to the AC field. On the other hand the Cooper pairs store energy in the form of kinetic and magnetic energy and introduce a purely inductive impedance, because they lag the electric field due to their inertia. The combined effect of the quasiparticles and the Cooper pairs produces a complex surface impedance

$$Z_s = R_s + jX_s. \quad (2.4)$$

The surface impedance can be calculated using the complex conductivity formulation given by Mattis and Bardeen [27]. For frequencies below the gap frequency ( $\nu_g =$

$2\Delta/h$ ) the complex conductivity  $\sigma = \sigma_1 - j\sigma_2$  is given by:

$$\frac{\sigma_1}{\sigma_n} = \frac{2}{\hbar\omega} \int_{\Delta}^{\infty} \frac{E^2 + \Delta^2 + \hbar\omega E}{\sqrt{E^2 - \Delta^2} \sqrt{(E + \hbar\omega)^2 - \Delta^2}} [f(E) - f(E + \hbar\omega)] dE \quad (2.5)$$

$$\frac{\sigma_2}{\sigma_n} = \frac{1}{\hbar\omega} \int_{\Delta}^{\Delta + \hbar\omega} \frac{E^2 + \Delta^2 - \hbar\omega E}{\sqrt{E^2 - \Delta^2} \sqrt{\Delta^2 - (E - \hbar\omega)^2}} [1 - 2f(E)] dE \quad (2.6)$$

where  $\sigma_n = 1/\rho_n$  is the normal-state conductivity of the superconductor just above  $T_c$ . In the temperature range  $T \ll T_c$ ,  $\sigma_1 \ll \sigma_2$ . In the case where  $k_B T \ll \Delta_0$  and  $\hbar\omega \ll \Delta_0$ , these two integrals can be simplified [28] to

$$\frac{\sigma_1(n_{qp})}{\sigma_n} = \frac{2\Delta_0}{\hbar\omega} \frac{n_{qp}}{N_0 \sqrt{2\pi k_B T} \Delta_0} \sinh(\xi) K_0(\xi) \quad (2.7)$$

$$\frac{\sigma_2(n_{qp})}{\sigma_n} = \frac{\pi\Delta_0}{\hbar\omega} \left[ 1 - \frac{n_{qp}}{2N_0\Delta_0} \left( 1 + \sqrt{\frac{2\Delta_0}{\pi k_B T}} e^{-\xi} I_0(\xi) \right) \right] \quad (2.8)$$

$$\xi = \frac{\hbar\omega}{2k_B T}, \quad (2.9)$$

where  $I_0$  and  $K_0$  are the zeroth-order modified Bessel functions of the first and second kind, and where we have used Eq. 2.3 to write these in term of  $n_{qp}$ . Here  $n_{qp}$  is the total quasiparticle density due to thermal generation and pair breaking by photons. The last step is important because we can now directly see that both  $\sigma_1$  and  $\delta\sigma_2 = \sigma_2 - \sigma_2(0)$  are proportional to  $n_{qp}$ . This is the basic detection mechanism of MKIDs: quasiparticles that are created by absorption of photons or thermal generation in the superconductor can be sensed through perturbations in the complex conductivity. From Eq. 2.7 and Eq. 2.8 it can be shown that the fractional changes in  $\sigma_1$  and  $\sigma_2$  are equal to fractional changes in  $n_{qp}$ <sup>1</sup>:

$$\frac{\delta\sigma_1}{\sigma_1} = \frac{\delta n_{qp}}{n_{qp}} \quad (2.10)$$

$$\frac{\delta\sigma_2}{\sigma_2 - \sigma_2(0)} = \frac{\delta n_{qp}}{n_{qp}} \quad (2.11)$$

On the other hand, a perturbation in the complex conductivity results in a per-

---

<sup>1</sup>An underlying assumption here is that the perturbation in the quasiparticle distribution function  $\delta f(E)$  has the same shape as  $f(E)$  [13].

turbation in the complex surface impedance of the film in the following way: In the case when the film thickness  $t$  is much smaller than the effective penetration depth  $\lambda_{eff}$  and  $t$  is smaller than the electron mean free path  $\ell_e$ <sup>2</sup>, we can simply write [28]

$$Z_s = \frac{1}{\sigma t} \quad (2.12)$$

$$= \frac{1}{(\sigma_1 - j\sigma_2)t} \quad (2.13)$$

$$\approx \frac{\sigma_1}{t\sigma_2^2} + j\frac{1}{t\sigma_2}. \quad (2.14)$$

Therefore, from Eq. 2.12 a fractional perturbation in conductivity is related to the fractional perturbation in surface impedance as

$$\frac{\delta Z_s}{Z_s} = -\frac{\delta \sigma}{\sigma}. \quad (2.15)$$

If we consider perturbation around zero temperature, we have  $Z_s(0) = jX_s(0)$  and  $\sigma(0) = -j\sigma_2(0)$ , and if we assume  $\sigma_1 \ll \sigma_2$  we can write, to first order:

$$\frac{\delta R_s}{X_s(0)} = \frac{\delta \sigma_1}{\sigma_2(0)} \quad (2.16)$$

$$\frac{\delta X_s}{X_s(0)} = -\frac{\delta \sigma_2}{\sigma_2(0)}. \quad (2.17)$$

Using Eq. 2.10 and Eq. 2.11 the above two equations can be written in terms of perturbations in quasiparticle density:

$$\frac{\delta R_s}{X_s(0)} = \frac{S_1(\omega)}{2N_0\Delta_0} \delta n_{qp} \quad (2.18)$$

$$\frac{\delta X_s}{X_s(0)} = \frac{-S_2(\omega)}{2N_0\Delta_0} \delta n_{qp} \quad (2.19)$$

---

<sup>2</sup>These conditions are met for the thicknesses and films that we use though out this thesis (60 nm Al and 20–40 nm TiN).

where  $S_1(\omega)$  and  $S_2(\omega)$  are defined in the limit  $\hbar\omega, k_B T \ll \Delta_0$  as

$$S_1(\omega) \cong \frac{2}{\pi} \sqrt{\frac{2\Delta_0}{\pi k_B T}} \sinh(\xi) K_0(\xi) \quad (2.20)$$

$$S_2(\omega) \cong 1 + \sqrt{\frac{2\Delta_0}{\pi k_B T}} e^{-\xi} I_0(\xi) , \quad (2.21)$$

and

$$\beta = \frac{S_2(\omega)}{S_1(\omega)} = \frac{\delta\sigma_2}{\delta\sigma_1} = \frac{|\delta X_s|}{\delta R_s} \quad (2.22)$$

is the ratio of the two perturbations. This ratio is important because it determines which response is stronger. It is also useful when comparing the observed response ratio in measurements to theory. Furthermore, it is convenient to express the perturbations in parameters in terms of  $\delta n_{qp}$  because as we will see later the perturbations in the incident optical power on the detector  $\delta P_o$  directly determines  $\delta n_{qp}$ .

The changes in the surface impedance can be very sensitively measured using a resonant circuit made from the superconductor. The concept is illustrated in Fig. 1.4 where the RLC circuit represents the detector. As photons break Cooper pairs inside the detector, the resonance frequency  $f_r$  and the quality factor  $Q_r$  of the circuit changes. This change can be probed by weakly coupling the resonator capacitively or inductively to a transmissionline called a “feedline”. By sending a microwave probe signal on the feedline tuned on the resonance frequency, the complex amplitude of the signal  $S_{21}$  changes by  $\delta S_{21}$  every time photons hit the detector. In the following sections we will calculate how  $\delta S_{21}$  is related to the changes in the incident optical power  $\delta P_o$ . We start by examining the quasiparticle lifetime and its steady-state value.

### 2.1.2 Quasiparticle lifetime

Quasiparticles can recombine over a lifetime  $\tau_{qp}$  and emit a phonon during the process. The lifetime depends on the quasiparticle density since for higher densities the

recombination probability is higher. As the temperature is reduced the thermally generated quasiparticles reduce and  $\tau_{qp}$  increases. However, it has been experimentally observed [29, 30, 31] that the lifetime saturates at a maximum level  $\tau_{max}$  for  $n_{qp} \lesssim n^* \approx 100 \mu\text{m}^3$  and has the form

$$\tau_{qp}^{-1} = \tau_{max}^{-1} + Rn_{qp} . \quad (2.23)$$

$R = 1/n^*\tau_{max}$  is called the recombination constant and is theoretically given by [32]

$$R = \frac{(2\Delta)^2}{2N_0\tau_0(k_B T_c)^3} \quad (2.24)$$

where  $\tau_0$  is the material-specific electron-phonon interaction time.

The quasiparticle population is governed by generation and recombination processes. These are thermal quasiparticle generation, excess quasiparticle generation, and quasiparticle recombination. We can write

$$\frac{dn_{qp}}{dt} = \Gamma_{gen} - \Gamma_{rec} \quad (2.25)$$

where  $\Gamma_{gen}$  and  $\Gamma_{rec}$  are the generation and recombination rates. To calculate the steady-state population  $n_{qp}$  we can set the generation and recombination rates equal. The generation rate consists of two terms

$$\Gamma_{gen} = \Gamma_{th} + \Gamma_e \quad (2.26)$$

where  $\Gamma_{th}$  is the thermal generation rate, and  $\Gamma_e$  is the excess quasiparticle generation rate from optical power incident on the detector and the readout power. We can write

$$\Gamma_e = \Gamma_o + \Gamma_a = \frac{\eta_o P_o}{\Delta_0} + \frac{\eta_a P_a}{\Delta_0} \quad (2.27)$$

where  $\eta_o \sim 0.7$  is the efficiency with which absorbed optical power generates quasiparticles [13],  $\eta_a$  is the efficiency with which absorbed readout power generates quasipar-

ticles,  $P_o$  is the incident optical power, and  $P_a$  is the absorbed readout power inside the resonator. For the readout power efficiency we can write an expression

$$\eta_a = \frac{N_{qp}^{read} \Delta}{\tau_{qp} P_a^{qp}} \quad (2.28)$$

where  $N_{qp}^{read}$  is the quasiparticle population created due to the readout and where  $P_a^{qp} = \chi_{qp} P_a$  is the absorbed power by the quasiparticles due to readout and  $\chi_{qp} \leq 1$  determines the proportionality.

The recombination rate depends on the total quasiparticle population and can be written as

$$\Gamma_{rec} = \frac{1}{2} N_{qp} (\tau_{max}^{-1} + \tau_{qp}^{-1}) = N_{qp} (\tau_{max}^{-1} + \frac{1}{2} R n_{qp}) \quad (2.29)$$

where  $N_{qp} = n_{qp} V$  is the total quasiparticle population in the superconducting volume  $V$ .

The thermal generation rate  $\Gamma_{th}$  is equal to the recombination rate at the thermally generated quasiparticle density at temperature  $T$

$$\Gamma_{th} = \Gamma_{rec}(n_{th}(T)) \quad (2.30)$$

where  $n_{th}$  is determined from Eq. 2.3. However,  $n_{th}$  can be made sufficiently small at low temperatures that it can become negligible. Solving for  $n_{qp}$  in Eq. 2.25 at steady-state we get

$$n_{qp} = n^* \sqrt{1 + 2\Gamma_e \tau_{max} / N^*} - n^* \quad (2.31)$$

where  $N^* = V n^*$ . The lifetime is given by using Eq. 2.31 in Eq. 2.23:

$$\tau_{qp} = \frac{\tau_{max}}{\sqrt{1 + 2\Gamma_e \tau_{max} / N^*}}. \quad (2.32)$$

Now we can calculate the perturbation in the quasiparticle population  $\delta N_{qp}$  in re-

sponse to a perturbation in the incident optical power  $\delta P_o$ :

$$\delta N_{qp} = \frac{\partial N_{qp}}{\partial P_o} \delta P_o = \frac{\partial N_{qp}}{\partial \Gamma_e} \frac{\partial \Gamma_e}{\partial P_o} \delta P_o. \quad (2.33)$$

The first factor can be calculated from Eq. 2.31 and is equal to  $\partial N_{qp}/\partial \Gamma_e = \tau_{qp}$ . The second factor can be calculated from Eq. 2.27 and is  $\partial \Gamma_e/\partial P_o = \eta_o/\Delta_0$ . Therefore,

$$\delta N_{qp} = \frac{\eta_o \tau_{qp}}{\Delta_0} \delta P_o. \quad (2.34)$$

Next we will examine the electrical resonant circuit that is used to sense the changes in the surface impedance.

## 2.2 Resonator circuit

In the previous sections we evaluated how a change in quasiparticle density affects the surface impedance. Here we will examine the resonator circuit that is used to sense the changes in the surface impedance. Fig. 2.1 (a) shows an equivalent circuit diagram for the resonator and readout mechanism. The resonator which is the RLC tank circuit is coupled capacitively to a feedline. A microwave voltage generator produces a signal that is transmitted through the feedline past the resonator and is amplified with an amplifier. When the signal is tuned near resonance the complex amplitude of the signal is affected by the resonator. The forward complex transmission  $S_{21}$  from port 1 to port 2 is shown in Appendix A to be

$$S_{21} \approx 1 - \frac{Q_r}{Q_c} \frac{1}{1 + 2jQ_r x} \quad (2.35)$$

$$x = \frac{\omega - \omega_r}{\omega_r} \quad (2.36)$$

where  $\omega_r = 2\pi f_r$  is the resonance frequency,  $x$  is the fractional frequency,  $Q_r$  is the resonance quality factor,  $Q_c$  is the coupling quality factor, and  $Q_i$  is the internal

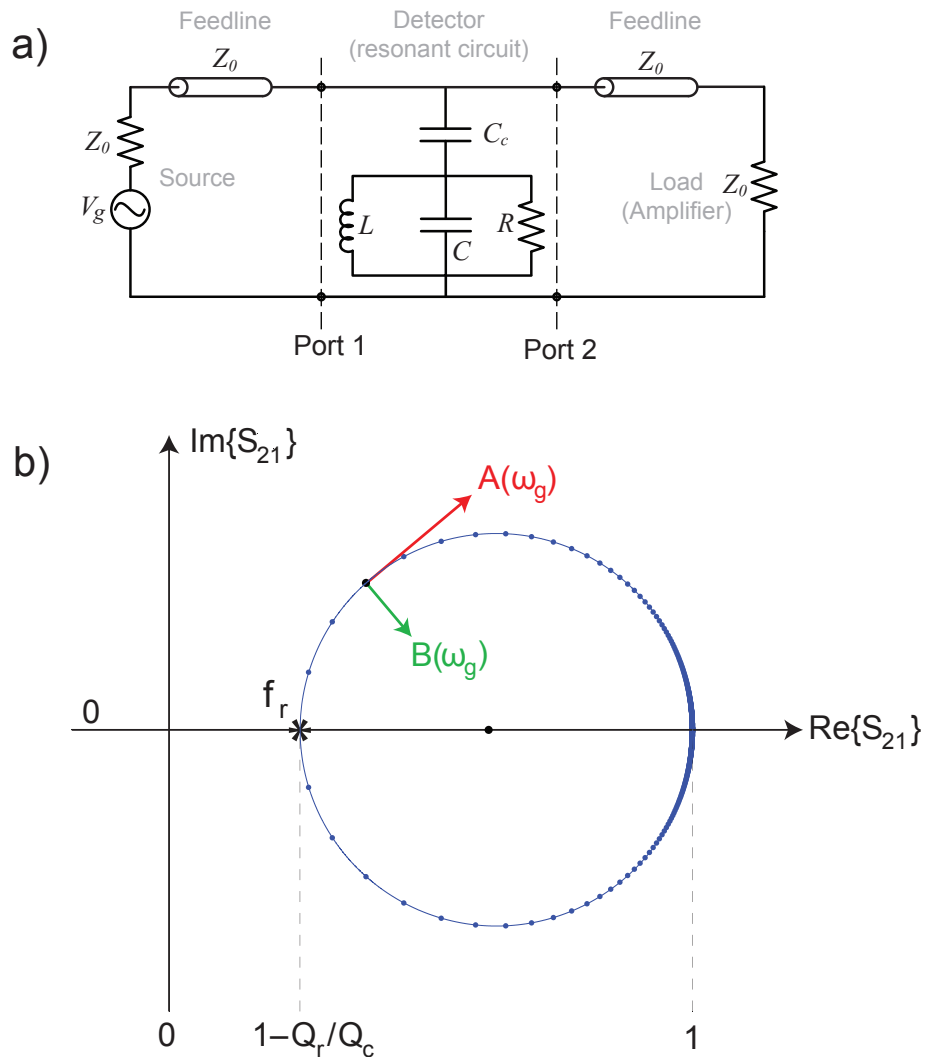


Figure 2.1: (a) Equivalent circuit illustration of a superconducting resonator coupled capacitively to a transmission line (“feedline”). The load impedance  $Z_0$  represents the amplifier’s input impedance. The voltage source and its impedance represent the microwave generator used to read out the resonator. (b) The circular trajectory of the complex transmission  $S_{21}$  as a function of frequency for the circuit in (a) is shown along with the resonance frequency  $f_r$ . The dots on the circle represent fixed frequency steps. The directions tangent and perpendicular to the resonance loop at a fixed generator frequency  $\omega_g = 2\pi f_g$  are indicated by the complex vectors  $A(\omega_g)$  and  $B(\omega_g)$ . These two directions correspond to the frequency and dissipation direction signals.

quality factor. These are related by (see Appendix A)

$$\frac{1}{Q_r} = \frac{1}{Q_c} + \frac{1}{Q_i}. \quad (2.37)$$

The transmission  $S_{21}$  traces a clockwise circle in the complex plane as the frequency is increased from below the resonance to above the resonance. This is shown in Fig. 2.1 (b). Far away from resonance  $S_{21} \rightarrow 1$ . On resonance  $S_{21}$  reaches a minimum value of  $\min(|S_{21}|) = 1 - \frac{Q_r}{Q_c}$ . The value of  $Q_r$  can be determined from the resonance bandwidth  $Q_r = \frac{f_r}{2\Delta\nu_r}$  where  $2\Delta\nu_r$  is defined as the frequency bandwidth spanning half the resonance circle in Fig. 2.1 (b). The value of  $Q_c$  and  $Q_i$  can be determined from

$$Q_c = \frac{Q_r}{1 - \min(|S_{21}|)} \quad (2.38)$$

$$Q_i = \frac{Q_r}{\min(|S_{21}|)}. \quad (2.39)$$

In practice however, the resonance circle will be affected by the measurement read-out circuit. Cable delay will cause the loop to become smaller, crossing itself, and impedance mismatch between the feedline and the load and source impedances will rotate the loop. These effects can be taken out by using a resonance fitting code.

When photons are absorbed in the resonator the surface impedance of the circuit changes which causes a change in the resonance frequency and quality factor. This in turn changes the complex transmission  $S_{21}$  which is measured. We can calculate the perturbation in  $S_{21}$  as a function of perturbations in fractional frequency  $x$  and  $Q_i$ . For slow perturbations compared to the resonance response time we can write

$$\delta S_{21}(t) = A(\omega)\delta x(t) + B(\omega)\delta Q_i^{-1}(t) \quad (2.40)$$

where  $A(\omega)$  and  $B(\omega)$  are

$$A(\omega) = \frac{\partial S_{21}}{\partial x} = 2jQ_c(1 - S_{21}(\omega))^2 \quad (2.41)$$

$$B(\omega) = \frac{\partial S_{21}}{\partial Q_i^{-1}} = \frac{1}{2j}A(\omega) \quad (2.42)$$

and  $\delta x(t) = \frac{\delta f_r(t)}{f_r}$ . The directions of the vectors  $A(\omega)$  and  $B(\omega)$  are tangent and perpendicular to the resonance circle as shown in Fig. 2.1 (b). These two directions are commonly referred to as the frequency and dissipation (or phase and amplitude) directions, respectively. For fast perturbations with frequency  $\nu$  the resonator ring-down response should also be included which acts as a low-pass filter when  $\omega = \omega_r$ . To include this effect we switch to the frequency-domain representation of Eq. 2.40

$$\delta S_{21}(\nu) = [A(\omega)\delta x(\nu) + B(\omega)\delta Q_i^{-1}(\nu)]\zeta(\nu) \quad (2.43)$$

where

$$\zeta(\nu) = \frac{1}{1 + j\nu/\Delta\nu_r}. \quad (2.44)$$

However, for our situation the perturbation in the signal is usually much slower than the resonator response time and  $\zeta \rightarrow 1$ .

To follow the notation of Zmuidzinas et al. [13] we define the following variables to rewrite Eq. 2.43 in terms of these:

$$\phi_g = \tan^{-1}2Q_r x \quad (2.45)$$

is the phase angle;

$$\chi_c = \frac{4Q_c Q_i}{(Q_c + Q_i)^2} = \frac{4Q_r^2}{Q_c Q_i} \lesssim 1 \quad (2.46)$$

is the coupling efficiency factor which reaches unity for optimum coupling  $Q_c = Q_i$ ;

and

$$\chi_g(\omega) = \frac{1}{1 + 4Q_r^2 x^2} \lesssim 1 \quad (2.47)$$

is the generator detuning efficiency which is maximized when the generator frequency is tuned on resonance,  $\omega = \omega_r$ . Using the above three definitions we can rewrite Eq. 2.41 and Eq. 2.42 as

$$A(\omega) = j \frac{Q_i}{2} \chi_c \chi_g e^{-2j\phi_g} \quad (2.48)$$

$$B(\omega) = \frac{Q_i}{4} \chi_c \chi_g e^{-2j\phi_g} . \quad (2.49)$$

We can now rewrite Eq. 2.43 using the above two equations

$$\delta S_{21}(\nu) = \frac{1}{4} \chi_c \chi_g Q_i e^{-2j\phi_g} [2j\delta x(\nu) + \delta Q_i^{-1}(\nu)] \zeta(\nu) + \delta S_a(\nu) . \quad (2.50)$$

We have added a noise term  $\delta S_a(\nu) = \delta I_a(\nu) + j\delta Q_a(\nu)$  representing the amplifier's additive white noise which has a noise power spectral density of

$$\text{PSD}(\delta I_a) = \text{PSD}(\delta Q_a) = \frac{k_B T_a}{2P_{\text{feed}}} \quad (2.51)$$

where  $T_a$  is the amplifier noise temperature and  $P_{\text{feed}}$  is the microwave generator power incident on the feedline. Note that part of  $P_{\text{feed}}$  is absorbed inside the resonator which is equal to

$$P_a = (1 - |S_{11}|^2 - |S_{21}|^2) P_{\text{feed}} = \frac{\chi_c \chi_g}{2} P_{\text{feed}} \leq \frac{1}{2} P_{\text{feed}} . \quad (2.52)$$

Another important noise source that must be included in Eq. 2.50 is the excess two-level system (TLS) frequency noise. This noise is intrinsic to the resonator and causes a jitter in the resonance frequency that is characterized by the fractional frequency noise power spectral density  $S_{\text{TLS}}(\nu)$  corresponding to fluctuations in  $x$ . It will be described in detail in Chapter 3. Because it is intrinsic it directly adds to the

frequency perturbation term. We can rewrite Eq. 2.50 to include it as follows:

$$\delta S_{21}(\nu) = \frac{1}{4} \chi_c \chi_g Q_i e^{-2j\phi_g} [2j\delta x(\nu) + 2\delta x_{\text{TLS}}(\nu) + \delta Q_i^{-1}(\nu)] \zeta(\nu) + \delta S_a(\nu) . \quad (2.53)$$

## 2.3 Resonator response

We can now start to calculate the relation between quasiparticle perturbations  $\delta n_{qp}$  and resonator circuit transmission perturbations  $\delta S_{21}$ . We start by calculating the perturbation in resonance frequency and quality factor. The resonance frequency in Fig. 2.1 (a) is simply (see Eq. A.22)

$$f_r = \frac{1}{2\pi\sqrt{LC}} . \quad (2.54)$$

A perturbation in the inductance is related to a perturbation in frequency as

$$\delta x = \frac{\delta f_r}{f_r} = \frac{-\delta L}{2L} . \quad (2.55)$$

We can write the total inductance  $L$  as the sum of the geometric inductance and the kinetic inductance  $L = L_m + L_{ki}$ . Only the kinetic inductance is perturbed so we can write

$$\delta x = \frac{-\delta L_{ki}}{2(L_{ki} + L_m)} = -\frac{\alpha \delta L_{ki}}{2 L_{ki}} = -\frac{\alpha \delta X_s}{2 X_s} , \quad (2.56)$$

where

$$\alpha = \frac{L_{ki}}{L_{ki} + L_m} \quad (2.57)$$

is defined as the kinetic inductance fraction. Using Eq. 2.19 in Eq. 2.56 we can now relate  $\delta x$  to  $\delta n_{qp}$ :

$$\delta x = \frac{\alpha S_2(\omega)}{4N_0\Delta_0} \delta n_{qp} . \quad (2.58)$$

We can follow the same logic for perturbations in the internal quality factor. We start by writing

$$Q_i^{-1} = \frac{R}{\omega L}. \quad (2.59)$$

A perturbation in the resistance is related to a perturbation in  $Q_i^{-1}$  as

$$\delta Q_i^{-1} = \frac{\delta R}{\omega L} = \alpha \frac{\delta R}{\omega L_{ki}} = \alpha \frac{\delta R_s}{X_s}. \quad (2.60)$$

Using Eq. 2.18 in the above equation we can now relate  $\delta Q_i^{-1}$  to  $\delta n_{qp}$  as

$$\delta Q_i^{-1} = \frac{\alpha S_1(\omega)}{2N_0 \Delta_0} \delta n_{qp}. \quad (2.61)$$

Note that we can write a similar relation between the internal quality factor  $Q_i$  and the total quasiparticle density  $n_{qp}$

$$Q_{qp}^{-1} = \chi_{qp} Q_i^{-1} = \frac{\alpha S_1(\omega)}{2N_0 \Delta_0} n_{qp} \quad (2.62)$$

where the factor  $\chi_{qp} \leq 1$  accounts for the portion of the internal resonator loss that is due to quasiparticles. Other loss mechanisms like radiation into free space and TLS loss (see Chapter 3) can contribute to  $Q_i^{-1}$  but are not affected by quasiparticles.

Using Eq. 2.34 together with Eq. 2.58 and Eq. 2.61 it is convenient to define the fractional frequency responsivity  $R_x$  and the loss responsivity  $R_{Q_i^{-1}}$  as

$$R_x = \frac{\delta x}{\delta P_o} = \frac{\alpha S_2(\omega) \eta_o \tau_{qp}}{4N_0 \Delta_0^2 V} \quad (2.63)$$

$$R_{Q_i^{-1}} = \frac{\delta Q_i^{-1}}{\delta P_o} = \frac{\alpha S_1(\omega) \eta_o \tau_{qp}}{2N_0 \Delta_0^2 V}. \quad (2.64)$$

We will later use the ratio between these two responses in both temperature sweep and black-body power sweep measurements in Chapter 3 and 4 to compare with the Mattis–Bardeen prediction given above.

We can combine Eq. 2.58, Eq. 2.61, and Eq. 2.62 with Eq. 2.53 to obtain a relation between  $\delta S_{21}$  and  $\delta n_{qp}$

$$\begin{aligned} \delta S_{21}(\nu) &= \frac{1}{4} \chi_c \chi_g \chi_{qp} e^{-2j\phi_g} [1 + j\beta(\omega)] \zeta(\nu) \frac{\delta n_{qp}}{n_{qp}} \\ &\quad + j e^{-2j\phi_g} \frac{\chi_c \chi_g}{2} Q_i \zeta(\nu) \delta x_{\text{TLS}} + \delta S_a(\nu). \end{aligned} \quad (2.65)$$

Finally, using Eq. 2.34 we can write the relationship between  $\delta S_{21}$  and the optical power  $\delta P_o$  as

$$\begin{aligned} \delta S_{21}(\nu) &= \frac{1}{4} \chi_c \chi_g \chi_{qp} e^{-2j\phi_g} [1 + j\beta(\omega)] \zeta(\nu) \frac{\eta_o \tau_{qp}}{\Delta_0 N_{qp}} \delta P_o \\ &\quad + j e^{-2j\phi_g} \frac{\chi_c \chi_g}{2} Q_i \zeta(\nu) \delta x_{\text{TLS}} + \delta S_a(\nu). \end{aligned} \quad (2.66)$$

From the above equation it is easy to write expressions for the frequency and dissipation direction responsivities (gains):

$$\frac{\text{Re}(\delta S_{21})}{\delta P_o} = \frac{\eta_o \chi_c \chi_{qp} \tau_{qp}}{4 N_{qp} \Delta_0} \quad (2.67)$$

$$\frac{\text{Im}(\delta S_{21})}{\delta P_o} = \frac{\beta(\omega) \eta_o \chi_c \chi_{qp} \tau_{qp}}{4 N_{qp} \Delta_0} \quad (2.68)$$

where we have assumed that  $\zeta(\nu) = 1$ . We will make this assumption from here on since the astronomical signals observed in the submillimeter and far-IR have very slow variations in time. We can see that the responsivity in the frequency direction is a factor of  $\beta(\omega)$  larger than the dissipation direction. This is a potential advantage for the frequency response. However, because of the extra TLS noise in this direction currently the dissipation response is more sensitive. In the next chapter we will examine this extra noise and try to find a resonator design that minimizes it.

## 2.4 Resonator sensitivity

In order to calculate the sensitivity of an MKID resonator we need to consider the noise sources contributing to the signal. These could be intrinsic noise like the TLS noise (see Chapter 3), thermal quasiparticle generation shot noise, quasiparticle recombination shot noise, or extrinsic noise like the photon shot noise in the optical power. We will calculate the noise equivalent power (NEP) at the input of the detector for each of these noise sources.

The power spectral density of shot noise in the generation rate  $\Gamma_{th}$  from thermal generation of quasiparticles is given by [13]

$$S_{\Gamma_{th}} = 2\Gamma_{th} = N_{th}(\tau_{max}^{-1} + \tau_{th}^{-1}) \quad (2.69)$$

where  $N_{th}$  is the thermal quasiparticle population at temperature  $T$  when the system is in thermal equilibrium (see Eq. 2.3), and  $\tau_{th}^{-1} = Rn_{th} + \tau_{max}^{-1}$  is the lifetime. The power spectral density of shot noise in the recombination rate  $\Gamma_r$  from the recombination of all quasiparticles is given by

$$S_{\Gamma_r} = 2\Gamma_r = N_{qp}(\tau_{max}^{-1} + \tau_{qp}^{-1}). \quad (2.70)$$

Both the above power spectra are defined for double-sided noise. With some calculation it can be shown [13] that the contribution of the above generation and recombination terms to the noise equivalent power is

$$\text{NEP}_{g-r}^2 = 2[N_{th}(\tau_{max}^{-1} + \tau_{th}^{-1}) + N_{qp}(\tau_{max}^{-1} + \tau_{qp}^{-1})] \left(\frac{\Delta_0}{\eta_o}\right)^2 \quad (2.71)$$

where the factor of 2 is to account for noise in positive and negative frequencies (single-sided spectra), and the two major terms correspond to  $\text{NEP}_{th}^2$  and  $\text{NEP}_r^2$ . For an optically loaded detector where the loading level is high and  $N_{qp}$  is dominated by the optical loading, we can write  $N_{qp}/\tau_{qp}$  in terms of  $P_o$  using Eq. 2.32 and Eq. 2.31.

After some calculation we can estimate the recombination NEP as

$$\text{NEP}_r \approx 2\sqrt{\frac{P_o\Delta_0}{\eta_o}}. \quad (2.72)$$

The photon noise equivalent power intrinsic to the incident optical signal is given by [13]

$$\text{NEP}_{ph}^2 = 2P_o h\nu(1 + n_0) \quad (2.73)$$

where  $n_0 = 1/(e^{h\nu/k_B T} - 1)$  is the photon occupation number and  $\nu$  is the photon frequency. The factor of two is for single-sided noise.

The amplifier noise contribution to NEP can be calculated by using Eq. 2.51 together with Eq. 2.67 or Eq. 2.68. The amplifier NEP contribution to the dissipation direction signal and to the frequency direction signal are:

$$\text{NEP}_{\text{diss}}^{\text{amp}} = \sqrt{2} \times \sqrt{\frac{k_B T_a}{2P_{\text{feed}}}} \times \frac{\delta P_o}{\text{Re}(\delta S_{21})} = \frac{4N_{qp} \Delta_0}{\eta_o \chi_c \chi_{qp} \tau_{qp}} \sqrt{\frac{k_B T_a}{P_{\text{feed}}}} \quad (2.74)$$

$$\text{NEP}_{\text{freq}}^{\text{amp}} = \sqrt{2} \times \sqrt{\frac{k_B T_a}{2P_{\text{feed}}}} \times \frac{\delta P_o}{\text{Im}(\delta S_{21})} = \frac{4N_{qp} \Delta_0}{\beta(\omega)\eta_o \chi_c \chi_{qp} \tau_{qp}} \sqrt{\frac{k_B T_a}{P_{\text{feed}}}} \quad (2.75)$$

where the factor of  $\sqrt{2}$  is for single-sided NEP.

The TLS NEP contribution to the frequency direction signal can be calculated by using Eq. 2.63 together with the TLS fractional frequency noise spectral density  $S_{\text{TLS}}$ :

$$\text{NEP}_{\text{TLS}}^2 = \frac{2S_{\text{TLS}}}{R_x^2} = 2 \left( \frac{4N_0 \Delta_0^2 V}{\alpha \eta_o S_2(\omega) \tau_{qp}} \right)^2 S_{\text{TLS}}. \quad (2.76)$$

The factor of 2 is for single-sided NEP assuming that  $S_{\text{TLS}}$  is double-sided. Now we have everything to write an expression for the total NEP in the frequency and

dissipation signal directions:

$$\begin{aligned} \text{NEP}_{\text{diss}}^2 &= 2P_o h\nu(1 + n_o) + 2[N_{th}(\tau_{max}^{-1} + \tau_{th}^{-1}) + N_{qp}(\tau_{max}^{-1} + \tau_{qp}^{-1})] \left(\frac{\Delta_0}{\eta_o}\right)^2 \\ &\quad + \left(\frac{4N_{qp} \Delta_0}{\eta_o \chi_c \chi_{qp} \tau_{qp}}\right)^2 \frac{k_B T_a}{P_{\text{feed}}} \end{aligned} \quad (2.77)$$

$$\begin{aligned} \text{NEP}_{\text{freq}}^2 &= 2P_o h\nu(1 + n_o) + 2[N_{th}(\tau_{max}^{-1} + \tau_{th}^{-1}) + N_{qp}(\tau_{max}^{-1} + \tau_{qp}^{-1})] \left(\frac{\Delta_0}{\eta_o}\right)^2 \\ &\quad + \left(\frac{4N_{qp} \Delta_0}{\beta(\omega) \eta_o \chi_c \chi_{qp} \tau_{qp}}\right)^2 \frac{k_B T_a}{P_{\text{feed}}} + 2 \left(\frac{4N_0 \Delta_0^2 V}{\alpha \eta_o S_2(\omega) \tau_{qp}}\right)^2 S_{\text{TLS}} \end{aligned} \quad (2.78)$$

where the above NEPs are single-sided.

### 2.4.1 Photon noise limited condition

It is useful to calculate the condition when  $\text{NEP}_{\text{TLS}} \leq \text{NEP}_{\text{ph}}$ ; i.e., photon noise-limited operation of the detector. We assume that the optical illumination power is high such that  $\Gamma_e \tau_{max}/N^* \gg 1$  which is the case for ground-based submillimeter astronomy. Using Eq. 2.32 and Eq. 2.27 this gives a quasiparticle lifetime  $\tau_{qp} \approx \sqrt{\tau_{max} n^* \Delta_0 V / 2\eta_o P_o}$ . We can further use Eq. 2.24 to substitute  $n^* \tau_{max}$  by  $2N_0 \tau_0 k_B T_c / F^2$  where  $F = 2\Delta_0 / k_B T_c \approx 3.52$ . Doing so we can set the required condition as

$$\text{NEP}_{\text{TLS}}^2 = \frac{32 \Delta_0^2 F^2 N_0 V P_o \Delta_0}{\alpha^2 S_2(\omega)^2 \tau_0 k_B T_c \eta_o} S_{\text{TLS}} < 2P_o h\nu(1 + n_o) = \text{NEP}_{\text{ph}}^2. \quad (2.79)$$

Rearranging the above we get

$$S_{\text{TLS}} < \frac{h\nu(1 + n_o) \alpha^2 S_2(\omega)^2 \tau_0 \eta_o}{8 \Delta_0^2 F^3 N_0 V}. \quad (2.80)$$

We can use the above equation to evaluate whether the TLS noise in a certain device is sufficiently low to be limited by the photon background noise. As an example,

for ground-based submillimeter astronomy at  $\lambda = 350 \mu\text{m}$  assuming an atmospheric temperature of 270 K gives  $n_0 \approx 6$ . For a typical MKID, if we assume a resonator active inductor volume  $V = 1000 \mu\text{m}^3$  made from aluminum ( $T_c = 1.2 \text{ K}$ ), electron-phonon interaction time  $\tau_0 = 438 \text{ nsec}$  [32], a resonance frequency  $f_r = 5 \text{ GHz}$ , and  $S_2 \sim 2.5$ , we get an upper limit for single-sided TLS fractional frequency noise power spectral density of

$$S_{\text{TLS}}^{\text{SS}} < \alpha^2 \times 5 \times 10^{-16} \text{ Hz}^{-1} . \quad (2.81)$$

## Chapter 3

# Two-level system (TLS) noise reduction for MKIDs

In this chapter we will discuss the details of a technique for reducing excess frequency noise in superconducting microwave resonators. Intrinsic noise in the form of an excess resonance frequency jitter exists in planar superconducting resonators that are made on dielectric substrates – usually crystalline silicon or sapphire [12, 33]. This noise can be a serious problem when these resonators are used as kinetic inductance detectors and can limit the sensitivity that is needed for astronomical observations. These resonators are also of interest in other applications including readout multiplexing of transition edge sensors [24], parametric amplifiers [25], and quantum computation [34], which could benefit from lower noise resonators. As we conclusively show in this chapter, this noise is due to fluctuations of the resonator capacitance [35]. In turn, the capacitance fluctuations are thought to be driven by two-level system (TLS) fluctuators in a thin layer on the surface of the device [36].

We will first give an introduction to TLS and their effects on resonators, and then will describe a novel design aimed for reducing TLS noise. We will show measurements of important resonator properties and noise, and will see that our design is indeed successful in significantly reducing TLS noise.

### 3.1 Introduction to two-level systems

Amorphous solids have very different thermal, acoustic, and dielectric bulk properties at low temperatures as compared to crystalline solids. In 1972 Phillips [37] and Anderson [38] introduced a model that successfully explains these properties observed in experiments. Their model attributes these properties to the presence of quantum two-level systems (TLS) in amorphous materials. TLS arise due to the disordered structure of amorphous materials because one or a group of atoms can move from one configuration to another configuration corresponding to two local potential energy minima. The atoms do this by quantum tunneling over an energy barrier to the other state. The difference between the energies in the two states arises from an energy difference between the two chemical bond configuration. The tunneling behavior of TLS can be quantum mechanically described as a particle in a double-potential well. Because of the random nature of these materials the energy minima and the barrier energy height are assumed to be random in this model, leading to a random, uniform distribution of TLS energy splittings. The atoms have an electric dipole moment which makes them electrically active each time they tunnel. These dipole moments can couple to electric fields, and therefore can affect the dielectric constant of the material and introduce additional dielectric loss. If TLS exist inside a microwave resonator, the electric fields from the resonator will couple to the dipoles of the TLS and power will be stolen from the resonator and turned into loss reducing the resonance quality factor.

The existence of TLS can also produce excess frequency noise in superconducting resonators. This is due to the random nature of TLS tunneling events causing a random fluctuation in the dielectric constant. The fluctuations could be caused by different mechanisms. These could be random emission or absorption of phonons. Another possibility could be the random tunneling of neighboring TLS creating a random potential energy landscape for each individual TLS. The microscopic picture has not been studied and is not clear, but whatever the cause it can create frequency

noise in resonators which can significantly impact the performance of MKIDs.

For these reasons it is important to evaluate the effect of TLS in superconducting resonators, and to find ways to reduce the loss and noise. Below we will describe the effects of TLS loss and noise on resonators in more detail.

## 3.2 Resonator loss from TLS

As explained above, TLS exist inside amorphous materials. Significant studies have been done to determine the effect and amount of TLS loss in superconducting qubits for quantum computing [39, 40] where low loss is essential for long coherence times, and in superconducting microwave resonators used for MKIDs [28, 41, 42] where high  $Q$ s are desirable. The details of the theory relevant to the case of MKIDs were carried out in Gao's PhD thesis work [28].

TLS have dipole moments that can couple to electric fields, and therefore can contribute an amount  $\epsilon_{\text{TLS}}(f, T)$  to the real (reactive) and imaginary (dissipative) parts of the dielectric constant  $\epsilon$  of the TLS-hosting material. First we look at the effect of the imaginary part.

In the case of weak electric fields  $|E| \ll E_c$  (or low microwave powers  $P \ll P_c$ ) where  $E_c$  and  $P_c$  are a critical field and power, the TLS contribution to the dielectric loss tangent  $\delta$  in a bulk material is given by [28, 43]:

$$\delta_{\text{TLS}}(f, T) = \frac{\text{Im}\{\epsilon_{\text{TLS}}(f, T)\}}{\text{Re}\{\epsilon\}} = \delta_0 \tanh\left(\frac{hf}{2k_B T}\right), \quad (3.1)$$

where  $\delta_0$  represents the TLS-induced loss tangent at zero temperature and weak electric fields, and is proportional to the density of TLS per unit volume and energy. The hyperbolic tangent factor comes from the thermal occupation probabilities of the two quantum states: when  $k_B T \ll hf$ , the TLS only occupy the ground state and maximum power absorption can happen which leads to  $\delta_{\text{TLS}}(f, T) \rightarrow \delta_0$ . In the

limit where  $k_B T \gg hf$ , the excited state is well occupied and stimulated emission cancels much of the absorption, leading to  $\delta_{\text{TLS}}(f, T) \propto hf/k_B T$  [13]. For the case of high microwave powers  $P$ , it can be shown [44, 28, 43] that the loss tangent becomes power dependent

$$\delta_{\text{TLS}}(P) = \frac{\delta_{\text{TLS}}(P=0)}{\sqrt{1 + P/P_c}} \quad (3.2)$$

where  $P_c$  is the critical power for TLS saturation and is related to the tunneling transition strength. This power dependence has been experimentally observed in superconducting resonators [28, 45, 40] and in superconducting qubits [39]. For the case of superconducting resonators, the internal resonator loss due to TLS ( $1/Q_i^{\text{TLS}}$ ) is related to the loss tangent by

$$\frac{1}{Q_i^{\text{TLS}}} = -\frac{\int_{V_h} \text{Im}\{\epsilon_{\text{TLS}}\} |\vec{E}(\vec{r})|^2 d\vec{r}}{\int_V \epsilon |\vec{E}(\vec{r})|^2 d\vec{r}} = F_{\text{TLS}} \delta_{\text{TLS}}(f, T) \quad (3.3)$$

where

$$F_{\text{TLS}} = \frac{\int_{V_h} \epsilon_h \vec{E}(\vec{r})^2 d\vec{r}}{\int_V \epsilon \vec{E}(\vec{r})^2 d\vec{r}} = \frac{w_h^e}{w^e}. \quad (3.4)$$

Here  $F_{\text{TLS}}$  is a filling factor that accounts for the fact that the TLS hosting material with  $\epsilon_h$  and volume  $V_h$  may only partially fill the resonator volume  $V$ , and is equal to the ratio of the electric energy  $w_h^e$  stored in the TLS hosting volume to the total electric energy  $w^e$  stored in the resonator [28]. For the case when  $P \ll P_c$ , we can write

$$\frac{1}{Q_i^{\text{TLS}}} = F_{\text{TLS}} \delta_0 \tanh\left(\frac{hf}{2k_B T}\right). \quad (3.5)$$

TLS also affects the reactive part of  $\epsilon$  which manifests itself by a resonance frequency shift in resonators. The change in the reactive part of epsilon is related to a change in resonance frequency

$$\frac{\Delta f_r}{f_r} = -\frac{F_{\text{TLS}} \text{Re}\{\epsilon_{\text{TLS}}\}}{2 \text{Re}\{\epsilon\}} \quad (3.6)$$

$$= -\frac{\int_{V_h} \text{Re}\{\epsilon_{\text{TLS}}\} |\vec{E}(\vec{r})|^2 d\vec{r}}{2 \int_V \epsilon |\vec{E}(\vec{r})|^2 d\vec{r}}. \quad (3.7)$$

The shift can be calculated by using the Kramers-Kroenig relationship between the real and imaginary parts of the dielectric constant and is equal to

$$\frac{\Delta f_r}{f_r} = \frac{f_r(T) - f_r(T=0)}{f_r} = \frac{F_{\text{TLS}}\delta_0}{\pi} \left[ \text{Re}\Psi\left(\frac{1}{2} + \frac{1}{2\pi i} \frac{hf}{k_B T}\right) - \ln \frac{hf}{k_B T} \right], \quad (3.8)$$

where  $\Psi$  is the complex digamma function [28, 43], and has negligible power dependence.

Equations 3.5 and 3.8 can be used to experimentally diagnose the presence of TLS in resonators and to quantify its amount: for a certain resonator we can sweep the bath temperature  $T$  over a wide range recording  $f_r(T)$  and  $Q_i(T)$ . We can then use equations 3.5 and 3.8 along with the Mattis–Bardeen equations describing the quasiparticle-induced change in  $f_r$  and  $1/Q_i$  (Eq. 2.56 and Eq. 2.60) to fit to the data and extract the  $F_{\text{TLS}}\delta_0$  factor.  $F_{\text{TLS}}$  can be determined numerically for the specific resonator geometry at hand if the specific location and geometry of the TLS hosting material are known. Also, knowledge of the distribution of the electric field in the resonator is needed. This has been demonstrated [28] for CPW resonators where a thick artificial layer of dielectric (e.g.,  $\text{SiN}_x$  or  $\text{SiO}_2$ ) was deposited on the CPW resonator so that  $F_{\text{TLS}}$  could be easily determined from EM simulations. The frequency shift and the internal quality factor were shown to agree with the predictions of Eq. 3.8 and Eq. 3.5. However, if the exact location and geometry of the TLS hosting material is not known, it would be difficult to diagnose the type of material hosting the TLS and to determine its loss tangent. This problem becomes more evident in the case of resonators that are fabricated on a crystalline substrate (like Si or sapphire) and do not use any deposited amorphous films. In these resonators even though amorphous materials are not used, a small amount of TLS loss and TLS frequency shift is still observed, but the location of the TLS are not evident. Gao et al. showed that in these resonators a thin (few nm) layer of TLS hosting material on the surface of the resonator is responsible for the TLS loss and frequency shift observed [46]. They used geometrical scaling of CPW resonator center strip widths  $s$  to argue

that the corresponding scaling of  $s^{-1}$  in TLS frequency shift can only be explained by a surface distribution and not a bulk distribution of TLS. This is because for a bulk distribution the filling factor  $F_{\text{TLS}}$  is fixed while for a 2D distribution it reduces as  $\sim s^{-1}$  as the CPW becomes wider. For TLS loss, Barends et al. [47] showed that by removing part of the silicon substrate in the CPW slot regions with high electric field,  $F_{\text{TLS}}$  can be reduced resulting in lower TLS loss. This can be understood by noting in Eq. 3.3 that the TLS from different locations in the resonator contribute to the loss with a scaling of  $|\vec{E}(\vec{r})|^2$ . Therefore, TLS located in the high-field regions are more important and should be considered in the resonator design process. There are many candidates for the TLS surface layer material in superconducting resonators. Native oxide layers from metals like Al and Nb, or native oxides from crystalline substrates like Si and sapphire can all be host material for TLS. Defect impurities or chemical residues left from fabrication processing steps like etching or other processes can also be responsible.

### 3.3 Resonator frequency noise from TLS

MKID resonators consistently show excess frequency noise [12, 33, 48, 42, 36]. The noise is a small time-dependent jitter of the resonance frequency  $f_r$  characterized by the frequency noise power spectral density  $S_{\delta f_r}$  in units of  $\text{Hz}^2/\text{Hz}$ , or the fractional frequency noise spectral density  $S_{\delta f_r/f_r}$  in units of  $1/\text{Hz}$ . This noise corresponds to fluctuations in the transmission  $S_{21}$  that are tangential to the resonance circle and is in excess of the amplifier noise. In contrast, noise in the perpendicular direction ( $S_{\delta 1/Q_r}$  ( $1/\text{Hz}$ )) corresponding to dissipation or  $Q$  fluctuations only comes from the amplifier and no excess noise is seen, even below the standard quantum limit [49].

The frequency and dissipation noise are illustrated in Fig. 3.1 where contribution from the TLS typically dominates the frequency noise in CPW resonators. The dissipation noise spectrum is flat except for a  $1/\nu$  gain noise below 10 Hz. The level

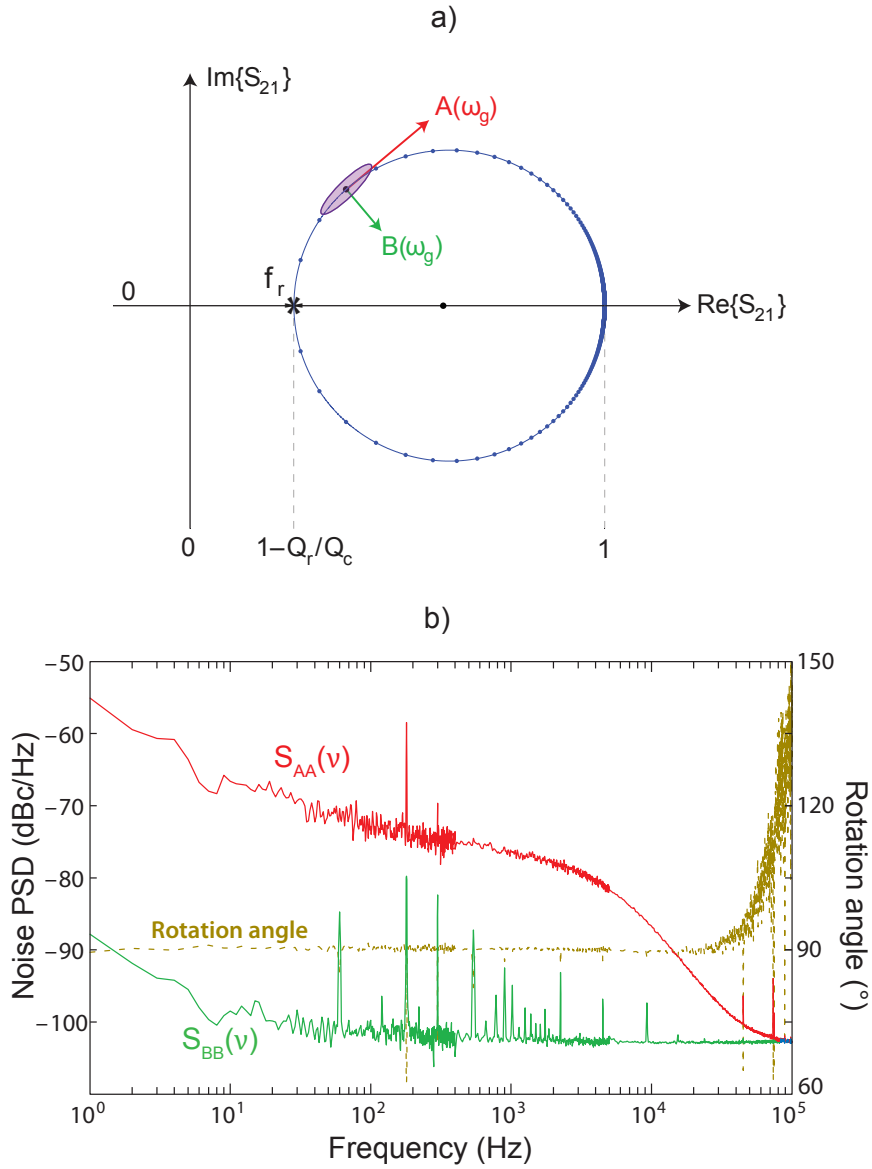


Figure 3.1: (a) The circular trajectory of the complex transmission  $S_{21}$  as a function of frequency for a resonator is shown along with the resonance frequency  $f_r$ . The dots on the circle represent fixed frequency steps. The directions tangent and perpendicular to the resonance loop at a fixed generator frequency  $\omega_g = 2\pi f_g$  are indicated by the complex vectors  $A(\omega_g)$  and  $B(\omega_g)$ . An ellipse representing the observed noise blob from the frequency and dissipation fluctuations is shown. The main axis of the ellipse is in the tangential direction corresponding to frequency fluctuations. (b) Noise power spectral density for fluctuations in the frequency direction (A) strongly dominated by TLS noise, and dissipation direction (B) limited by the amplifier noise for a Nb/Si superconducting microresonator. The rotation angle between the major axis of the noise ellipse and the B direction at each frequency is  $90^\circ$  inside the resonator response bandwidth. Figure (b) reproduced from [48].

corresponds to the amplifier noise floor which can be measured when the frequency is tuned far from resonance. The frequency noise spectrum typically has a  $1/\nu$  shape below 10 Hz, a  $1/\nu^{0.5}$  shape above 10 Hz, and a rolloff that happens at the smaller of the resonator bandwidth ( $f_r/2Q_r$ ) or the intrinsic noise bandwidth  $\Delta\nu_n$ .

TLS noise is observed to scale with microwave readout power as  $P^{-1/2}$  and with temperature as  $T^{-\beta}$  with  $\beta = 1.5-2$  [48, 42]. The power dependence is similar to the low-temperature TLS loss saturation effect in Eq. 3.2. Using these observations Gao et al. developed a semiempirical model [36] for TLS noise in superconducting resonators. In this model the TLS fractional frequency ( $\delta f_r/f_r$ ) noise power spectral density at high microwave readout powers is given by

$$S_{\text{TLS}} = \kappa(\nu, \omega, T) \frac{\int_{V_h} |\vec{E}(\vec{r})|^3 d^3r}{4 \left( \int_V \epsilon |\vec{E}(\vec{r})|^2 d^3r \right)^2} \quad (3.9)$$

where  $\kappa(\nu, \omega, T)$  is defined as the noise spectral density coefficient and captures the  $\nu^{-1/2}$  spectral shape and the dependence on microwave frequency  $\omega$  and temperature. The formula readily reproduces the power scaling as  $|E|^{-1} \propto P^{-1/2}$ , similar to what is experimentally observed. This model has been confirmed experimentally through observation of geometrical scaling of TLS noise with CPW center strip width  $s$  where it was observed [36] that noise scales as  $s^{-1.58}$ . Based on strong evidence discussed in Section 3.2 that TLS have a surface distribution, they numerically calculated the  $\vec{E}(\vec{r})$  field for their CPW resonators assuming a surface distribution of TLS, and used that result in their Eq. 3.9 to show that they get the same scaling as their experiment.

### 3.4 A microwave resonator design for reduced TLS noise

Motivated by the implications of the semiempirical noise model discussed above, we started an effort to design and measure a new resonator geometry that could reduce

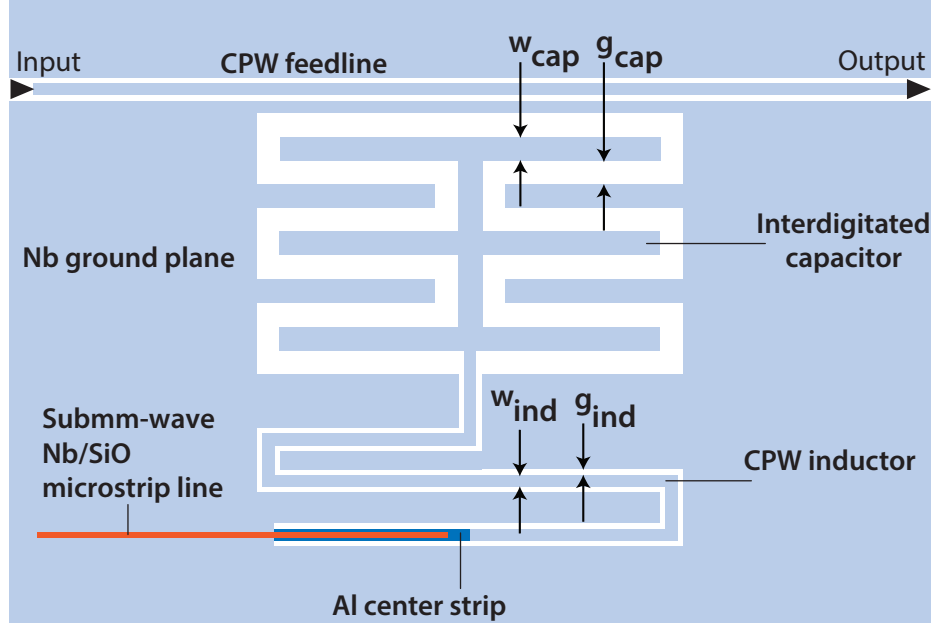


Figure 3.2: Schematic illustration of an interdigitated capacitor (IDC) resonator used in this work.  $w_{cap}$  and  $s_{cap}$  are large to reduce TLS noise. For illustration purpose the dimensions are not to scale and the capacitor shown has only 5 fingers on each side. The actual devices have more fingers. The resonator is capacitively coupled to a CPW feedline. The resonator is mainly made from Nb on a Si substrate except for a  $\sim 1$ -mm-long aluminum-on-Si section. The CPW inductor is short-circuited at the Al end where the current is maximum. The mm/submm radiation can be brought to the resonator with a low-loss microstrip line where it is absorbed in the Al section.

TLS noise. Several different resonator geometries were designed in the beginning, but in the end one design turned out to be most effective which is described in this chapter and for which measurements were taken.

A key prediction of the noise model in Eq. 3.9 is that the noise contributions from individual TLS located on the resonator surface are weighted by  $|\vec{E}|^3$ . This implies that TLS located in high  $E$ -field areas are the main contributors to the noise. The high  $E$ -field section of a resonator is its capacitive portion, and so by redesigning this portion one could potentially lower the noise. This can be done by widening the electrode spacings in the capacitor which spreads the  $E$ -field distribution in a way that less electric field lines go through the surface TLS layer, effectively reducing the filling factor  $F_{\text{TLS}}$  defined in Eq. 3.4.

We used this insight to develop a modified resonator geometry [35] in which the capacitive section of a conventional  $\lambda/4$  CPW resonator has been replaced by an interdigitated capacitor (IDC) structure with wide finger spacings (Fig. 3.2). The inductive low  $E$ -field section was left unchanged as compared to our conventional CPW resonators. This makes it possible to directly compare our noise results with regular CPW resonators. Furthermore, since we were planning to use these resonators as MKIDs for photon detection (initially with the MKIDcam instrument [50] and later with the MUSIC instrument [17]; see Fig. 3.12), it was important to keep the inductive section narrow to maintain a high kinetic inductance fraction ( $\alpha$ ) needed for maximum responsivity. The details of the actual fabricated devices are explained next.

### 3.4.1 Device details

Figure 3.3 shows a picture of the fabricated resonators along with the device box. There are 8 resonators on the chip corresponding to 2 different resonator geometries (4 of each geometry). Both geometries have IDCs but with different size.

The first geometry (Fig. 3.3 (a)) has an IDC made of 19 fingers on each side of the vertical strip in the middle of the IDC. Finger width and spacing are  $w_{cap} = 10 \mu\text{m}$  and  $g_{cap} = 10 \mu\text{m}$ . The IDC is  $1040 \mu\text{m} \times 390 \mu\text{m}$  giving a capacitor area of  $0.40 \text{ mm}^2$  and a capacitance value of  $C_{10-10} \approx 2.0 \text{ pF}$ . It is made from 200-nm-thick Nb on a  $450\text{-}\mu\text{m}$ -thick crystalline silicon substrate (with a thin native oxide layer expected to be present due to air exposure) using a photoresist mask and an  $\text{SF}_6$  plasma etch. The distance between the IDC and the feedline as well as the IDC width controls the coupling of the resonator to the feedline  $Q_c$ .

The narrow CPW meander acts as a CPW inductor that is short-circuited on one end. Since it is relatively short it acts as a lumped-element inductor. As mentioned before, this design was intended for use as an MKID for the MKIDcam [50]

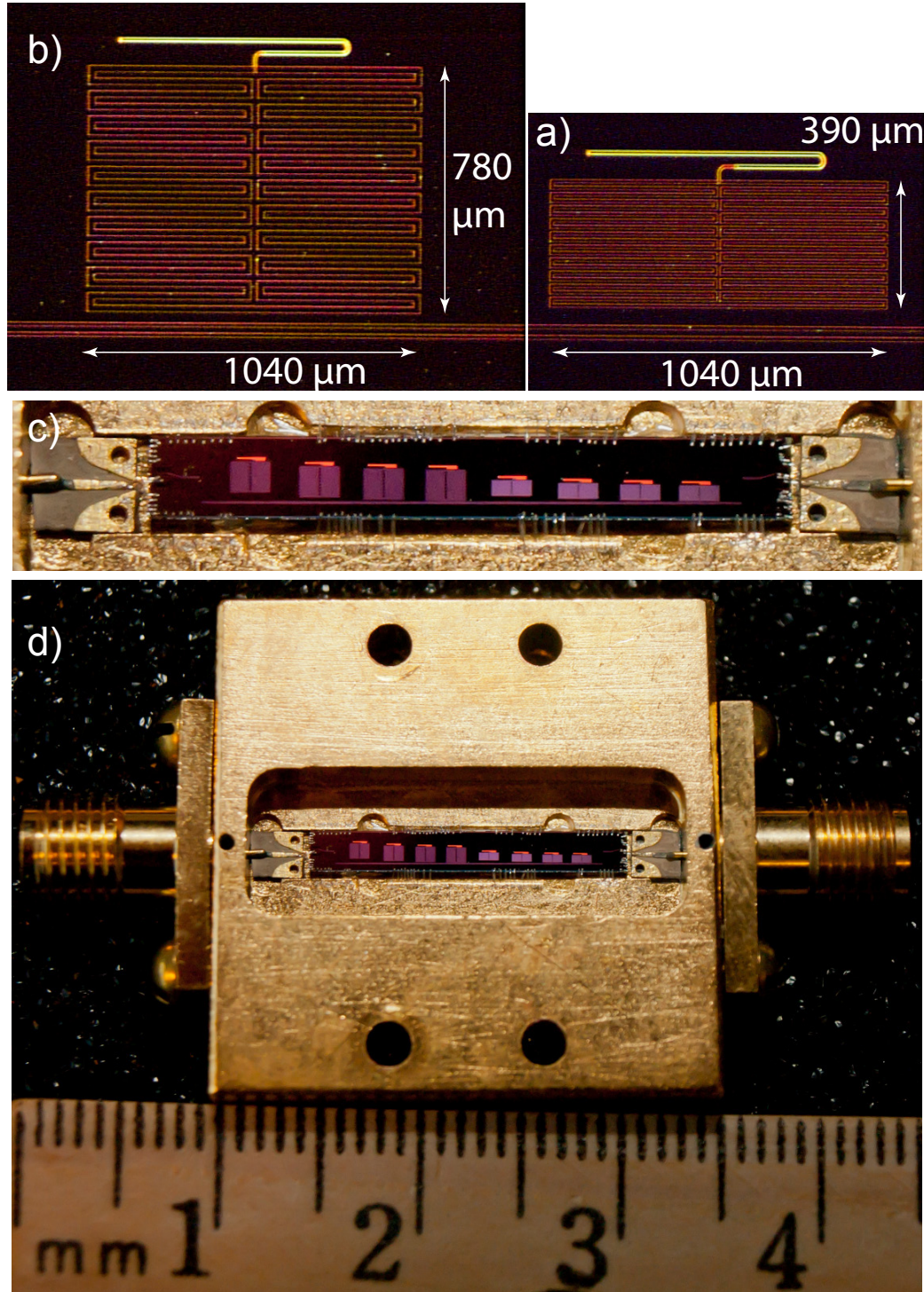


Figure 3.3: (a) Photograph of an IDC resonator in the first group with  $w_{cap} = 10 \mu\text{m}$  and  $g_{cap} = 10 \mu\text{m}$ . (b) An IDC resonator in the second group with  $w_{cap} = 20 \mu\text{m}$  and  $g_{cap} = 20 \mu\text{m}$ . (c) Device chip with the 8 resonators mounted inside a test box. Wirebonds between chip and duroid circuit board and metal box are visible. (d) Measurement box with SMA connectors on both sides.

and MUSIC [17] instruments, and therefore it was designed to be as close to an actual photon sensor as possible which would help in identifying any unforeseen issues. Hence, part of the length of the inductor was made of a 1-mm-long CPW with the center strip made from 60-nm-thick aluminum and the ground planes made from 200-nm-thick Nb. This section would act as the photon sensory part. The millimeter/submillimeter radiation collected using a separate antenna would then travel on a Nb/SiO<sub>2</sub>/Nb microstrip line reaching the beginning of the Al CPW section at the shorted end. The microstrip line would then combine with the CPW turning into a Nb/SiO<sub>2</sub>/Al microstrip line. The radiation would then be absorbed in the aluminum creating quasiparticles in the resonator (see Fig. 3.2). Since Al has a lower superconducting energy gap ( $\nu_g^{Al} \approx 90$  GHz) than Nb ( $\nu_g^{Nb} \approx 700$  GHz), the Al section also keeps the quasiparticles trapped so they don't escape. However, we did not include the microstrip line in the actual fabricated devices since the experiment was intended to be done with the devices inside a dark cryostat for dark noise testing (no optical window to couple radiation from). In order to tune the resonance frequency and space the four resonances  $\sim 50$  MHz apart, a short extra length of pure Nb CPW inductor ( $l_{Nb} = 54\text{--}134 \mu\text{m}$ ) is inserted between the Nb IDC and the Al CPW inductor.

The design of the second geometry (Fig. 3.3 (b)) is the same as the first design except for the IDC dimensions. It has  $w_{cap} = 20 \mu\text{m}$  and  $g_{cap} = 20 \mu\text{m}$  and is  $1040 \mu\text{m} \times 780 \mu\text{m}$  giving a capacitor area of  $0.81 \text{ mm}^2$  and a capacitance value of  $C_{20-20} \approx 2.4$  pF.

Fig. 3.3 (c) and (d) show the chip with the 8 resonators mounted inside a test box. The box is made from oxygen-free high-purity copper that has been plated with a nonmagnetic gold layer to avoid exposing the magnetic-field-sensitive resonators [51] to unwanted magnetic fields. The signal is brought in through the SMA coaxial connection on one side and read out from the other side. The center pin of the coaxial connector is soldered to a microstrip line on a duroid circuit board. The microstrip line transitions to a CPW on this board and is brought to the chip using wirebonds where it connects to the on chip CPW bond pads.

Before describing the measurements on this device we will mention a few important design considerations that are important for IDC resonators.

### 3.4.2 Some design considerations

In order to reduce TLS noise as much as possible, the capacitor area and electrode spacings ( $w_{cap}$  and  $s_{cap}$ ) have to be made as large as possible. However, the IDC can quickly get too big resulting in several issues. One is that the IDC could act as a distributed element with propagating modes rather than a lumped capacitor. This would result in nonzero microwave currents in the capacitor that can introduce parasitic inductance reducing the effective capacitance and also reduce the kinetic inductance fraction in case the resonator is being used as an MKID. This can happen if the size is larger than  $\sim \lambda/20$  where  $\lambda$  is the wavelength of the propagating mode. For a 5 GHz resonator on a silicon substrate  $\sim \lambda/20 = 1.2$  mm assuming a CPW propagating mode. The IDCs in our resonators are close to the limit of lumped-element performance. We simulated the capacitors in Sonnet [52] and confirmed that they are close to being lumped-element, although some amount of currents were produced in the capacitors.

Another concern is microwave radiation into the substrate from the capacitor which could reduce the internal quality factor of the resonator. This can happen in certain types of large IDC or CPW structures if not properly designed. For example, from a TLS noise point of view, one could use a “fat” CPW resonator where the center strip width and gaps are increased to reduce noise. However, such a structure can radiate into space significantly reducing the quality factor [13]. To minimize microwave radiation it is important to design the structure so that opposite polarity conductors are always close to each other canceling the radiation from opposite polarity currents. This is also important for large IDC structures and in fact became an issue in our initial design where we had used a slightly different IDC structure. The lost power through radiation can be checked using an electromagnetic simulation software like

Sonnet [52] by looking at  $1 - |S_{11}|^2$  for a one-port circuit element like an IDC, or by running a two-port simulation for the whole resonator with a feedline and looking at  $1 - |S_{11}|^2 - |S_{21}|^2$ , where  $S_{11}$  and  $S_{21}$  are the microwave scattering parameters.

Another important issue for an array of MKID resonators on a chip is the limited space availability for each resonator. Interdigitated capacitors with wide finger spacings can take a significant amount of area on chip and are not necessarily the best option for use in tightly packed MKID arrays. For example, parallel-plate capacitor structures on silicon-on-insulator substrates [53] can take much less area for the same amount of capacitance and could provide an alternate solution for size. Additionally, it has been suggested that such capacitors could potentially have very low TLS noise because the crystalline silicon dielectric in between the plates is nearly free of TLS. If the metal/substrate interface is carefully fabricated to avoid any oxidation layers or other sources of thin TLS-containing layers, the capacitor could be almost TLS free [13].

## 3.5 Measurements

### 3.5.1 Low-temperature resonance frequencies and quality factors

The device shown in Fig. 3.3 was cooled down to 60 mK inside a dilution refrigerator. A network analyzer was used to measure the transmission through the device. The microwave signal goes through the feedline and is amplified at the output of the box using a cryogenic HEMT (high electron mobility transistor) amplifier mounted on the 4 K stage inside the cryostat. The signal is further amplified by a room temperature amplifier and is read out by the network analyzer. The excitation frequency is swept through the resonances on the array and a computer records the complex transmission  $S_{21}$ . Figure 3.4 shows  $S_{21}$  versus frequency for the device. The resonators are in two

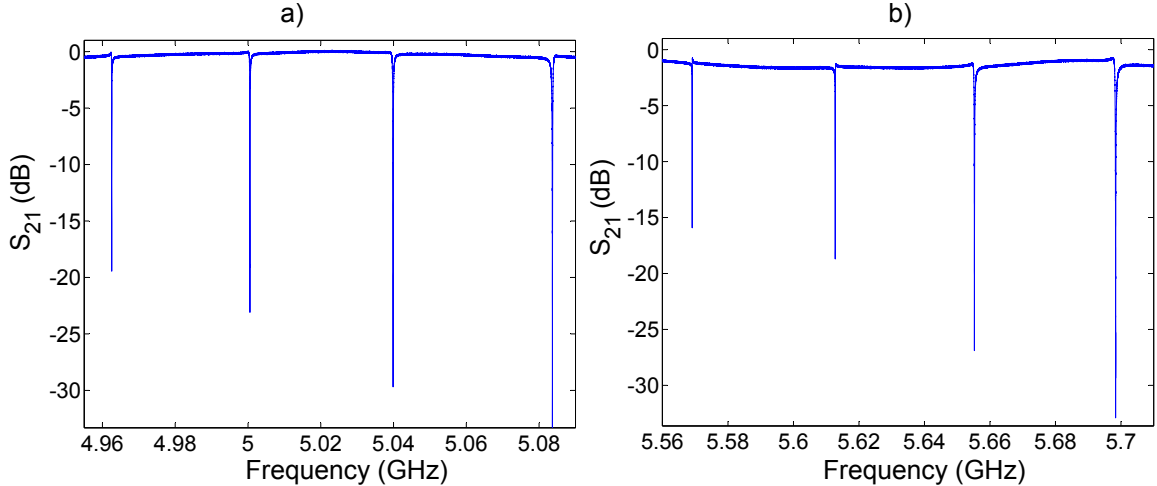


Figure 3.4: (a) Forward transmission  $S_{21}$  for resonators number 1–4. (b) Forward transmission  $S_{21}$  for resonators number 5–8. Measurements were at  $T = 60$  mK and  $P_{\text{feed}} = -95$  dBm.

groups of 4 spaced by  $\sim 40$  MHz in each group and the groups are separated by 0.5 GHz. This is inline with our simulations. We used a fitting code developed by J. Gao [28] to fit to the resonance loops and extract the resonator parameters (resonance frequency  $f_r$ , total quality factor  $Q_r$ , internal quality factor  $Q_i$ , and coupling quality factor  $Q_c$ ). These are listed in table 3.1.

We find that the resonance frequencies are  $\sim 2\%$  smaller than their design values which is expected due to the kinetic inductance of Al which was not taken into account in the simulations. The  $Q_c$ 's however do not closely match their design values. For the lowest  $Q_c$  resonators in each group the measured values are roughly two times larger than the design values. In group 1 (resonator no. 1–4) the ratio gets smaller for higher  $Q_c$ 's. Group 2 does not exactly follow this trend and resonator no. 5 has a ratio of  $\sim 3$ . We did not use CPW grounding straps to connect the CPW feedline ground planes together, so it is possible that unwanted slot-line modes on the CPW feedline are responsible for the variation [54]. Ground straps were not used because the additional fabrication processing required could affect the noise performance of the resonators since it involves the deposition and partial removal of an additional dielectric layer and via holes.

Table 3.1:  $f_r$ ,  $Q_r$ ,  $Q_i$ ,  $Q_c$ , and  $Q_c^*$  for 8 IDC resonators.  $Q_c$  is the measured coupling quality factor, and  $Q_c^*$  is the design value.

Res #	$f_r$ (GHz)	$Q_r$	$Q_i$	$Q_c$	$Q_c^*$
1	4.961	$5.35 \times 10^4$	$4.53 \times 10^5$	$6.06 \times 10^4$	$5.2 \times 10^4$
2	4.999	$2.96 \times 10^4$	$4.05 \times 10^5$	$3.20 \times 10^4$	$2.6 \times 10^4$
3	5.038	$1.81 \times 10^4$	$4.93 \times 10^5$	$1.88 \times 10^4$	$1.3 \times 10^4$
4	5.083	$1.43 \times 10^4$	$5.42 \times 10^5$	$1.47 \times 10^4$	$0.65 \times 10^4$
5	5.567	$1.44 \times 10^5$	$7.64 \times 10^5$	$1.77 \times 10^5$	$5.2 \times 10^4$
6	5.611	$6.08 \times 10^4$	$4.12 \times 10^5$	$7.13 \times 10^4$	$2.6 \times 10^4$
7	5.653	$1.81 \times 10^4$	$3.15 \times 10^5$	$1.92 \times 10^4$	$1.3 \times 10^4$
8	5.697	$1.27 \times 10^4$	$4.16 \times 10^5$	$1.31 \times 10^4$	$0.65 \times 10^4$

Bath temperature was  $T = 60$  mK and readout power  $P_{\text{feed}} = -95$  dBm.

### 3.5.2 Temperature sweep

As explained in Section 3.2 a very effective diagnostic technique is to measure resonator properties as a function of bath temperature which can identify any effects from TLS. Furthermore, the kinetic inductance fraction  $\alpha$  and superconductor energy gap  $\Delta$  can be extracted from the sweeps. We measured  $S_{21}$  for a range of bath temperatures from 60–400 mK for all 8 resonators at  $P_{\text{feed}} = -95$  dBm. As an example, Fig. 3.5 (a) shows the transmission magnitude versus frequency for resonator number 3 in this temperature range and Fig. 3.5 (b) shows the complex  $S_{21}$  resonance loop for the same resonator with temperature.

We used our fitting code to find the resonator parameters at each temperature. Fig. 3.6 (a) shows the fractional frequency shift  $\Delta f_r/f_r = (f_r(T) - f_r(T = 60 \text{ mK}))/f_r(T = 60 \text{ mK})$  as function of temperature. Figure 3.6 (b) shows the internal resonator loss  $1/Q_i$  as a function of temperature. In both plots the curves clearly split in two groups corresponding to the two different resonator geometries (resonator no. 1–4 and 5–8). This is not too surprising since  $\alpha$  could be different for the two resonator geometries even though they have the same inductor. One explanation could be that the different IDCs are contributing a small amount of inductance that

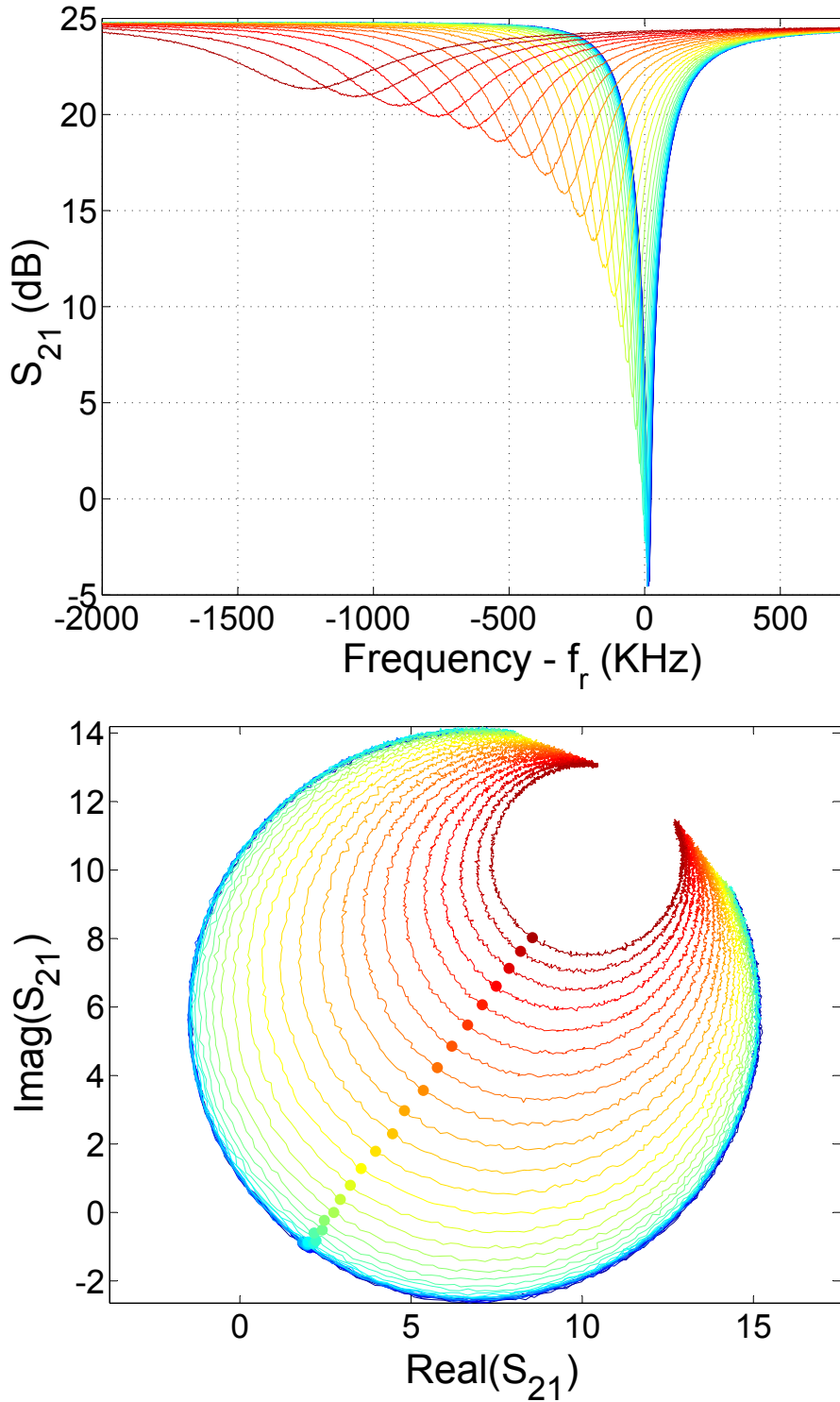


Figure 3.5: This figure shows a bath temperature sweep measurement for resonator no. 3 from  $T = 60\text{--}400$  mK in steps of 10 mK using  $P_{\text{feed}} = -95$  dBm. A constant cable delay of  $\tau = 29$  nsec has been taken out. (a) Magnitude of transmission  $S_{21}$  versus frequency. (b) Complex transmission  $S_{21}$  resonance loops. The fitted resonance frequencies at each temperature are shown by the dots.

can affect  $\alpha$  which affects the curves. The fact that the resonators in each group follow almost the same curve gives confidence that the measurement and the resonance fitting routine is accurate for resonators with different parameters.

The inset of Figure 3.6 (a) and (b) shows a closeup of the low temperature parts. For  $\Delta f_r/f_r$  there are no anomalous shifts evident that could point to the effects of TLS in the resonators. The signature frequency shift due to TLS (Eq. 3.8) has a negative minimum at  $T \approx \hbar\omega/2k_B$  which for our resonators is between 120–140 mK. At these temperatures the effects of the shifts from superconductivity from Al ( $T_c = 1.2$  K) are starting to become significant and could mask the effects of any TLS. But more importantly the absence of clear TLS effects could be due to the large finger widths and gaps in the IDCs giving a small TLS filling factor  $F_{\text{TLS}}$  (Eq. 3.4). For  $1/Q_i$  the inset shows that the curves remain constant below  $\sim 150$  mK and then quickly increase. It seems that the TLS loss (Eq. 3.5) below  $\sim 150$  mK is nearly canceled by the increase in loss from superconductivity (Eq. 2.62) until above  $\sim T_c/10$  where superconductivity dominates.

We extracted  $\alpha$  and  $\Delta$  numerically by fitting  $\Delta f_r/f_r$  and  $1/Q_i$  for each curve to Mattis-Bardeen equations Eq. 2.56 and Eq. 2.60, respectively. We used data points above  $T = 250$  mK where superconductivity dominates over TLS effects. The equations are highly degenerate in  $\alpha$  and  $\Delta$  [55], and it is usually difficult to accurately determine both parameters. The best fits were obtained when we assumed a fixed  $\Delta = 1.76k_B T_c$  with  $T_c = 1.2$  mK which is a very reasonable amount for Al with thickness  $t = 60$  nm, and seemed to satisfy all fits. Since the actual frequencies at  $T = 0$  K should not be very different from the values at  $T = 60$  mK we did not use an additional fitting parameter to account for any constant shifts in frequency. The extracted  $\alpha$ s are listed in Table 3.2 for fits to  $\Delta f_r/f_r$  (listed as  $\alpha_a$ ) and to  $1/Q_i$  (listed as  $\alpha_b$ ). The values are consistent in each group and also agree with the observation that group 1 should have a smaller  $\alpha$  since the response is slower. There is a  $\sim 7\%$  difference between  $\alpha_a$  and  $\alpha_b$  in resonators 1–4, and  $\sim 10\%$  difference for resonators 5–8 which are acceptable.

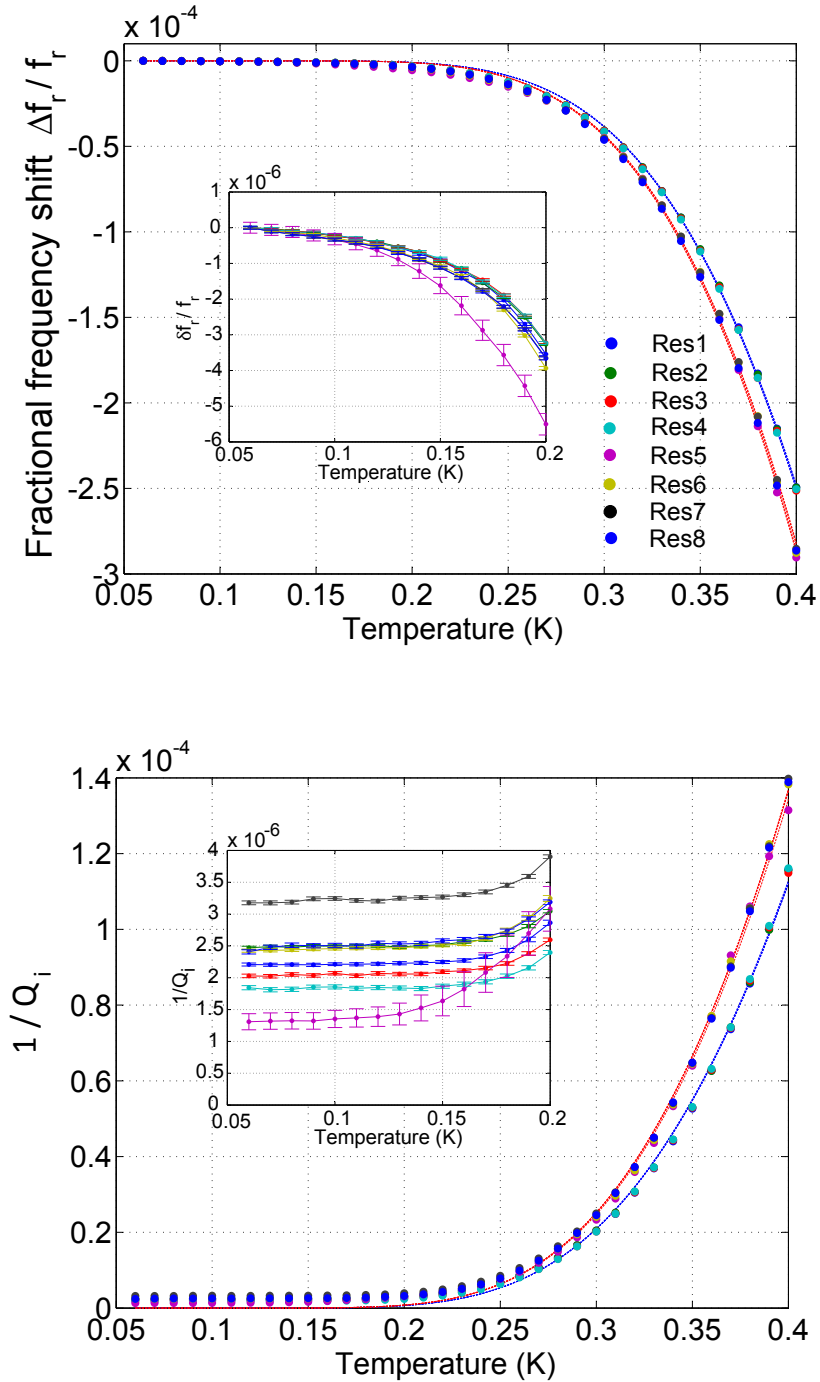


Figure 3.6: (a) Fractional frequency shifts vs. temperature for 8 IDC resonators. The group of 4 red lines and 4 blue lines are fits to resonators 1–4 and 5–8, respectively. The inset shows a closeup of the same plot at lower temperatures. Lines are not fits in the inset. (b) Internal loss for 8 IDC resonators. The group of 4 red lines and 4 blue lines are fits to resonators 1–4 and 5–8, respectively. Inset shows a closeup of the lower temperatures. Lines are not fits in the inset.

Table 3.2: Kinetic inductance fraction  $\alpha$  for 8 IDC resonators.  $\alpha_a$  is for fits to  $\Delta f_r/f_r$  and  $\alpha_b$  is for fits to  $\Delta Q_i^{-1}$

Res #	1	2	3	4	5	6	7	8
$\alpha_a$	0.037	0.037	0.038	0.038	0.044	0.043	0.043	0.044
$\alpha_b$	0.041	0.041	0.041	0.041	0.047	0.048	0.048	0.048

Fitted values have  $\lesssim 1\%$  error confidence bounds.  $\Delta_0 = 1.76k_B \times 1.2 \text{ K}$ .

We were unable to get realistic parameters when fitting the data over the full temperature range by accounting for TLS and superconductivity at the same time. For the frequency data this seems to be mainly caused by the near-linear behavior of the data between  $T = 60 \text{ mK}$  to  $150 \text{ mK}$  which could not be reproduced by the equations. Similarly for the dissipation data the constant loss at low temperatures cannot be produced unless  $F_{\text{TLS}}\delta_0$  in Eq. 3.5 is made negligibly small ( $\lesssim 10^{-8}$ ) and a constant loss is added. It is possible that the constant low loss at low temperatures is caused by radiation into free space from the IDCs, but this is a pure speculation.

The ratio of the response in frequency direction to the response in the dissipation direction (see E. 2.58 and 2.61),  $\beta = S_2(\omega, T)/S_1(\omega, T) = (2\delta f_r/f_r)/\delta Q_i^{-1}$ , can be used to check whether the data is consistent with Mattis-Bardeen theory. Figure 3.7 shows this for both resonator groups. The curves follow straight lines. We have excluded data points below  $200 \text{ mK}$  from the fit since their behavior is possibly contaminated by TLS. The average value and standard deviation of the inverse slopes for group 1 is  $\beta \sim 4.34$  and  $\text{STD}=0.02$ , and for group 2 is  $\beta \sim 4.12$  and  $\text{STD}=0.07$ . From Eq. 2.22 for a  $5 \text{ GHz}$  Al resonator we expect  $3 \lesssim \beta \lesssim 5$  for this temperature range. The observed ratio is close to the Mattis-Bardeen theory prediction but seems to lack the variation with temperature, especially for group 1. It is not clear why we observe such a constant ratio over this temperature range.

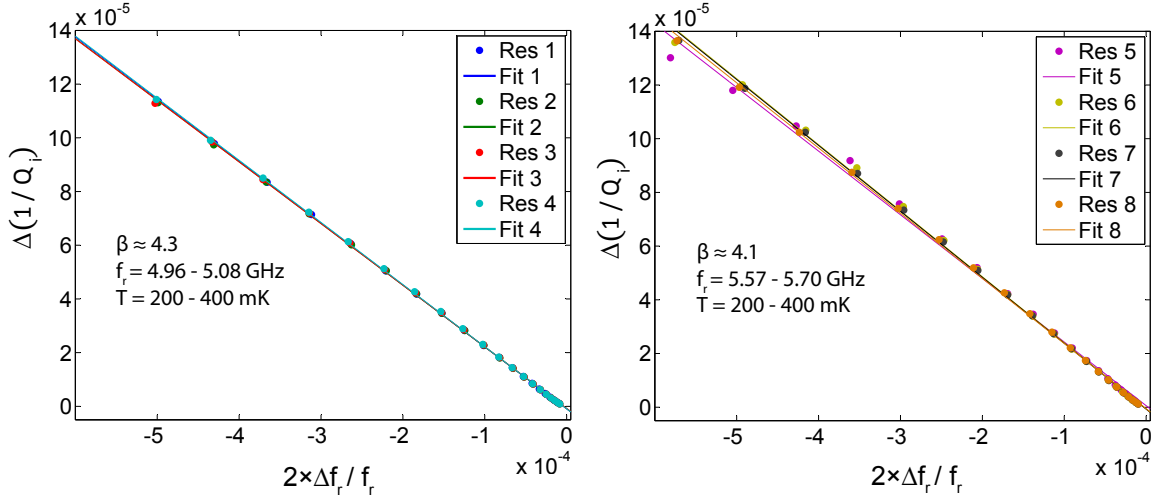


Figure 3.7: This plot shows the frequency response  $2\Delta f_r/f_r$  versus dissipation response  $\Delta Q_i^{-1}$  for 8 IDC resonator (4 in each group) measured using temperature data from 200 mK to 400 mK. The lines are linear fits to the data.

### 3.5.3 Noise measurement technique and data analysis

We used a homodyne readout system for measuring noise in our resonators. This system is routinely used for MKIDs as a standard measurement technique [12] to both readout the resonance loops and to measure noise, and is illustrated in Fig. 3.8. A synthesizer is used to provide the microwave readout signal. Half of the power goes through a controllable attenuator (Atten 1) that is used to tune the resonator readout power, and then goes inside the cryostat where it goes through a fixed attenuation of  $\sim 40$  dB to suppress room-temperature thermal radiation from entering the device box. The signal goes through the device feedline where it excites the resonators and is then amplified using a cryogenic HEMT (high electron mobility transistor) amplifier mounted on the 4 K stage of the cryostat and further amplified by a room temperature amplifier. Subsequently the signal is mixed in a quadrature (IQ) mixer with the other half of the signal. A second controllable attenuator (Atten 2) is used before the mixer to keep the RF port at constant optimum power to avoid saturation and changes in mixer properties during power sweep measurements. Therefore, Atten 1 + Atten 2 (in dB) is kept constant. The mixer output voltages I and Q are proportional to the in-phase and quadrature amplitudes of the transmitted signal. The outputs go

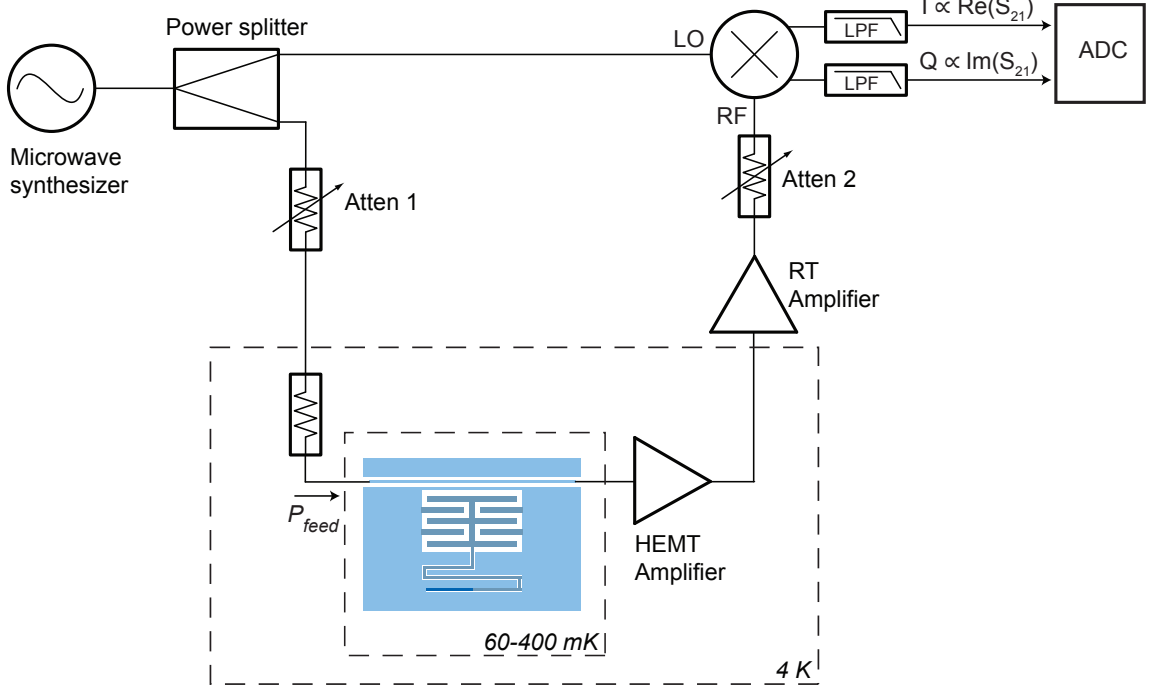


Figure 3.8: Diagram of experimental setup for measuring noise using a homodyne detection scheme

through low-pass anti-aliasing filters (100 KHz) and are digitized at a sampling rate of 200 KHz and stored on a computer for processing. As the generator frequency is swept through a resonance, a loop in the IQ plane is formed (see Fig. 3.1 (a)). We used our fitting code to find the resonance frequency and other parameters from each IQ loop. Time domain noise data were taken by fixing the frequency to the resonance frequency  $f_r$  and recording the I and Q fluctuations for 10 seconds.

To analyze the noise data for each resonator we first subtract the center of the resonance loop from the time stream data to center the loop on the IQ-plane origin. Then the data is rotated around the origin such that the I and Q axes correspond to tangent and perpendicular directions to the resonance circle at the resonance point where the noise was taken. As mentioned in Section 3.3 these directions correspond to fluctuations in the resonance frequency ( $\delta f_r$ ) and dissipation ( $\delta 1/Q_r$ ) of the resonator. We then calculate the frequency-domain power spectra for the noise voltage in these two directions. Finally, using the resonator parameters determined from fits to the

resonance loops we convert the voltage spectra to fractional frequency noise ( $S_{\delta f_r/f_r}$ ) and dissipation noise ( $S_{\delta 1/Q_r}$ ).

As a an alternative method, we also used the procedure described by Gao et al. to analyze the noise data using the frequency-domain noise covariance matrix [48]. In this method the noise covariance matrix is diagonalized to obtain the frequency and dissipation directions at each noise frequency. Results from both analysis methods agree with each other for our noise data.

### 3.5.4 Noise results and discussion

We measured noise for 8 IDC resonators using the readout system in Fig. 3.8. Fractional frequency noise power spectra for resonator no. 5 are shown in Fig. 3.9 for a range of readout powers at  $T = 120$  mK. In order to determine the TLS noise power spectrum ( $S_{\text{TLS}}$ ) we have subtracted the amplifier contribution to the total fractional frequency noise ( $S_{\delta 1/2Q_r}$ ) from the total fractional frequency noise ( $S_{\delta f_r/f_r}$ ). This is because the amplifier noise is uncorrelated with the TLS noise. We observe that  $S_{\text{TLS}}$  has a typical TLS noise spectral shape [48]. This can be more clearly seen in the highest power curve since TLS noise is more strongly expressed. Between  $10 \text{ Hz} \lesssim \nu \lesssim 10 \text{ KHz}$  the spectrum has a  $\sim \nu^{-1/2}$  shape where it starts to roll off at above this range due to the resonator response function. At  $\nu \lesssim 10 \text{ Hz}$  the spectrum picks up a  $1/\nu$  gain noise due to the readout system. Unfortunately, above a power of  $P_{\text{feed}} = -95$  dBm the resonator goes into the nonlinear saturation regime and noise could not be measured above this level. The power dependence of the TLS noise also has a typical behavior and varies as  $P_{\text{feed}}^{-1/2}$  inside the resonator bandwidth. The power dependence is more clearly seen in Fig. 3.10 which will be discussed below. At high frequencies the amplifier noise dominates which scales as  $P_{\text{feed}}^{-1}$  as expected. This is because of the second attenuator in our setup (See Fig. 3.8) which is used to keep the mixer power constant. From the data, TLS noise at  $\nu = 1 \text{ Hz}$  is  $\sim 1 \times 10^{-18} \text{ Hz}^{-1}$  and at  $\nu = 1 \text{ KHz}$  is  $\sim 1.4 \times 10^{-20} \text{ Hz}^{-1}$  for the highest readout power  $P_{\text{feed}} = -97$  dBm.

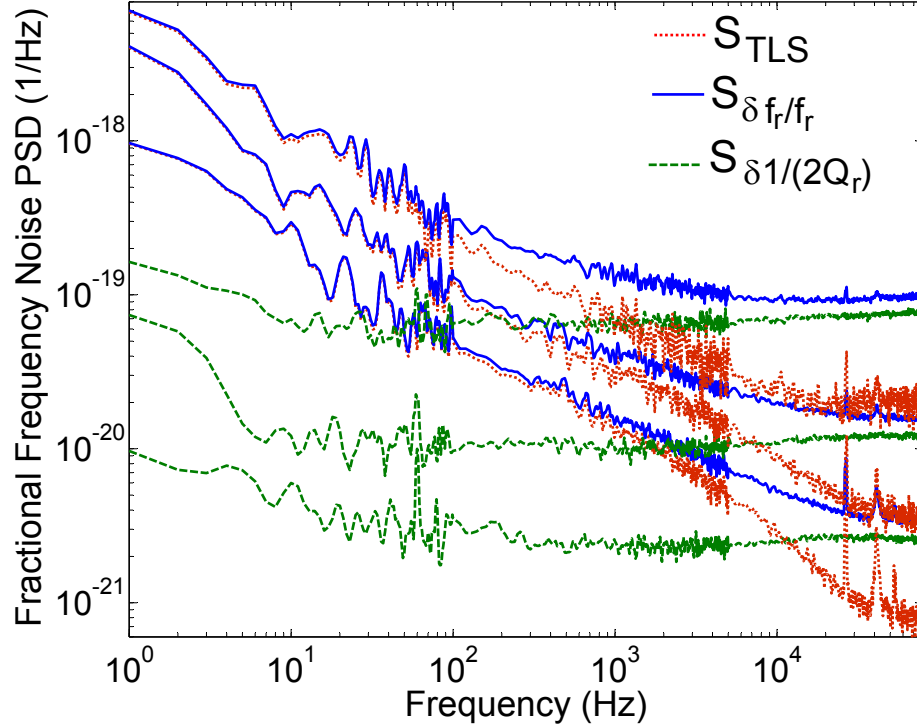


Figure 3.9: Fractional frequency noise power spectral density (single-sided) for 3 different microwave readout powers for resonator no. 5. From top to bottom the 3 curves in each group correspond to  $P_{\text{feed}} = -109, -103,$  and  $-97$  dBm. For each power the total fractional frequency noise ( $S_{\delta f_r/f_r}$ ), the TLS contribution to fractional frequency noise ( $S_{\text{TLS}}$ ), and the amplifier contribution to the fractional frequency noise ( $S_{\delta 1/2Q_r}$ ) are plotted. Data was taken at  $T = 120$  mK. Resonator parameters are listed in Table 3.1 and Table 3.2. (Figure reproduced from [35])

This power corresponds to a stored resonator energy  $E = 1.4 \times 10^{-18}$  J equivalent to  $n_{ph} = 3.8 \times 10^5$  microwave photons and a maximum capacitor voltage of 0.85 mV.<sup>1</sup>

Noise data for the other resonators gives comparable values. However, since the magnitude of voltage noise caused by TLS scales with  $Q_c$  (for  $Q_c$ -limited  $Q_r$ ), resonator no. 5 was the only one that had a high enough  $Q_c$  for the TLS voltage noise to rise significantly above the amplifier voltage noise. As a result, TLS noise in the other resonators was heavily affected by the amplifier noise which makes noise subtraction difficult and not very accurate. However, this already was a good sign that TLS noise in these resonators is significantly reduced.

In order to compare our results with CPW resonators and with other published noise data we have plotted our measured fractional frequency noise as a function of the stored microwave energy inside the resonator in units of microwave photons ( $n = E/hf_r$ ) in Fig. 3.10 along with various resonator geometries and materials published in the literature. The plotted noise is at a frequency of 1 KHz and for our IDC resonator is extracted by averaging the data over a small bandwidth around 1 KHz. We have plotted an additional data point which corresponds to a 2 dB higher readout power of  $P_{feed} = -95$  dBm. This is the maximum power before the resonator enters the nonlinear regime and becomes discontinuous [56, 57].

The IDC resonator data corresponds to the stars with a red line (F). Compared with (E) which is for a 200 nm Nb on Si  $\lambda/4$  CPW resonator with a 3–2 geometry, noise is dramatically reduced by a factor of 35! This confirms the hypothesis that the noise is predominantly produced in the capacitive portion of the resonator and not coming from the inductor. It had been suggested [61] at the time that the noise is due to quasiparticle trapping and release at the metal-dielectric interface which would manifest its effect on the inductor where the microwave current exists. Our results definitely show that this is not the case, since we were able to significantly reduce the

---

<sup>1</sup>It should be noted that the concept of internal resonator traveling wave power ( $P_{int} = V_+^2/2Z_r$ ) usually quoted for CPW resonators is not applicable to lumped-element resonators since there are no traveling waves inside the resonator. Correct comparison between different resonator types can be made using, e.g., resonator energy ( $E$ ) or equivalent photon number ( $n_{ph} = E/hf_r$ ).

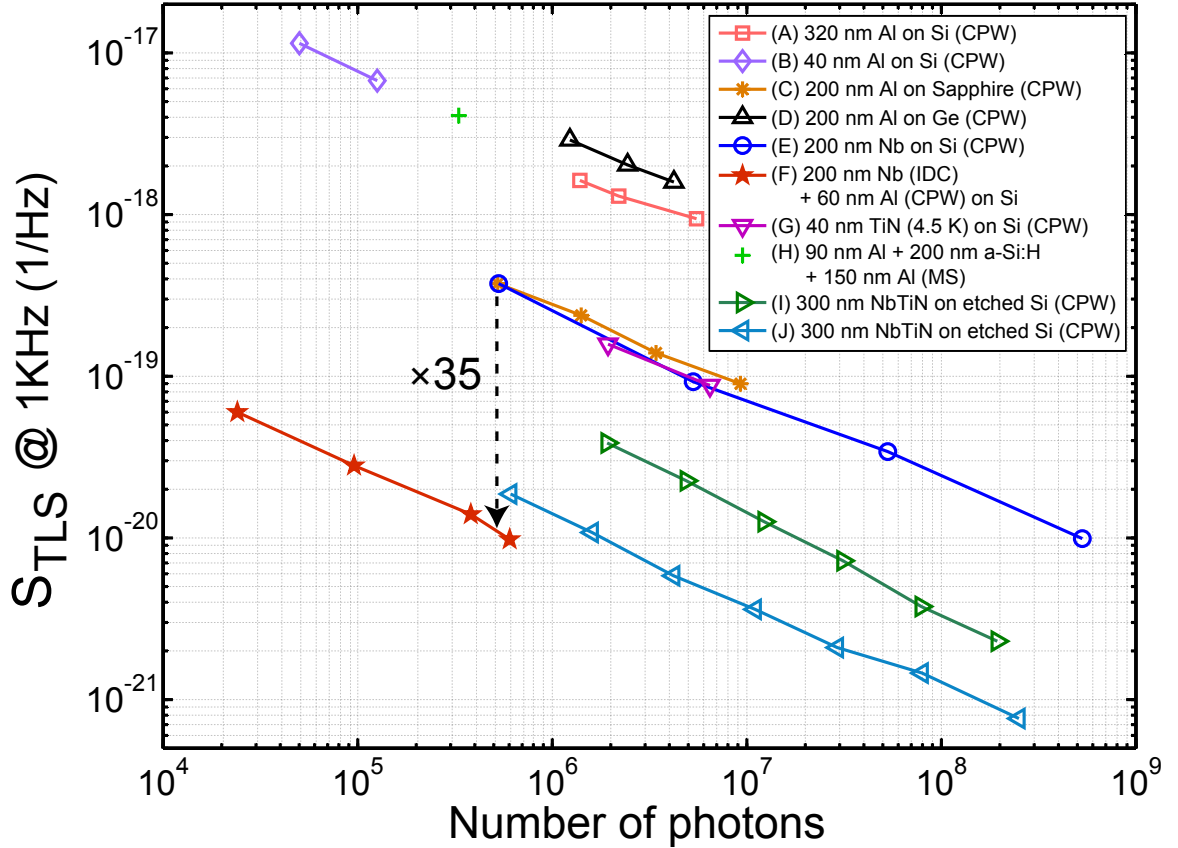


Figure 3.10: Two-level system fractional frequency noise measured at 1 KHz for a variety of resonator geometries and materials is plotted as a function of stored microwave energy measured in units of photons ( $n_{ph} = E/hf_r$ ). Data are as follows: (A) 320 nm Al on Si, center strip width  $s = 3 \mu\text{m}$  and gap  $g = 2 \mu\text{m}$   $\lambda/4$  coplanar waveguide (CPW) (abbreviated to 3-2),  $f_r = 5.8$  GHz,  $T = 120$  mK [48]; (B) 40 nm Al on Si,  $\lambda/4$ , 3-2, 4.8 GHz, 120 mK [48]; (C) 200 nm Al on sapphire,  $\lambda/4$ , 3-2, 4 GHz, 120 mK [48]; (D) 200 nm Al on Ge, 3-2,  $\lambda/4$ , 8 GHz, 120 mK [48]; (E) 200 nm Nb on Si, 3-2,  $\lambda/4$ , 5.1 GHz, 120 mK [48]; (F) 200 nm Nb IDC on Si with 60 nm Al 6-2 CPW inductor, 5.6 GHz, 120 mK (This thesis) [35]; (G) 40 nm TiN ( $T_c = 4.5$  K) on Si, 3-2, 6 GHz, 100 mK [58]; (H) 4- $\mu\text{m}$ -wide microstrip, 93 nm Al + 200 nm a-Si:H + 154 nm Al,  $\lambda/2$ , 9 GHz,  $\sim 150$  mK [59]; (I) 300 nm NbTiN on Si, 3-2,  $\lambda/4$ , 4.4 GHz, 310 mK [60]; (J) 300 nm NbTiN on Si, 6-2, 2.64 GHz,  $\lambda/4$ , 310 mK [60]. Arrow indicates 35 times lower noise from the IDC resonator compared to data (E). Noise is single-sided.

noise by only changing the capacitor and not changing the inductor. We have also shown that by making large finger widths and spacings in the capacitive section of the resonator  $F_{\text{TLS}}$  can be dramatically reduced resulting in much lower noise. This means that a larger capacitor size generally should reduce the TLS noise.

Interesting recent noise results from Barends et al. are the data curves (I) and (J) in Fig. 3.10 which also support our conclusions. The data are for 2 CPW resonators with 6-2 and 3-2 geometry made from NbTiN on Si where the silicon substrate has been etched inside the CPW slot region to reduce  $F_{\text{TLS}}$ . As can be seen, these resonators also show much lower noise compared to the other CPW data where no such etching was used. For the wider geometry they report  $S_{\text{TLS}}(1 \text{ KHz}) = 7.6 \times 10^{-22} \text{ Hz}^{-1}$  at 310 mK,  $f_r = 2.64 \text{ GHz}$ , and  $n_{ph} = 2.5 \times 10^8$ . Correct comparison between our IDC resonator and these two CPW resonators can be made if we take into account the higher power and higher temperature for the CPW resonator (TLS noise scales with  $P^{-1/2}$  and with  $\sim T^{-1.7}$  [42]). Doing so we see that this noise is actually  $\sim 10$  times higher than the IDC resonator noise in similar conditions. However, the advantage of the CPW resonator is that it is significantly smaller in area than the IDC resonator which becomes important in large arrays of MKIDs.

### 3.5.5 Dark NEP

The noise equivalent power (NEP) in the frequency direction for a dark (optically unloaded) resonator can be calculated using the measured noise spectra along with the measured fractional frequency responsivity and lifetime. We can calculate the frequency direction response from Eq. 2.63

$$\frac{df_r/f_r}{dP_o} = \frac{\alpha S_2 \eta_o \tau_{qp}}{4N_0 \Delta_0^2 V} \frac{1}{\sqrt{1 + (2\pi f \tau_{qp})^2}} \frac{1}{\sqrt{1 + (2\pi f \tau_{res})^2}} . \quad (3.10)$$

where we have added the last two factors from rolloff due to resonator ring time and quasiparticle lifetime. Dividing the noise spectra by the above equation (similar to Eq.

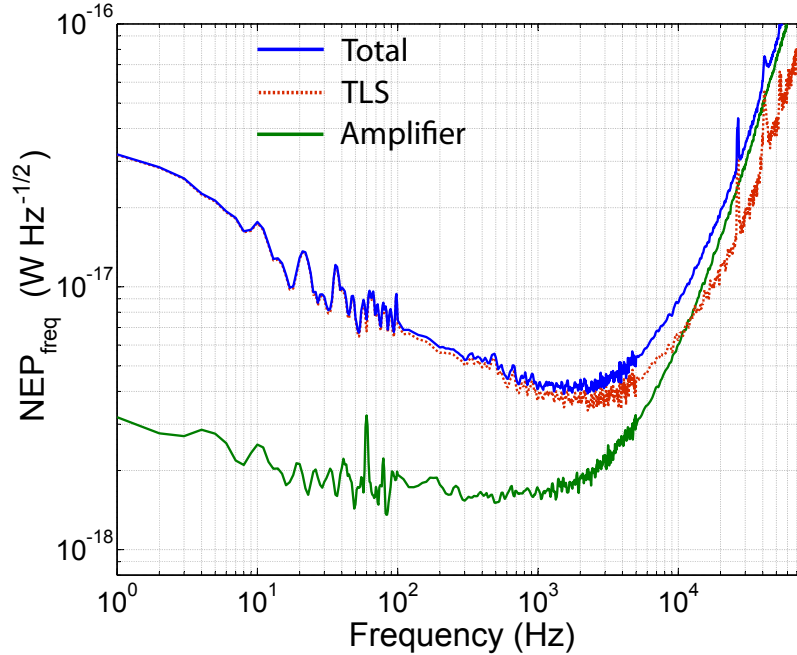


Figure 3.11: Dark noise equivalent power for frequency direction readout. TLS contribution and amplifier contribution to total NEP are indicated.

2.76) we arrive at the frequency direction NEP which is plotted in Fig. 3.11. We have assumed the following values in this calculation:  $\alpha = 0.047$  and  $\Delta_0 = 1.76 \times k_B \times 1.2$  K (from Table 3.2), resonator parameters from Table 3.1, and  $\tau_{qp} = 50 \mu\text{sec}$  (an estimate based on measurements not shown here), and TLS noise at  $P_{\text{feed}} = -97$  dBm ( $n_{ph} = 3.8 \times 10^5$ ). At  $\nu = 1$  Hz we get  $\text{NEP}_{\text{freq}} = 3.2 \times 10^{-17} \text{ W Hz}^{-1/2}$  and at  $\nu = 1$  KHz we get  $\text{NEP}_{\text{freq}} = 4.1 \times 10^{-18} \text{ W Hz}^{-1/2}$ .

For ground-based submillimeter astronomy at  $\lambda = 1$  mm assuming an incident optical power  $P_o = 10$  pW on the detector, we get a photon background NEP of  $\text{NEP}_{\text{ph}} = 2.8 \times 10^{-16} \text{ W Hz}^{-1/2}$  (see Eq. 2.73) and a recombination NEP of  $\text{NEP}_r = 4.0 \times 10^{-17} \text{ W Hz}^{-1/2}$  (see Eq. 2.72). It is important to note that the NEP plot in Fig. 3.11 is for a dark (optically unloaded device) and cannot be directly compared to the optically loaded calculation above as the device biasing conditions are different.

### 3.6 IDC resonators for the multiwavelength submillimeter kinetic inductance camera (MUSIC)

Based on the design explained in this chapter we developed and optimized an IDC resonator for use in the multiwavelength submillimeter kinetic inductance camera (MUSIC) instrument [17]. This is an astronomical instrument currently being developed for the Caltech Submillimeter Observatory and is planned for deployment in 2012. It will have 2304 MKIDs made with IDC resonators distributed in 576 spatial pixels for four observation bands (850  $\mu\text{m}$ , 1100  $\mu\text{m}$ , 1300  $\mu\text{m}$ , and 2000  $\mu\text{m}$ ). A total of 8 tiles each with 288 resonators coupled to a single feedline comprise the focal plane. A photograph of a section of one of the chips (2 chips per tile) is shown in Fig. 3.12 where four IDC resonators can be seen at the bottom. The resonators in the photo have the same IDCs as shown in Fig. 3.3 (a) but with longer CPW inductors to lower the frequencies as part of the readout electronics requirements. The details of these devices, their performance, and the instrument itself can be found in the literature [62, 17, 18, 63, 64, 65, 50, 66, 55].

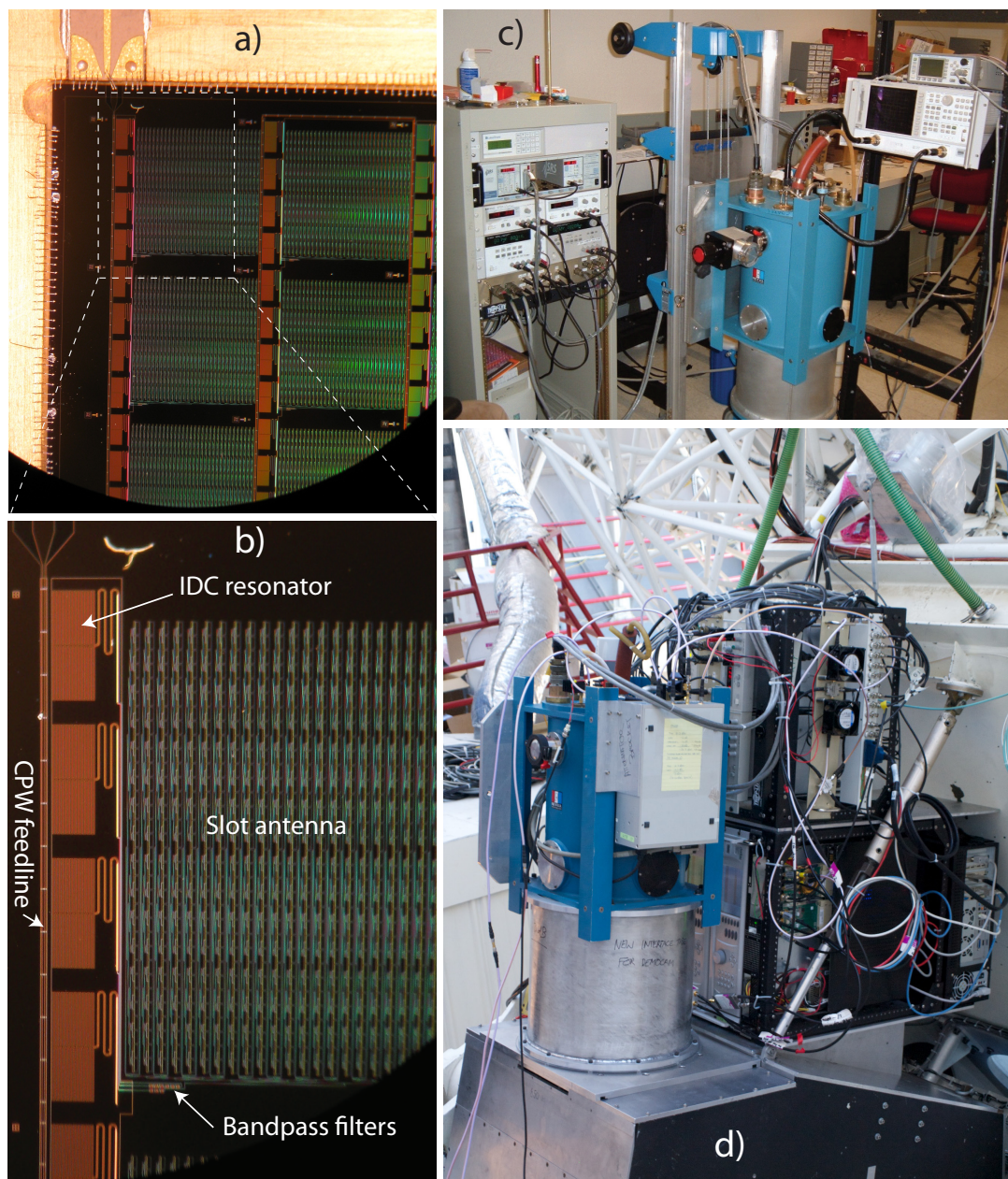


Figure 3.12: (a) and (b) Photographs show a section of the focal plane of a precursor instrument (Democam) to MUSIC (multiwavelength submillimeter kinetic inductance camera). Four IDC resonator MKIDs can be seen at the bottom. The single-polarization antenna feeds the optical power via a microstrip line to a band-selecting filter bank which separates the signal into four observation bands. Power from each band is coupled to an MKID resonator where it is absorbed in the aluminum section of the inductor creating a signal which is read out using the feedline. (c) The Democam cryostat and a microwave network analyzer setup being used to read out the resonators in the laboratory at Caltech. (d) The full Democam instrument mounted on the back of the telescope at the Caltech Submillimeter Observatory for an engineering run in 2010.

## 3.7 Chapter summary

In this chapter we reviewed aspects of the two-level system theory that are relevant to MKIDs. Namely TLS loss and noise which both exist in superconducting resonators and can affect the internal resonator loss and introduce noise in the resonance frequency. Noise in MKIDs can affect the detection sensitivity and has to be minimized as much as possible, especially for sensitive astronomical observations. Based on our understanding of the source of the TLS noise and its scaling with geometry, we designed and measured a new type of resonator for reduced noise. These resonators use large interdigitated capacitors with wide finger widths and spacings in combination with a narrow CPW inductor to keep the responsivity high. The increase in the size of the capacitor causes a reduction in the TLS volume filling factor which reduces the noise significantly. We show this by measuring noise in our devices and comparing to various other resonator geometries published in the literature. We see that noise is reduced by a factor of 35 as compared to a relevant CPW geometry and material design. Our result conclusively shows that the capacitor is mainly responsible for the TLS noise and not the inductor.

## Chapter 4

# Submillimeter/far-infrared imaging arrays using $\text{TiN}_x$ MKIDs

In this chapter we present design details and measurements of large arrays of submillimeter-wave MKIDs aimed for operation at  $\lambda = 350 \mu\text{m}$ . We used a relatively new superconductor,  $\text{TiN}_x$ , in our resonators that has significant advantages over more conventionally used superconductors like aluminum or niobium. Specifically, MKIDs made from  $\text{TiN}_x$  have internal quality factors an order of magnitude higher than other resonator types and also have very high kinetic inductance fractions both of which can dramatically improve performance. Additionally, because of its high normal-state surface resistance,  $\text{TiN}_x$  can be used as an efficient radiation absorbing material and can bypass the need for separate antennas to collect radiation. Using this feature, we designed the inductive section of our resonators to absorb the radiation and at the same time act as a detector. This idea was originally introduced by Doyle et al. [67] where they used aluminum as absorbing material. However, aluminum has a very high electrical conductivity and it can be challenging to design efficient radiation absorbers using aluminum. We will go through the analytical and numerical design steps for our resonators, and will present two specific resonator and array designs.

The key to advances in radiation detection technology is often lower NEP detectors. Our  $\text{TiN}_x$  resonators are a step in this direction. However, once the photon

background noise limit is reached, significant increase in sensitivity is only possible by significantly increasing the number of pixels in the array if we want to avoid long integration times. To demonstrate the feasibility of large arrays of submillimeter MKIDs, we fabricated highly packed arrays with  $\sim 256$  pixels using our  $\text{TiN}_x$  lumped-element resonators. A major potential problem in tightly packed arrays is the microwave interaction that can happen between resonators causing crosstalk which can render the detectors useless. As will be shown in Chapter 5, our second resonator design (B) circumvents this problem by carefully designing the resonators' geometry. In this chapter we will present design details and measurements relevant to other aspects of the detector, mainly absorption efficiency and sensitivity. We begin by reviewing different resonator designs that are generally used for MKIDs.

## 4.1 MKID resonator types

There are two main aspects to consider in an MKID resonator design. One is the coupling mechanism of photons into the sensitive section of the resonator, and the other is the design of the resonator itself. There are various types of MKIDs that differ based on these two aspects.

The most traditional type consists of a quarter-wave ( $\lambda/4$ ) or half-wave ( $\lambda/2$ ) coplanar waveguide (CPW) transmission line resonator. The  $\lambda/4$  version (shown in Fig. 4.1 (a)) is short-circuited at one end and is capacitively coupled to a through transmission line (usually a CPW) on the open end, and has a frequency of  $f_r = c/4l\sqrt{\epsilon_{eff}}$ . Here  $c$  is the speed of light,  $l$  is the resonator length, and  $\epsilon_{eff}$  is the effective dielectric constant of the transmission line. In the example shown in Fig. 4.1 (a) most of the resonator is made from niobium (Nb) except for a  $\sim 1$  mm section at the short-circuited side that is made of Al. This resonator design was initially used in our group for the Democam imaging instrument [68] which later developed into the MUSIC instrument [17] with a modified resonator design. Radiation is coupled

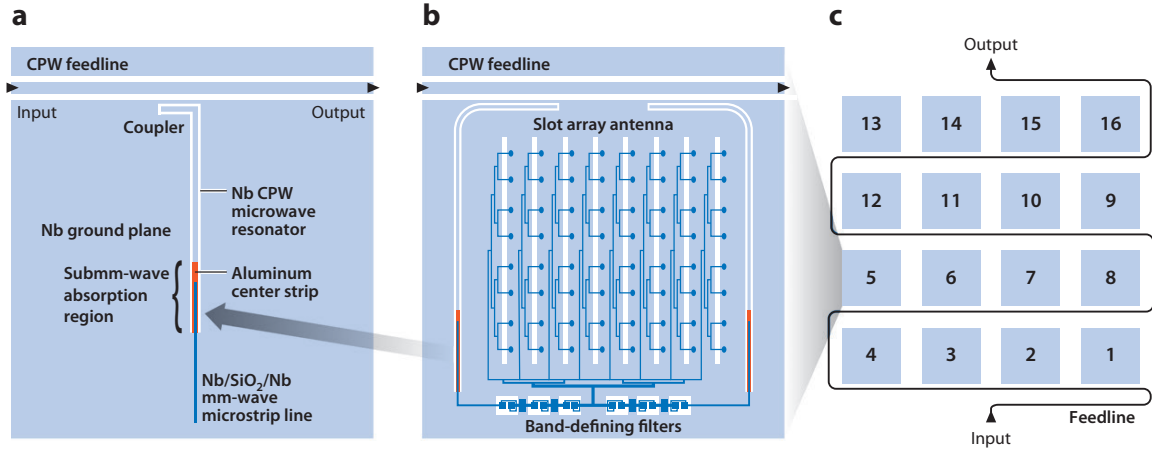


Figure 4.1: This figure illustrates the antenna-coupled microwave kinetic inductance detector (MKID) arrays developed at Caltech/JPL. (a) A  $\lambda/4$  coplanar-waveguide (CPW) resonator is coupled to a CPW feedline. Millimeter-wave radiation is brought to the resonator using a niobium microstrip line and is absorbed by the aluminum section of the CPW resonator’s center strip. (b) A phased-array multislot antenna, two CPW MKIDs, and on chip band-defining filters are used to make a dual-band pixel. (c) A  $4 \times 4$  pixel array is multiplexed using a single feedline. (Figure reproduced from [13])

to the MKIDs via a multislot phased-array antenna (Fig. 4.1 (b)). This type of antenna, developed at Caltech and JPL [69, 70], produces a narrow beam pattern by combining signals from an array of slots in phase using a summing network of low-loss microstrip transmission lines. The optical power splits in two, passes through an in-line band-defining filter, and is then absorbed in the aluminum inductor section of the MKIDs which is lossy at above the Al gap frequency ( $\sim 90$  GHz). This is made possible because the microstrip line and the CPW share the Al ground plane in this 1 mm section. References [71, 41, 55] document the first attempt to efficiently couple radiation using this method.

An improved version of the previous design is shown in Fig. 4.2. A description along with measurement results for this design - dubbed the “IDC-resonator” - was given in Chapter 3. Here the capacitive portion (open-end) of the CPW resonator is replaced by an interdigitated capacitor (IDC) structure (compatible with CPW architecture) with 10–20  $\mu\text{m}$  electrode spacing as compared to the 2  $\mu\text{m}$  spacing used for the inductor. The IDC behaves approximately as a lumped element, while the

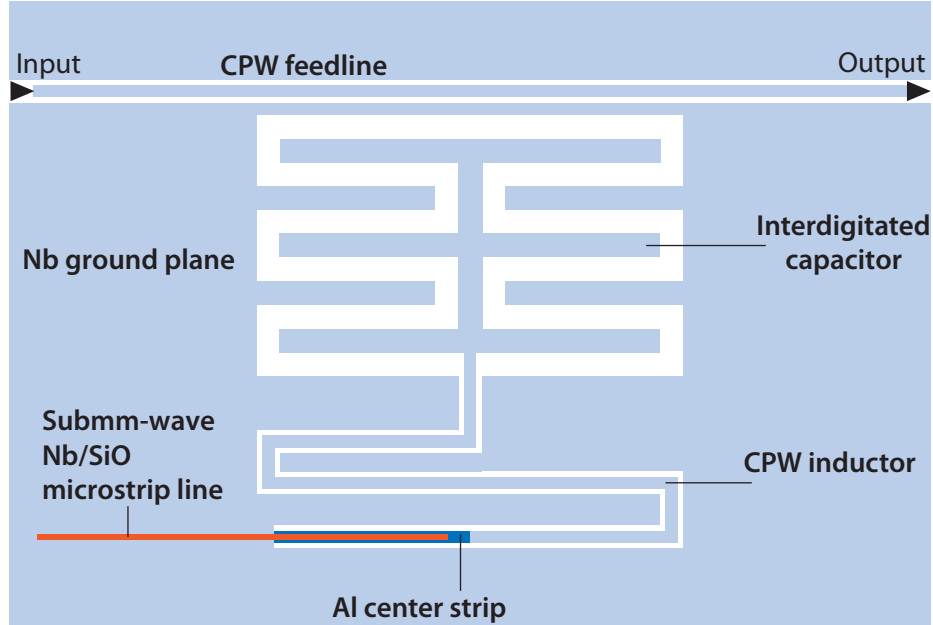


Figure 4.2: A schematic illustration of an interdigitated capacitor (IDC) resonator. The IDC is nearly lumped-element and the CPW inductor is distributed. The resonator is capacitively coupled to a CPW feedline. The inductor is short circuited at the aluminum end where the mm/submm radiation is absorbed. The radiation is brought to the resonator by a low-loss microstrip line.

inductor is distributed. As was shown in Chapter 3 the large electrode spacing in the IDC reduces the strength of the electric field which dramatically reduces the two-level system noise in the resonator’s frequency [35]. The CPW inductor is kept narrow to increase  $\alpha$ . This “hybrid” resonator design is currently being used for the detectors in the MUSIC instrument [18, 17, 62] (See Fig. 3.12).

In another type of MKID developed by Yates et al. [72] a hemispherical silicon lens is used to focus the radiation on a twin-slot antenna. Each resonator has a twin-slot antenna incorporated at the shorted end of the CPW where the short acts as the feed point to the twin-slot antenna.

A much simpler and very clever design proposed by Doyle et al. [67] is the lumped-element kinetic inductance detector (LeKID). This design alleviates the need for an antenna all together by using the inductor itself as a radiation absorber. The resonator consists of a single-line inductor meander and an interdigitated capacitor (Fig.

4.3 (a)). By tuning the width and spacing of the inductor mesh lines the inductor can be made to look like a thin absorptive sheet with an effective normal-state sheet resistance matched to the impedance of incoming photons with energy above the superconducting energy gap. The array is back illuminated; the photons travel through the substrate and are absorbed in the resonators on the back side (Fig. 4.3 (c)). Fresnel reflection of radiation entering the silicon substrate can be eliminated by using an antireflection layer. A superconducting back short can be used to increase the absorption efficiency. The absorbed power creates quasiparticles in the inductor causing a frequency and dissipation signal. In this design the inductor is the photosensitive portion of the resonator since the microwave current is large, whereas the capacitor electrodes have much lower current and therefore are essentially blind to the incident radiation. One important advantage of this radiation coupling mechanism over the antenna-coupled MKIDs is that submillimeter radiation above  $\sim 700$  GHz (Nb gap frequency) can be detected. This is because the Nb microstrip lines in the multislotted antenna scheme become lossy above this frequency and efficient coupling becomes impossible.

The challenge in designing a LeKID is that the material properties of the superconductor determine the resonator parameters but also determine the radiation absorption efficiency. Traditionally very thin Al or a hybrid combination Al and Nb have been used [73]. However, Al has a very low sheet resistance that makes impedance matching difficult. Nb has higher sheet resistance than Al but it has a very short quasiparticle lifetime and small  $\alpha$  which greatly reduce the responsivity. Currently the NIKA camera [74] for the IRAM 30-m telescope is using LeKIDs made from 20 nm thin Al films for the  $\lambda = 2$  mm band. An interesting variation to the LeKID design using microstrip lines was suggested by Brown et al. [75].

The resonators and measurements presented in this chapter are for a LeKID type of resonator. These arrays can be easily made with a single layer of superconducting metal film deposited on a silicon substrate and patterned using conventional optical lithography. Instead of Al we use  $\text{TiN}_x$  for the superconductor which has several

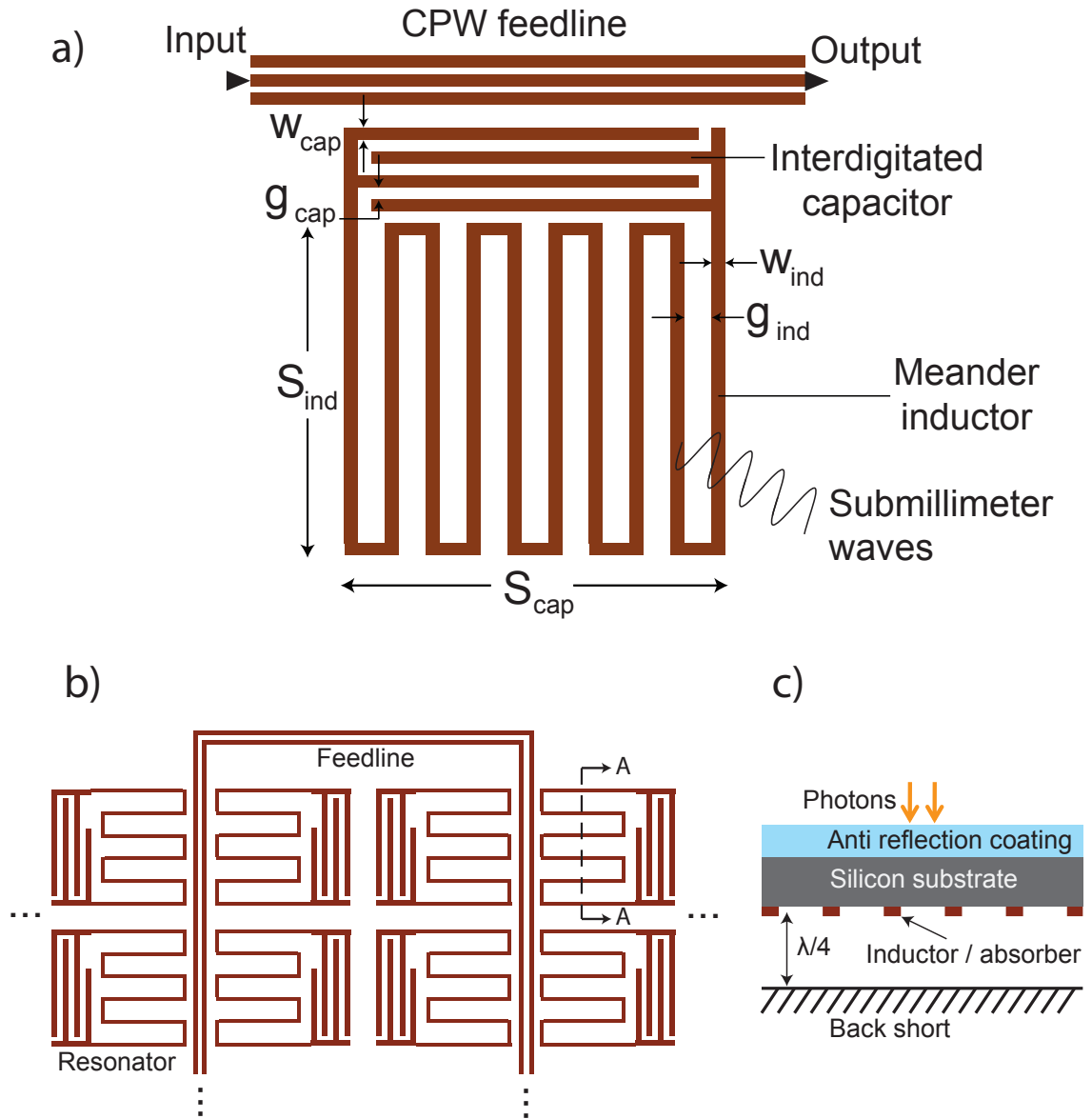


Figure 4.3: (a) Schematic illustration of a lumped-element kinetic inductance detector (LeKID). The resonator consists of a single-line inductor meander and an interdigitated capacitor. Coupling to the feedline (CPW or CPS) can be capacitive (like here) or inductive (as in (b)). The inductor acts as a 1-D absorptive mesh for photons above the superconductor gap energy and obviates the need for a separate antenna. (b) Illustration of a 2x8 section of the geometry of a close-packed LeKID array, with dark regions representing metallization (TiN<sub>x</sub> or Al). (c) Cross-sectional view along A-A in (b) of a resonator showing the illumination mechanism and the metal back short

advantages over Al as will be explained later in Section 4.6.2. TiN has a much higher resistivity than Al making it easy to impedance match, has good quasiparticle lifetimes and very large  $\alpha$ , and has very low microwave loss allowing very high  $Q$ s, and is therefore ideal for lumped-element direct absorption resonators. In the next sections we will explain in detail our resonator designs.

## 4.2 Lumped-element kinetic inductance detectors

In the previous section we presented an overview of various types of MKIDs. Here, we will specifically describe the type we have used in this work: the lumped-element kinetic inductance detector (LeKID), or simply lumped-element resonator. We start by explaining with more detail how submillimeter/far-IR radiation is coupled to the inductor in these resonators and how geometrical parameters determine the optical efficiency. After that we will switch to the microwave aspects of the design and present analytical approximations for the capacitance and inductance values. These will aid in the fast initial design of the basic resonator properties like absorption efficiency and the resonance frequency. Subsequently we can follow up with more accurate EM simulations to fine tune the parameters.

### 4.2.1 Radiation coupling method

As explained above, the inductor meander section of the resonator acts as a radiation absorber. The meander section is similar to metallic micromesh absorbers used in bolometers [76]. The absorption can be optimized by choosing the proper inductor line width  $w$  and meander pitch  $p$  for a certain film sheet resistance  $R_s$  and substrate relative permittivity  $\epsilon_r$ . We can calculate the absorptivity of the meander grid if we make the following assumptions: The meander is on an infinite plane that has an infinite number of lines; the film has a sheet resistance of  $R_s$  and thickness  $t$  much smaller than the penetration depth; the dielectric substrate has thickness  $d$  and

refractive index  $n = \sqrt{\epsilon_r}$ ; the radiation is unpolarized; the radiation makes only a single pass at the meander (i.e., there is no reflecting backshort under the meander grid); the radiation is incident normally on the surfaces.

According to Ulrich et al. [77] the effective sheet resistance that the meander presents to incident radiation parallel to the lines is

$$R_{eff} = \frac{1}{\eta_{fill}} \times R_s , \quad (4.1)$$

where  $\eta_{fill} = w/p$ . This can be understood by noting the nonuniform spatial distribution of the average surface current in the plane of the meander grid. The surface current has to flow through a cross section that is smaller by the factor  $\eta_{fill}$  which increases the effective surface resistance by  $1/\eta_{fill}$ .

The transmission and reflection coefficients at the top surface where the radiation originally enters are [78]:

$$T_1 = \frac{4n}{(n+1)^2} \quad (4.2)$$

$$R_1 = \frac{(n-1)^2}{(n+1)^2} . \quad (4.3)$$

The transmission, reflection, and absorption coefficients at the plane of the meander grid are:

$$T_2 = \frac{4n}{(n+1 + Z_0/R_{eff})^2} \quad (4.4)$$

$$R_2 = \frac{(1-n + Z_0/R_{eff})^2}{(n+1 + Z_0/R_{eff})^2} \quad (4.5)$$

$$A_2 = \frac{4nZ_0/R_{eff}}{(n+1 + Z_0/R_{eff})^2} , \quad (4.6)$$

where  $Z_0 = 377 \Omega$  is the free space impedance. These equations remain accurate to within a few percent for angles of incidence up to 60 deg [78]. In general because of the substrate there will be multiple reflections between the two surfaces resulting in

Fabry–Perot fringes in the total transmission  $T_m$ , total reflection  $R_m$ , and absorption  $A_m$  of the meander inductor. These coefficients are

$$T_m = \frac{T_1 T_s T_2}{1 + T_s^2 R_1 R_2 \pm 2T_s \sqrt{R_1 R_2} \cos \delta} \quad (4.7)$$

$$R_m = \frac{R_1 + T_s^2 R_2 - 2T_s \sqrt{R_1 R_2} \cos \delta}{1 + T_s^2 R_1 R_2 \pm 2T_s \sqrt{R_1 R_2} \cos \delta} \quad (4.8)$$

$$A_m = \frac{T_1(1 - T_s T_2 - T_s^2 R_s)}{1 + T_s^2 R_1 R_2 \pm 2T_s \sqrt{R_1 R_2} \cos \delta}; \quad (4.9)$$

The plus sign applies when  $Z_0/R_{eff} > n-1$ , and the minus sign is for when  $Z_0/R_{eff} < n-1$ .  $T_s$  is the transmission of the substrate with thickness  $d$ , and  $\delta = (2\pi/\lambda)2nd$  is the phase difference between each succeeding reflection. The absorption can be maximized if an antireflection coating is used on top of the substrate. In that case, the substrate will look like a semi-infinite medium to the meander grid and we can simply maximize absorption by maximizing  $A_2$  with respect to  $Z_0/R_{eff}$  which gives the optimum value

$$R_{eff} = \frac{Z_0}{n+1}. \quad (4.10)$$

By combining Eq. 4.1 with Eq. 4.10 we arrive at the optimum condition for maximum absorption in the meander

$$R_s \times \frac{p}{w} = \frac{Z_0}{1 + \sqrt{\epsilon_r}} \quad (4.11)$$

which is in terms of the dimensions of the meander. Using a superconducting back-short to reflect back the power transmitted through the meander one can reach close to 100% absorption efficiency [79, 73]. An alternative way to model the meander absorption is to use a transmission line circuit model with a shunt impedance to represent the meander impedance [77, 73].

One important parameter that hasn't been taken into account in the above analysis is the geometrical inductance of the meander section. Metal mesh filters similar to our inductor meander can be used as high-pass inductive filters for submillimeter radiation because of the inductive impedance that such grids possess. Ulrich et al. calculated to first order the effective sheet reactance for a set of infinite parallel lines

(“inductive grid”) [77, 80]:

$$X_{\text{eff}} = \frac{p}{\lambda} \ln(\operatorname{cosec}\left(\frac{\pi w}{2p}\right)) Z_0 \quad (4.12)$$

where  $\lambda$  is the free-space wavelength of the submillimeter radiation. Radiation with electric field polarization perpendicular to the lines does not see this inductance. The addition of the inductance changes the sheet impedance of the meander in the submillimeter and reduces the absorption efficiency. As an example, for our resonator design A (see Fig. 4.5(a)),  $X_s \sim 30 \Omega$ . In practice because the meander lines are connected in our design the currents can flow in opposite direction close to each other reducing the effective inductance. The inductance can be tuned out by varying the thickness of the substrate and the distance to the back short but it will reduce the absorption bandwidth [73].

Next we will switch to the microwave side of things and present approximations for the capacitance and inductance values of the resonator. These can be very useful for the initial design of a lumped-element resonator.

### 4.2.2 Analytical approximations for capacitance and inductance

LeKIDs use interdigitated capacitors (IDC) and usually meandered inductor lines for the resonator (see Fig. 4.3). Here we discuss an approximate analytical calculation of the capacitance of the IDC and the geometrical inductance of a meandered inductor.

Engan et al. [81] calculated the capacitance per unit width per pair of strips for an infinitely long array of parallel metallic strips. Assuming that the IDC has many fingers (strips), we can approximate the total capacitance for an IDC with  $N_{\text{cap}}$

number of finger pairs<sup>1</sup> and length  $S_{cap}$  (see Fig. 4.3) [82]:

$$C = \epsilon_0(1 + \epsilon_r) \frac{K(k)}{K(k')} \times N_{cap} S_{cap} . \quad (4.13)$$

Here  $\epsilon_0$  is the permittivity of free space,  $\epsilon_r$  is the relative dielectric constant of the substrate,  $k = \cos(\pi\chi_{gap}/2)$  where  $\chi_{gap} = g_{cap}/(g_{cap} + w_{cap})$  is gap fraction,  $k' = \sqrt{1 - k^2}$ , and  $K(k)$  is the elliptic integral. It is convenient to use the shorthand notation  $K_{cap} = K(k)$  and  $K'_{cap} = K(k')$ . Because an IDC and a meandered inductor are complementary structures we can write the corresponding formula for the geometric inductance of a meander line with  $N_{ind}$  line pairs and length  $S_{ind}$  [82]:

$$L = \frac{\mu_0}{2} \frac{K'_{ind}}{K_{ind}} \times N_{ind} S_{ind} . \quad (4.14)$$

For the simple case when  $w_{cap} = g_{cap}$  and  $w_{ind} = g_{ind}$ ,  $K(k') = K(k)$  we can simplify the above two equations to

$$C = \epsilon_0(1 + \epsilon_r) N_{cap} S_{cap} \quad (4.15)$$

$$L = \frac{\mu_0}{2} N_{ind} S_{ind} . \quad (4.16)$$

The resonance frequency (not taking into account the effect of superconductivity) can now be calculated as

$$\omega_r = \frac{1}{\sqrt{LC}} = \frac{\nu_{ph}}{\sqrt{S_{cap} S_{ind} N_{cap} N_{ind}}} \sqrt{\frac{K_{ind} K'_{cap}}{K_{cap} K'_{ind}}} \quad (4.17)$$

where  $\nu_{ph} = c/\sqrt{\epsilon_{eff}}$  is the phase velocity and  $\epsilon_{eff} = (1 + \epsilon_r)/2$  is the effective dielectric constant. The above formulae are only rough estimates for  $L$ ,  $C$ , and  $\omega_r$  at very low (DC) frequencies. Parasitic inductance in the IDC and parasitic capacitance in the inductor will affect the actual value of  $L$  and  $C$  at higher frequencies around the resonance frequency of the resonator (typically around a few GHz). Additionally, because these formulae are based on an infinite number of pairs, they are more ac-

<sup>1</sup>There are 2 finger pairs in the capacitor and 5 line pairs in the inductor in Fig. 4.3

curate when  $N_{cap}$  and  $N_{ind}$  are large. As an example, let's calculate the capacitance for the IDC in design A and B resonators (see Fig. 4.5 and 4.6). For design A, with  $w_{cap} = s_{cap} = 10 \mu\text{m}$ ,  $S_{cap} = 930 \mu\text{m}$ , and  $\epsilon_r = 11.9$ , the formula gives  $C = 0.21$  pF which matches closely a simulation value of 0.198 pF at DC and 0.2 pF at 1.4 GHz. For design B, with  $w_{cap} = s_{cap} = 5 \mu\text{m}$ ,  $S_{cap} = 500 \mu\text{m}$ , and  $\epsilon_r = 11.9$ , the formula gives  $C = 0.40$  pF while simulation at DC gives 0.36 pF and at 1.4 GHz gives 0.38 pF. It's important to note that the inductance calculated from Eq. 4.14 gives only the geometric inductance and does not include the kinetic inductance from the superconductor. For TiN films, since  $\alpha$  is close to unity, the kinetic inductance dominates.

In the previous two sections we provided analytical approximations that can be used in the initial design of a lumped-element kinetic inductance detector. In the next section we will use these to show how we designed our first resonator which later became our design A. Design B was based on the same methods described here.

### 4.3 Approximate analytical design of a lumped-element resonator

We designed our first lumped-element resonator based on a series of simple requirements and assumptions. We begin with the meandered inductor section first and then go to the capacitor section. Once these two are parameterized we can calculate the required geometrical dimensions for proper operation of the detector.

### 4.3.1 Inductor meander

As explained in Section 4.2.1 from the impedance matching condition (Eq. 4.11) we have

$$\eta_{fill} = \frac{w}{p} = R_s \times \frac{1 + \sqrt{\epsilon_r}}{Z_0} \approx \frac{R_s}{90 \Omega} \quad (4.18)$$

where  $w = w_{ind}$  is the width of the inductor line,  $p = g_{ind} + w_{ind}$  is the meander pitch,  $Z_0 = 377 \Omega$ , and we have taken  $\epsilon_r = \epsilon_{Si} = 11.4$  for far-infrared frequencies at 1.5 K [83]. In order for the meander section to fill the optical beam on the device, we take the dimension of the meander section to be  $a = F\lambda = 3 \times 350 \mu\text{m} \approx 1 \text{ mm}$  in width and length (Fig. 4.5) where  $F$  is the optical beam F-number for CCAT [84] and  $\lambda$  is the submillimeter radiation wavelength incident on the resonator. In order for the meander section not to act as a diffraction grating, the spacing between the meander lines must not exceed the wavelength inside the substrate

$$p \leq \lambda/2\sqrt{\epsilon_r} \quad (4.19)$$

where the factor of two is a safety factor. This means that the total number of strips (neglecting the connecting strips) in the meander section should be at least

$$N_m = \frac{a}{p} \geq \frac{F\lambda}{\lambda/2\sqrt{\epsilon_r}} = 2F\sqrt{\epsilon_r} \approx 20. \quad (4.20)$$

We can write the inductance of the meander section as

$$L \approx L_{kin} = N_m \times (L_s \frac{a}{w}) = \eta_{fill} \times L_s (\frac{a^2}{w^2}) \quad (4.21)$$

where  $L_s$  is the surface inductance of the TiN film. Here we have made the assumption that kinetic inductance dominates over geometric inductance due to the high  $\alpha$  for TiN. From Eq. 4.18 and Eq. 4.19 we have

$$w \leq \eta_{fill} \frac{\lambda}{2\sqrt{\epsilon_r}}. \quad (4.22)$$

We introduce a width tuning factor  $\chi_w$

$$w = \chi_w \times w_{max} \quad (4.23)$$

where  $\chi_w \leq 1$  and

$$w_{max} = \eta_{fill} \frac{\lambda}{2\sqrt{\epsilon_r}}. \quad (4.24)$$

We can now rewrite Eq. 4.21 as

$$L_{kin} = \frac{4\epsilon_r F^2 L_s}{\eta_{fill}} \times \frac{1}{\chi_w^2} \quad (4.25)$$

where  $\chi_w$  is our adjustable design parameter.

### 4.3.2 Interdigitated capacitor

We can rewrite Eq .4.15 for an IDC with equal finger width  $w_c$  and gap with  $g_c$ :

$$C = \frac{1}{Z_0 c_0} (1 + \epsilon_r) a N_c \quad (4.26)$$

where  $c_0$  is the speed of light and  $N_c$  is the number of finger pairs in the IDC. For an  $a = 1$ -mm-long finger length this gives a capacitance of  $C_{pair} = 110$  fF per finger pair. In order to minimize the TLS noise from the capacitor, we fix the finger and gap width to  $w_c = g_c = 10 \mu\text{m}$  based on our previous IDC resonator design described in Chapter 3 and reported in [35]. Also, in order to minimize the blind (insensitive) surface area of the resonator we limit the IDC area to  $\lesssim 10\%$  of the total resonator area. Therefore

$$A_c = 2N_c(w_c + g_c)a \lesssim 0.1 \text{ mm}^2 \quad (4.27)$$

which yields  $N_c \sim 2$  finger pairs. Next we will calculate the resonance frequency from which we will be able to get the dimensions for the inductor meander.

### 4.3.3 Resonance frequency

The resonator will have a resonance frequency that is now readily calculated by  $f_r = 1/2\pi\sqrt{LC}$ . Substituting for  $L$  from Eq. 4.21 and for  $C$  from Eq. 4.26 we get

$$f_r = \frac{\chi_w}{4\epsilon_r F} \left[ \left( \frac{1 + \sqrt{\epsilon_r}}{1 + \epsilon_r^{-1}} \right) \frac{\nu_{gap} \nu_a}{N_c} \right]^{1/2} \quad (4.28)$$

where  $\nu_a = c_0/a = 300$  GHz and we have used the Mattis–Bardeen relationship

$$L_s = \frac{R_s}{\pi^2 \nu_{gap}}. \quad (4.29)$$

For TiN with  $T_c = 4.5$  K,  $\nu_{gap} \approx 340$  GHz. Putting all the values inside Eq. 4.28 we arrive at

$$f_r \approx \chi_w \times 3 \text{ GHz}. \quad (4.30)$$

By choosing  $\chi_w = 5/9$  we get a resonance frequency  $f_r \approx 1.67$  GHz which is in the 1–2 GHz range that we were aiming for. Assuming that  $R_s = 15 \Omega$  for the TiN film, we get  $w = 5 \mu\text{m}$  and  $p = 30 \mu\text{m}$ . An inductor line width smaller than this would start to become too narrow and could cause limitation in terms of resonator readout power handling. These numbers were used as a starting point which led to our original design called design A. Before we proceed to the design details of the fabricated resonators we will first review different feedline types and the design method for setting the coupling (external) quality factor of the resonator.

### 4.3.4 Coupling quality factor and feedline

There are several different options for the feedline. Traditionally coplanar-waveguide (CPW) feedlines have been used. Depending on the resonator structure, the CPW can be finite-ground or the ground plane can extend all across the chip. The main advantage of CPWs is their ease of fabrication since they can be made with a single layer of metallization. However, one of their drawbacks is that CPWs can support

two propagation modes (even and odd). The odd mode, called the coupled slot-line mode, is an unwanted mode and needs to be suppressed for proper operation [54]. In our devices this is done by employing periodic grounding straps along the length of the feedline connecting the two CPW ground planes. These bridges use via-hole contacts to the ground planes, and therefore add to the fabrication complexity by two extra layers of lithography. Furthermore, it is also important to properly ground the CPW ground planes to the sample box ground to avoid microstrip line modes. This is done by using lots of wirebonds between the box and the chip ground plane.

Another type of feedline is the microstrip feedline [59]. It also requires several layers of lithography. One advantage is that the fields are highly confined between the signal lines and are not easily perturbed by the surrounding structures. However, this also means that coupling to it is more difficult which results in higher  $Q_c$ 's.

Another type of feedline is the coplanar strip (CPS) feedline. The CPS feedline has several advantages over CPW feedlines. First, it supports only a single propagating mode with currents flowing in opposite directions in the two strips. Second, CPS feedlines don't require bridges and so can be made with a single layer of lithography. However, one drawback is that they require a balun to connect to standard CPW/coax ports. If included on the chip, the balun will take away some chip area. Broadband uniplanar balun designs exist [85, 86, 87] which also do not require via holes. Third, since resonators employing CPS feedlines do not have ground planes covering the surface of the chip or around the resonators, they might be less sensitive to surrounding magnetic fields like the earth field due to flux focusing effects, unlike CPW resonators [51]. One disadvantage of CPS feedlines is that they can potentially support a microstrip line mode between the strips and the distant ground plane of the sample box. A side effect is that resonators can couple much more strongly ( $\sim 10$  times) to this mode than the intended CPS mode which will reduce  $Q_c$  substantially and can cause additional  $Q_c$  variation. By using proper balun type impedance transformers it should be possible to avoid launching these modes, but this is a subject that requires more investigation. In our lumped-element resonator designs, we have

used either CPW or CPS feedlines. Particularly, in design A we used a CPS feedline and in design B we used a CPW feedline.

The resonator can be coupled to the feedline in three ways: capacitively, inductively, or a combination of both. Traditionally in MKID resonators, capacitive coupling is mostly used where the capacitive portion of the resonator is coupled to the feedline. This is done by bringing the whole capacitive portion of the resonator or an extended part of the capacitor metallization close to feedline where the electric field is stronger. Capacitive coupling usually provides stronger coupling than inductive coupling and therefore provides lower  $Q_c$  values. For situations where a higher  $Q_c$  is required usually inductive coupling is the solution. In inductive coupling the inductive portion of the resonator is brought close to the feedline where the magnetic field is stronger. In both capacitive and inductive coupling  $Q_c$  can be tuned by changing the distance between the resonator and the feedline or by changing the geometry such that a bigger portion of the capacitor or inductor is in proximity to the feedline. For lumped-element resonators the process of finding the right distance from the feedline and the geometry of the coupling element is mainly a trial and error process involving a lot of simulation time, and is sometimes quite nonintuitive. In order to extract  $Q_c$  for a certain resonator and feedline design, the most accurate method is to model the whole structure in an electromagnetic simulator like Sonnet [52] and look at the microwave transmission  $S_{21}$  along the feedline ports. Then by exporting the  $S_{21}$  data to a program like MATLAB we can numerically fit  $S_{21}$  to our circuit model explained in Appendix A (Eq. A.47). If there are no lossy components ( $Q_c$ -limited quality factor) in the simulation  $Q_c$  can be simply calculated by looking at the 3 dB bandwidth of the resonance in the  $S_{21}$  data. Care should be taken to match the port impedances with the feedline characteristic impedance otherwise the calculated  $Q_c$  will be incorrect. This is due to reflections that cause standing waves on the feedline which change the effective impedance the resonator sees and therefore changes  $Q_c$  depending on the location of the resonator along the feedline. This effect has been indeed observed in actual resonator arrays where a periodic sinusoidal-like

$Q_c$  variation was seen [88]. In order to minimize this effect we reduced the mismatch in our actual arrays by using an impedance transformer (on chip or off chip).

### 4.3.5 Electromagnetic simulations

After designing the resonator using the previous analytical techniques we used Sonnet software [52] to run full electromagnetic simulations on the design. For lumped-element resonators since there is minimal ground plane area (unlike CPW resonators) simulation speed is generally OK. We mostly used the adaptive frequency sweep feature in Sonnet to find the resonance frequencies which is very convenient. Using two to three consecutive simulations to zoom-in on the resonance feature enough data points can be obtained to determine the quality factor accurately. We used Matlab to fit our circuit model to the  $S_{21}$  data. One of the convenient features of Sonnet is the ability to specify a sheet inductance for the metallization layer which does not degrade the simulation speed. This allows accurate determination of the resonance frequency and also allows the determination of the kinetic inductance fraction  $\alpha$ . This can be done in several ways. One way is to compare the resonance frequency when the metals are perfect conductors to the case when the superconducting sheet inductance is nonzero. This method is most accurate when  $\alpha$  is large and is effective for TiN resonators. Another method is to directly simulate the inductor with and without a sheet inductance and compare. Running simulations on an array of resonators in Sonnet is possible but can very quickly become time consuming for two reasons. According to the Sonnet manual the size of the matrix inversion computation time grows with the number of subsections  $N$  as  $\sim N^3$ . Furthermore, most of the time it is not sufficient to run a simulation once and repeated simulations are required to determine the frequencies and especially the  $Q$ 's. Fig. 4.4 shows a Sonnet simulation for a  $4 \times 4$  section of a larger 256 pixel array using dual-polarization lumped-element resonators coupled to a CPS feedline. The geometry was divided in 19000 subsections using 3 GB of memory. Simulation time per frequency point was  $\sim 15$  min, and a

total of  $\sim 90$  frequency points were simulated to accurately determine  $Q_c$  for each resonance. The minimum feature size was  $5 \mu\text{m}$ . We used a  $2.5 \mu\text{m}$  cell size and a  $5 \times 5 \text{ mm}$  box. One of the problems often encountered in Sonnet simulations was when resonances with  $Q_c$ 's over  $\sim 1$  million in the GHz range were simulated. The software does not seem to have enough accuracy at this level and  $S_{21}$  points start to fluctuate making it impossible to extract the  $Q$ . A trick that sometimes works is to include a small amount of resistive loss inside the resonator so that  $1/Q_i$  is nonzero. This way the simulation gives smooth  $S_{21}$  data.

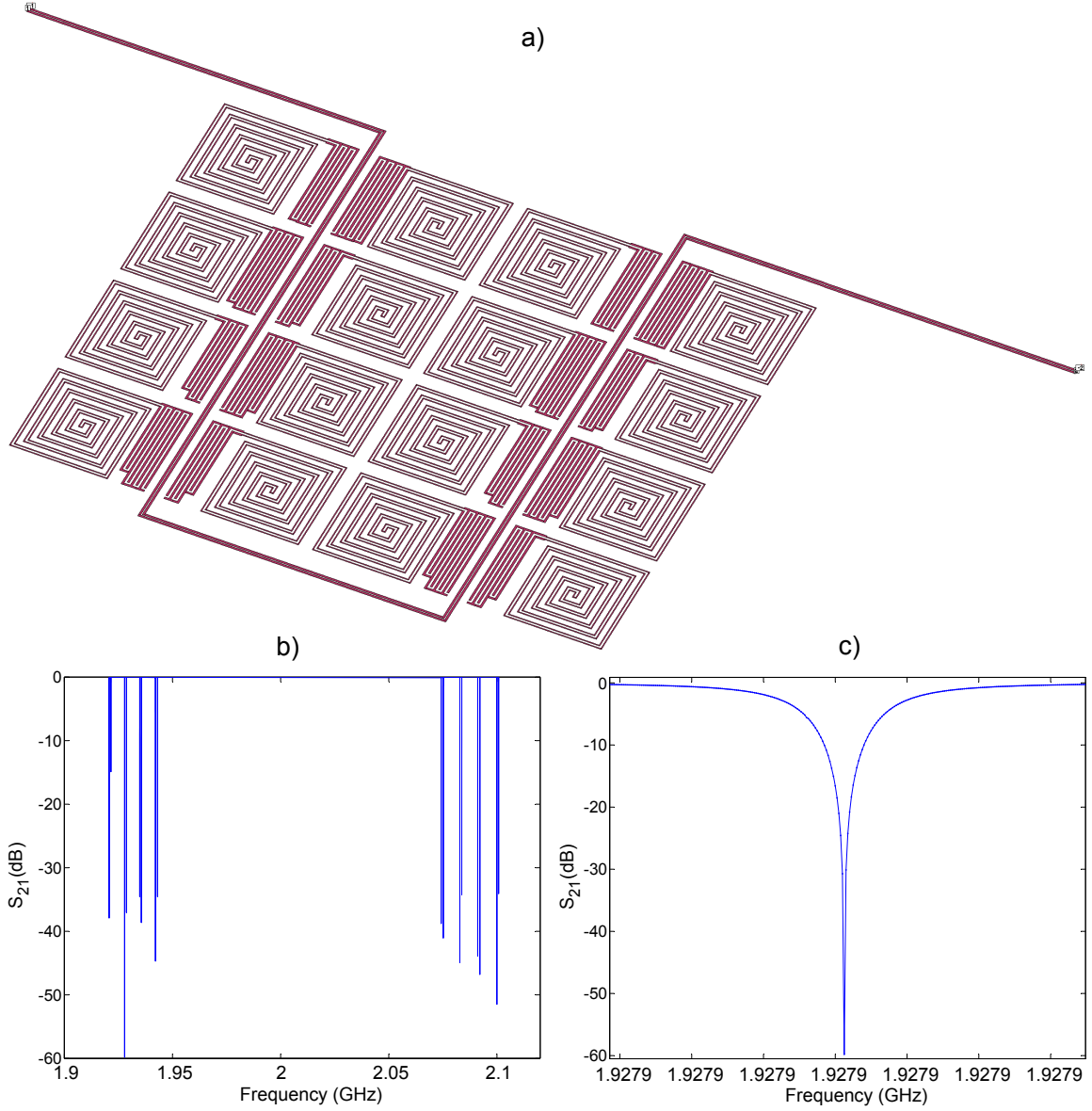


Figure 4.4: (a) A  $4 \times 4$  section of a 256 pixel array of lumped-element dual-polarization resonators coupled to a CPS feedline modeled in Sonnet. A sheet inductance of  $L_s = 6.14$  pH was used to model the superconducting TiN film. (b) Simulation of the microwave forward transmission  $S_{21}$  through the CPS feedline of the circuit in (a). The resonators were distributed in a checkerboard pattern across the chip (visible in capacitor size difference) to avoid crosstalk. The apparent frequency pattern with 8 groups of 2 resonances is due to this. The frequency spacing between each pair was designed to be 1 MHz. The simulation gives an average spacing of 891 KHz and standard deviation of 95 KHz for the 16 resonators. (c) A zoom-in on a resonance with  $Q = Q_c = 584000$

## 4.4 Resonator and array designs

In this section we will describe two specific resonator and array designs that were fabricated and measured. Both resonator arrays were initially designed using the approximations given above. Then they were simulated and fine-tuned in Sonnet. The first design (A) was our first lumped-element resonator design. It suffered from large microwave crosstalk between resonators which resulted in other problematic side effects including nonuniform frequency spacing and very large variation in  $Q_c$ . After a few new design iterations we developed design B. In this design, the resonator inductor section is spiral shaped for dual polarization absorption, and has a CPS-like geometry where two conductors carrying opposite polarity currents run close to each other. Each resonator also has a grounding shield around it. These modifications resulted in almost complete elimination of crosstalk, much more uniform frequency spacing and much less  $Q_c$  variation. A complete description of crosstalk and related measurements is provided in Chapter 5. We ran a series of measurements on these arrays to demonstrate their basic operation. These are described in the following measurements section.

### 4.4.1 Design A (“meander”)

This is our first lumped-element resonator design using  $\text{TiN}_x$  configured in a tightly packed array [89]. The design closely follows the original Cardiff proposal [67]: we use a lumped-element resonator with a meandered single-line inductor and an interdigitated capacitor (IDC). A schematic of the resonator along with a photograph of the fabricated resonator is shown in Fig. 4.5 (a) and (b). The whole resonator array is made from a single layer of  $t = 40$ -nm-thick  $\text{TiN}_x$  film with transition temperature  $T_c = 4.1$  K, sheet (kinetic) inductance  $L_s = 6.9$  pH, and sheet resistance  $R_s = 20$   $\Omega$ . The dimensions follow closely our analytical design from Section 4.3. The inductor consists of thirty-two 0.9-mm-long strips with a width of  $w = 5$   $\mu\text{m}$  and a spacing of

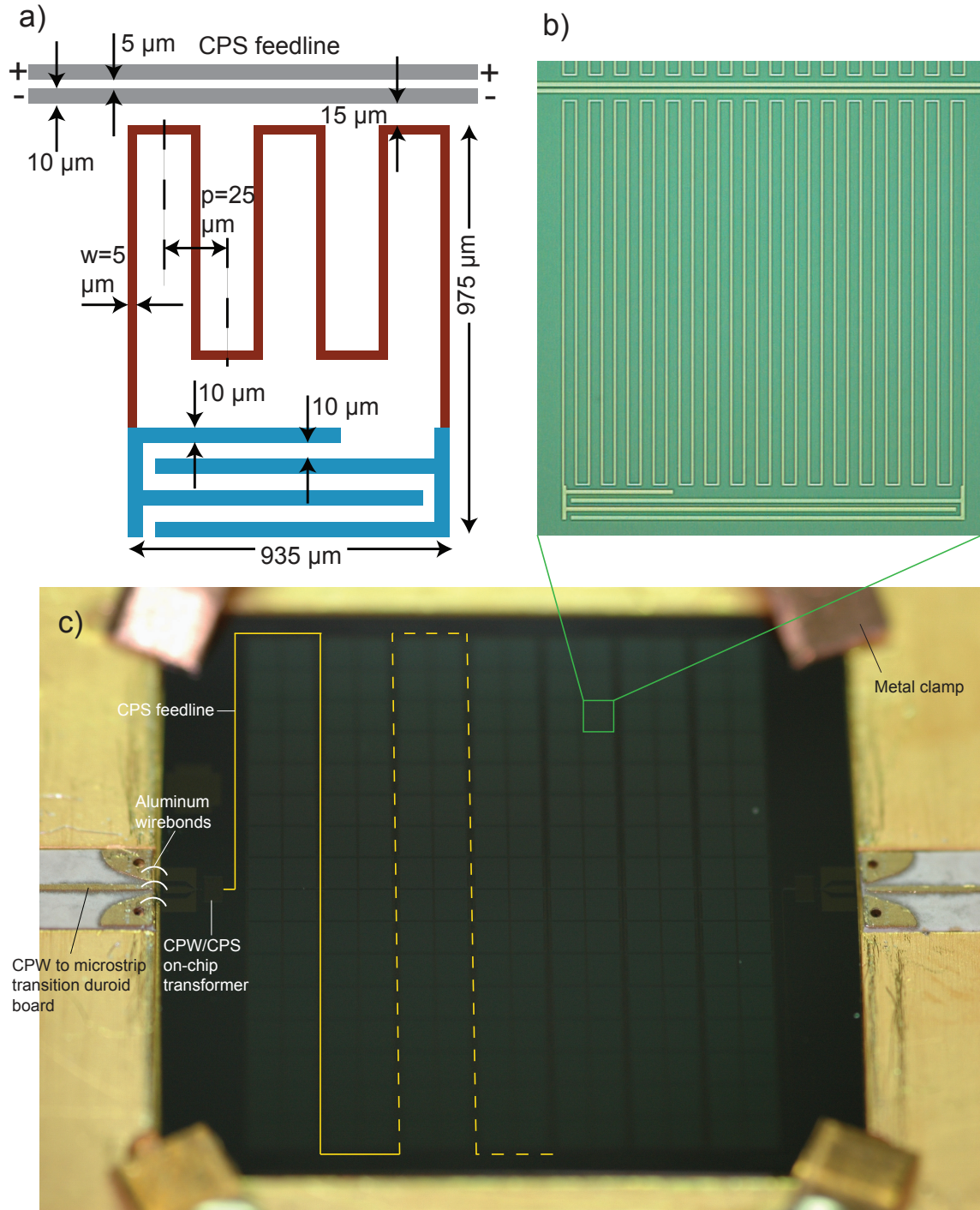


Figure 4.5: **Design A** (a) Schematic of resonator design A. Dimensions are not to scale and the number of meanders have been reduced for better visibility. The inductor is colored in red, the capacitor in blue, the feedline in gray. (b) Photograph of a design A resonator. (c) Photograph of the array mounted on the device box (gold plated copper) showing CPW-microstrip circuit board transition, aluminum wire bonds, and four retaining clips. The wirebonds connect to on chip CPW bonding pads that gradually narrow down to become the feedline.

$p = 25 \mu\text{m}$ . The total inductance is  $L \approx 60 \text{ nH}$  at 1.5 GHz, and kinetic inductance fraction  $\alpha = 0.74$ . The inductor volume is  $V \approx 5900 \mu\text{m}^3$ . The total size of the pixel is  $935 \mu\text{m} \times 975 \mu\text{m}$ . We used our initial estimate for  $R_s$  to select the fill factor  $w/p$  needed to achieve efficient submillimeter absorption using Eq. 4.11. For the silicon substrate we used the low-temperature (1.5 K) value of the dielectric constant in the far-infrared ( $\epsilon_{Si} = 11.4$ ) [83]. The coupling to the feedline is inductive and was designed for a coupling quality factor  $Q_c \approx 1.7 \times 10^6$  using Sonnet simulations. This corresponds to a spacing between the inductor and the feedline of  $15 \mu\text{m}$ .

The capacitor has four  $935 \mu\text{m} \times 10 \mu\text{m}$  fingers with relatively large  $10 \mu\text{m}$  gaps to reduce two-level system noise and dissipation [35]. The capacitor area is kept to  $\sim 10\%$  of the total area in order to minimize dead space. The length of the capacitor fingers can be varied to tune the resonance frequencies in the array. At maximum finger length, the capacitance is  $C \approx 0.2 \text{ pF}$ .

We fabricated a  $16 \times 14$  array of these resonators (Fig. 4.5 (c)). Readout is accomplished using a single coplanar strip (CPS) feedline. The CPS has a gap width of  $5 \mu\text{m}$  and strip width of  $10 \mu\text{m}$  corresponding to a characteristic impedance  $Z \approx 141 \Omega$ ; a relatively high value as compared to Al or Nb feedlines. It is hard to reduce the impedance to lower values because the gap becomes too small and problematic for fabrication of a long feedline. We used two CPW to CPS transformers on each side of the feedline to match to the  $50 \Omega$  connections. However, later we realized that these transformers were not designed to properly handle CPS-type modes and could cause more reflections. Later we switched to using balun type transformers [85]. On the array the physical gap between pixels is  $65 \mu\text{m}$  in both directions. This corresponds to  $\sim 18\%$  dead area on the array due to this spacing, but still highly compact compared to other MKID arrays. The resonator frequencies were designed (in Sonnet) to be separated by 1.3 MHz, again very compact in frequency space as compared to other MKID arrays. The lowest frequency resonator is at the top left of the array and the 224 frequencies increase linearly across the columns from top to bottom. This is achieved by changing the length of a single finger in the IDC from

full size (min frequency) to zero (maximum frequency). The feedline runs across the resonators vertically and connects to the input and output side SMA connectors using circuit board transitions and wirebonds. Four metal clamps are used to secure the chip on a metal lip under the chip. A lid is used to close the box on the front side. The box is open on the back side to allow radiation through the silicon.

#### 4.4.2 Design B (“spiral”)

Here we present our improved lumped-element resonator used for design B [89]. A diagram of the of the resonator is shown in Fig. 4.6 (a) and a photograph of the fabricated resonator is shown Fig. 4.6 (b). The TiN film is  $\sim 20$  nm thick with  $T_c = 3.6$  K,  $L_s = 11.7$  pH, and  $R_s = 30 \Omega$ . The inductor is a coplanar strip (CPS) with  $w = 5 \mu\text{m}$  strips and  $g = 10 \mu\text{m}$  gap. The spacing between each CPS pair is  $p = 45 \mu\text{m}$ . The inductor has a total inductance of  $L = 43$  pH at 1.5 GHz, and  $\alpha = 0.91$ . The inductor volume is  $V \approx 1156 \mu\text{m}^3$ . The total size of the pixel is  $\sim 645 \mu\text{m} \times 500 \mu\text{m}$ . Due to CCAT optical requirements we used half the pixel size in design A in order to be able to Nyquist sample the optical beam ( $\sim 4$  pixel per beam). The ratio  $p/w$  was tuned using Eq. 4.11, where we used an effective width  $w_{eff} = 2w$  instead of  $w$  accounting for the two strips in the CPS. The spiral shape was chosen to allow absorption in both polarizations [75]. However, later simulations [90] revealed that the absorption efficiency per polarization mode in this design concept is roughly half of design A. This can be understood by noting the area of the spiral is now made up of 4 triangles, only 2 of which are sensitive to each polarization reducing the efficiency in each polarization by half, making the total unpolarized efficiency equal to single polarization efficiency in design A.

The capacitor has fourteen  $0.5 \text{ mm} \times 5 \mu\text{m}$  fingers with  $5 \mu\text{m}$  gaps. These dimensions are smaller than in design A reducing the pixel size, but at a cost of increased TLS noise level. The increased number of fingers allows for wider frequency tunability and better current uniformity in the inductor. At maximum finger length, the

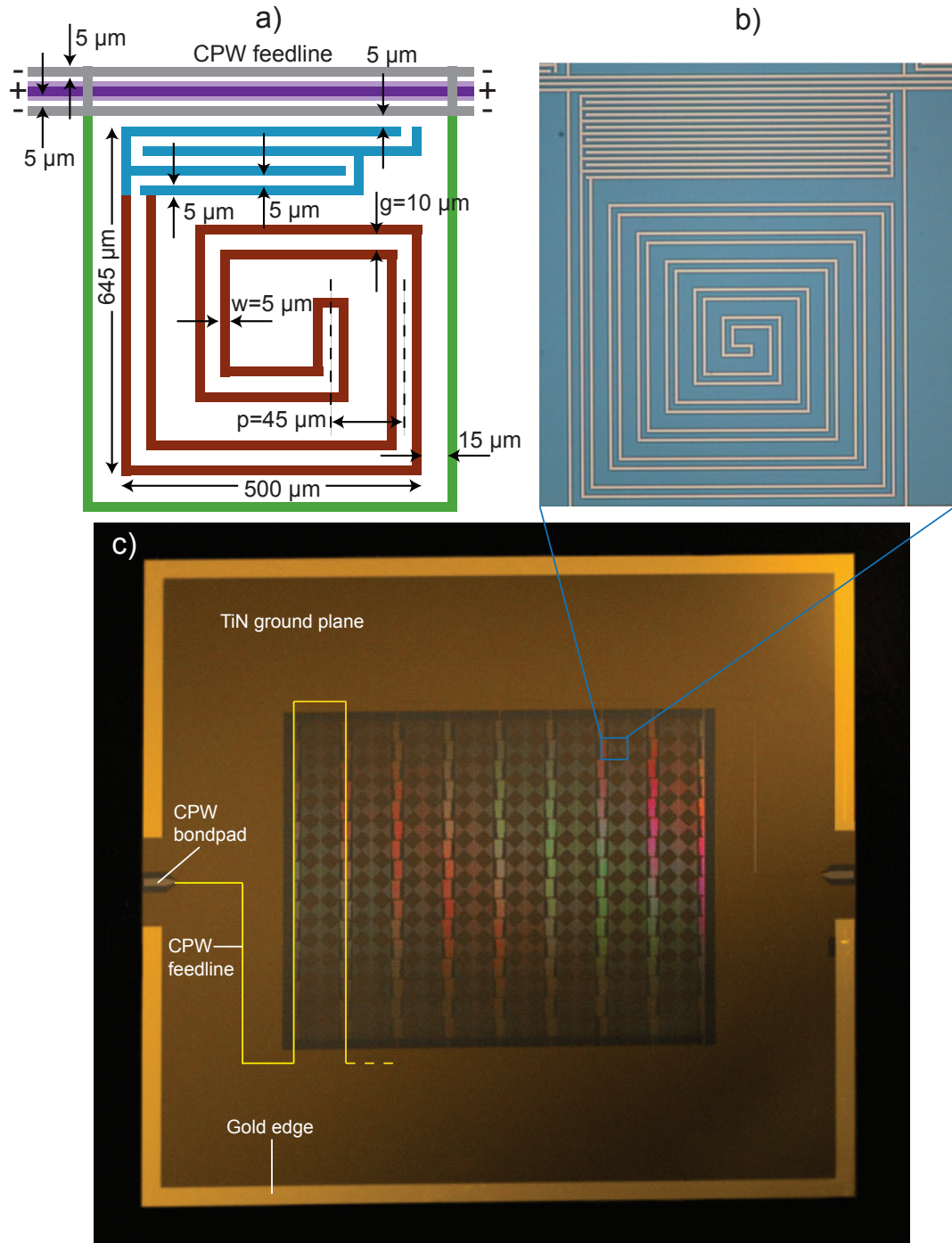


Figure 4.6: **Design B** (a) Schematic of resonator design B. Dimensions are not to scale and the number of turn in the spiral have been reduced for better visibility. The inductor is colored in red and the capacitor is in blue. The ground planes of the CPS feedline and the CPW straps (made from  $\text{TiN}_x$ ) are in gray, the CPW center line made from Nb is in dark purple, and the  $\text{SiO}_2$  dielectric layer is in light purple (which also covers the Nb). The grounding shield is in green. (b) Photograph of a design B resonator. (c) Photograph of the array chip. CPW bond pads and the CPW feedline are indicated. A large TiN ground plane extends to the edge. A narrow thin gold film at the edge and gold wire bonds improve thermal contact.

capacitance is  $C = 0.38$  pF. The coupling to the feedline is capacitive and was designed using Sonnet for  $Q_c \approx 3.8 \times 10^5$ , corresponding to the expected optical loading from CCAT roughly giving the same  $Q_i$ . This corresponds to a spacing between the IDC and the feedline of  $5 \mu\text{m}$ . We chose a capacitive coupling rather than inductive because in the case of inductive coupling resonators between feedline segments would face each other with their capacitors. This would have raised the inter-resonator cross-coupling to a higher level. Another point we considered to avoid causing cross-coupling was to tune the frequency by changing the length of finger pairs rather than single fingers. This way, we avoid exposing a single finger by shielding it with the other one. This was not done in the case of design A where a single finger was used to tune the frequency.

We fabricated a  $16 \times 16$  array of these resonators (Fig. 4.6 (c)) and used a finite-ground coplanar waveguide (CPW) feedline ( $Z = 115 \Omega$ ) as opposed to a CPS feedline. We added grounding straps at intervals of  $500 \mu\text{m}$  connecting CPW ground strips to eliminate the unwanted coupled slot-line mode [54]. We used Nb instead of TiN for the CPW centerline in order to reduce the impedance mismatch to the  $50 \Omega$  connections, helping to reduce the observed  $Q_c$  variability across the array (see Fig. 5.22). The physical gap spacing between pixels is  $\sim 35 \mu\text{m}$  in both directions. This is again a highly compact array with  $\sim 17 \%$  dead area due to this spacing. To further reduce crosstalk, the resonator frequencies are split into two groups of 128: a high-frequency band (H) and a low-frequency band (L) that are separated by 100 MHz, and are distributed in a checkerboard pattern in the array (see Fig. 5.19 and Fig. 5.7). The frequency spacing between resonances was designed to be 1.25 MHz and 2.2 MHz in the L and H bands, respectively. Starting from the top left and going down in the first column, we have resonator L1 (the lowest frequency in the L band), H1 (lowest in the H band), L2, H2,  $\dots$ , L8, H8. In the second column we have H9, L9,  $\dots$  etc. This pattern distributes the resonators in a way that keeps resonators that are close in frequency farther apart physically, reducing the pixel-pixel crosstalk. Crosstalk measurements are presented in Chapter 5. In order to improve thermal

contact between the chip and the metal box we added a narrow layer of thin gold over the TiN ground plane at the edge of the chip, and used gold wire bonds along the edge of the ground plane for heat sinking and good ground connections. Insufficient heat sinking can cause unwanted substrate heating effects when running black-body and temperature sweep measurements.

Fig. 4.7 (a) shows the device mounting box. It is made from oxygen-free high-purity copper that has been plated with a nonmagnetic gold layer to avoid exposing the magnetic-field-sensitive resonators to unwanted magnetic fields. The signal is brought in through the SMA coaxial connection on one side and read out from the other side. The center pin of the coaxial connector is soldered to a microstrip line on a duroid circuit board. The microstrip line transitions to a CPW on this board and is brought to the chip using wirebonds where it connects to the on chip CPW bond pads. Fig. 4.7 (b) shows the back side of the box where radiation is incident through the aperture on the silicon substrate. An antireflection layer can be used to match the silicon to free space. Fig. 4.7 (c) shows a photograph of an earlier version of this design where we used a CPS feedline and did not have a grounding shield around the resonators. The crosstalk measurements for design B in Chapter 5 were performed on this earlier array design.

As will be shown in Chapter 5, design B has considerably lower crosstalk than design A. In design B the use of a double-wound (CPS) inductor places conductors with opposite polarities in close physical proximity, resulting in a good degree of cancellation of the resonator's electromagnetic fields. This confines the fields closer to the structure, reducing stray interactions between nearby resonators in a close-packed array. The grounding shield around each resonator further helps in confining the fields. As a positive side effect of the proximity of opposite polarity conductors, the geometrical inductance in design B is reduced resulting in a larger kinetic inductance fraction  $\alpha$  compared to design A.

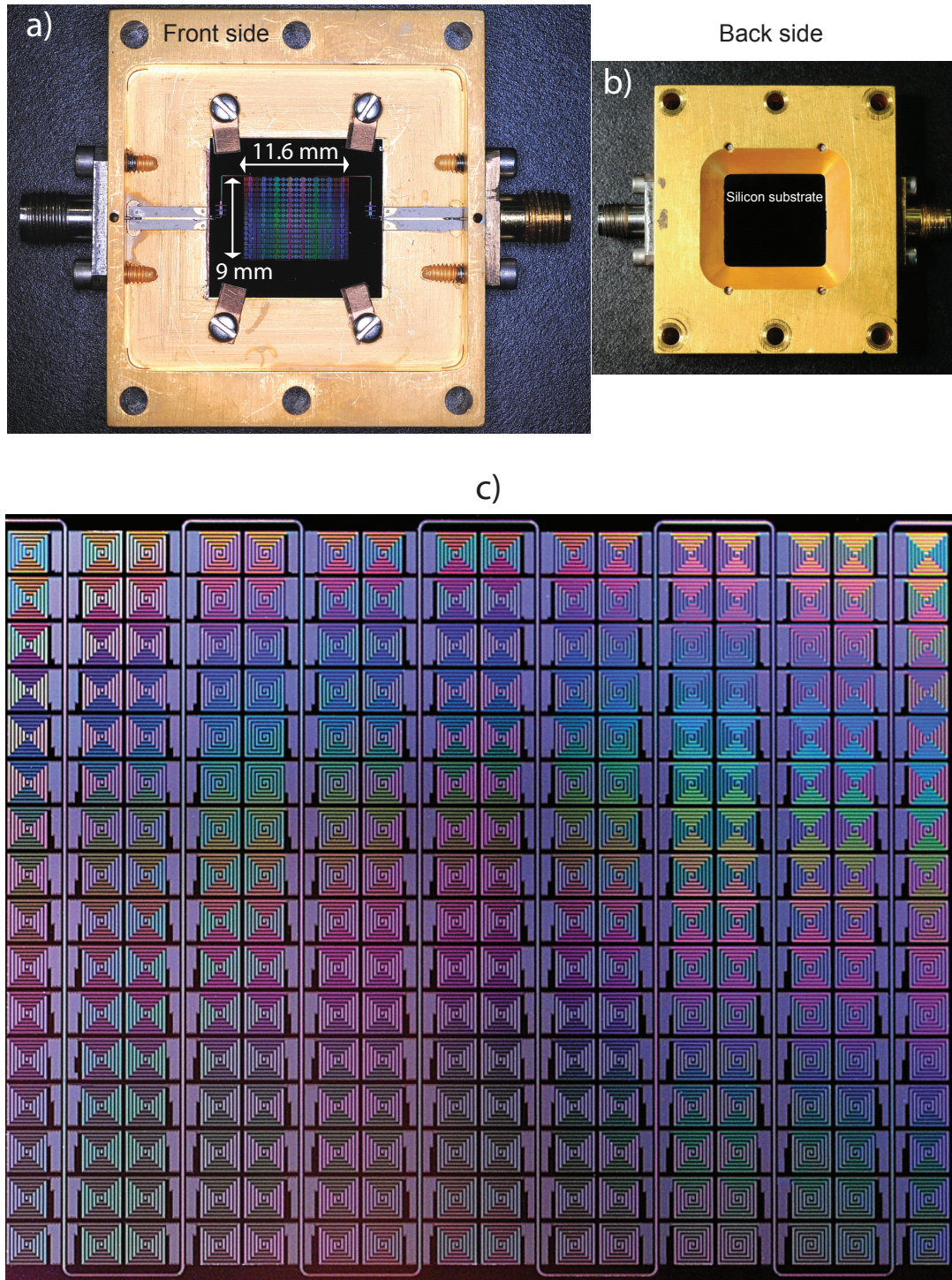


Figure 4.7: (a) Device mounting box (gold plated copper) showing microstrip-CPW transition circuit board, SMA coaxial connectors, four retaining clips, and the detector array. (b) Back side of the mounting box showing an aperture for radiation coupling. The illumination side of the silicon substrate is visible. (c) A photograph of an earlier version of a 16x16 array of design B (dual-polarization) pixels but with no resonator ground shield and a CPS feedline instead of a CPW feedline

### 4.4.3 Fabrication method

First, a layer of  $\text{TiN}_x$  film is sputtered onto an ambient-temperature, high-resistivity ( $> 10 \text{ k}\Omega \text{ cm}$ )  $\langle 100 \rangle$  silicon substrate. The substrate is cleaned with hydrofluoric acid (HF) prior to deposition. UV projection lithography is used followed by inductively coupled plasma etching using  $\text{BCl}_3/\text{Cl}_2$  to pattern the resonator structures and the CPS feedline, all in one layer, for design A. For design B the feedline is a CPW line with periodic  $\text{TiN}_x$  ground straps spaced  $500 \mu\text{m}$  apart. To avoid shorts caused by the straps, the centerline is initially not patterned and a 200-nm-thick insulating layer of  $\text{SiO}_2$  is deposited on top using RF magnetron sputtering from a high-purity fused-silica target. A thin layer of niobium is then deposited using DC magnetron sputtering, and is patterned using an inductively coupled plasma etcher and a mixture of  $\text{CCl}_2\text{F}_2$ ,  $\text{CF}_4$ , and  $\text{O}_2$ , to create the centerline of the CPW feedline. The  $\text{SiO}_2$  layer is then patterned using a buffered oxide etch (BOE) to remove  $\text{SiO}_2$  from over the resonators.

## 4.5 Measurements

In this section we will present measurements for array designs A and B shown in Fig. 4.5 and Fig. 4.6, and discuss the results.

### 4.5.1 Setup

The arrays shown in Fig. 4.5 and Fig. 4.6 were mounted in a sample box shown in Fig. 4.7 and cooled down to temperatures below 50 mK inside a dilution refrigerator. A network analyzer is used to excite the resonators on the array using a microwave probe signal that goes through the feedline and is amplified at the output of the box using a cryogenic SiGe transistor amplifier [16] mounted on the 4 K stage inside the cryostat. The signal is further amplified by a room temperature amplifier and

is read out by the network analyzer. The excitation frequency is swept through the resonances on the array and the network analyzer records the complex transmission  $S_{21}$  loops formed by the resonances on a computer. The measurement system is shown in Fig. 5.24. For crosstalk measurements a microwave synthesizer is used in combination with the network analyzer to pump on specific resonances. This is explained in detail in Chapter 5 where crosstalk measurements are presented. For measurements in this chapter the synthesizer is turned off.

## 4.5.2 Design A measurements

### 4.5.2.1 Film $T_c$ measurement

The TiN film for this devices was 40 nm thick. We measured the superconducting transition temperature by observing the average microwave transmission  $S_{21}$  of the feedline as we warmed up the fridge from below  $T_c$  to above  $T_c$ . This is shown in Fig. 4.8. At temperatures well below  $T_c$  the transmission is high but as we get closer to  $T_c$  the number of thermally generated quasiparticles increases introducing microwave loss and lowering the average transmission. At just above  $T = T_c \approx 4.1$  K the microwave transmission becomes very low. This is because of the high normal-state resistivity of TiN films.

### 4.5.2.2 Low-temperature resonance frequencies and quality factors

We measured forward transmission  $S_{21}$  of the array using the setup illustrated in Fig. 5.24. The device was cooled down to 100 mK and a readout power  $P_{\text{feed}} = -90$  dBm was applied to the device using a network analyzer. The measured transmission is shown in Fig. 5.16. The resonance frequencies and quality factors were extracted by fitting the resonance features using our fitting routine. The resulting frequencies and frequency spacings are shown in Fig. 5.18 and Fig. 5.20 (a), respectively. Using

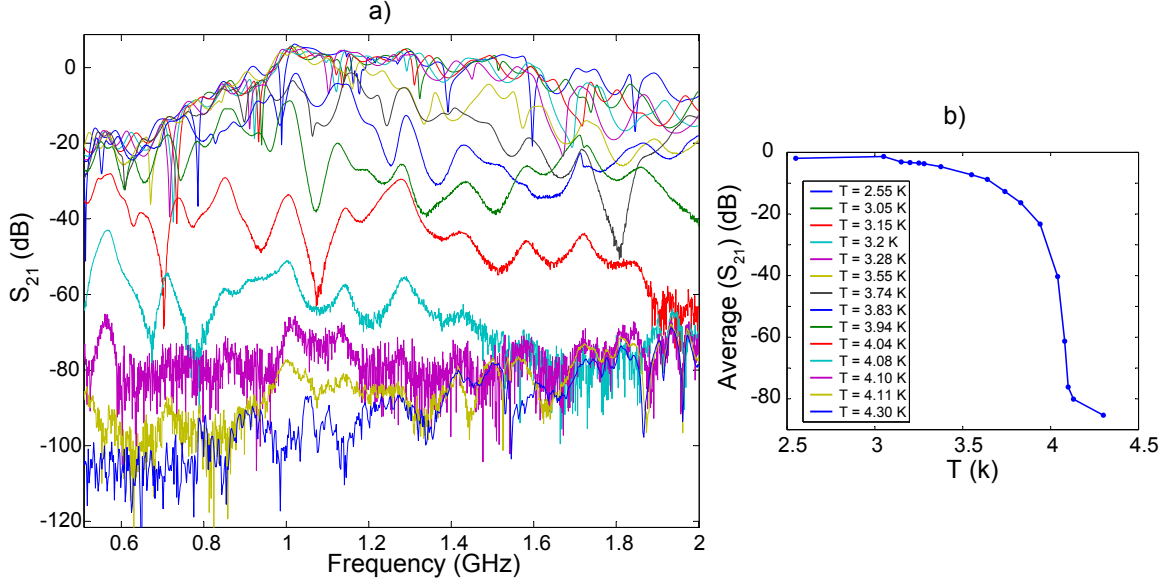


Figure 4.8: (a) Forward microwave transmission  $S_{21}$  through the feedline for design A array measured for a range of bath temperatures between 2.55–4.3 K. (b) The average transmission indicates a  $T_c \approx 4.1$  K for the TiN array in design A.

the same fitting routine we extracted the quality factors. The  $Q_c$ 's are shown in Fig. 5.21 (a) and the  $Q_i$ 's are shown in Fig. 5.22 (a). A detailed discussion of these measurements is provided in Sections 5.6.2 through 5.6.3.

#### 4.5.2.3 Bath temperature sweep

A very effective diagnostic technique is to probe the resonator properties as a function of bath temperature. We measured  $S_{21}$  for a range of bath temperatures from 50–800 mK for 4 individual resonances on this device. Fig. 4.9 (a) shows the transmission magnitude versus frequency for resonator number 1 in this temperature range and Fig. 4.9 (b) shows the complex  $S_{21}$  resonance loop for the same resonator with temperature. We used our fitting routine to extract the resonance frequencies and quality factors as a function of temperature. The fractional frequency shift and internal quality factor are shown in Fig. 4.10 (a) and (b) respectively. At temperatures above  $\sim T_c/10 \approx 400$  mK the behavior is dominated by the Mattis-Bardeen contribution: As  $T$  is increased the population of thermally generated quasiparticles increases (Eq. 2.3) generating

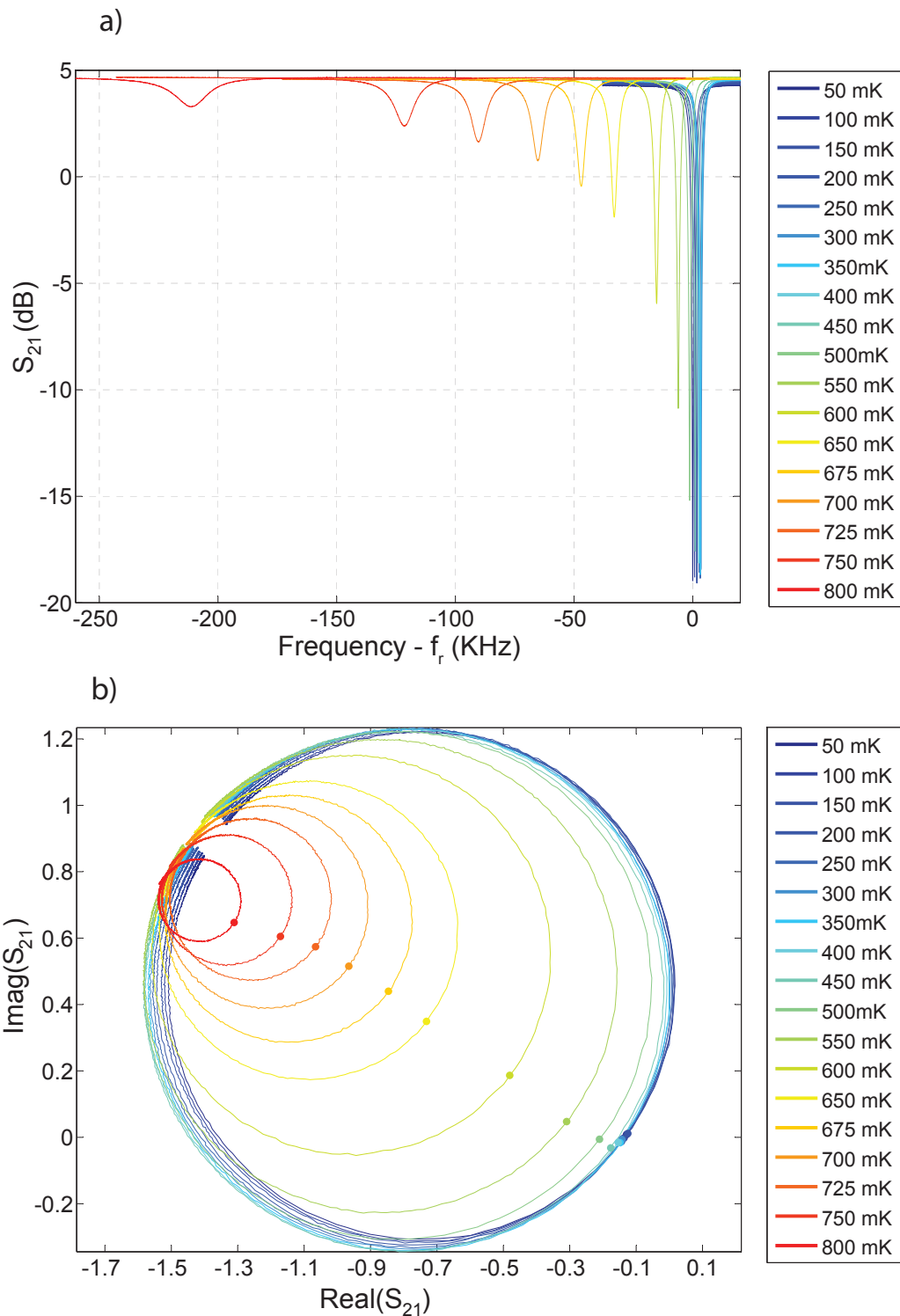


Figure 4.9: Bath temperature sweep of a lumped-element resonator in design A (resonator no. 1) from 50–800 mK. (a) Magnitude of transmission  $S_{21}$  versus frequency. The resonance frequency at 50 mK is  $f_r = 1.353$  GHz, the feedline readout power is  $P_{\text{feed}} = -90$  dBm,  $Q_c = 525,000$ , film  $T_c = 4.1$  K. (b) Complex transmission  $S_{21}$  resonance loops. The fitted resonance frequencies are shown by the dots.

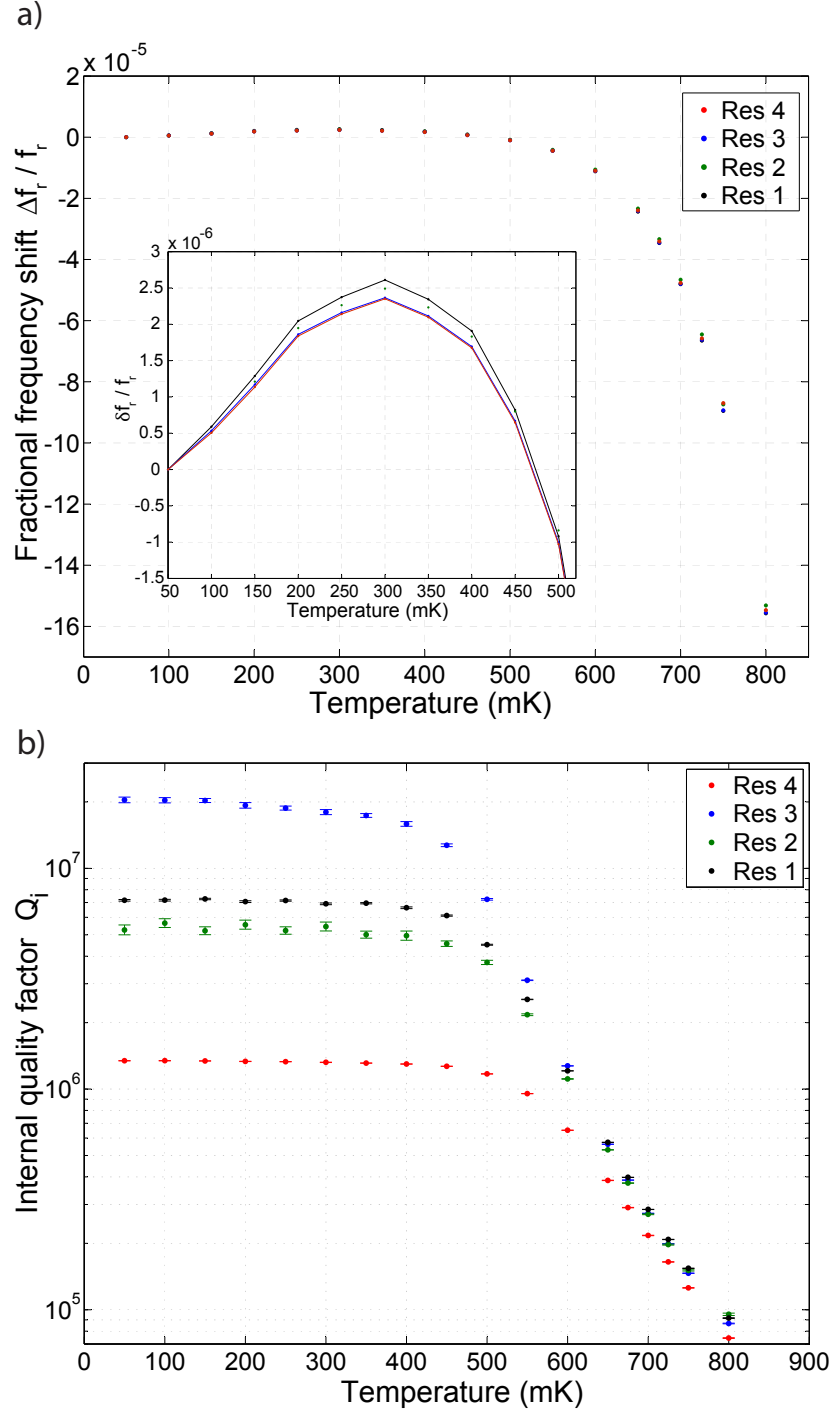


Figure 4.10: (a) Fitted fractional frequency shifts for 4 lumped-element resonators on array A from the bath temperature sweep data. The inset shows a zoom-in of the same plot at lower temperatures where TLS effects can be observed. (b) Fitted internal quality factors for 4 lumped-element resonators on array A. The resonance frequencies  $f_r$  at low temperature and the coupling quality factors  $Q_c$  for resonators number 1 to 4 were: 1.353 GHz, 1.438 GHz, 1.441 GHz, and 1.522 GHz, and  $5.25 \times 10^5$ ,  $1.659 \times 10^6$ ,  $4.93 \times 10^5$ , and  $1.447 \times 10^6$ .

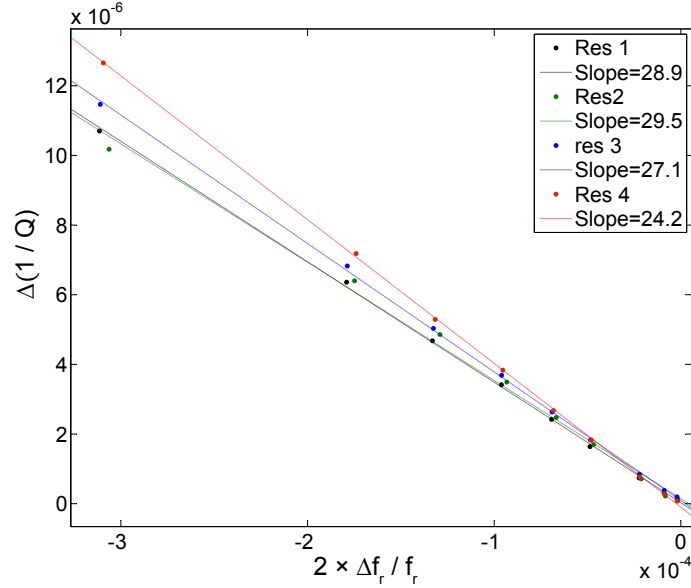


Figure 4.11: This plot shows the ratio of the frequency response  $2\Delta f_r/f_r$  to the dissipation response  $\Delta Q^{-1}$  for 4 resonators in array design A, measured using bath temperature sweep data from 500 mK to 800 mK. The average response ratio for the 4 resonances is 27.4.

microwave loss ( $\propto \sigma_1$ ) inside the superconductor reducing the  $Q$ , and at the same time increasing the kinetic inductance ( $\propto 1/\sigma_2$ ) which shifts the resonance to lower frequency. However, at  $T \lesssim 400$  mK the increase in  $f_r$  with increasing  $T$  is indicative of the existence of two-level systems (TLS) in the resonator dominating the behavior. The internal quality factors  $Q_i$  are very high at low temperatures and do not seem to be affected by TLS. This is probably because the readout power is high enough to drive the TLS into their excited state reducing the net TLS loss. Other loss mechanisms are dominating the  $Q_i$  at these low temperatures. The very similar frequency shifts for the 4 resonators gives confidence that the observed behavior is repeatable and applies to the rest of the resonances on the array.

The ratio of the response in frequency direction to the response in the dissipation direction,  $\beta = (2\delta f_r/f_r)/\delta Q^{-1}$ , is an important quantity. It determines which signal has a better quality under similar noise conditions. For our TiN array this ratio has been measured using the temperature sweep data and is shown in Fig. 4.11 for the 4 resonances. The curves follow a straight line. We have excluded the low temperature

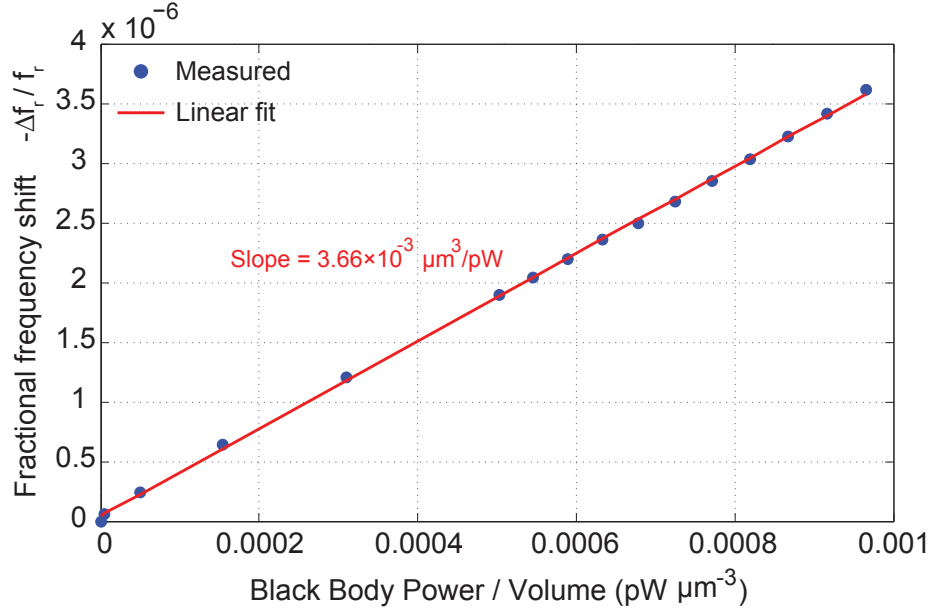


Figure 4.12: Plot shows the fractional frequency response  $\Delta f_r/f_r$  as a function of black-body power ( $\lambda \sim 215 \mu\text{m}$ ) per unit inductor volume for a design A resonator. The radiation was produced using a temperature-controlled black-body source. The slope of the response is  $3.66 \times 10^{-3} \mu\text{m}^3/\text{pW}$ . Other parameters are  $V = 5900 \mu\text{m}^3$ ,  $t = 40 \text{ nm}$ ,  $T_c = 3.6 \text{ K}$ ,  $T = 300 \text{ mK}$ ,  $f_r = 1.3406 \text{ GHz}$ ,  $Q(\text{dark}) \approx Q_c = 9 \times 10^5$ ,  $P_{\text{feed}} = -90 \text{ dBm}$ . Credit: P.K. Day

data points from the fit because their behavior is dominated by TLS. The average value of the slopes is  $\beta \sim 27.4$ . In conventional Al CPW resonators  $\beta_{\text{Al}} \sim 4$ . The much higher ratio means that for this TiN device (with  $T_c = 4.1$ ) K it is easier to get high signal-to-TLS noise ratio in the frequency direction (or equivalently lower  $\text{NEP}_{\text{TLS}}$ ) and less stringent requirements on TLS noise levels.

#### 4.5.2.4 Black-body response

The response of an MKID can be more directly measured by illuminating the resonator with submillimeter radiation from a temperature-controlled black-body source mounted inside the cryostat. For this array design, the response for a  $T_c = 3.6 \text{ K}$  device was measured by Dr. Peter Day at JPL and is shown in Fig. 4.12. The resonance fractional frequency shift  $\Delta f_r/f_r$  is shown as a function of the black-body power incident on the resonator per unit inductor volume. A  $\sim 30\%$  reflection from

the silicon surface was taken into account. The incident power is normalized by the inductor volume  $V$  so that the slope is a measure of normalized fractional frequency responsivity (see Eq. 2.63). This allows for easier comparison between different inductor designs. A normalized fractional frequency responsivity of  $3.66 \times 10^{-3} \mu\text{m}^3/\text{pW}$  was measured.

The device was illuminated through a 0.1 inch aperture in front of the black-body and a  $\lambda = 215 \mu\text{m}$  ( $\sim 1.4 \text{ THz}$ ) metal mesh bandpass filter with a bandwidth of  $\delta\nu/\nu \sim 20\%$  and in-band transmission of  $\sim 80\%$ . The apertures was positioned at 1 inch distance from the array. Using temperature sweep data and quasiparticle lifetime measurements, it is possible to theoretically estimate the response. By comparing the theoretical response to the measured black-body response, the optical efficiency of the absorptive meander inductor section was estimated to be  $\sim 70\%$  for single polarization radiation [91], comparable to the front/back power division ratio expected for silicon. This measurement confirms the basic operation of array design A when using the frequency signal of the resonators.

It is theoretically possible to increase the absorption efficiency of the meander to near 100% by using a reflecting back short under the array in order to reflect back the part of the incident radiation that does not get absorbed at first pass, and to tune out the parasitic reactance of the meander lines. By adding an antireflection layer on the silicon substrate, we could avoid the  $\sim 30\%$  Fresnel reflection off of the silicon substrate increasing the incident power on the detector. This is illustrated in Fig. 4.3 (c) and has been demonstrated for Al lumped-element resonators [79].

### 4.5.3 Design B measurements

#### 4.5.3.1 Film $T_c$ measurement

The TiN film for this devices was 20 nm thick. We used a four-point probe measurement technique to measure the superconducting transition temperature for this

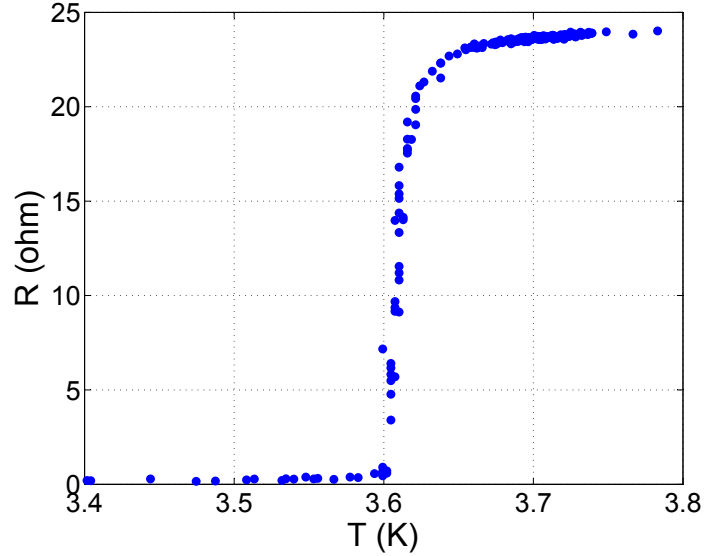


Figure 4.13: Film  $T_c$  measurement using a four-point probe DC technique for array design B. The plot indicates  $T_c \approx 3.6$  K. Credit: B.H. Eom

device at  $\sim$  DC. The film we used for the measurement was from the same chip as the array. Figure 4.13 shows that  $T_c \approx 3.6$  K. It should be noted that it is possible for  $T_c$  values measured at DC to be different from values measured at microwave frequencies. This is especially true for TiN films where variations in the gap parameter have been observed on the film depending on location [92]. Because of this the DC resistance in the film could remain zero as long as there is a small pathway for the probing current to go through that has not reached the resistive state. Therefore, it is possible that  $T_c^{DC} \geq T_c^{MW}$ . Nevertheless, we used the DC measured  $T_c$  in our analysis.

#### 4.5.3.2 Low-temperature resonance frequencies and quality factors

For the device in design B we measured forward transmission  $S_{21}$  of the array using the setup illustrated in Fig. 5.24. The device was cooled down to 25 mK and a readout power  $P_{\text{feed}} = -93$  dBm was applied to the device using a network analyzer. The measured transmission is shown in Fig. 5.17. The resonance frequencies and quality factors were extracted by fitting the resonance features using our fitting routine. The

resulting frequencies and frequency spacings are shown in Fig. 5.19 and Fig. 5.20 (b), respectively. Using the same fitting routine we extracted the quality factors. The  $Q_c$ 's are shown in Fig. 5.21 (b) and the  $Q_i$ 's are shown in Fig. 5.22 (b). A detailed discussion of these measurements is provided in Sections 5.6.2 through 5.6.3.

### 4.5.3.3 Bath temperature sweep

A bath temperature sweep from 12 mK to 150 mK was taken for the this array for two resonators. The device was from the same wafer that included several design B arrays. The resonators were probed with feedline powers of  $P_{\text{feed}} = -101, -96,$  and  $-91$  dBm. Higher powers caused the resonators to go above their critical point where they would enter the nonlinear bifurcation regime caused by the kinetic inductance nonlinearity which is now known to happen in TiN resonators [13]. Fig. 4.14 shows the temperature sweep of the resonances at  $P_{\text{feed}} = -91$  dBm. There was no detectable difference in the frequency response at the other two lower powers. Both resonators show very similar behavior first slightly going down in frequency and then going up which is the signature of TLS. The two resonators had frequencies of 1.96 GHz and 1.98 GHz which give  $\hbar\omega/2k_B \approx 47$  mK which is the expected position of the minimum in the curve according to TLS theory, and that's what we observed. Unfortunately our measurement setup was not able to probe higher temperatures at the time but according to the data at hand we think that TLS are present in these resonators. The similarity of the two curves at all powers also indicates the uniformity of the response in the array.

### 4.5.3.4 Black-body response

We measured the response of 7 resonators on an array B device using a temperature-controlled black-body mounted inside the cryostat. The array was cooled down to 35 mK. The device was illuminated through a 0.29 inch aperture in front of the black-body and a  $\lambda = 215 \mu\text{m}$  ( $\sim 1.4$  THz) metal mesh bandpass filter with a bandwidth

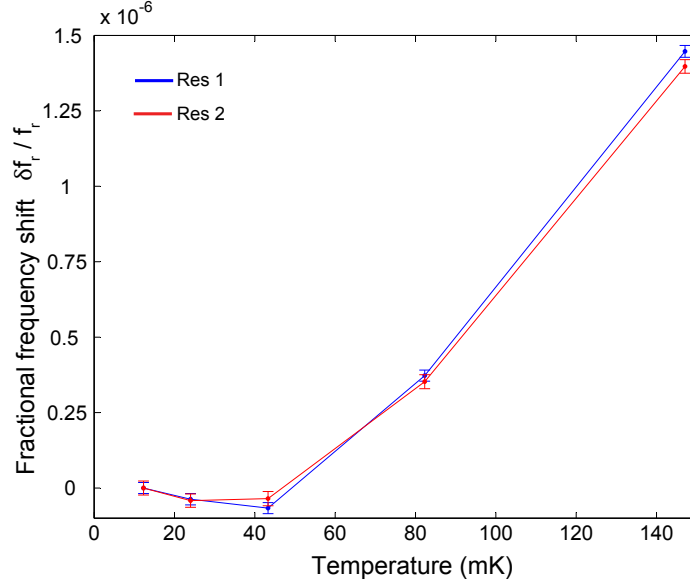


Figure 4.14: Fitted fractional frequency shifts for 2 lumped-element resonators on array B from the bath temperature sweep data. The two resonators had frequencies of 1.96 GHz and 1.98 GHz, and  $Q_c$ 's of  $1.23 \times 10^5$  and  $0.97 \times 10^5$ .

of  $\delta\nu/\nu \sim 20\%$  and in-band transmission of  $\sim 80\%$ . The apertures was positioned at 1 inch distance from the array. The black-body temperature  $T_{BB}$  was swept from 10 K to 40 K in steps of 2 K, in each step allowing  $\sim 30$  min time for the temperature to stabilize. We measured the microwave transmission of the array using a feedline power  $P_{\text{feed}} = -90$  dBm above which the resonators would start to enter the nonlinear bifurcation regime. Figure 4.15 shows the magnitude and complex value of the transmission  $S_{21}$  for resonator number 7 as the black-body temperature is changed. Both a frequency and a dissipation response can be seen.

We used our fitting code to fit to each of the resonance loops from the seven resonators and extracted  $f_r$ ,  $Q_i$ ,  $Q_c$ , and  $Q_r$  for the lowest black-body temperature ( $T_{BB} = 10$  K). The fitted resonator parameters are shown in Table 4.1. The power incident on the  $0.5 \text{ mm} \times 0.5 \text{ mm}$  surface area of a resonator at each black-body temperature was calculated taking into account a 30% reflection at the silicon-air interface. The fractional frequency response,  $-\Delta f_r/f_r = (f_r(T_{BB} = 10 \text{ K}) - f_r(T_{BB})) / f_r(T_{BB} = 10 \text{ K})$  and the dissipation response  $\Delta(1/Q_i) = 1/Q_i(T_{BB}) - 1/Q_i(T_{BB} = 10 \text{ K})$  are plotted in Fig. 4.16 (a) and (b) as a function of incident black-body power per unit

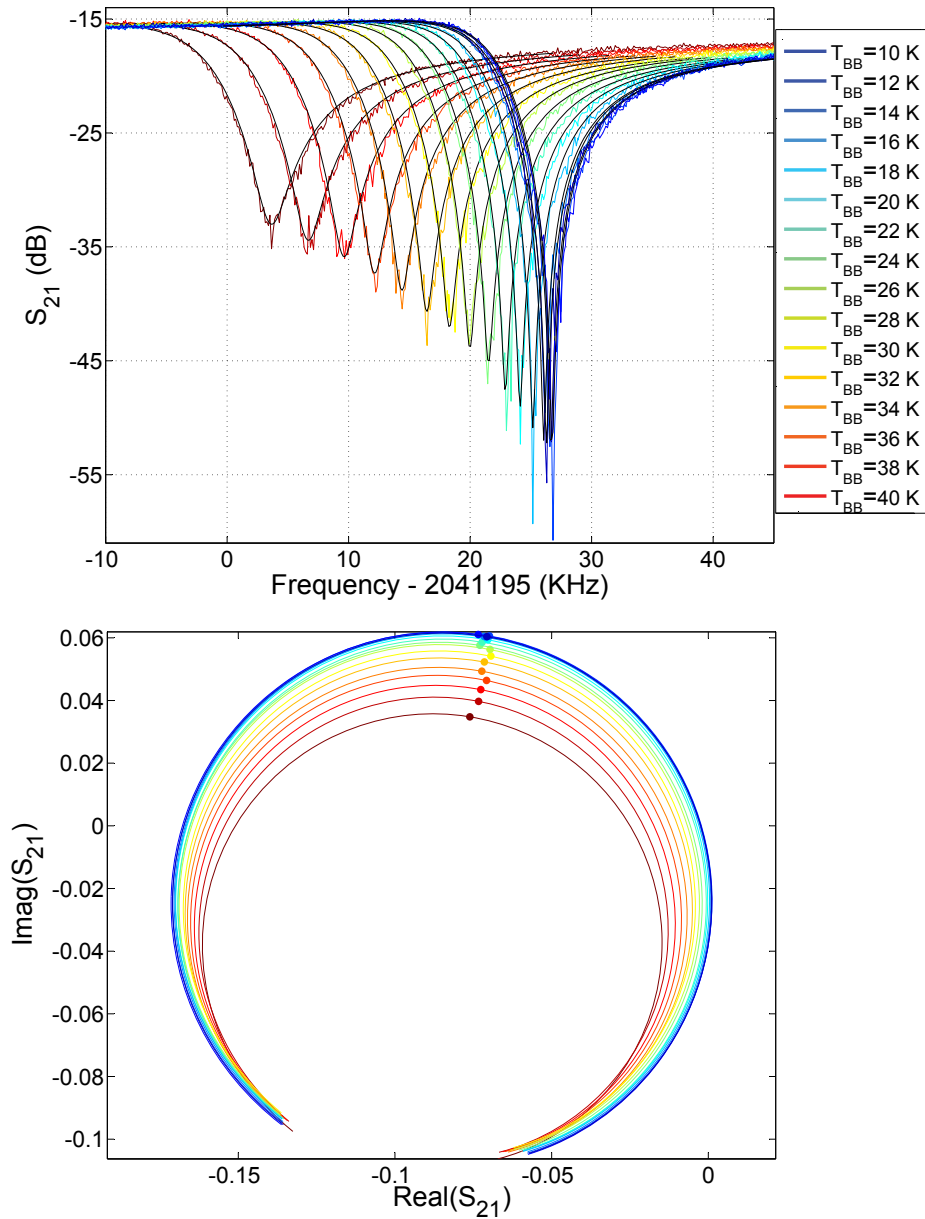


Figure 4.15: Black-body temperature sweep of resonator no. 7 for array design B. Measured magnitude versus frequency and complex amplitude of  $S_{21}$  are plotted in (a) and (b). The fitted curves are plotted in black in (a) and the fitted resonance points are indicated by the dots in (b). Measurement conditions were  $T=35$  mK and  $P_{\text{feed}} = -90$  dBm. Resonator parameters are  $f_r = 2.041$  GHz,  $Q_c = 150,000$ , and  $Q_i(T_{BB} = 10 \text{ K}) = 9,280,000$ .

Table 4.1: Measured  $f_r$ ,  $Q_c$ , and  $Q_i$  for 7 resonators on array design B

Res #	$f_r$ (GHz)	$Q_c$	$Q_i(T_{BB} = 10 \text{ K})$
1	2.014	127,000	$2.0 \times 10^7$
2	2.026	123,000	$1.8 \times 10^7$
3	2.031	69,000	$2.4 \times 10^7$
4	2.032	43,000	$1.2 \times 10^7$
5	2.038	107,000	$1.6 \times 10^7$
6	2.039	184,000	$1.8 \times 10^7$
7	2.041	150,000	$0.93 \times 10^7$

Bath temperature was  $T = 35 \text{ mK}$  and readout power  $P_{\text{feed}} = -90 \text{ dBm}$ .

inductor volume for 7 resonators.

The signals in both directions are very similar for all 7 resonators indicating a uniform response across the array. The small “hook” at low powers ( $\leq 1 \text{ pW}$ ) in Fig. 4.16 (a) is probably caused by the heating of the substrate since it was later discovered that the chip was not effectively thermally heat sunk. From the bath temperature data in Fig. 4.14 we know that TLS exist in these resonators. The heating could cause a TLS-induced shift that affects the frequency response shape. Later measurements with a better heat sunk device (see Fig. 4.6 (c)) did not indicate the existence of this feature in the data.

The curvature at higher powers in Fig. 4.16 (a) and (b) is particularly interesting. We discovered later from manufacturer specifications that the bandpass filter in front of the black-body can leak in power at above the passband in a small frequency window that was not accounted for in our power calibration. This extra power causes the curves to appear to bend upwards in our plots. It can be shown that by taking into account the actual filter transmission versus frequency the curves (especially the frequency response) become more linear. Since we did not have the real filter transmission function available, we did not recalibrate the power in these plots which will cause a slight overestimation of the responsivities.

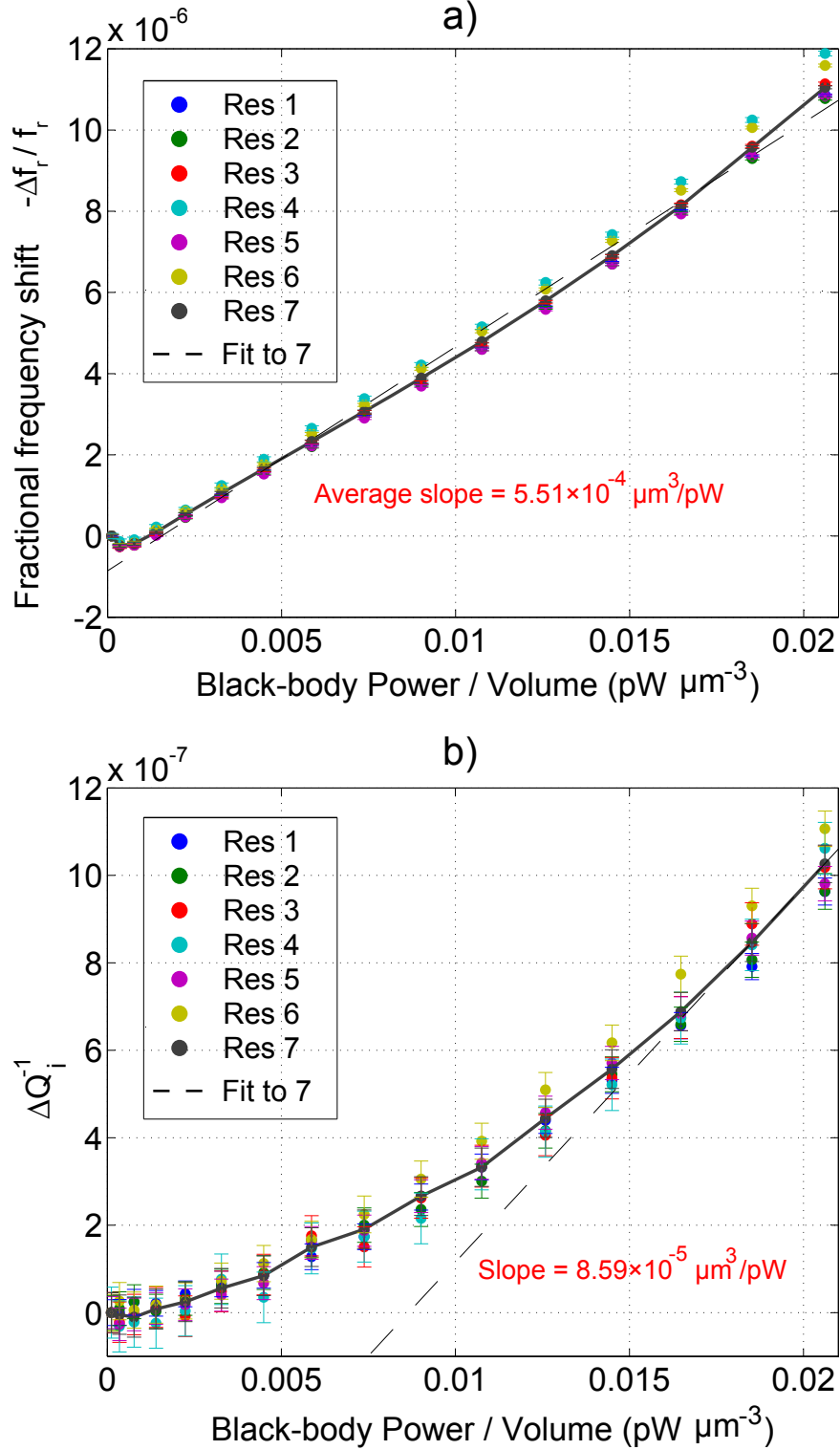


Figure 4.16: Measured fractional frequency response (a) and dissipation response (b) for 7 resonators on array design B. The error bars are indicated. The solid lines indicate the trajectory for res 7. The dashed line in (a) is the average linear fit for the 7 resonators. The dashed line in (b) is a fit to the last 2 data points for res 7. Resonator parameters are  $V = 1156 \mu\text{m}^3$ ,  $t = 20 \text{ nm}$ ,  $T_c = 3.6 \text{ K}$ ,  $T = 35 \text{ mK}$ , and  $P_{\text{feed}} = -90 \text{ dBm}$ .  $f_r$  and  $Q$  for the 7 resonators are listed in Table 4.1.

Table 4.2: Amplifier-limited noise equivalent power and responsivity using dissipation readout for 7 resonators on array design B

Res #	$dS_{21}/dP_{BB}(\text{pW}^{-1})$	$\text{NEP}_{\text{diss}}^{\text{amp}} (\text{W Hz}^{-1})$
1	0.0074	$5.0 \times 10^{-16}$
2	0.0072	$5.2 \times 10^{-16}$
3	0.0045	$8.3 \times 10^{-16}$
4	0.0029	$1.3 \times 10^{-15}$
5	0.0064	$5.8 \times 10^{-16}$
6	0.0093	$4.0 \times 10^{-16}$
7	0.0082	$4.5 \times 10^{-16}$

Performing a linear fit on the frequency response data and averaging over the slopes for the 7 resonators gives an average response of  $5.51 \times 10^{-4} \mu\text{m}^3/\text{pW}$ . By comparing this number with an expected thermal response measured from a bath temperature sweep one could potentially obtain an estimate for the optical efficiency of the spiral inductor absorber. Simulations performed by Dr. Nuria Llombardt [90] indicate that the efficiency is  $\lesssim 35\%$  for each polarization, giving a total of  $\lesssim 35\%$  efficiency for unpolarized radiation.

For the dissipation response, from the slope of the curves in Fig. 4.16 (b) calculated from the two highest power data points, we get a response  $dQ_i^{-1}/dP_{BB} \sim 7.5 \times 10^{-8} \text{ pW}^{-1}$  with little variation between the 7 resonators. We can make an estimate for the amplifier-limited noise equivalent power ( $\text{NEP}_{\text{amp}}^{\text{diss}}$ ) for these resonators. For example, for resonator number 6 with  $Q_c = 180,000$  and  $Q_i = 8.5 \times 10^5$  at  $T_{BB} = 40$ , we get  $dS_{21}/dQ_i^{-1} = 1/4 \times \chi_c \times Q_i = 125,000$ , and responsivity  $dS_{21}/dP_{BB} \approx 0.0093 \text{ pW}^{-1}$ . Assuming an amplifier noise temperature of  $T_n = 2$  K, we get an  $S_{21}$  noise level of  $\sigma_{S_{21}} = \sqrt{kT_n/2P_{\text{feed}}} = 3.7 \times 10^{-6} \text{ Hz}^{-1/2}$ . Therefore,  $\text{NEP}_{\text{amp}}^{\text{diss}} = 3.7 \times 10^{-6} \text{ Hz}^{-1/2} / 0.0093 \text{ pW}^{-1} \approx 4.0 \times 10^{-16} \text{ W Hz}^{-1/2}$  which is only within a factor of 2–3 above the photon background noise for CCAT conditions. The NEP and responsivity values for all 7 resonators are shown in table 4.2. These numbers essentially demonstrate the basic operation of array design B.

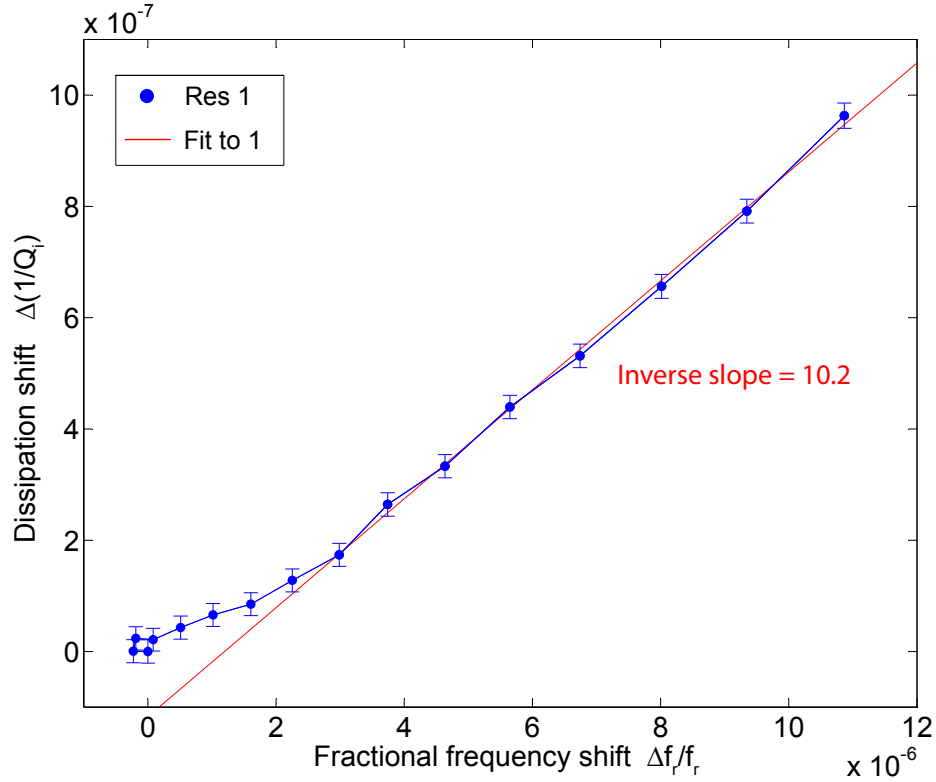


Figure 4.17: This figure shows the dissipation response plotted against the frequency response for the black-body measurement on resonator #1 in array design B. The red line is a fit to the data.

An interesting observation is the ratio of the frequency to dissipation response. In Fig. 4.17 we have plotted this for resonator number 1. Other resonators show a very similar trend. We have discarded the lowest 9 temperature points in the linear fit since they are dominated by non-Mattis-Bardeen (M-B) behavior. The average inverse slope for the 7 resonators is  $\sim 10$ . Twice this number,  $\sim 20$ , can be compared to the usual theoretical prediction from M-B for the slope (Eq. 2.22). From M-B,  $2 \lesssim \beta \lesssim 10$  for  $0.05 \text{ K} \leq T \leq 0.8 \text{ K}$  for a  $T_c = 3.6 \text{ K}$  TiN resonator with  $f_r = 2 \text{ GHz}$  [13], which is significantly lower than the black-body-deduced value. This points to the fact that the physics of  $\text{TiN}_x$  resonators cannot be simply explained by M-B theory.

Two important parameters that affect  $\text{NEP}_{\text{amp}}^{\text{diss}}$  are  $\chi_c$  and  $y_a$  where  $y_a = \Gamma_a/\Gamma_o = \eta_a \chi_c P_{\text{feed}}/2\eta_o P_o$  (see Eq. 2.27). The NEP is minimized when  $\chi_c = 1$  (which happens

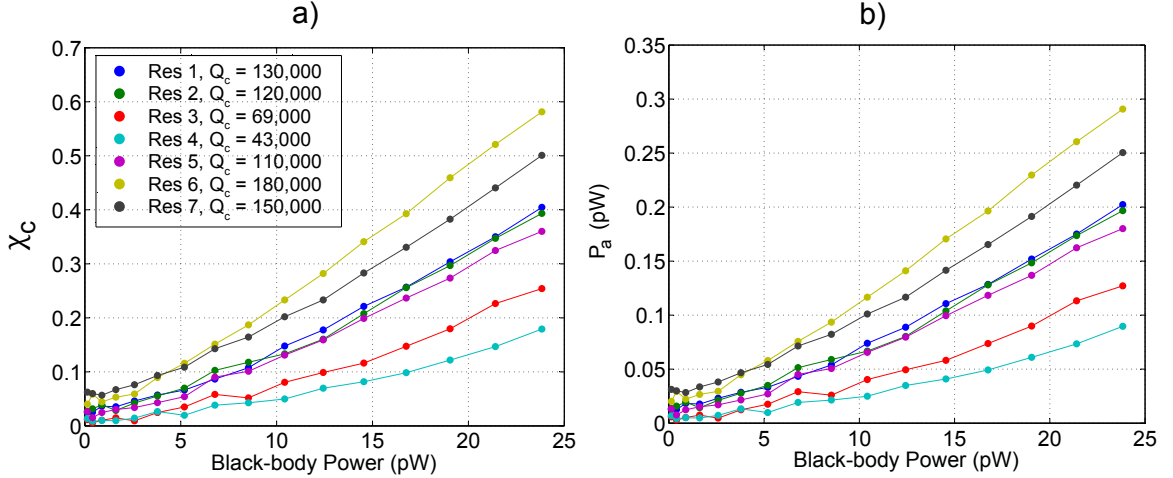


Figure 4.18: (a) A plot of  $\chi_c$  versus black-body power  $P_{BB}$ . The inset shows the  $Q_c$ 's for the 7 resonators. (b) Absorbed readout power inside the resonator  $P_{read}$  versus  $P_{BB}$

when  $Q_i = Q_c$ ) and  $y_a \lesssim 1$  [13]. The latter happens when the readout power absorbed inside the resonator ( $P_a = \chi_c P_{feed}/2$ ) is not very different from the incident optical power  $P_o$  (assuming that  $\eta_a$  is not very different from  $\eta_o \approx 0.7$ ). A rough estimate for  $P_o$ , the actual optical loading from the telescope, in the case of the 350  $\mu\text{m}$  band for CCAT is  $P_o \sim 42$  pW. The assumptions made are: pixel absorption efficiency of 100% (using a backshort), telescope optical path efficiency of 50%, sky temperature of 270 K, atmospheric emissivity of 50%, optical detection bandwidth of 90 GHz, dual polarization pixels (factor of 2), and Nyquist sampling of the diffraction-limited optical beam (factor of 1/4). These are very optimistic assumptions and the actual optical power could be lower by a factor of two. It is clear that the maximum optical power from the black-body in our measurement is only  $\sim 60\%$  of the maximum telescope optical power, and probably not sufficient to simulate the actual situation in the detectors. We have plotted  $\chi_c$  and  $P_a$  as a function of the black-body power in Fig. 4.18. Looking at the value of  $\chi_c$  at the highest available power and extrapolating up to 42 pW we see that resonator 6 and 7 will have  $\chi_c \sim 1$ , close to optimum condition. However, looking at the readout power absorbed ( $P_a$ ) and extrapolating, we see that at 42 pW resonator 6 and 7 will have  $P_a \sim 0.5$  pW which is a factor of 82 lower than the optimum condition. This corresponds to a factor of 9 higher NEP assuming

that the responsivity is constant. It should be noted that the exact optimum will depend of  $\eta_a$  which is not well known and therefore there is a degree of uncertainty involved. Nevertheless, we take that  $P_a$  is far away from optimum condition. It was later discovered that the reason why we could not use a higher readout power which caused the resonances to break was the highly nonlinear kinetic inductance of  $\text{TiN}_x$  films. Ongoing developments in our group have now made it possible to probe  $\text{TiN}_x$  resonators using readout powers  $\sim 100\times$  larger than the critical power. Even though our measurements might not exactly simulate the optimum telescope conditions, they have served to demonstrate the basic operation of  $\text{TiN}_x$  resonator arrays for submillimeter wave detection and have opened the path for optimization of these designs.

Up to this point we have not explained in detail why we chose to use  $\text{TiN}_x$  in our LeKID resonators. In the remaining part of this chapter we review this case and show that the use of  $\text{TiN}_x$  has several advantages over materials like Al and can potentially result in improved sensitivity.

## 4.6 Material-dependent sensitivity in MKIDs

Over the last  $\sim 10$  years different superconducting materials have been explored for use with MKIDs. Aluminum resonators particularly have been extensively explored within various research groups. For ground-based observations where  $N_{qp}$  is dominated by the sky optical loading power, sensitive coplanar-waveguide (CPW) Al MKID detectors limited by the photon background noise have been recently demonstrated in the lab [72]<sup>2</sup>. Our own group has demonstrated near-background-limited detection<sup>3</sup> using Al MKIDs in an engineering run at the Caltech Submillimeter Ob-

---

<sup>2</sup>The measured NEP in this work was at a signal modulation frequency of  $\nu = 500$  Hz, far away from the unwanted  $1/f$  noise originating from the readout system, amplifier gain variation, and the black-body source temperature variations.

<sup>3</sup>At signal modulation frequencies of  $\sim 0.01$ – $0.1$  Hz. The frequency depends on the scan speed of the telescope.

servatory [63, 18, 17, 62]. For space-based observations the photon background noise is much lower than ground. Therefore, for background-limited operation the detectors need to have NEPs of order  $\sim 10^{-19}$ – $10^{-20}$   $\text{WHz}^{-1/2}$ , depending on application (imaging or spectroscopy). Such sensitivity is hard to reach using conventional MKID technologies including aluminum MKIDs. Current efforts for space-based observing using Al MKIDs have resulted in demonstration of dark (electrical) NEPs of  $7 \times 10^{-19}$   $\text{WHz}^{-1/2}$  [93] and  $3.3 \times 10^{-19}$   $\text{WHz}^{-1/2}$  [94, 95].

In this work, we have been using  $\text{TiN}_x$  films for our MKID material to design large arrays of submillimeter detectors for ground telescopes like CCAT or potential future space telescopes. These films have shown excellent properties suitable for ultrasensitive detection using MKIDs [58]. In the next sections we will review these properties and show that  $\text{TiN}_x$  resonators have significant advantages which justify the use of  $\text{TiN}_x$  in our designs. We start by describing the  $\text{TiN}_x$  fabrication process that was used for making the arrays described in this thesis. We then review various material-dependent parameters that are important in determining the sensitivity.

#### 4.6.1 $\text{TiN}_x$ film fabrication

The  $\text{TiN}_x$  films in this work were produced at the Microdevices Laboratory of the Jet Propulsion Laboratory by Dr. Henry G. Leduc and colleagues. The films were made by reactive magnetron sputtering onto ambient-temperature, 100-mm-diameter, high-resistivity ( $> 10 \text{ k}\Omega \text{ cm}$ )  $\langle 100 \rangle$  silicon substrates. A hydrofluoric acid (HF) solution was used to remove any native oxides and to hydrogen terminate the surface. The titanium sputtering target was 99.995% pure, and the sputtering gases ( $\text{N}_2$  and Ar) were 99.9995% pure [58]. Fig. 4.19(a) shows a plot of  $T_c$  versus nitrogen flow rate. As can be seen,  $T_c$  is highly sensitive to nitrogen content in nonstoichiometric  $\text{TiN}_x$  [96] and approaches 4.5 K for stoichiometric TiN. Microresonator structures were then fabricated using deep UV projection lithography followed by inductively-coupled plasma etching using a chlorine chemistry ( $\text{BCl}_3/\text{Cl}_2$ ). The exact sputtering chamber

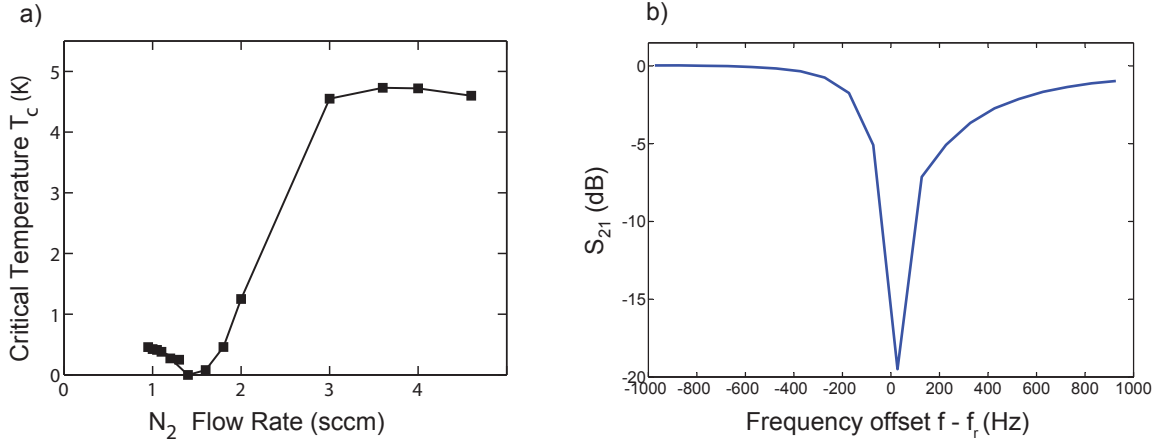


Figure 4.19: (a) The critical temperature of reactively sputtered  $TiN_x$  films as a function of the  $N_2$  flow rate. (b) A deep resonance in array design A measured at  $T = 100$  mK and  $P_{gen} = -90$  dBm with  $f_r = 1.53$  GHz,  $Q_r = 3.6 \times 10^6$ , and  $Q_i = 3 \times 10^7$ . The device was a  $14 \times 16$  close-packed array of lumped-element resonators made using a  $t = 40$  nm  $TiN_x$  film with  $T_c = 4.1$  K,  $R_s = 25\Omega$ , and  $L_s = 8.4$  pH. In addition, six resonances with  $Q_i > 2 \times 10^7$  were seen, and  $> 50$  had  $Q_i > 10^7$ . Figures reproduced from [58]

conditions and details can be found in [58].

Material properties of  $TiN_x$  and its growth mode are highly dependent on a wide range of parameters including film thickness, substrate temperature, bias, and crystallinity [97]. References for properties of  $TiN_x$  films developed under various conditions can be found in [96, 97, 98, 92, 99].

#### 4.6.2 Film properties and advantages of $TiN_x$ resonators

$TiN_x$  resonators have several advantages over more conventional resonator materials like Al. These are explained below.

Our  $TiN_x$  films resulted in exceptionally low microwave loss MKID resonators [58]. Fig. 4.19 (b) shows a deep resonance measured on an array fabricated using the described fabrication method. We measured a record-high internal quality factor  $Q_i = 3 \times 10^7$  for this resonance indicating that  $Q_{i,max} \geq 3 \times 10^7$  for our  $TiN_x$  films. Several of our arrays produced since then have shown consistently high  $Q_i$ 's above

$1 \times 10^7$  across the array (see Fig. 5.21 and 5.22). Following this work, similar high-Q resonators reaching  $Q_i \sim 1 \times 10^7$  made from TiN films were reported by Vissers et al. [97].

The surface resistance of our TiN<sub>x</sub> films were considerably higher than more conventional Al, Nb, or Ta films used for MKIDs. For our films with  $0.7 \text{ K} \leq T_c \leq 4.5 \text{ K}$  and  $20 \text{ nm} \leq t \leq 100 \text{ nm}$ , the normal state resistivity was typically  $\rho_n \approx 100 \mu\Omega \text{ cm}$  with  $\text{RRR} = \rho_n(300 \text{ K})/\rho_n(4 \text{ K}) \approx 1.1$  [58]. A similar study by Diener et al. [100] reported  $\rho_n \approx 130 \mu\Omega$ . The surface resistance can be calculated from  $R_s \approx \rho_n/t$  for thin films (see Eq. 2.12). This high surface resistance directly translates into a high superconducting surface inductance  $L_s \approx \hbar R_s/\pi\Delta$  and guarantees a very high kinetic inductance fraction  $\alpha$  approaching unity (depending on the specific geometry of the inductor). Resonators in our array design A (see Fig. 4.5) had  $T_c = 4.1 \text{ K}$ ,  $t = 40 \text{ nm}$ ,  $R_s \approx 20 \Omega$ ,  $L_s = 6.9 \text{ pH}$ , and  $\alpha = 0.74$ , and resonators in design B (see Fig. 4.6) had  $T_c = 3.6 \text{ K}$ ,  $t = 20 \text{ nm}$ ,  $R_s \approx 30 \Omega$ ,  $L_s = 11.7 \text{ pH}$ , and  $\alpha = 0.91$  [89]. For comparison, a  $t = 100\text{-nm}$ -thick aluminum film (with  $T_c \approx 1.2 \text{ K}$ ) has typically  $L_s \sim 0.1 \text{ pH}$ .

In terms of internal quality factor, the best Al resonators to date have  $Q_{i,\text{max}}(\text{Al}) \sim 2 \times 10^6$ .  $Q_{i,\text{max}}$  is the maximum internal quality factor of the resonator when loss from quasiparticles has been minimized so that other sources of loss such as TLS loss and radiation loss are dominating. For Al, thick films with  $t \geq 100 \text{ nm}$  have to be used to get the highest  $Q_{i,\text{max}}$  values. For these films the kinetic inductance fraction  $\alpha(\text{Al}) \sim 0.05$  [28] which gives a surface impedance quality factor  $Q_s(\text{Al}) = \alpha \times Q_{i,\text{max}}(\text{Al}) \sim 10^5$ . For TiN resonators  $Q_s(\text{TiN}) = \alpha \times Q_{i,\text{max}}(\text{TiN}) \geq 2 \times 10^7$ , which is two orders of magnitude larger than for Al.

Quasiparticle lifetimes for our TiN films were measured from various far-IR, UV, and x-ray photon detection experiments in our group<sup>4</sup>. For the  $T_c = 4 \text{ K}$  films it was found that  $\tau_{\text{max}} \approx 15 \mu\text{s}$ , for  $T_c = 1.1 \text{ K}$  it was found that  $\tau_{\text{max}} \approx 100 \mu\text{s}$ , and for  $T_c = 0.8 \text{ K}$  it was found that  $\tau_{\text{max}} \approx 200 \mu\text{s}$  [58]<sup>5</sup>. The lifetime of our  $T_c = 1.1$

<sup>4</sup>The lifetime measurements were performed by other members of our group.

<sup>5</sup>The scaling is roughly as  $T_c^{-2}$ , as expected. This is because  $\tau_0 \propto T_c^{-3}$  in to Eq. 2.24 according

K TiN films (similar to  $T_c$  for Al) are in the same range as seen for Al films with  $t = 20\text{--}40$  nm thickness while they are an order of magnitude shorter than the best thick ( $t \geq 100$  nm) Al films (2 ms) [30, 101]. A study on TiN resonators by Diener et al. [100] reported a lifetime of  $\sim 200\text{--}300$   $\mu\text{s}$  for  $T_c = 0.8$  K material with  $t = 50$  nm, in agreement with our results. However, they also reported unusually high lifetimes of up to 5.6 ms for some resonators on the same chip. The reason for this discrepancy is unclear.

The last material-dependent parameter to consider is the electronic density of states  $N_0$ . To this date the best estimate for  $N_0$  for our TiN films comes from the results of Dridi *et al.* [102] which leads to  $N_0(\text{TiN}) = 8.7 \times 10^9$   $\text{eV}^{-1} \mu\text{m}^{-3}$  [58]. However, there exists a level of uncertainty in this value because the effect of electron-electron interactions and the dynamics of the electron-lattice interaction on the energy band structure have not been taken into account, which could have a significant effect on  $N_0$  [103]. Further investigation in this regard is needed. The value for aluminum is  $N_0(\text{Al}) = 1.72 \times 10^{10}$   $\text{eV}^{-1} \mu\text{m}^{-3}$  [12] which is about a factor of two higher than the current estimate for TiN.

TiN<sub>x</sub> resonators have several additional advantages as well. One is the high surface resistance of these films which makes it easy to design good far-IR absorbers. Since the detector arrays in this work are intended for operation at free-space wavelengths of around 350  $\mu\text{m}$  (860 GHz), Nb multislotted antennas and microstrip lines [17] could not be used as a radiation coupling mechanism due to the resistive loss above the Nb superconducting energy gap ( $\sim 700$  GHz). Therefore, the inductive portion of our lumped-element resonators was designed to act as direct absorbers of radiation [89, 67] (see Fig. 4.3), taking advantage of the high resistivity of TiN.

Another advantage is the high surface inductance of TiN which allows for high kinetic inductance ( $L_k$ ) inductors to be made. This pushes the resonators to lower frequencies and smaller surface areas per resonator on the array. Lower frequency

---

to theory [32].

resonators allow for increased frequency multiplexing density by reducing the resonance bandwidth for a fixed quality factor. This means more resonators can be put on a chip and more can be read out using the available electronics bandwidth.

To summarize,  $\text{TiN}_x$  has several advantages over more conventional materials such as aluminum:

1. The ultra-low microwave loss of TiN enables extremely high quality factors;
2. It has high surface inductance that greatly increases  $\alpha$  which in turn increases the responsivity to photo-generated quasiparticles and lowers the NEP;
3. It has a high kinetic inductance which reduces the resonance frequency, thereby increasing the multiplexing density and reducing the resonator footprint;
4. It has high surface resistance which makes it easy to design good far-IR absorbers;
5. The transition temperature is tunable over a wide range ( $0 < T_c < 5$  K) by changing the nitrogen content, which allows for optimization of the detector response over a wide range of loading conditions.

## 4.7 Chapter summary

We reviewed various types of MKIDs and introduced new designs based on lumped-element resonators which are simpler to operate and produce than other types of MKIDs. After providing general analytical design methods for the resonator and simulation techniques, we presented two specific resonator and array designs (A and B) along with their design details. Design A resonators have a single-line inductor meander following closely the original Cardiff proposal while our new design B has a modified geometry with a CPS spiral inductor to reduce microwave crosstalk [89]. We briefly reviewed fabrication details for a 224 pixel array of design A resonators and

a 256 pixel array of design B resonators. We measured various resonator and array properties for both arrays showing resonator responsivities and calculated estimates for the noise equivalent power (NEP) for design B based on our measurements. Our results demonstrate the basic operation of  $\text{TiN}_x$  lumped-element resonators on highly packed arrays and open the path for integration in large-scale focal-plane imaging arrays for telescopes like CCAT or future space telescopes. We also showed that MKIDs made from  $\text{TiN}_x$  films have superior properties as compared to Al films. Particularly their very high internal quality factor ( $Q_i$ ) and kinetic inductance fraction ( $\alpha$ ) provides an opportunity for dramatic improvement in sensitivity.

## Chapter 5

# Crosstalk reduction for superconducting microwave resonator arrays

To demonstrate the feasibility of large arrays of submillimeter-wave MKIDs at  $\lambda = 350$  microns, we fabricated arrays with  $\sim 250$  lumped-element resonators [89, 104, 67]. As explained in Chapter 4, the resonator structures were designed to act as direct absorbers of radiation, taking advantage of highly resistive  $\text{TiN}_x$  films [58] to achieve a good impedance match to the incoming radiation. We demonstrated the basic operation of the first-generation arrays (design A; see Fig. 4.5) by measuring the response to a  $\lambda = 215 \mu\text{m}$  bandpass-filtered black-body source (see Fig. 4.12), with the results indicating  $\sim 70\%$  absorption efficiency (single polarization).

Although the optical response measurements for our initial design (A) were encouraging, the electromagnetic coupling between resonators combined with the high packing density (in real space and frequency space) resulted in large microwave crosstalk. We initially detected this problem through observation of nonuniform resonance frequency spacings and very large variations in resonance quality factors across our arrays. Similar effects had also been reported for arrays developed at Cardiff [79], but no detailed analysis or effective solution was available.

In this chapter we identify the cause for the high inter-pixel coupling as being due

to the large dipole moment of each resonator interacting with nearby resonators. To reduce the dipole moments, we modified the resonator geometry in design B (see Fig. 4.6) so that sections with opposite charge densities and currents are close together. As another precaution, we added a grounding shield around each resonator (Details of this new design (B) were previously provided in Chapter 4). We present a detailed circuit model, identify the source of the crosstalk, present a measurement technique for quantifying crosstalk, and finally present measurement results for our improved resonator and array design which shows negligible crosstalk.

In Sections 5.1, 5.2, and 5.3 we describe a simple model for coupling between two resonators and confirm its validity using electromagnetic simulations. In Section 5.4 we construct circuit models for full-size arrays of type A and B, and calculate the frequency pattern, voltage distribution pattern, and quality factor for these arrays based on measured and simulated model parameters. In section 5.5 we quantitatively define crosstalk and analytically calculate its value for both designs based on our model. In section 5.6 we present measurement results for array frequencies, resonance quality factors, and crosstalk, and compare to the model predictions. To measure crosstalk in the lab, in Section 5.6.4 we describe a method using a simple “pump-probe” technique and present measurement results for both arrays. These results show that crosstalk is high ( $\sim 57\%$ ) for design A, but is dramatically reduced to  $\leq 2\%$  thanks to modifications in design B. The general procedure, design guidelines, and measurement techniques in this work are applicable to future large-scale arrays of microwave resonator detectors for telescopes such as CCAT.

## 5.1 Coupled resonators model

A simple circuit can be used to model electromagnetic coupling between adjacent resonators in our arrays [89]. The coupling can be capacitive, inductive, or a combination of the two. For purposes of discussion we assume a net capacitive coupling.

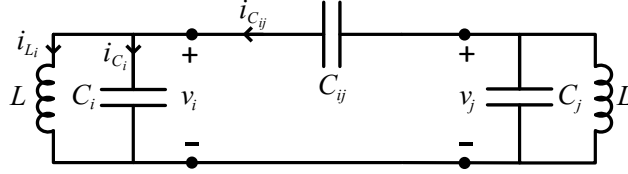


Figure 5.1: Circuit representation of two coupled resonators with a cross-coupling capacitor  $C_{ij}$ , inside an array of coupled resonators with size  $N$

Figure. 5.1 shows two resonators (i and j) coupled with a cross-coupling capacitor  $C_{ij}$ , with  $C_i$  and  $C_j$  being the capacitances of the interdigitated capacitors (IDC) and  $C_i, C_j \gg C_{ij}$ . (If the coupling were inductive,  $C_{ij}$  would be replaced by an inductor  $L_{ij}$  where  $L_{ij} \gg L$  and a similar analysis as explained below would follow). The inductors  $L_i$  and  $L_j$  represent the inductive section of each resonator (e.g., meander, spiral, etc.), and are the same for all the resonators by design; i.e.,  $L_i = L_j = L$ . The two resonators shown are part of an array of resonators with size  $N$ , representing the full focal plane array, where all the  $N$  resonators are coupled. It is easy to see that if all the resonators are uncoupled (i.e.,  $C_{ij} = 0$ ), the  $N$  natural resonance modes are

$$f_{0k} = 1/2\pi\sqrt{LC_k}, \quad k = 1, 2, \dots, N. \quad (5.1)$$

However, if  $C_{ij} \neq 0$ , the equations of motion for the circuit are coupled and we need to solve an eigenvalue problem. We can write

$$v_i(t) = L \frac{d}{dt} i_{L_i}(t) \quad (5.2)$$

where  $v_i(t)$  and  $i_{L_i}(t)$  are the time-dependent voltage and current for the inductor  $L_i$ , and have sinusoidal time dependence of the form

$$v_i(t) = \text{Re} \left( V_i e^{j\omega t} \right) \quad (5.3)$$

$$i_{L_i}(t) = \text{Re} \left( I_{L_i} e^{j\omega t} \right), \quad (5.4)$$

where  $\omega$  is the angular frequency. From Kirchhoff's current law we can write

$$i_{L_i}(t) = -i_{C_i}(t) - \sum_{\substack{j=1 \\ j \neq i}}^N i_{C_{ij}}(t) = -C_i \frac{dv_i(t)}{dt} - \frac{d}{dt} \left( \sum_{\substack{j=1 \\ j \neq i}}^N C_{ij} (v_i(t) - v_j(t)) \right) \quad (5.5)$$

where we have summed over all the currents contributed by the other coupled resonators in the array. We can now substitute for  $i_{L_i}(t)$  in Eq. 5.2 and apply the Fourier transform to obtain the steady-state solution

$$V_i = \omega^2 L \left( C_i V_i + \sum_{\substack{j=1 \\ j \neq i}}^N C_{ij} (V_i - V_j) \right) \quad . \quad (5.6)$$

Applying the same method to the other resonators and rewriting the equations in matrix form we get

$$\begin{bmatrix} C_1 + \sum_{j=1}^N C_{1j} & -C_{12} & \cdots & -C_{1N} \\ -C_{21} & C_2 + \sum_{j=1}^N C_{2j} & \cdots & \vdots \\ \vdots & \vdots & \ddots & \vdots \\ -C_{N1} & -C_{N2} & \cdots & C_N + \sum_{j=1}^N C_{Nj} \end{bmatrix} \begin{bmatrix} V_1 \\ V_2 \\ \vdots \\ V_N \end{bmatrix} = \frac{1}{\omega^2 L} \begin{bmatrix} V_1 \\ V_2 \\ \vdots \\ V_N \end{bmatrix} \quad . \quad (5.7)$$

In short format, this is an eigenvalue equation

$$\mathbf{\Lambda} |V^k\rangle = \lambda_k |V^k\rangle, \quad (5.8)$$

where  $\mathbf{\Lambda}$  is the above capacitance matrix,  $|V^k\rangle$  is the  $k$ th eigenvector, and  $\lambda_k$  is the  $k$ th eigencapacitance which is of the form  $1/\omega_k^2 L$ . The solution to this eigenvalue equation gives the  $N$  eigenfrequencies  $f_k$  of the coupled resonator array

$$f_k = 1/2\pi \sqrt{L\lambda_k}, \quad k = 1, 2, \dots, N. \quad (5.9)$$

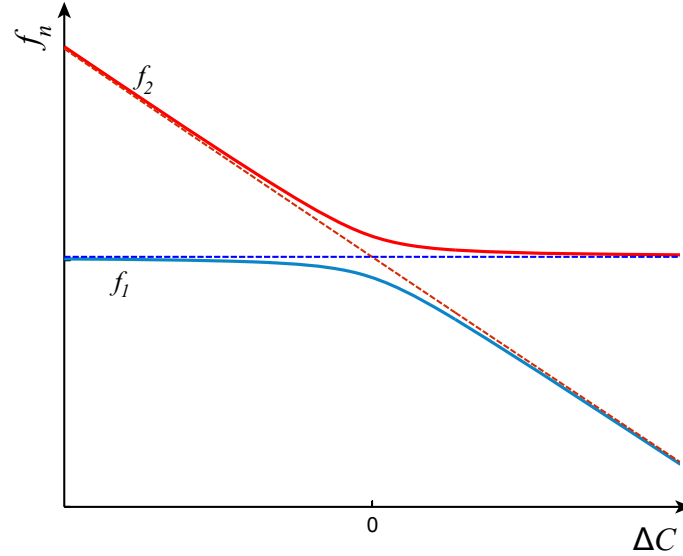


Figure 5.2: A sketch of Eq. 5.9 showing the two eigenfrequencies  $f_n$  as a function of capacitance difference  $\Delta C = C_2 - C_1$  (solid lines). The dashed lines indicate the eigenfrequencies in the case where there is no coupling between the resonators.

In the simple case where  $N = 2$ , the capacitance eigenvalues are

$$\lambda_k = \bar{C} + C_{12} \pm \sqrt{C_{12}^2 + (\Delta C)^2/4}, \quad k = 1, 2, \quad (5.10)$$

where  $\bar{C} = (C_1 + C_2)/2$  and  $\Delta C = C_2 - C_1$ . Note that in the special case where  $C_1 = C_2 = C$ ,  $\lambda_1 = C + 2C_{12}$  and  $\lambda_2 = C$ .

The behavior of the eigenfrequencies described in Eq. 5.9 is shown in Fig. 5.2 for the case of  $N = 2$ . As one can see, when  $|\Delta C| \gg C_{12}$ , the eigenfrequencies are unperturbed from their uncoupled case, and approach the uncoupled solution asymptotes. However, when  $|\Delta C| \ll C_{12}$ , the eigenfrequencies deviate from the asymptotes creating an avoided crossing pattern, which is a signature property of coupled resonators.

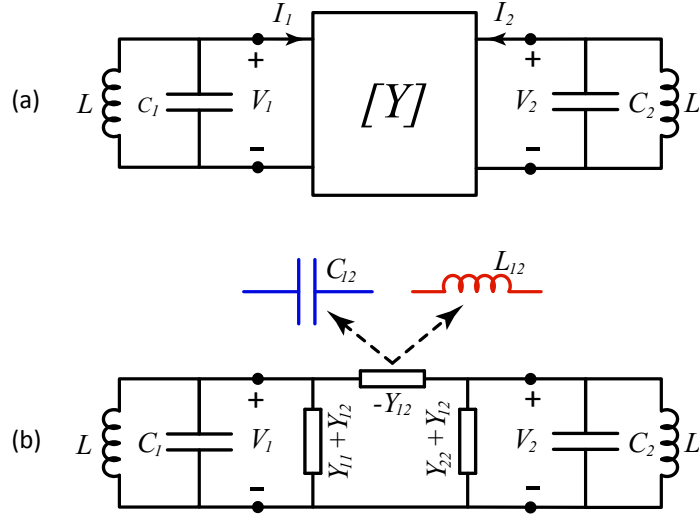


Figure 5.3: (a) General circuit representation of cross-coupling between two resonators with an admittance matrix  $Y$ . (b) General circuit representation of cross-coupling using a  $\pi$ -equivalent representation for the  $Y$ -matrix. A coupling capacitor  $C_{12}$  or inductor  $L_{12}$  are indicated as possible realizations of element  $-Y_{12}$ .

## 5.2 Calculation of coupling elements from $\delta f_{\text{split}}$

The actual values for  $C_1$ ,  $C_2$ , and  $L$  for a specific pixel and array design can be extracted by simulating each component in an electromagnetic (EM) simulation software like Sonnet [52]. However, the value of the coupling element ( $C_{12}$  or  $L_{12}$ ) is difficult to extract from direct simulation. Therefore, we will explain below a method by which we can indirectly extract these values using a combination of simulation and simple circuit calculations [89].

To present a more general coupling scenario, in Fig. 5.3(a) we have shown a coupling circuit in the form of a general admittance matrix  $Y$  connected to the two resonators. We have

$$\begin{bmatrix} I_1 \\ I_2 \end{bmatrix} = \begin{bmatrix} Y_{11} & Y_{12} \\ Y_{21} & Y_{22} \end{bmatrix} \begin{bmatrix} V_1 \\ V_2 \end{bmatrix} \quad (5.11)$$

where  $Y_{11} = Y_{22}$  (symmetry) and  $Y_{12} = Y_{21}$  (reciprocity). By examining the details of this circuit, one can see that in a case where  $C_1 = C_2 = C$ , the voltages are either

symmetric or antisymmetric. For the “symmetric mode”:

$$V_1 = V_2 \quad (5.12)$$

$$I_1 = I_2 = I_S = (Y_{11} + Y_{12})V_1 = jB_\Sigma V_1, \quad (5.13)$$

and for the “antisymmetric” mode:

$$V_1 = -V_2 \quad (5.14)$$

$$I_1 = -I_2 = I_A = (Y_{11} - Y_{12})V_1 = jB_\Delta V_1. \quad (5.15)$$

To satisfy the resonant condition for both modes, we can write:

$$\frac{1}{j\omega_S L} + j\omega_S C + jB_\Sigma = 0 \quad (5.16)$$

$$\frac{1}{j\omega_A L} + j\omega_A C + jB_\Delta = 0 \quad (5.17)$$

where  $\omega_S = 2\pi f_S$  and  $\omega_A = 2\pi f_A$  refer to the symmetric and antisymmetric mode frequencies. Rewriting Eq. 5.16 and Eq. 5.17 and subtracting the two we get

$$(\omega_S^2 - \omega_A^2)LC = \omega_A L B_\Delta - \omega_S L B_\Sigma. \quad (5.18)$$

We define

$$\bar{\omega} \triangleq \frac{\omega_S + \omega_A}{2} \triangleq 2\pi \bar{f} \quad (5.19)$$

$$\delta\omega \triangleq \omega_S - \omega_A \triangleq 2\pi \delta f_{\text{split}} \quad (5.20)$$

where  $\delta f_{\text{split}}$  is the “splitting frequency”. Depending on the type of coupling the sign of  $\delta f_{\text{split}}$  can change:

$$\begin{cases} \delta f_{\text{split}} \geq 0 & \text{for capacitive coupling} \\ \delta f_{\text{split}} \leq 0 & \text{for inductive coupling.} \end{cases} \quad (5.21)$$

This can be easily understood by noting that for the antisymmetric mode, in capacitive cross-coupling (as in Fig. 5.1 with  $C_1 = C_2$ ) the equivalent circuit will have an added capacitor in parallel with the resonator circuit, which will increase the net capacitance, while in inductive cross-coupling there will be an added inductance in parallel with the resonator which will reduce the net inductance. The quantity  $|\delta f_{\text{split}}|$  is a measure of the cross-coupling strength and increases as the coupling gets stronger. Using Eq. 5.19 and Eq. 5.20 together with Eq. 5.18 we get:

$$2C\delta\omega = \left(1 - \frac{1}{2} \frac{\delta\omega}{\bar{\omega}}\right)B_{\Delta} - \left(1 + \frac{1}{2} \frac{\delta\omega}{\bar{\omega}}\right)B_{\Sigma}. \quad (5.22)$$

Since  $|\delta\omega| \ll \bar{\omega}$  we have:

$$C\delta\omega \approx \frac{1}{2}(B_{\Delta} - B_{\Sigma}) = +jY_{12}. \quad (5.23)$$

The general Y-matrix in Fig. 5.3(a) can be realized into a  $\pi$ -equivalent circuit shown in Fig. 5.3(b), with  $-Y_{12}$  as the admittance of the coupling element across the circuit. It is reasonable in our pixels to assume that the two admittance elements  $Y_{11} + Y_{12}$  are very small, and that the dominating coupling element is  $-Y_{12}$ . Moreover,  $Y_{11} + Y_{12}$  only adds a small amount of equal frequency shift to both pixels, and can be ignored for our purpose. Setting  $-Y_{12}$  equal to the admittance of the actual coupling element (capacitor  $C_{12}$  or inductor  $L_{120}$  depending on the sign of  $\delta f_{\text{split}}$ ), it is easy to show that

$$C_{12} \approx \left(\frac{\delta f_{\text{split}}}{\bar{f}}\right)C \quad \text{for capacitive coupling} \quad (5.24)$$

$$L_{12} \approx \left(-\frac{\bar{f}}{\delta f_{\text{split}}}\right)L \quad \text{for inductive coupling}. \quad (5.25)$$

These two equations allow us to determine the value of the coupling element assuming that we know  $\delta f_{\text{split}}$ . To obtain  $\delta f_{\text{split}}$ , we used simulations of two coupled pixels to extract the symmetric and antisymmetric frequencies. These simulation will be explained next.

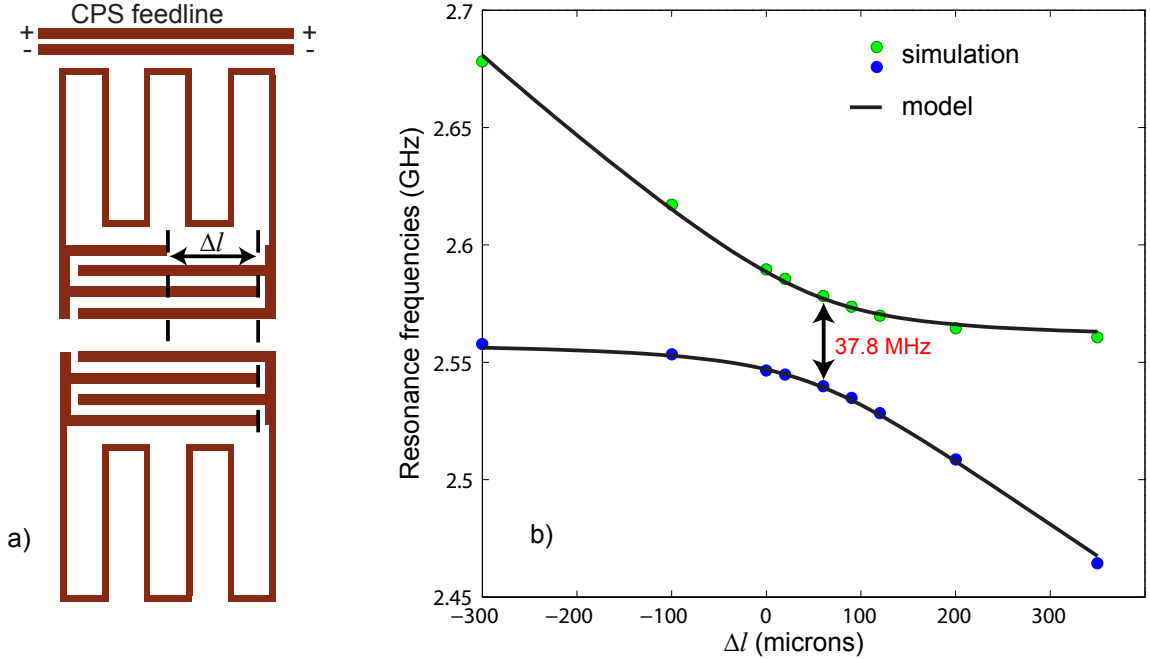


Figure 5.4: (a) Schematic example of two coupled resonators where the length difference of the capacitors is indicated. Dimensions are not to scale. (b) Resonance frequencies of two coupled resonators in (a) when the finger length of one capacitor is changed show an avoided level crossing indicating a cross-coupling strength of  $\delta f_{\text{split}} = 37.8$  MHz. The circles are simulation results from Sonnet and the lines are a fit to Eq. 5.9. (Figure reproduced from [89])

### 5.3 Simulation of coupled pixels

We used Sonnet software [52] to directly simulate our coupled resonators to extract  $\delta f_{\text{split}}$ . Fig. 5.4(a) shows the schematic of two such coupled resonators. We run multiple simulations, each time slightly changing the capacitance value of one resonator (using its IDC finger length) and keeping the other capacitance constant. The resulting frequencies are shown in Fig. 5.4(b) (circles) where the horizontal axis is proportional to capacitance difference. As the difference in capacitance approaches zero, an avoided crossing appears. Our circuit model (Eq. 5.9 and Eq. 5.10) agrees well with this behavior as is evident from the solid lines in Fig. 5.4(b), which are from a fit to Eq. 5.9. The minimum separation in the two curves is equal to  $\delta f_{\text{split}}$  and can be used in Eq. 5.24 or Eq. 5.25 to estimate the value of the coupling element. In fact, this is the method that we use to determine the values of the coupling capacitances

in our actual arrays [89]. The slight offset around zero in the curve is due to the proximity of one resonator to the feedline. In our later two-resonator simulations, we corrected this by bringing the feedline in proximity to both resonators, as illustrated later in Fig. 5.5. This did not affect the splitting frequency results. This also makes sure that both resonators are coupled with the same strength to avoid any accidental frequency shifts due to the added feedline coupling impedances, and mimics the actual situation on the array.

In Fig. 5.5 we can see a view of the actual resonator simulation geometry file in Sonnet. The resonator design is type A (see Section 4.4.1). The simulation box size has to be large enough to avoid any parasitic coupling to the metallic box walls (perfect conductors, indicated in red). The box top cover is made of copper and is at a distance of 5 mm from the substrate to avoid loss from eddy currents due to fields extending above the surface. The bottom of the box is open air representing the actual optical illumination side.

In order to identify whether the nature of the coupling is capacitive or inductive for a certain pixel design and orientation, simulations can be used to distinguish the symmetric and antisymmetric modes. The symmetric mode will generally have a stronger coupling to the feedline (lower  $Q_c$ ) compared to the antisymmetric mode, since the currents injected in the feedline will be in-phase as opposed to 180 out-of-phase. This observation will yield the sign of  $\delta f_{\text{split}}$ . Fig. 5.6 shows how the two modes appear in a typical simulation. We will present cross-coupling simulation results for a combination of several different pixel and array designs next.

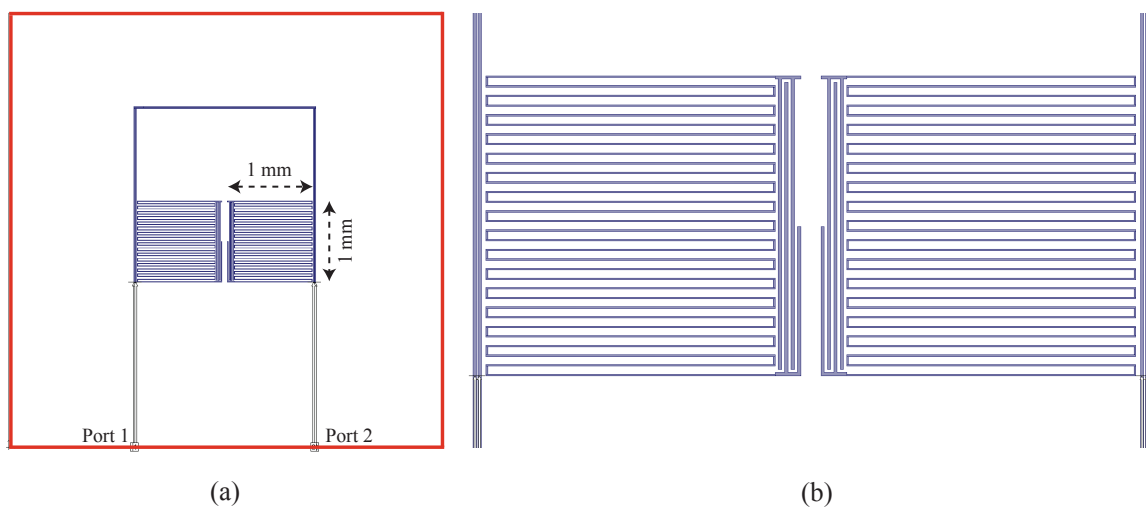


Figure 5.5: Actual Sonnet geometry for two coupled resonators. (a) A view of the complete simulation box with the perfect conductor walls indicated in red. The feedline passes next to both resonators for an accurate simulation. (b) Zoom-in of the resonator area

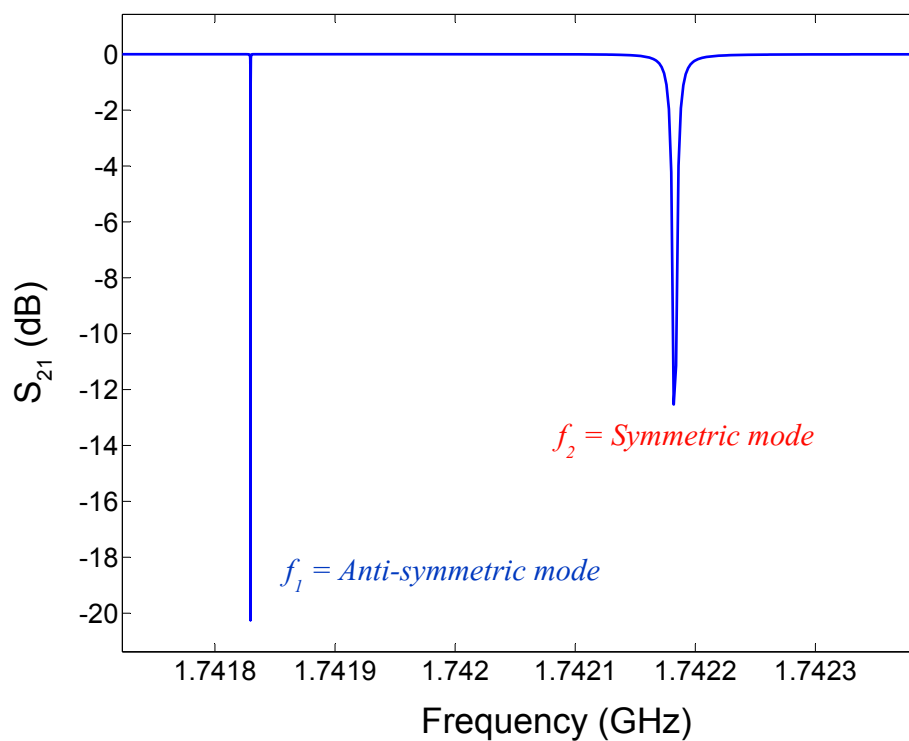


Figure 5.6: Sonnet simulation of two coupled resonators indicating the two coupled modes.  $Q_c$  for the symmetric mode is significantly lower.

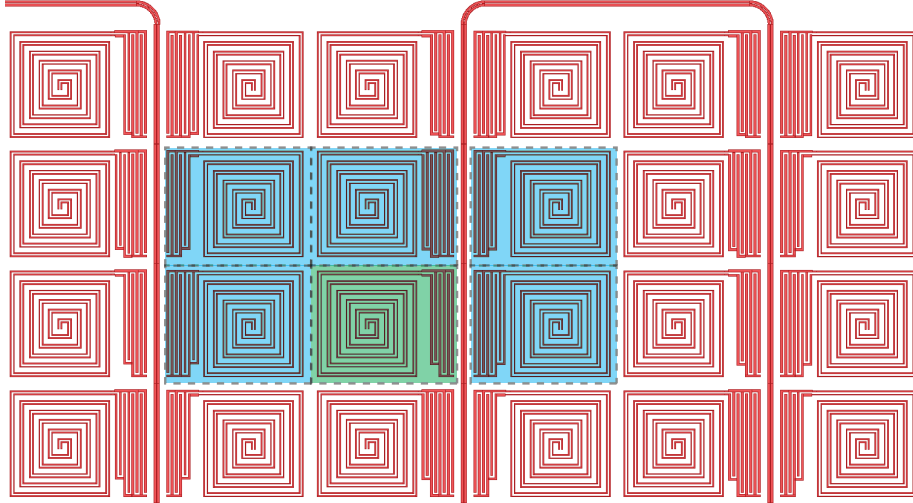
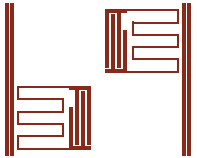
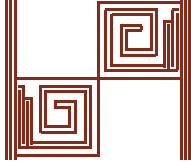
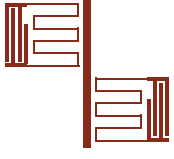
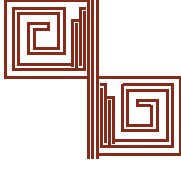


Figure 5.7: Five unique nearest-neighbors (blue) to a general pixel (green) are indicated in a section of an MKID array. Cross-coupling splitting frequencies for these orientations are listed in Table 5.1 for two different designs.

## 5.4 Full array circuit model and simulation

In order to predict the behavior of a complete array of size  $N$ , we calculated the eigenfrequencies  $f_n$  for an equivalent circuit. The circuit consists of identical inductors attached to the  $N$  ports of a capacitance network that takes into account all of the nearest neighbor resonator couplings using the actual positions of the resonators with respect to each other and with respect to the feedline, as presented in Eq. 5.7. The values for the  $C_{ij}$  were calculated by first simulating all the nearest-neighbor two-resonator configurations in each array in Sonnet and extracting their corresponding splitting frequencies  $\delta f_{\text{split}}$ . There are five unique nearest-neighbor orientations in our array, for which we performed Sonnet simulations. These orientations are indicated in Fig. 5.7 where a section of the array is shown. The splitting frequencies for two designs (A and B) from these simulations are listed in Table 5.1. One can see that the splitting frequencies for design B are considerably smaller than design A and also smaller than the frequency spacing between resonances. This already is an indication that design B has lower crosstalk than design A. This will become more evident later on in this chapter where crosstalk measurements and simulations will be presented.

Table 5.1: Coupling splitting frequencies

Design A			Design B		
Configuration	$\delta f_{\text{split}}$ (MHz)	$C_{ij}$ (fF)	Configuration	$\delta f_{\text{split}}$ (MHz)	$C_{ij}$ (fF)
	36.2	4.34		0.20	0.034
	60.4	7.25		1.75	0.30
	8.6	1.03		0.25	0.043
	28.2	3.34		1.18	0.20
	6.9	0.83		0.35	0.060

### 5.4.1 Array eigenfrequencies

We used Eq. 5.24 together with Table 5.1 to convert the  $\delta f_{\text{split}}$  values into corresponding  $C_{ij}$ 's to fill in the elements of the capacitance matrix in Eq. 5.7. We also used direct simulations to determine the value of the meander or spiral inductor  $L$ , and the capacitance of the IDCs  $C_i$ . These are listed in Sections 4.4.1 for design A and Section 4.4.2 for design B.

After solving Eq. 5.7, we get the array frequency eigenvalues for both designs, which are plotted in Fig. 5.8 (a) and (b). For each design we have plotted two cases: one for when there is no cross-coupling ( $C_{ij} = 0$ ), and one for when  $C_{ij}$  and are set to their real values indicated in Table 5.1. In design B it is evident that the cross-coupling has almost no effect on the eigenfrequencies, and that the pixels should be nearly free of crosstalk. In design A, the cross-coupling clearly has a significant effect that is perturbing the frequencies causing an inverted S-shape. The frequency separations between adjacent frequencies have been plotted in Fig. 5.8 (c) and (d), where the intended separation is plotted in red. It is clear that the highly scattered separation in design A is far from the intended uniform 1.3 MHz spacing, while for design B, except for periodic spikes, the design is much better. The small spikes are due to the small but remaining pixel cross-coupling.

The specific inverted-S shape of the curve for design A in Fig. 5.8(a) is a characteristic feature of highly coupled arrays [89]. This has been further explored in Fig. 5.9 where we have plotted the eigenfrequencies for design A and B for a range of coupling strengths by scaling the values in Table 5.1 by the same factor  $\xi$  for a set of selected  $\xi$ . At  $\xi = 0$  there is no cross-coupling, and at  $\xi = 2$  there is twice as much coupling as the actual array. As can be seen in Fig. 5.9 (a), the S-shape gradually disappears as we reduce the strength of the coupling, and becomes negligible by the time it is down by a factor of 16. A similar S-shape eventually also appears in both bands of array B when we artificially scale up the coupling strength significantly, but for the actual array the effect is negligible thanks to the much smaller splitting

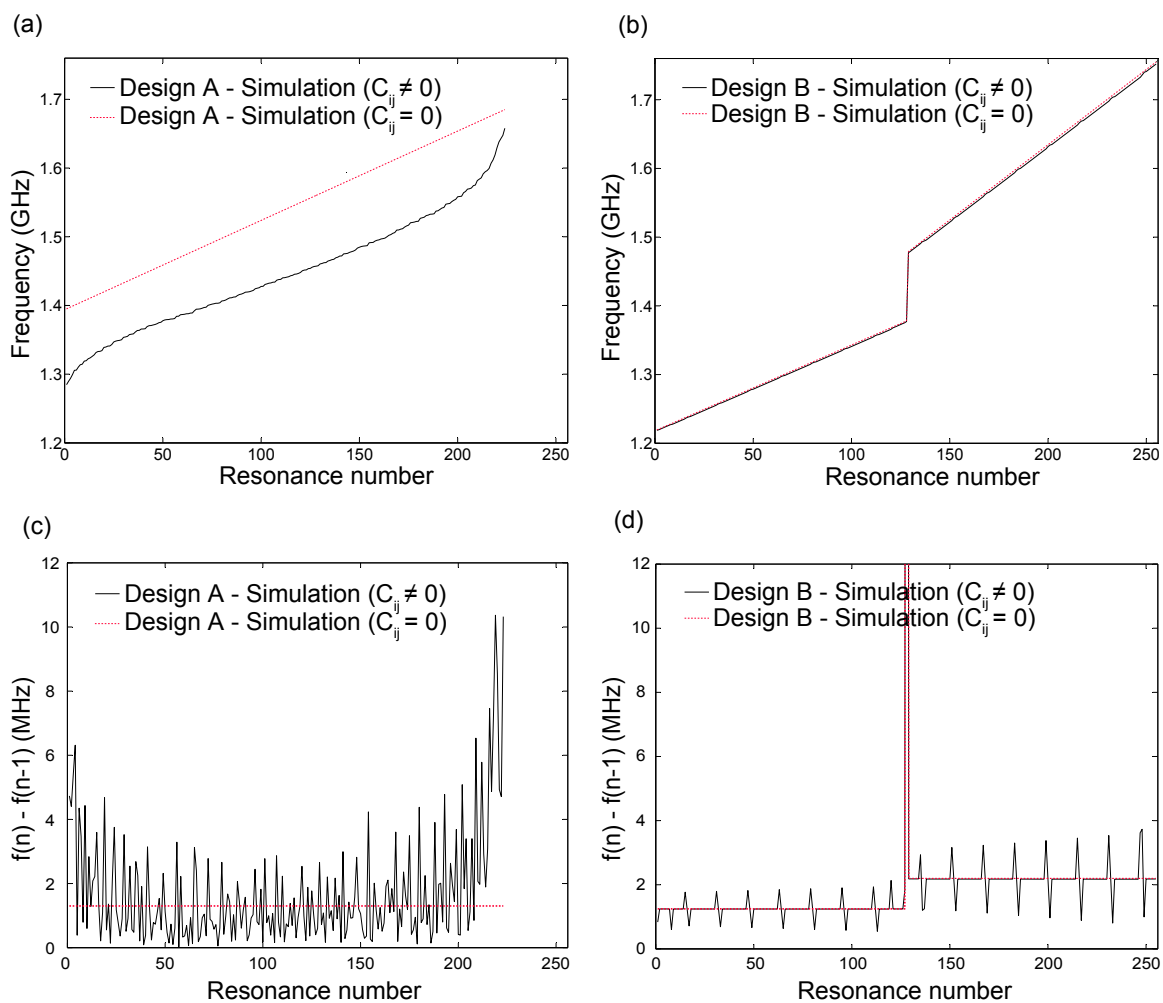


Figure 5.8: Matlab simulations of array resonance frequencies and frequency spacings for designs A and B. The red curves show the initially intended design and are for when there is no cross-coupling ( $C_{ij}(i \neq j) = 0$ ). In plot (d) the frequency separation in the middle of the array is 100 MHz which was intentionally put to separate the two high- and low-frequency bands.

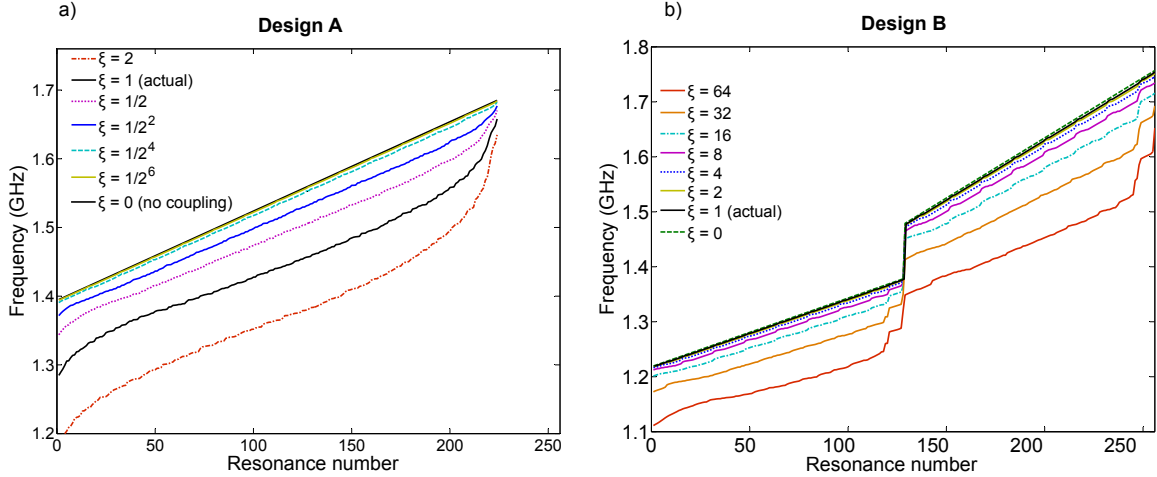


Figure 5.9: A series of simulations showing how the frequency curve shape evolves as the coupling strength is varied by tuning the scaling factor  $\xi$

frequencies and the checkerboard frequency scheme.

An interesting pattern of ripples appears when we plot the eigenfrequencies of an array as a function of the coupling strength scaling factor  $\xi$ . This is shown in Fig. 5.10 for design A. As is expected, the plotted 224 eigenfrequencies have an overall decreasing trend in frequency as we increase  $\xi$ , since the coupling capacitances  $C_{ij}$  are increasing. However, a less expected observation is that none of the eigenfrequencies cross the other ones during this ‘evolution’, as can be seen in the zoomed-in plots. In depth analysis of this effect is out of the scope of this thesis, but a quantum mechanical equivalent to this repulsion effect exists in electronic energy level diagrams in atomic physics, where it has been termed the “Wigner–von Neumann non-crossing rule” [105]. In algebraic terms, the eigenvalues of a Hermitian matrix depending on  $N$  continuous real parameters cannot cross except at a manifold of  $N-2$  dimensions [106]. In our case, we have only one parameter  $\xi$ , and therefore no crossings are allowed. If however, we introduced two or more scaling parameters for the coupling strengths, e.g.,  $\xi_1, \xi_2, \dots, \xi_N$ , it is theoretically possible to have intersections where they would have a dimensionality of  $N-2$ . The observed non-crossing effect holds true for design B as well, but the level of ripples is negligible and only becomes apparent when  $\xi \gg 1$ .

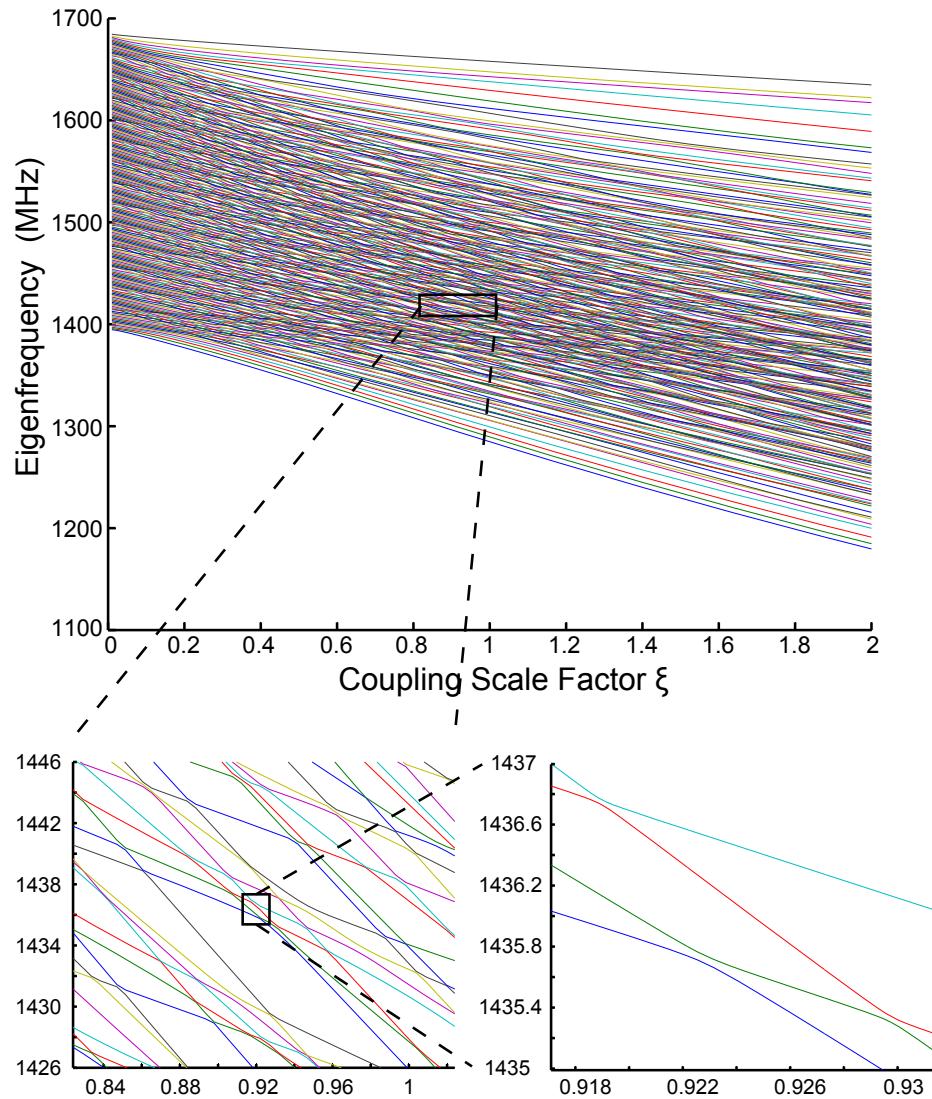


Figure 5.10: The evolving pattern of 224 eigenfrequencies of design A are plotted as a function of the coupling strength scaling factor  $\xi$ . At  $\xi = 1$  the coupling strengths are equal to their actual values. The smaller plots are for a magnified area, and show that the individual eigenfrequencies do not cross each other.

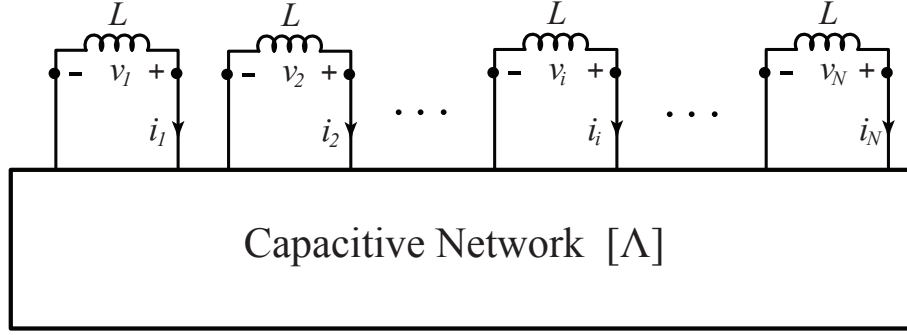


Figure 5.11: Circuit representation of an array of  $N$  coupled resonators indicating  $N$  ports where the inductors are connected to the capacitive network

### 5.4.2 Array eigenvectors

Equation 5.7 also yields the normalized eigenvectors  $|V^k\rangle = |V_1, V_2, \dots, V_n, \dots, V_N\rangle$  for each of the resonance modes  $k$ . The eigenvectors represent the distribution of the voltages across the inductors shown in Fig. 5.11 for mode  $k$ . We can calculate the distribution of the energy in a specific mode  $k$  across the array. First we calculate the total energy in each mode  $k$ . We have

$$i_i = \frac{d}{dt} \left( C_i v_i + \sum_{\substack{j=1 \\ j \neq i}}^N C_{ij} (v_i - v_j) \right) = \frac{d}{dt} \sum_{j=1}^N \Lambda_{ij} v_j, \quad (5.26)$$

where  $\Lambda_{ij}$  is the  $ij$ th matrix element in  $\Lambda$ , and all the currents and voltages pertain to mode  $k$ . In Fourier space

$$I_i = j\omega \sum_j \Lambda_{ij} V_j. \quad (5.27)$$

The instantaneous energy at time  $t$  stored inside the capacitive network  $k$  is

$$W_C(t) = \int_0^t \sum_{i=1}^N (i_i v_i) dt, \quad (5.28)$$

where we have summed over the powers at all ports  $i = 1, \dots, N$ . Substituting Eq. 5.26 into the above, we get

$$W_C(t) = \int_0^t \sum_{i=1}^N \left( \frac{d}{dt} \sum_{j=1}^N \Lambda_{ij} v_j \right) v_i dt \quad (5.29)$$

$$= \frac{1}{2} \int_0^t \frac{d}{dt} \left( \sum_{ij} \Lambda_{ij} v_i v_j \right) dt \quad (5.30)$$

$$= \frac{1}{2} \sum_{ij} \Lambda_{ij} v_i v_j, \quad (5.31)$$

where the factor  $\frac{1}{2}$  is because of summing twice over all the elements. The average energy in the capacitive network is

$$E_C = \frac{1}{T} \int_0^T W_C dt = \langle W_C \rangle = \left\langle \frac{1}{2} \sum_{ij} \Lambda_{ij} v_i v_j \right\rangle, \quad (5.32)$$

where  $T = 1/f_k$ . Putting in the time-dependent voltages from Eq. 5.3, we get

$$E_C = \sum_{ij} \left\langle \frac{1}{2} \Lambda_{ij} \operatorname{Re}(V_i e^{j\omega t}) \operatorname{Re}(V_j e^{j\omega t}) \right\rangle \quad (5.33)$$

$$= \frac{1}{8} \left\langle \sum_{ij} \Lambda_{ij} (V_i e^{j\omega t} + V_i^* e^{-j\omega t}) (V_j e^{j\omega t} + V_j^* e^{-j\omega t}) \right\rangle \quad (5.34)$$

$$= \frac{1}{4} \sum_{ij} \Lambda_{ij} \operatorname{Re}(V_i V_j^*) \quad (5.35)$$

$$= \frac{1}{4} \langle V^k | \Lambda | V^k \rangle \quad (5.36)$$

$$= \frac{1}{4} \lambda_k \langle V^k | V^k \rangle \quad (5.37)$$

$$= \frac{1}{4} \frac{1}{\omega_k^2 L}. \quad (5.38)$$

On resonance, the energy inside the inductive portion of the mode is equal to the capacitive energy. Therefore, the total average energy stored in resonance mode  $k$  is

$$E_{tot} = E_C + E_L = \frac{1}{2} \lambda_k = \frac{1}{2} \frac{1}{\omega_k^2 L}. \quad (5.39)$$

On the other hand, the average energy associated with each voltage  $V_n$  for mode  $k$  is

$$E_n = \frac{1}{2} \lambda_k V_n^2. \quad (5.40)$$

Therefore, from Eq. 5.39, the normalized energy associated with voltage  $V_n$  is simply

$$e_n = \frac{E_n}{E_{tot}} = V_n^2. \quad (5.41)$$

It should be noted that since the matrix  $\Lambda$  is a real Hermitian matrix, its eigenvectors are real. Therefore,  $-1 \leq V_n \leq +1$ .

We calculated the normalized energy distribution for both designs A and B using Eq. 5.41 [89]. An example for a specific mode is shown in Fig. 5.12 (a) and (b) where the colors show the amount of normalized energy contributed by each physical resonator to the resonance mode. The rows and columns are along the physical dimensions of the array. The plots are for an arbitrarily chosen mode number  $k = 68$  for both designs. In an uncoupled array ( $\xi = 0$ ), this mode number would purely correspond to the resonator in position #68 in array A, and in position #135 in array B, indicated by arrows in the figure. This is because the designed resonance frequencies in array A have a simple uncoded linear pattern, while in array B they have been distributed in a coded checkerboard pattern, as was explained in Chapter 4. The plots show that the mode is highly delocalized for design A whereas it is highly localized for design B. The energy in each of the four diagonal nearest neighbor pixels in design B is more than 40 dB lower than the main pixel.

In Fig. 5.12 (c) and (d) the evolution of normalized energy distribution has been plotted for a range of coupling strengths scaled by  $\xi$ . We can see that when  $\xi = 0$  only one voltage is excited:  $n=68$  for design A and  $n=135$  for design B. These correspond to the physical resonator location on each array, respectively. As  $\xi$  increases, delocalized nonzero voltages appear sharing the energy of the mode with each other. These delocalized voltages only appear in design B when  $\xi$  is significantly

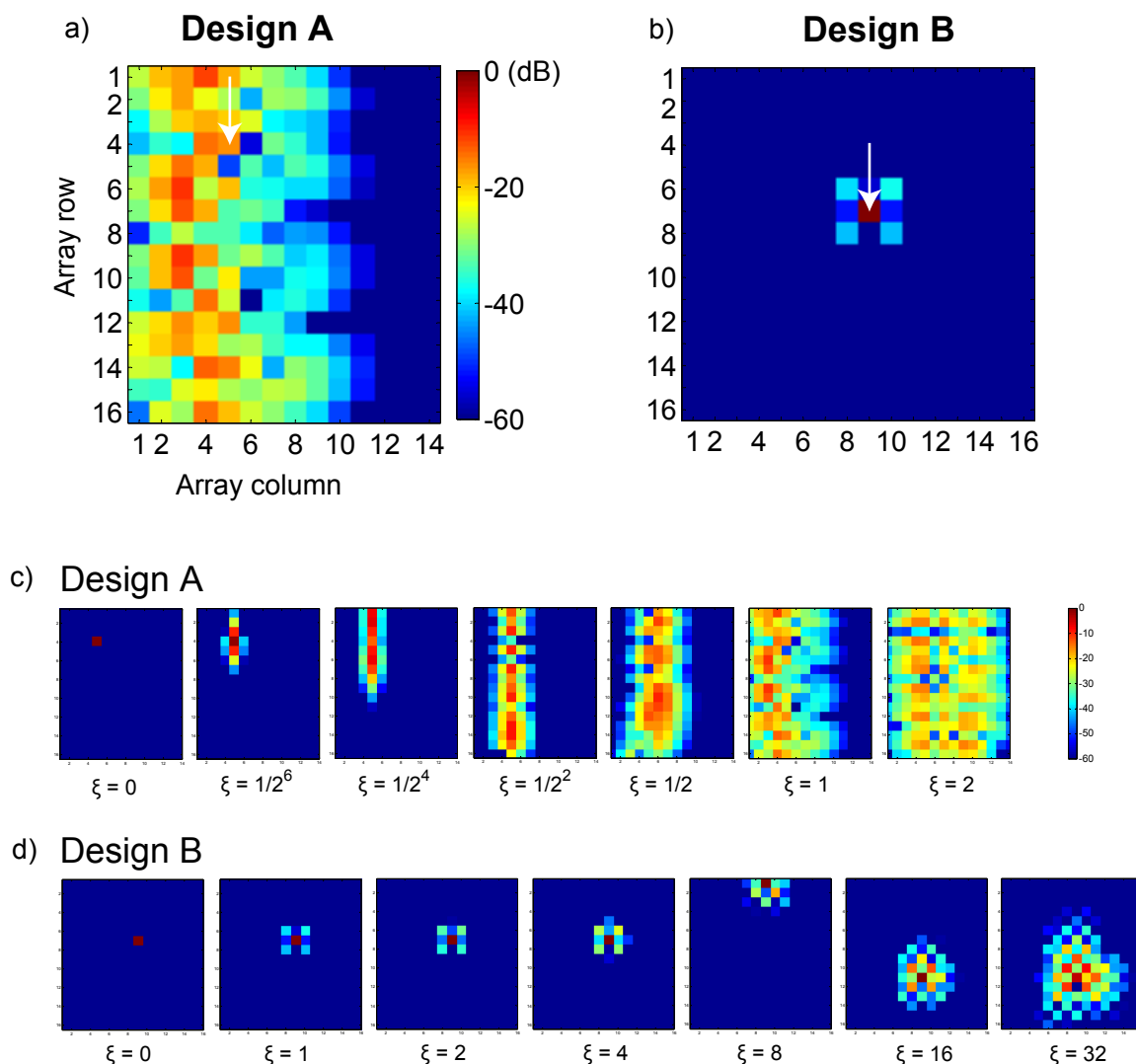


Figure 5.12: (a),(b) Normalized energy ( $20 \times \log_{10} V_n$ ) in voltages  $V_1$  to  $V_N$  across the array for a specific mode number (#68) in both arrays is shown in color. In an uncoupled array, this mode number would purely correspond to the resonator in position #68 in array A, and in position #135 in array B (indicated by arrows). However, due to strong coupling in array A, energy is distributed over many resonators, while in array B the energy is well localized. (c),(d) Evolution of normalized energy distribution for a range of coupling scaling factor  $\xi$ . When  $\xi = 0$  only resonance numbers 68 and 135 are excited in arrays A and B, respectively. As  $\xi$  is increased from zero, delocalized nonzero voltages start to appear. (a) and (b) are for when  $\xi = 1$ . (Figures (a) and (b) reproduced from [89])

larger than one, whereas in design A they appear at values as low as  $\xi = 1/2^4$ .

The results from these simulations strongly indicate that crosstalk is dramatically reduced in design B. This conclusion is confirmed by direct measurements and simulations of the crosstalk, which will be presented later in the chapter.

### 5.4.3 Array eigenfrequency quality factors

From Fig. 5.6 it is evident that cross-coupling also affects the resonance quality factors. In order to evaluate the effect on a full-size array, we used a simple circuit model shown in Fig. 5.13. First, we assumed that the effect from the coupling capacitances ( $C_c$ ) and the feedline on the voltages  $V_1$  to  $V_N$  are negligible. In other words, we assumed that we could use the solution to the eigenvalue problem defined in Eq. 5.8 for the case where we also have the coupling capacitors ( $C_c$ ) and a feedline. This assumption is justified since  $C_c \ll C_n$ . Secondly, because  $1/(\omega C_n) \gg Z_c/2$ , we substituted each resonator and its coupling capacitance by a current source injecting current in the feedline:

$$I_n \approx j\omega C_c V_n . \quad (5.42)$$

The result is an array of current sources along the feedline as shown in Fig. 5.13(c). The value for  $C_c$  is determined by simulating a single resonator in Sonnet and extracting the simulated  $Qc$ . Then by using Eq. A.32 we convert  $Qc$  into  $C_c$ . In order to calculate the  $Qc$  of a specific eigenfrequency of the cross-coupled array, we first calculate the currents  $I_n^L$  and  $I_n^R$  at both ends of the feedline as

$$I_n^R = I_n \times \frac{Z_{in}^L}{Z_{in}^L + Z_{in}^R} \times \frac{e^{-j\theta_n^R}(1 - \Gamma)}{1 - \Gamma e^{-2j\theta_n^R}} \quad (5.43)$$

$$I_n^L = I_n \times \frac{Z_{in}^R}{Z_{in}^L + Z_{in}^R} \times \frac{e^{-j\theta_n^L}(1 - \Gamma)}{1 - \Gamma e^{-2j\theta_n^L}} , \quad (5.44)$$

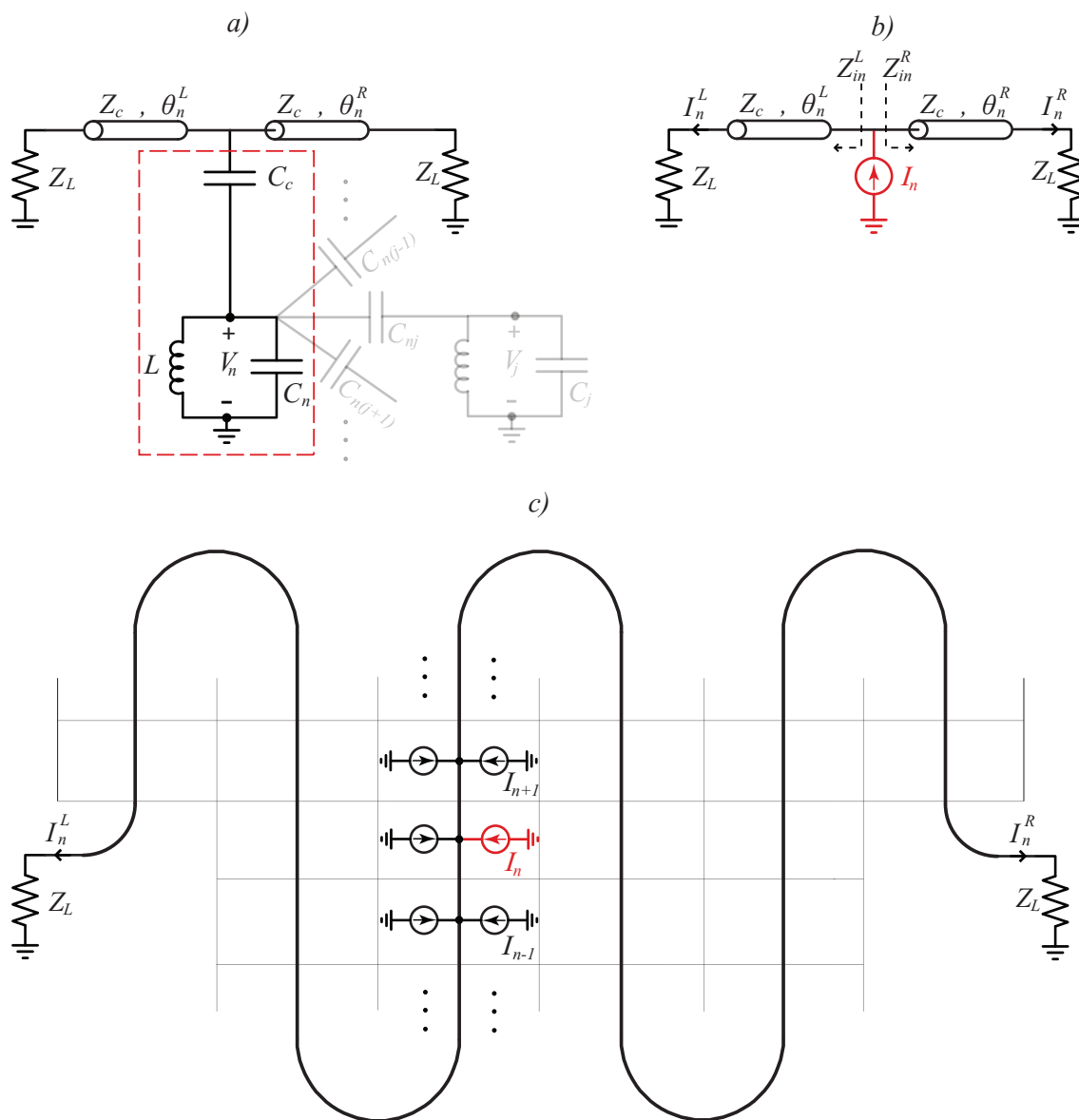


Figure 5.13: (a) Circuit model for array of  $N$  resonators. Each resonator is coupled to the feedline with a coupling capacitor  $C_c$ . The feedline has impedance  $Z_c$ , and each section  $n$  has length  $L_n$ . (b) Approximate circuit where each resonator section indicated in red in (a) has been replaced by a current source. (c) Circuit model for the full-size array with current sources located at the resonator positions along the feedline.

where

$$Z_{in}^R = Z_c \frac{Z_L + jZ_c \tan \theta_n^R}{Z_c + jZ_L \tan \theta_n^R} \quad (5.45)$$

$$Z_{in}^L = Z_c \frac{Z_L + jZ_c \tan \theta_n^L}{Z_c + jZ_L \tan \theta_n^L} \quad (5.46)$$

$$\Gamma_R = \frac{Z_L - Z_c}{Z_L + Z_c}, \quad (5.47)$$

and where  $Z_L$  is the load impedance,  $Z_c$  is the feedline characteristic impedance,  $\theta_n^R$  and  $\theta_n^L$  are the electrical lengths of the section of the feedline on the right and left of the resonator,  $Z_{in}^R$  and  $Z_{in}^L$  are the impedances seen looking into the feedline, and  $\Gamma$  is the load reflection coefficient. Summing over all the contributing current sources on the left and right gives us the total currents at each end of the feedline

$$I_R = \sum_{n=0}^N I_n^R \quad (5.48)$$

$$I_L = \sum_{n=0}^N I_n^L. \quad (5.49)$$

Therefore, the total average dissipated power in the two load impedances is

$$P_{\text{diss}} = \frac{1}{2} \text{Re}(Z_L) |I_R|^2 + \frac{1}{2} \text{Re}(Z_L) |I_L|^2. \quad (5.50)$$

Now we can calculate  $Q_c$  for each resonance mode  $k$  as

$$Q_c^k = \frac{\omega_k \times E_{\text{stored}}}{P_{\text{diss}}} = \frac{\omega_k \times \frac{1}{2} \lambda_k}{P_{\text{diss}}}, \quad (5.51)$$

where we used Eq. 5.39 for  $E_{\text{stored}}$ . It can be seen from Eq. 5.43 and Eq. 5.44 that the currents at the loads depend on the phase lengths of the feedline seen from each resonator, and therefore constructive and destructive interference of these currents results in varying dissipations at the loads, which can ultimately result in large variations in  $Q_c$ . We calculated the  $Q_c$ 's for array designs A and B using physical array parameters described in Table 5.2 and resonator circuit parameters described in

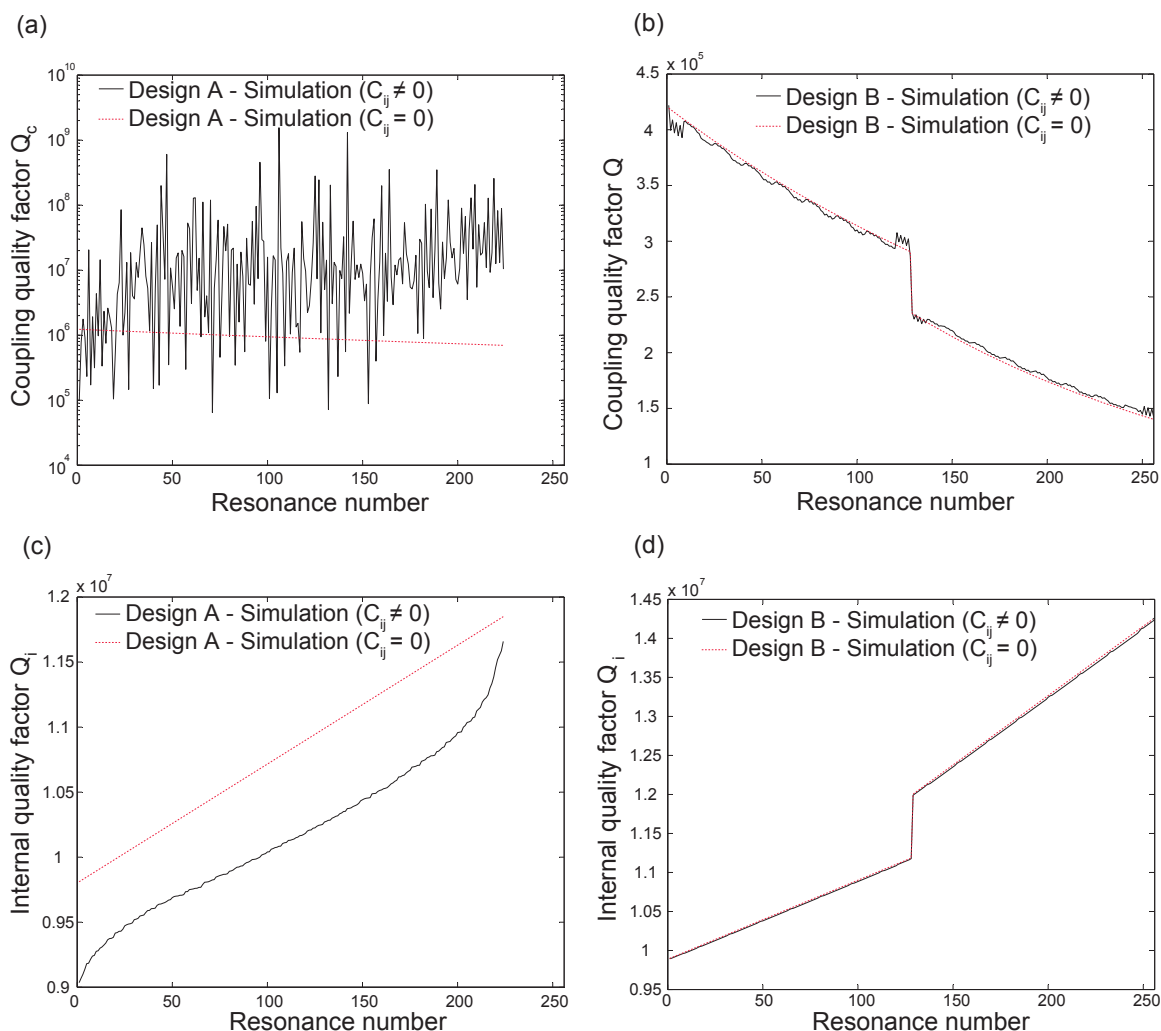


Figure 5.14: Matlab simulations of array coupling quality factors and internal quality factors for designs A and B. The red curves show the initially intended design and are for when there is no cross-coupling ( $C_{ij}(i \neq j) = 0$ ). In (a) large variations in  $Q_c$  up to 4 orders of magnitude can be seen due to cross-coupling. In (b) the variations are very small due to negligible cross-coupling.

Section 4.4. Since we used transformers to match the load to the feedline impedance, we make the assumption that  $Z_L = Z_c$ . This assumption should be valid as long as the actual amplifier and source impedances are close to  $50 \Omega$ . The calculation results are shown in Fig. 5.14 (a) and (b).

Design A shows large variations in  $Q_c$  up to 4 orders of magnitude. This is due to the many number of nonzero components in the voltage eigenvectors resulting in many different interference patterns for the currents on the feedline. In contrast,

Table 5.2: Physical parameters used for calculating  $Q_c$  and  $Q_i$  for full-size cross-coupled arrays

Design	$Z_c(\Omega)$	$\epsilon_{eff}$	$l_f$ ( $\mu\text{m}$ )	$l_s$ ( $\mu\text{m}$ )	$C_c$ (fF)	$Q_c$	$R(\mu\Omega)$	$Q_i$
A	141.05	20.15	147239	1000	0.44	$1.7 \times 10^6$	53.6	$1 \times 10^7$
B	115.2	20.34	112045	535	1.46	$3.82 \times 10^5$	33.6	$1 \times 10^7$

$l_f$  is the total length of the feedline.  $l_s$  is the feedline length between adjacent pixels.

design A shows very small variations in  $Q_c$  due to the very small cross-coupling.

We can also calculate the effect of cross-coupling on the internal coupling factors  $Q_i$  for each mode  $k$  using the same model and by adding a series resistance  $R$  to the inductor for each resonator to simulate resistive loss. We assume that adding a series resistance does not significantly change the solutions to the eigenvalue problem in Eq. 5.8, which is justified since  $|\omega L| \gg R$ . We can write the resistive power loss for each voltage node  $n$  as

$$P_{res}^n = \frac{1}{2}R|I_L^n|^2 \quad (5.52)$$

where  $I_L^n$  is the current through the inductor and resistor, and

$$|I_L^n| \approx \frac{|V_n|}{\omega_k L}. \quad (5.53)$$

The total resistive power loss for mode  $k$  is then

$$P_{res} = \sum_{n=0}^N P_{res}^n = \frac{1}{2} \frac{R}{(\omega_k L)^2} \sum_{n=0}^N |V_n|^2 = \frac{1}{2} \frac{R}{(\omega_k L)^2}. \quad (5.54)$$

From this, the internal quality factor  $Q_i$  for each mode is

$$Q_i^k = \frac{\omega_k \times E_{\text{stored}}}{P_{res}} = \frac{\omega_k \times \frac{1}{2} \lambda_k}{\frac{1}{2} \frac{R}{(\omega_k L)^2}} = \frac{\omega_k L}{R}. \quad (5.55)$$

The above result is exactly the same as the quality factor of a single series resonator circuit with a resistive element  $R$ , an inductive element  $L$ , and a capacitive element  $\lambda_k$ . We conclude that to first order,  $Q_i^k$  is affected by cross-coupling only through changes to the eigenfrequencies  $\omega_k$ . Fig. 5.14 (c) and (d) show calculated  $Q_i$  for arrays A and B using physical parameters from Table 5.2. The  $C_c$  values correspond to the single-resonator  $Q_c$  value using Eq. A.32. The  $R$  values correspond to the single-resonator  $Q_i$  value. For both designs we can see that  $Q_i$  follows a similar pattern to the eigenfrequencies for that design, as previously shown in Fig. 5.8 (a) and (b).

## 5.5 Pixel crosstalk

In this section, we study the microwave crosstalk between pixels in our arrays. As previously mentioned, the crosstalk is due to electromagnetic coupling between resonators caused by the high pixel packing density (in real space and frequency space) in our designs. In an array where crosstalk exists, the resonance modes do not correspond to individual physical resonators (pixels) but in fact correspond to a group of many resonators coupled to each other through parasitic elements. This was illustrated in Fig. 5.12. Moreover, in a cross-coupled array different modes can share physical resonators with each other. Therefore, when photons hit one of the pixels, a number of resonance modes are perturbed instead of a single mode. This would make it difficult to map the pixels on the sky when running actual observations. In this case one solution would be to “deconvolve” the signals by calibrating the focal plane, but this is a complicated method that we like to avoid.

We identified the cause for the high inter-pixel coupling in design A as being due to the large dipole moment of each resonator interacting with nearby resonators [89]. Large dipole moments can be generated by relatively large distances between opposite charge densities and currents inside the resonator. The interactions between these dipole moments were modeled using cross-coupling capacitors in the previous

sections. To reduce the dipole moments, we modified the resonator geometry in design B so that sections with opposite charge densities and currents are close together. As another precaution, we added a grounding shield around each resonator. The details of this design were described in Section 4.4.2.

In order to quantitatively evaluate crosstalk, in this section we will present a definition for crosstalk and present a model to calculate crosstalk analytically [89]. Our definition for crosstalk is related to the experimental method with which we use to measure crosstalk. One method to measure crosstalk is to illuminate a single physical resonator on the array with submillimeter photons and to look for a response in other resonances. This approach is difficult because confining the far-IR light to one pixel requires a complicated optical setup. Instead, we developed a very simple “pump-probe” technique where we apply a microwave “pump” tone to a resonance mode and observe the response from the other resonances. Since the resonance modes in a coupled array share physical resonators, perturbing one mode will also perturb all other modes who share resonators with that mode. This technique exploits the fact that the kinetic inductance of a superconductor generally is nonlinear [13], [107] and can change as a function of the microwave current:

$$L_{kin}(I) \approx L \left( 1 + \frac{I^2}{I_*^2} \right), \quad (5.56)$$

where  $I$  is the microwave current in the inductor, and  $I_*$  sets the scale of the non-linearity and is often comparable to the DC critical current. By applying a strong microwave pump tone to one of the resonance modes  $p$  with frequency  $f_0^p$ , the microwave currents in the inductors that participate in that mode cause the inductance values to increase slightly according to Eq. 5.56, so the mode frequency decreases to a new value  $f^p$  that may be characterized by the frequency shift  $\delta f^p = (f^p - f_0^p)$ . In an array where the pixels are coupled, this will also result in shifts in other modes, and by comparing these shifts to  $\delta f^p$  we can experimentally measure crosstalk for each mode. If  $f_0^k$  and  $f^k$  are the frequency of a certain “probed” mode  $k$  when the pump

is applied on-resonance and off-resonance respectively, then a quantitative measure of the crosstalk may be defined as

$$\chi_{kp} = \frac{\delta f^k}{\delta f^p} = \frac{f^k - f_0^k}{\delta f^p}. \quad (5.57)$$

In the next section we analyze the effect of the nonlinearity-induced shifts in the inductances by generalizing Eq. 5.8 to include nonequal inductors, and by noting that  $\delta f^p/f_0^p \sim 10^{-6}$  in our measurements, so the use of linear perturbation theory is very well justified.

### 5.5.1 Crosstalk simulation

In the case where the inductors in the array have different values, we can generalize Eq. 5.6 as

$$V_i = \omega^2 L_i \left( C_i V_i + \sum_{\substack{j=1 \\ j \neq i}}^N C_{ij} (V_i - V_j) \right), \quad (5.58)$$

where  $L_i$  ( $i = 1, \dots, N$ ) are the inductors in each resonator. In matrix form, the eigenvalue equation becomes

$$\mathbf{L}\mathbf{\Lambda}|V^k\rangle = \frac{1}{\omega_k^2}|V^k\rangle, \quad (5.59)$$

where

$$\mathbf{L} = \begin{bmatrix} L_1 & 0 & \cdots & 0 \\ 0 & L_2 & \cdots & \vdots \\ \vdots & \vdots & \ddots & \vdots \\ 0 & 0 & \cdots & L_N \end{bmatrix}. \quad (5.60)$$

Because the inductors in our circuit are made from superconducting TiN, we will use Eq. 5.56 to write

$$L_i = L + \delta L_i, \quad (5.61)$$

where

$$\delta L_i = L \frac{I_i^2}{I_*^2}. \quad (5.62)$$

We now define

$$\delta \mathbf{L} = \begin{bmatrix} \delta L_1 & 0 & \cdots & 0 \\ 0 & \delta L_2 & \cdots & \vdots \\ \vdots & \vdots & \ddots & \vdots \\ 0 & 0 & \cdots & \delta L_N \end{bmatrix} \quad (5.63)$$

$$\omega^k = \omega_0^k + \delta \omega^k \quad (5.64)$$

$$|V^k\rangle = |V_0^k\rangle + |\delta V^k\rangle, \quad (5.65)$$

where  $\omega_0^k$  and  $|V_0^k\rangle$  refer to the eigenfrequencies and eigenvoltages for the unperturbed case (i.e., when the pump tone is off). Since in our measurements  $\delta \omega^k / \omega^k \ll 1$  we can make the approximation

$$\frac{1}{(\omega^k)^2} \approx \frac{1}{(\omega_0^k)^2} \left( 1 - 2 \frac{\delta \omega^k}{\omega_0^k} \right). \quad (5.66)$$

Using Eq. 5.63–5.66 in Eq. 5.59, we can write

$$\begin{aligned} \frac{1}{(\omega_0^k)^2} \left( 1 - 2 \frac{\delta \omega^k}{\omega_0^k} \right) (|V_0^k\rangle + |\delta V^k\rangle) &= L \mathbf{\Lambda} (|V_0^k\rangle + |\delta V^k\rangle) \\ &\quad + \delta \mathbf{L} \mathbf{\Lambda} (|V_0^k\rangle + |\delta V^k\rangle). \end{aligned} \quad (5.67)$$

By keeping only the first-order terms in the above equation and after multiplying both sides from the left by  $\langle V_0^k|$  we get

$$-2 \frac{\delta \omega^k}{(\omega_0^k)^3} \langle V_0^k | V_0^k \rangle + \frac{1}{(\omega_0^k)^2} \langle V_0^k | \delta V^k \rangle = \langle V_0^k | L \mathbf{\Lambda} | \delta V^k \rangle + \langle V_0^k | \delta \mathbf{L} \mathbf{\Lambda} | V_0^k \rangle. \quad (5.68)$$

Since for the unperturbed case

$$L \mathbf{\Lambda} |V_0^k\rangle = \frac{1}{(\omega_0^k)^2} |V_0^k\rangle, \quad (5.69)$$

Eq. 5.68 simplifies to

$$\frac{\delta\omega^k}{\omega_0^k} = -\frac{1}{2}\langle V_0^k | \frac{\delta\mathbf{L}}{L} | V_0^k \rangle . \quad (5.70)$$

Now we make use of the fact since the change in the kinetic inductance in our experiment is very small we can approximate the current in each inductor  $L_i$  as

$$I_i = \frac{V_i}{j\omega L_i} \approx \frac{V_i}{j\omega L} , \quad (5.71)$$

and therefore

$$\delta L_i \approx L \frac{|V_i|^2}{V_*^2} , \quad (5.72)$$

where  $V_*^2 = (\omega L)^2 I_*^2$ . Now we can write

$$\frac{\delta\omega^k}{\omega_0^k} = -\frac{1}{2V_*^2} \langle V_0^k | \begin{bmatrix} |V_1^p|^2 & 0 & \cdots & 0 \\ 0 & |V_2^p|^2 & \cdots & \vdots \\ \vdots & \vdots & \ddots & \vdots \\ 0 & 0 & \cdots & |V_N^p|^2 \end{bmatrix} | V_0^k \rangle , \quad (5.73)$$

where  $V_i^p$  are the voltages associated with the pumped mode  $p$  which is generally different from the observed mode  $k$ . Rewriting Eq. 5.73 we get

$$\frac{\delta\omega^k}{\omega_0^k} = -\frac{1}{2V_*^2} \sum_{i=0}^N |V_i^k|^2 |V_i^p|^2 . \quad (5.74)$$

The above equation tells us that if we pump on mode  $p$ , the amount of fractional shift in frequency of mode  $k$  depends on the extent of overlap of the two unperturbed modes  $p$  and  $k$ . By setting  $k = p$ , we can calculate the shift of the pumped mode as

$$\frac{\delta\omega^p}{\omega_0^p} = -\frac{1}{2V_*^2} \sum_{i=0}^N |V_i^p|^4 . \quad (5.75)$$

Finally, combining the last two equations yields an expression for the crosstalk values

$$\chi_{kp} = \frac{\delta\omega^k}{\delta\omega^p} = \frac{\omega_0^p}{\omega_0^k} \frac{\sum_{i=0}^N |V_i^k|^2 |V_i^p|^2}{\sum_{i=0}^N |V_i^p|^4} . \quad (5.76)$$

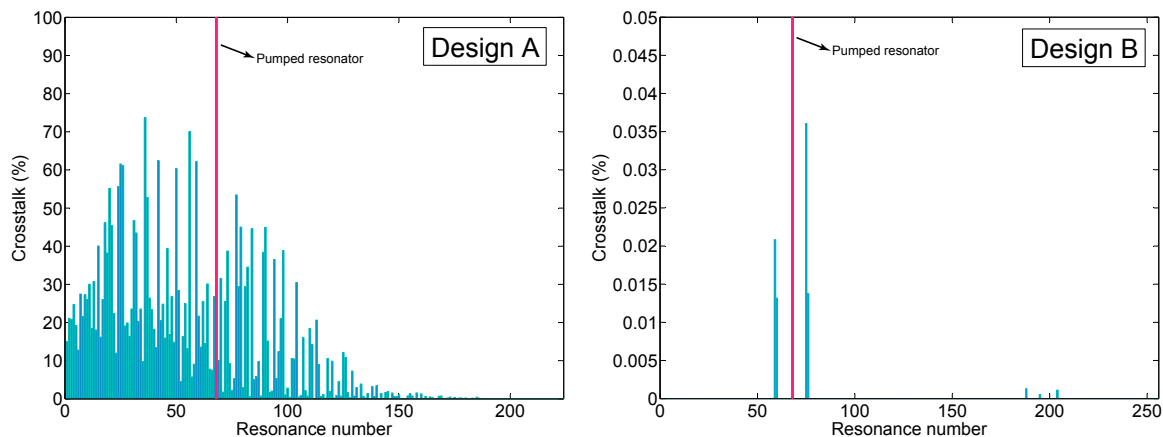


Figure 5.15: Crosstalk simulations for full-size arrays A and B. In both simulations mode number 68 (indicated in red) is pumped. By definition, crosstalk for the pumped mode is 100%. Note that the scales are very different in the two plots. (Figure reproduced from [89])

This result demonstrates that modes whose “energy overlap” is large will have significant crosstalk.

Figure 5.15 shows crosstalk simulated for both arrays A and B using Eq. 5.76. In both simulations an arbitrary mode number (#68) was pumped. The simulations show that crosstalk is very high in design A (up to  $\sim 75\%$ ) where many other modes are affected by the pump, while in design B there is almost no crosstalk down to a level of  $\sim 0.04\%$ .

## 5.6 Measurements

In this section measurements of array frequencies, quality factors, and crosstalk are presented for array design A and B.

### 5.6.1 Measurement setup

The setup used for measuring the array frequencies and coupling quality factors is simple. The device is installed in a sample holder box as shown in Fig. 4.7, mounted in a cryogenic dilution refrigerator, and cooled down to 100 mK or below. A network analyzer is used to excite the resonances by sending microwave power through coaxial cables inside the fridge and onto the device. The power reaching the feedline on the chip is denoted as  $P_{\text{feed}}$ . The transmitted signal power on the other end of the feedline is amplified by a low-noise cryogenic InP high-electron-mobility transistor (HEMT) or SiGe transistor amplifier cooled to 4 K. The signal is further amplified using room temperature amplifier and read out with the network analyzer. For measuring crosstalk, a microwave synthesizer and power combiner are added to this setup which is explained in detail in section 5.6.4. The measurement setup is shown in Fig. 5.24.

### 5.6.2 Frequency

Using the setup detailed in Fig. 5.24 with the synthesizer turned off, we measured the microwave forward transmission  $S_{21}$  for both designs A and B. These are shown in Fig. 5.16 for design A and in Fig. 5.17 for design B (for both bands). The general background transmission for design A shows relatively large ripples which are due to the impedance mismatch between the high-impedance TiN CPS feedline and  $50 \Omega$  loads. In design B these ripples are much smaller since we used lumped-element transformers on both sides of the feedline to match to  $50 \Omega$ . The frequency spacing is also much more uniform in design B.

From the  $S_{21}$  data and by using our resonance fitting code we extracted the resonance frequencies for both designs. These are shown in Fig. 5.18 and Fig. 5.19, where they are also compared to simulation. As can be seen, the simulations are in excellent agreement with measurements for both arrays, confirming our circuit model for

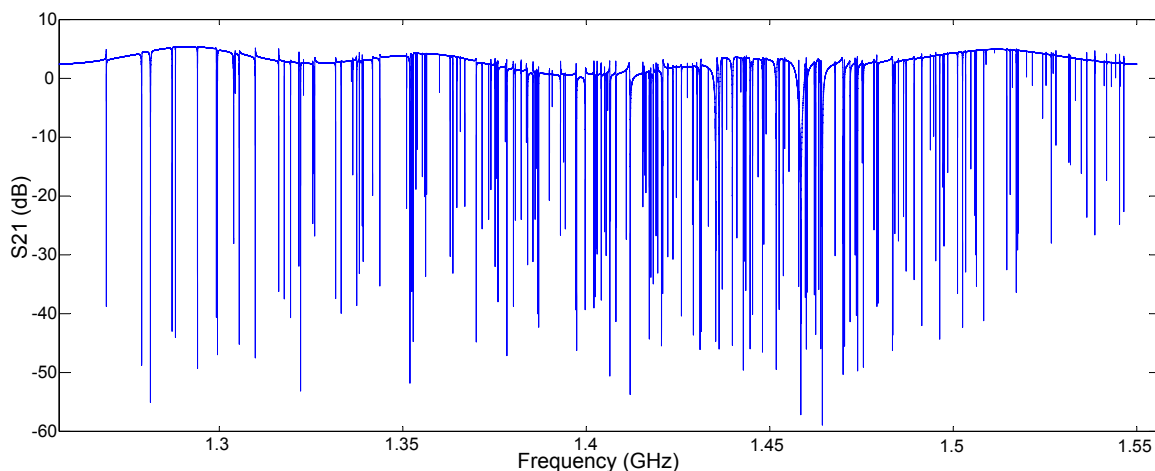


Figure 5.16: Measured forward transmission for design A array. Measurement was done at  $T = 100$  mk and  $P_{\text{feed}} = -90$  dBm. The device is a  $14 \times 16$  close-packed array of type A lumped-element resonators made using a  $t = 40$  nm TiN film with  $T_c = 4.1$  K,  $R_s = 20 \Omega$ , and  $L_s = 6.9$  pH. About 210 out of 224 resonances showed up.

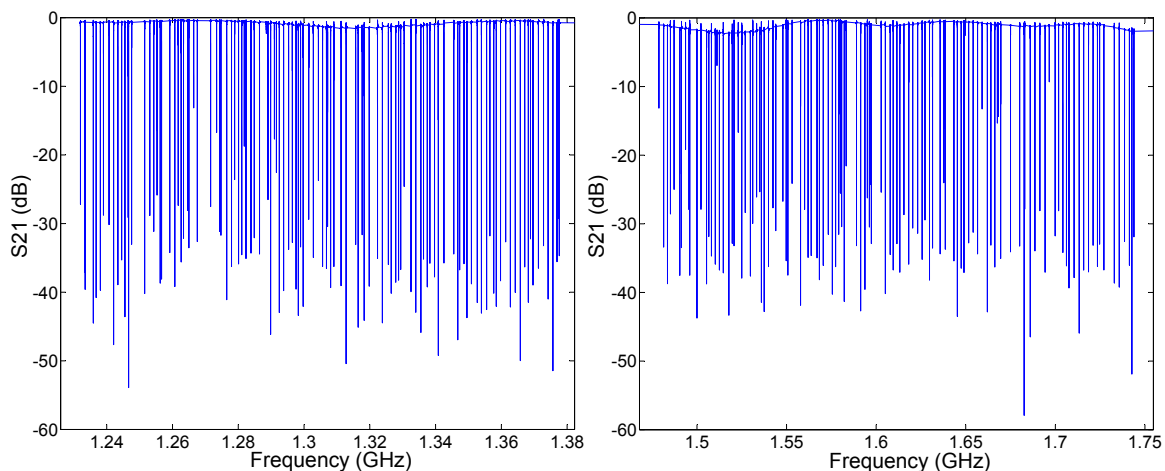


Figure 5.17: Measured forward transmission for design B array. Measurement was done at  $T = 25$  mk and  $P_{\text{feed}} = -93$  dBm. The device is a  $16 \times 16$  close-packed array of type B lumped-element resonators made using a  $t = 20$  nm TiN film with  $T_c = 3.60$  K, estimated  $R_s = 30 \Omega$ , and  $L_s = 11.7$  pH. The array had a CPW feedline with ground straps, tapered CPW transformers, and gold wirebonds to the box. About 118 of 128 resonances in the lower band and 122 of 128 in the higher band showed up.

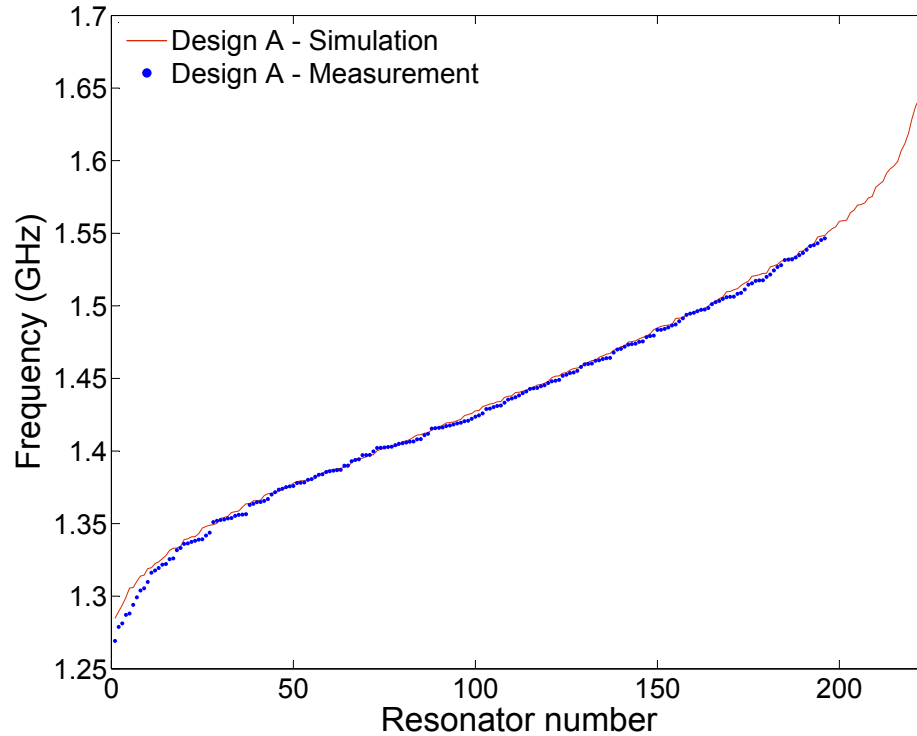


Figure 5.18: Measurement of array resonance frequencies for design A and comparison to simulation

coupled resonator arrays. The small variations in the curves could partly be caused by the cross-coupling, which are also predicted by the model, but can also be due to shifts caused by random film thickness variation or geometrical variation during fabrication, or trapped magnetic flux. Furthermore, if due to these variations several frequencies get sufficiently close together, they will become cross-coupled which will result in further scattering of resonance frequencies.

The measured frequency spacing between consecutive resonances are shown in Fig. 5.20. For design A, the initially intended fixed spacing was 1.3 MHz, but a large variation exists due to the high cross-coupling. The measurement shows a much more uniform spacing in design B compared to A. For design B, the spacing was designed to be 1.25 MHz and 2.20 MHz in the low (L) and high (H) bands, respectively, with a 100 MHz separation between the bands. The measured mean spacing for band L is 1.25 MHz with a standard deviation of 0.63 MHz and for band H is 2.19 MHz with a standard deviation of 1.11 MHz. The measured spacing between the bands is 101

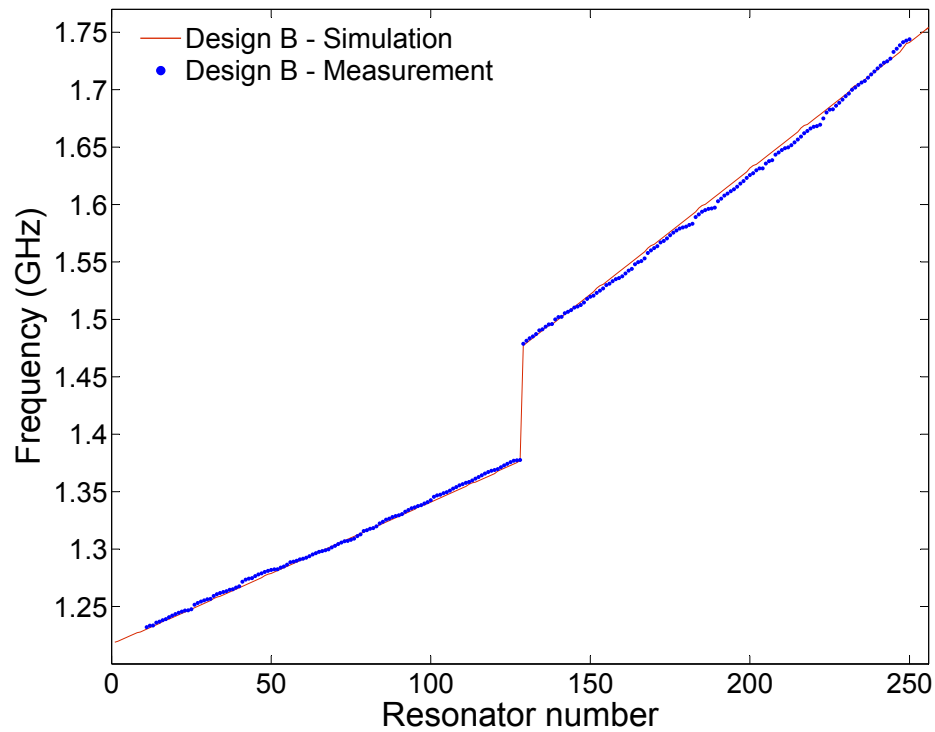


Figure 5.19: Measurement of array resonance frequencies for design B and comparison to simulation. There is a low(L)- and a high(H)-frequency band that are separated by 101 MHz.

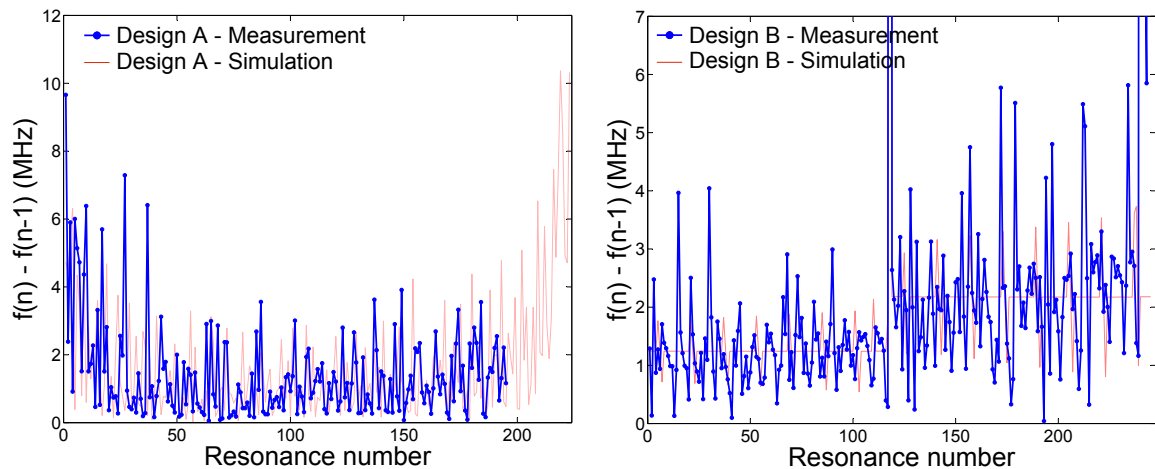


Figure 5.20: Measurements of array resonance frequency spacings for designs A and B, and comparison to simulation. The sudden jump in the middle is due to the 101 MHz separation between the L and H bands.

MHz. For both designs, the measured spacings are compared to simulation.

### 5.6.3 Quality factor

Using the measured  $S_{21}$  data and our fitting code we extracted the coupling quality factor  $Q_c$  and internal quality factor  $Q_i$  for resonances in design A and B. These are shown in Fig. 5.21 and 5.22.

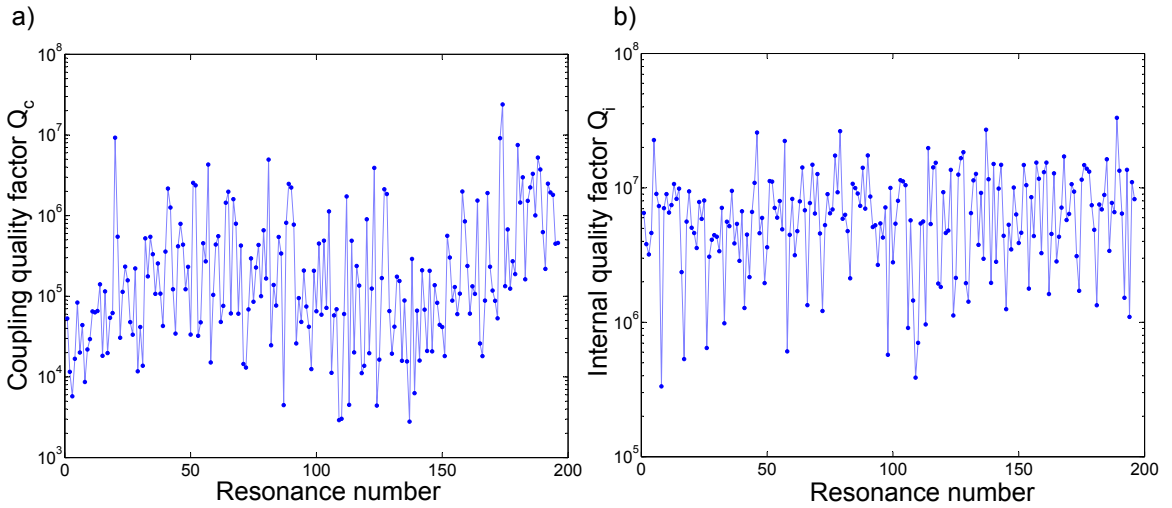


Figure 5.21: (a) Measured coupling quality factor  $Q_c$  for array A. (b) Measured internal quality factor  $Q_i$  for array A. There are six resonances with  $Q_i \sim 2 \times 10^7$ , and  $\geq 50$  with  $Q_i \sim 10^7$ . There is one resonator with  $Q_i = 3 \times 10^7$ .

For design A although the resonators were designed to have  $Q_c^* = 1.7 \times 10^6$ , the measured  $Q_c$  values show a very large scatter  $0.002 \leq Q_c^*/Q_c \leq 6$ , more than 3 orders of magnitude. The level of variation is similar to our simulation result shown in Fig. 5.14 (a). The large variation and the offset between the measurement and simulation could be due to various reasons. One is the fact that cross-coupling is very large for design A which results in large constructive or destructive interference of the currents on the feedline for each resonance mode resulting in large variations in  $Q_c$ . Another possibility could be due the propagation of an unwanted microstrip line mode on the CPS feedline with the metal box lid acting as the ground plane for the mode. The resonators can have a much higher coupling to such a mode (up to 10 times) which

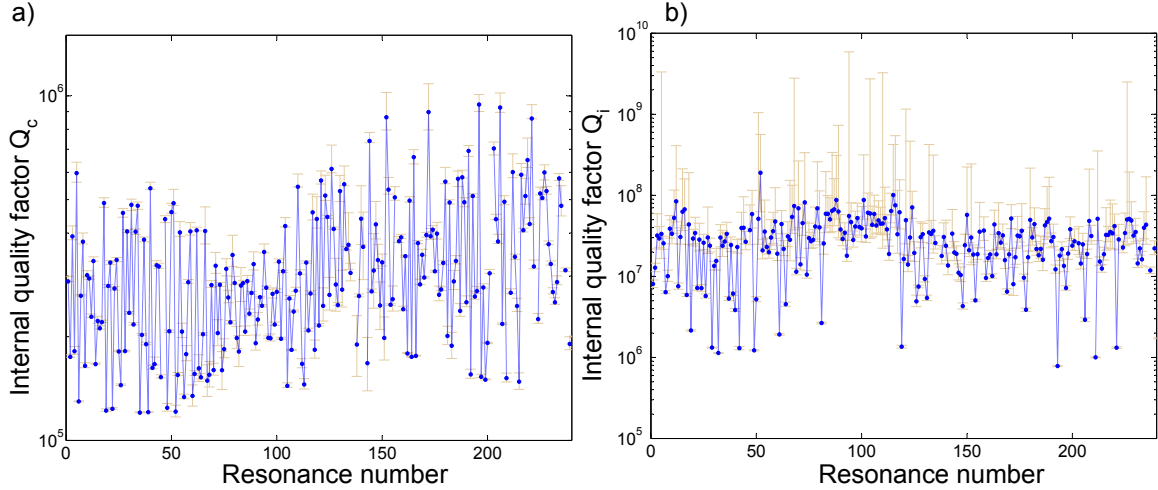


Figure 5.22: (a) Measured coupling quality factor  $Q_c$  for array B. (b) Measured internal quality factor  $Q_i$  for array B. Fitting error bars are indicated.

would reduce the  $Q_c$ 's. It is very likely that such a mode exists in design A because our initial transformers used in this array were not properly designed to handle CPS modes, and were acting as an asymmetric point along the feedline structure. Such asymmetric features are known to be the source of unwanted propagating modes [54]. Another reason could be due to the amplifier and source impedances not being close to  $50\Omega$ . Further investigation is necessary to eliminate  $Q_c$  variation and to obtain agreement between design and measurement.

For design B,  $Q_c$  varies less than an order of magnitude (see Fig. 5.22 (a)) and is between  $1.2\text{--}6 \times 10^5$  (factor of 5) in the lower frequency band, and between  $1.5\text{--}9.4 \times 10^5$  in the high-frequency band (factor of 6.3). This is a big improvement as compared to design A. There could be several reasons for this improvement. One obvious reason is the fact that design B has much less cross-coupling, as was shown in Fig. 5.14 (b). Another reason is the use of a finite-ground CPW feedline with periodic grounding straps connecting CPW ground strips to eliminate the possible unwanted coupled slot-line mode [54]. Even though we used a proper transformer design for this array, it would still be possible for the slot-line mode to get excited if there were no CPW ground straps. Another reason is that we used Nb instead of TiN for the CPW centerline in order to reduce the impedance mismatch to the  $50\Omega$

connections. However, the question still remains to why we still have  $Q_c$  variation. One possibility is that there could be microstrip line modes between the CPW center strip and the metal box lid ground plane, even though we used ample wirebonds between the chip CPW ground planes and the box. Further systematic investigation is needed to clarify this.

The average internal quality factor  $Q_i$  is very high in both arrays (Fig. 5.21 (b) and 5.22 (b)). In array A, the accidental large  $Q_c$  values mainly caused by cross-coupling enabled an accurate deep probe of the microwave loss of the TiN film. This is because the larger the  $Q_c$  values, the more accurate our resonance fitting code becomes in determining  $Q_i$ . In array A, we observed six resonances with  $Q_i \sim 2 \times 10^7$ , and  $\geq 50$  with  $Q_i \sim 10^7$ . There was one resonator with  $Q_i = 3 \times 10^7$ . The measured resonance loop for this resonance is shown in Fig. 5.23. This indicates a lower limit to the surface impedance quality factor  $Q_s = \alpha Q_i \geq 2 \times 10^7$  for the TiN film in this array, where  $\alpha = 0.74$  is the kinetic inductance fraction [58]. It should be noted that the cross-coupling of the resonators in this array does not affect our interpretation of  $Q_s$  because as was shown in Eq. 5.55  $Q_i$  of a coupled mode is only affected by the frequency of the mode. Also, as was shown in Fig. 4.10 all resonances displayed the same frequency versus temperature curve and follow the Mattis–Bardeen prediction. The variation in  $Q_i$  is not well understood. Some possible causes include film property variation across the array or simple dust particle contaminations on top of the resonator structures creating excess dielectric loss.

Measurements of array B show similarly high values of  $Q_i \geq 10^7$  (see Fig. 5.22 (b)). Several other arrays of this type have also shown consistent high values. However, because cross-coupling in these arrays is very small,  $Q_c$  is lower and closer to the design value. Therefore, probing very high  $Q_i$  resonances is more difficult and hence the upper error bounds from the fits for the  $Q_i$  data is quite large and some fits indicating unrealistically high  $Q_i$  are questionable. Still, the average fitting results are consistent with the data from array A.

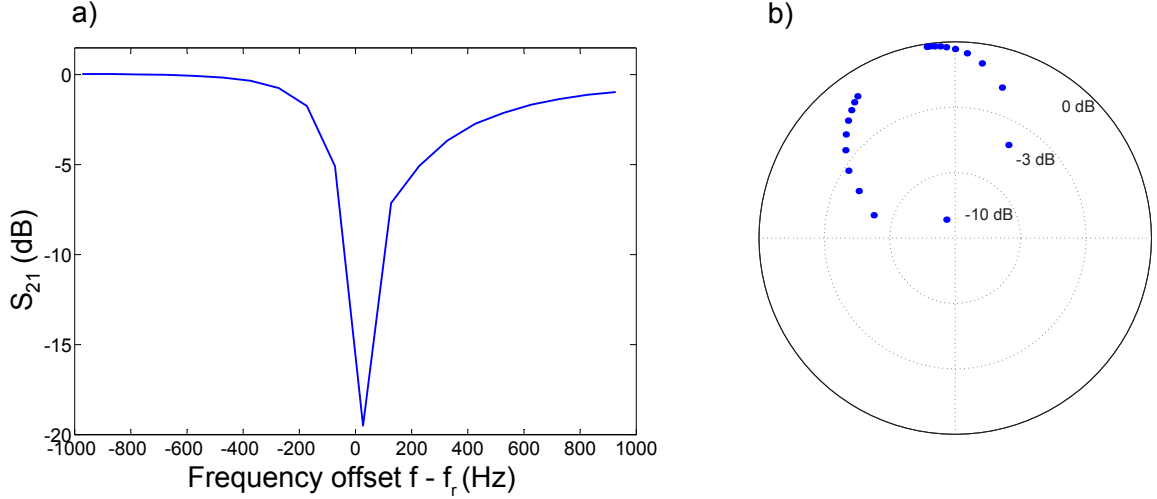


Figure 5.23: (a) A deep resonance in array design A measured at  $T = 100$  mK and  $P_{gen} = -90$  dBm with  $f_r = 1.53$  GHz,  $Q_r = 3.6 \times 10^6$ , and  $Q_i = 3 \times 10^7$ . (b) The polar  $S_{21}$  plot clearly shows the expected resonance loop.

### 5.6.4 Crosstalk

Having presented various measurements for the two arrays in the previous sections, now we turn our attention to measuring crosstalk. The setup for crosstalk measurement is illustrated in Fig. 5.24 where a synthesizer provides microwave power (pump) at the frequency of one of the resonance modes  $f_0^p$ . All the resonances were probed using a network analyzer in a relatively low power mode ( $P_{feed} \sim -100$  dBm where  $P_{feed}$  is the microwave power on the feedline), so that the pump power was dominant ( $\sim -80$  dBm). For both arrays A and B we measured a group of resonances not too far from the pumped resonance. Fig. 5.25 (a) shows measured transmission for array A when the pump tone is put on resonance (red) and turned off (blue). The pump tone appears smeared out which is due to the large network analyzer IF bandwidth that was used. During the measurement our network analyzer generated a spurious tone located at 20 MHz lower frequency than the pump, but since it was far away from any resonances, it was harmless to our measurement. Fig. 5.25 (b) shows a closeup of the pumped resonance which shifted by 2.2 KHz. We used our resonance fitting code to accurately determine every resonance. Fig. 5.25 (c) shows a closeup of one of the probed resonances as an example. The induced shift from the crosstalk between

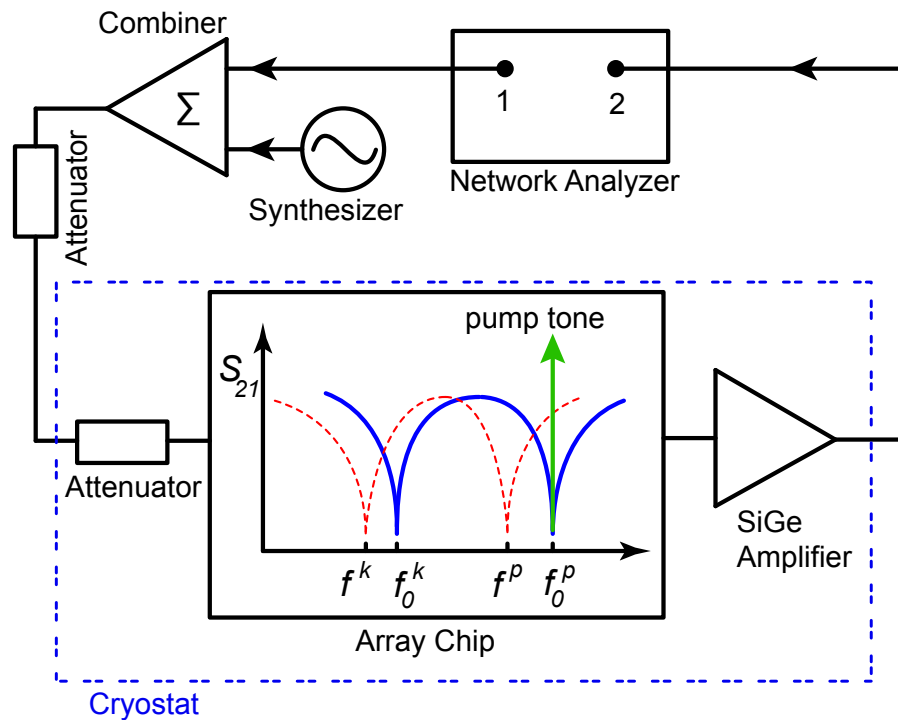


Figure 5.24: Illustration of the setup for measuring the resonances and the crosstalk. For the crosstalk measurements the resonators are cooled down to below 100 mK in a cryogenic refrigerator, and are read out using a network analyzer. A SiGe transistor amplifier [16] at 4 K is used to amplify the signal. The synthesizer pump power is combined with readout power using a 3 dB power combiner. The pump signal frequency is tuned on a resonance (blue curve) which causes the resonance to shift (red curve). A nearby coupled resonance also shifts as a result. (Figure reproduced from [89])

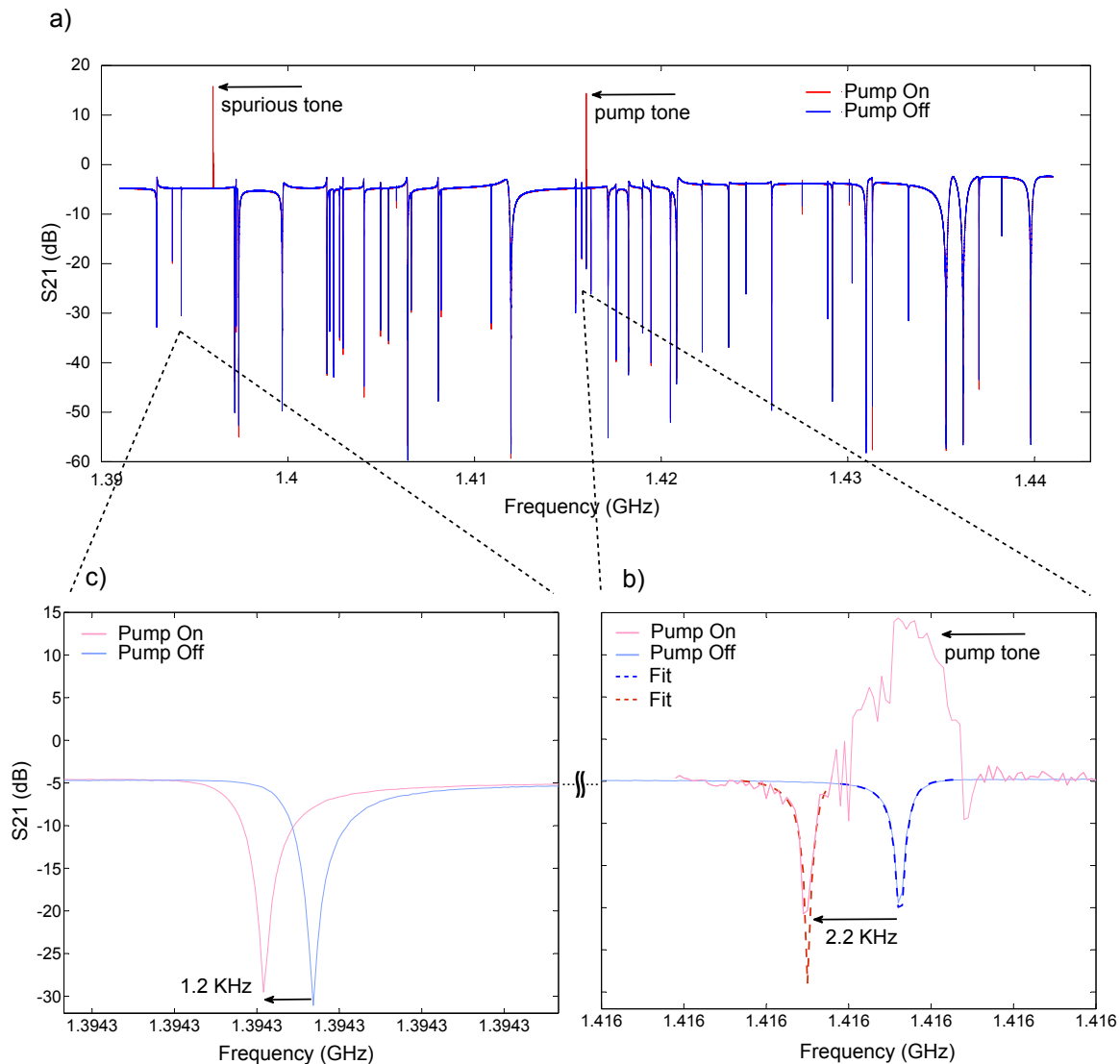


Figure 5.25: (a) Transmission measurement for array A when the pump tone is turned on and off. (b) Closeup of the pumped resonance before and after the pump was turned on. The bump on the resonance is the pump tone. (c) Closeup of one of the probed resonances and its shifted version after the pump was turned on

the two modes is 1.2 KHz, which gives a crosstalk of 52% between these two modes. In a similar way measurements were taken for array B. Full crosstalk measurement results are shown in Fig. 5.26. As is evident, Fig. 5.26 (a) shows that design A is dominated by crosstalk as large as 57%. Fig. 5.26 (b) shows that by going to design B, crosstalk dramatically reduces down to a maximum of 2% [89]. The error bars are a result of the fits to the resonances by our fitting code adapted from [28] used to fit the data from the network analyzer. Because the network analyzer scans were taken

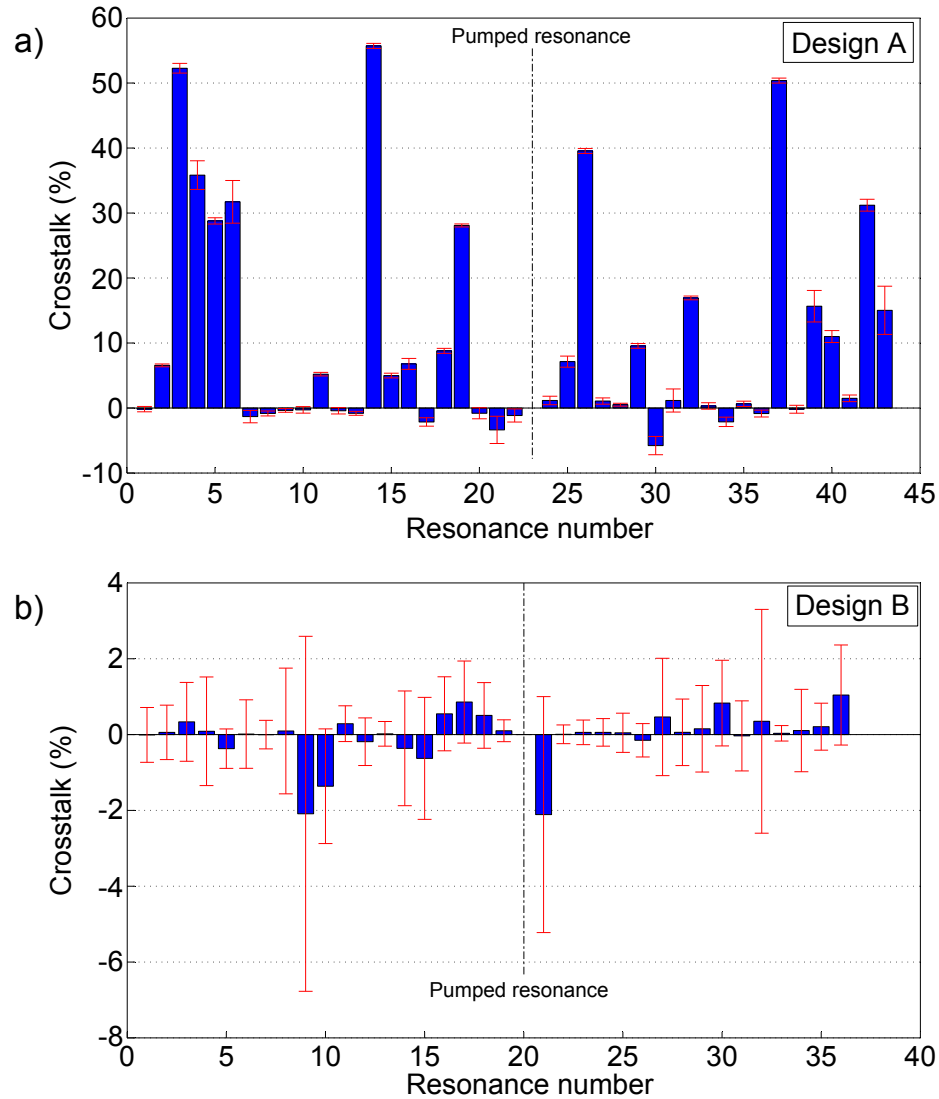


Figure 5.26: Crosstalk measurement results for designs A and B. The (frequency) position of the pumped resonance is shown by the dashed line. The red bars indicate the measurement error. Note the scales of the two plots are very different. (Figure reproduced from [89])

at relatively low power, longer measurement times were required which made the data susceptible to various noise sources including network analyzer frequency drift and magnetic fields affecting the resonance positions [51]. The simulations shown in Fig. 5.15 support the measurements and suggest that the actual crosstalk in design B could be much lower than the experimental upper limit of 2%. These results conclusively show that design B is superior to design A in terms of crosstalk.

# Appendix A

## Resonator circuit transmission $S_{21}$

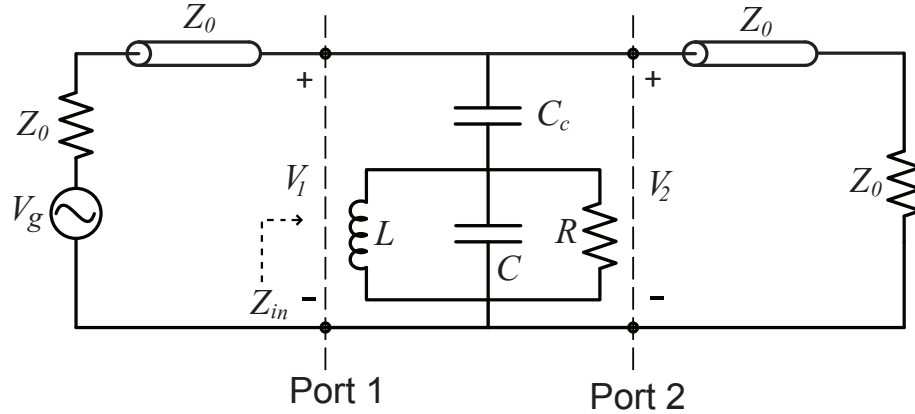


Figure A.1: Equivalent circuit for a superconducting resonator detector. The resonator is capacitively coupled to a feedline. The load impedance  $Z_0$  represents the amplifier input impedance. The voltage source and its impedance represent the microwave generator.

Here we will calculate the microwave forward transmission  $S_{21}$  from port 1 to 2 for the resonator circuit shown in Fig. A.1.

We first start by the definition of scattering parameters

$$S_{11} = \frac{V_1^-}{V_1^+} \Big|_{V_2^+ = 0} \quad (\text{A.1})$$

$$S_{21} = \frac{V_2^-}{V_1^+} \Big|_{V_2^+ = 0} \quad (\text{A.2})$$

where  $V_1^+$  and  $V_1^-$  are the incident and reflected waves off of port 1, and  $V_2^+$  and  $V_2^-$

are the incident and reflected waves off of port 2. The voltages at port 1 and 2 are

$$V_1 = V_1^+ + V_1^- \quad (\text{A.3})$$

$$V_2 = V_2^+ + V_2^- = V_2^- \quad (\text{A.4})$$

where in the last equation  $V_2^+ = 0$  because port 2 is terminated in a matched load.

We can write

$$V_1^+ = \frac{V_1}{1 + S_{11}}. \quad (\text{A.5})$$

Furthermore, we can write

$$S_{11} = \frac{Z_{in} - Z_0}{Z_{in} + Z_0} \quad (\text{A.6})$$

where  $Z_{in}$  is the input impedance looking into port 1 with port 2 terminated in a matched load, and  $Z_0$  is the load impedance representing the amplifier input impedance. Using the above equations we can write

$$S_{21} = (1 + S_{11}) \frac{V_2}{V_1} \quad (\text{A.7})$$

$$= \frac{2Z_{in}}{Z_{in} + Z_0} \frac{V_2}{V_1} \quad (\text{A.8})$$

$$= \frac{2Z_{in}I_1}{(Z_{in} + Z_0)I_1} \frac{V_2}{V_1} \quad (\text{A.9})$$

$$= \frac{2V_1}{V_g} \frac{V_2}{V_1} \quad (\text{A.10})$$

$$= \frac{2V_2}{V_g}. \quad (\text{A.11})$$

Now we can proceed with calculating the voltage  $V_2$ . The circuit in Fig. A.1 can be simplified if we use a Norton equivalent circuit for the generator voltage source. The Norton equivalent impedance  $Z_g$  is the impedance seen from the tank circuit as shown in Fig. A.2 (a) and is equal to

$$Z_g = \frac{Z_0}{2} + \frac{1}{j\omega C_c}. \quad (\text{A.12})$$

The circuit is simplified if we use the Norton admittance  $Y_g$

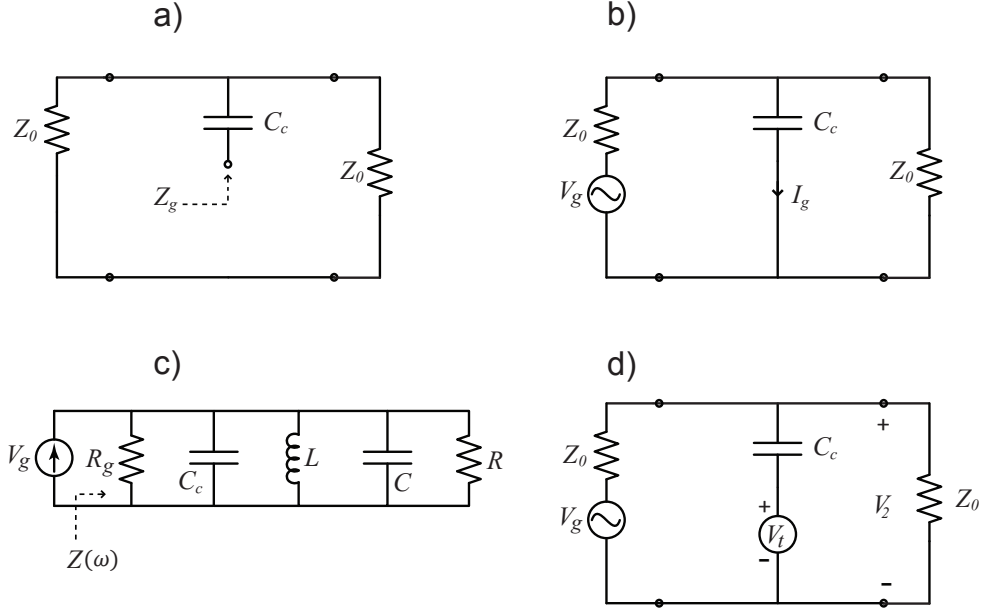


Figure A.2: (a) Circuit for calculating the Norton equivalent source impedance  $Z_g$ . (b) Circuit for calculating the Norton equivalent current source  $I_g$ . (c) Equivalent circuit for the circuit shown in Fig. A.1. (d) Equivalent circuit for calculating the output voltage  $V_2$  in Fig. A.1 where the tank circuit has been replaced by a voltage source

$$Y_g = \frac{1}{Z_g} \quad (\text{A.13})$$

$$= \frac{j\omega C_c}{1 + \frac{1}{2}Z_0 j\omega C_c} \quad (\text{A.14})$$

$$\approx j\omega C_c \left(1 - \frac{1}{2}Z_0 j\omega C_c\right) \quad (\text{A.15})$$

$$= j\omega C_c + \frac{1}{2}Z_0 (\omega C_c)^2 \quad (\text{A.16})$$

$$= j\omega C_c + \frac{1}{R_g(\omega)} \quad (\text{A.17})$$

where

$$R_g(\omega) = \frac{2Z_0}{(Z_0 \omega C_c)^2}. \quad (\text{A.18})$$

In Eq. A.15 the approximation is based on  $\omega C_c Z_0 \ll 1$  which is true for when  $\omega$  is close to the resonant frequency  $\omega_r$ .

To calculate the Norton equivalent current source  $I_g$  we short the tank circuit to

ground as shown in Fig. A.2 (b). The short circuit current  $I_g$  is

$$I_g = \frac{V_g}{Z_0 + (Z_0 \parallel 1/(j\omega C_c))} \times \frac{Z_0}{Z_0 + 1/(j\omega C_c)} \quad (\text{A.19})$$

$$= \frac{V_g}{Z_0 + 2/(j\omega C_c)} \quad (\text{A.20})$$

$$= \frac{V_g}{2Z_g} . \quad (\text{A.21})$$

The resulting circuit is shown in Fig. A.2 (c). We can now calculate the resonance frequency  $\omega_r$  and quality factor  $Q_r$ :

$$\omega_r^2 = \frac{1}{L(C + C_c)} \quad (\text{A.22})$$

and

$$Q_r = \omega_r R_{\parallel} (C + C_c) \quad (\text{A.23})$$

$$= \frac{R_{\parallel}}{\omega_r L} \quad (\text{A.24})$$

$$\approx \omega_r R_{\parallel} C \quad (\text{A.25})$$

where  $R_{\parallel}$  is the total resistance

$$R_{\parallel} = R \parallel R_g \quad (\text{A.26})$$

$$= \frac{1}{1/R + 1/R_g} \quad (\text{A.27})$$

The internal quality factor of the circuit  $Q_i$  (from dissipation in internal resistance) is equal to

$$Q_i = \omega_r R (C + C_c) \quad (\text{A.28})$$

$$\approx \omega_r R C \quad (\text{A.29})$$

and the coupling quality factor of the circuit to the outside (from dissipation in outside

terminations) is

$$Q_c = \omega_r R_g (C + C_c) \quad (\text{A.30})$$

$$Q_c \approx \omega_r R_g C \quad (\text{A.31})$$

$$= \frac{2}{Z_0 \omega_r C_c} \times \frac{C}{C_c} . \quad (\text{A.32})$$

We can see that the total quality factor derived in Eq. A.25 is related to Eq. A.29 and Eq. A.32 by

$$\frac{1}{Q_r} = \frac{1}{Q_i} + \frac{1}{Q_c} . \quad (\text{A.33})$$

We can see this by writing:

$$\frac{1}{Q_r} = \frac{1}{\omega_r R_{\parallel} C} \quad (\text{A.34})$$

$$= \frac{1}{\omega_r R C} + \frac{1}{2} Z_0 \omega_r C_c \frac{C}{C} \quad (\text{A.35})$$

$$= \frac{1}{Q_i} + \frac{1}{Q_c} . \quad (\text{A.36})$$

Now we continue with calculating the transmission  $S_{21}$  for the circuit. The goal is to calculate  $V_2$  as a function of  $V_g$ . To do this we first calculate the impedance  $Z(\omega)$  in Fig. A.2 (c). We can write

$$\frac{1}{Z(\omega)} = \frac{1}{R_{\parallel}} + \frac{1}{j\omega L} + j\omega C . \quad (\text{A.37})$$

After a few rearrangements we get

$$Z(\omega) = \frac{R_{\parallel}}{1 + \frac{jR_{\parallel}}{\omega L} \left( \frac{\omega^2}{\omega_r^2} - 1 \right)} . \quad (\text{A.38})$$

For frequencies close to  $\omega_r$  we can write  $\omega = \omega_r + \delta\omega$  and use the approximation

$$\omega^2 - \omega_r^2 \approx 2\omega_r\delta\omega \quad (\text{A.39})$$

along with Eq. A.24 to simplify Eq. A.38 to

$$Z(\omega) = \frac{R_{\parallel}}{1 + 2jQ_r x} \quad (\text{A.40})$$

where  $x = \frac{\omega - \omega_r}{\omega_r}$ . The tank circuit in Fig. A.1 can now be replaced by an equivalent voltage source  $V_t$  equal to

$$V_t = I_g \times Z(\omega) \quad (\text{A.41})$$

$$= \frac{V_g}{2Z_g} \times \frac{R_{\parallel}}{1 + 2jQ_r x} \quad (\text{A.42})$$

as shown in Fig. A.2 (d). Now we can calculate  $V_2$  using voltage superposition:

$$V_2 = V_g \frac{Z_0 \parallel \frac{1}{j\omega C_c}}{(Z_0 \parallel \frac{1}{j\omega C_c}) + Z_0} + V_t \frac{Z_0/2}{Z_0/2 + \frac{1}{j\omega C_c}}. \quad (\text{A.43})$$

Substituting for  $V_t$  from Eq. A.42 we get

$$V_2 = \left( V_g + j\omega C_c Z_0 \frac{V_g R_{\parallel}}{2Z_g} \frac{1}{1 + 2jQ_r x} \right) \left( \frac{1}{2 + j\omega C_c Z_0} \right). \quad (\text{A.44})$$

Using Eq. A.11 we can now write

$$S_{21} = \left( 1 + j\omega C_c Z_0 \frac{R_{\parallel}}{2Z_g} \frac{1}{1 + 2jQ_r x} \right) \left( \frac{2}{2 + j\omega C_c Z_0} \right). \quad (\text{A.45})$$

The above equation can be simplified by approximating  $Z_g \approx \frac{1}{j\omega C_c}$  and approximating the factor on the right-hand side by unity. We then get

$$S_{21} \approx 1 - (\omega_r C_c Z_0)^2 \frac{R_{\parallel}}{2Z_0} \frac{1}{1 + 2jQ_r x}. \quad (\text{A.46})$$

Finally, using Eq. A.25 and Eq. A.32 we can write

$$S_{21}(\omega) \approx 1 - \frac{Q_r}{Q_c} \frac{1}{1 + 2jQ_r x} . \quad (\text{A.47})$$

The above equation is regularly used to describe the resonance circles shown in Fig. 3.1 (a) observed in measurements.

# Bibliography

- [1] D. Leisawitz, W. Danchi, M. DiPirro, L. Feinberg, D. Gezari, M. Hagopian, W. Langer, J. Mather, S. Moseley, M. Shao, R. Silverberg, J. Staguhn, M. Swain, H. Yorke, and X. Zhang, “Scientific motivation and technology requirements for the SPIRIT and SPECS far-infrared/submillimeter space interferometers,” in *UV, Optical, and IR Space Telescopes and Instruments*, ser. Proceedings of SPIE—The International Society for Optical Engineering, vol. 4013, 2000, pp. 36–46, Conference on UV, Optical, and IR Space Telescopes and Instruments, Munich, Germany, Mar 29–31, 2000.
- [2] R. Giovanelli, J. Carpenter, S. Radford, T. Sebring, T. Soifer, G. Stacey, J. Zmuidzinas, and the CCAT Collaboration, “CCAT,” White paper, Astro2010, 2009. [Online]. Available: <http://www.ccatobservatory.org/docs/ccat-reports-publications/Giovanelli-CCAT.pdf>
- [3] T. Phillips and J. Keene, “Submillimeter Astronomy,” *Proceedings of the IEEE*, vol. 80, no. 11, pp. 1662–1678, Nov 1992.
- [4] A. Noriega-Crespo, P. Morris, F. Marleau, S. Carey, A. Boogert, E. van Dishoeck, N. Evans, J. Keene, J. Muzerolle, K. Stapelfeldt, K. Pontoppidan, P. Lowrance, L. Allen, and T. Bourke, “A new look at stellar outflows: Spitzer observations of the HH 46/47 system,” *Astrophysical Journal Supplement Series*, vol. 154, no. 1, pp. 352–358, Sep 2004.

- [5] K. Irwin, G. Hilton, D. Wollman, and J. Martinis, “X-ray detection using a superconducting transition-edge sensor microcalorimeter with electrothermal feedback,” *Applied Physics Letters*, vol. 69, no. 13, pp. 1945–1947, Sep 23 1996.
- [6] B. Cabrera, R. M. Clarke, P. Colling, A. J. Miller, S. Nam, and R. W. Romani, “Detection of single infrared, optical, and ultraviolet photons using superconducting transition edge sensors,” *Applied Physics Letters*, vol. 73, no. 6, pp. 735–737, 1998. [Online]. Available: <http://link.aip.org/link/?APL/73/735/1>
- [7] K. Irwin, G. Hilton, J. Martinis, S. Deiker, N. Bergren, S. Nam, D. Rudman, and D. Wollman, “A Mo-Cu superconducting transition-edge microcalorimeter with 4.5 eV energy resolution at 6 keV,” *Nuclear Instruments and Methods in Physics Research Section A: Accelerators, Spectrometers, Detectors and Associated Equipment*, vol. 444, no. 1–2, pp. 184–187, Apr 2000, 8th International Workshop on Low-Temperature Detectors (LTD-8), Dalfsen, Netherlands, Aug 15–20, 1999.
- [8] A. Peacock, P. Verhoeve, N. Rando, A. vanDordrecht, B. Taylor, C. Erd, M. Perryman, R. Venn, J. Howlett, D. Goldie, J. Lumley, and M. Wallis, “Single optical photon detection with a superconducting tunnel junction,” *Nature*, vol. 381, no. 6578, pp. 135–137, May 1996.
- [9] Science Frontiers Panels; Program Prioritization Panels; Committee for a Decadal Survey of Astronomy and Astrophysics; National Research Council, *Panel Reports—New Worlds, New Horizons in Astronomy and Astrophysics*. The National Academies Press, 2011. [Online]. Available: [http://www.nap.edu/openbook.php?record\\_id=12982](http://www.nap.edu/openbook.php?record_id=12982)
- [10] W. Holland, W. Duncan, B. Kelly, K. Irwin, A. Walton, P. Ade, and E. Robson, “SCUBA-2: A large format submillimetre camera on the James Clerk maxwell telescope,” in *Millimeter and Submillimeter Detectors for Astronomy*, ser. Proceedings of SPIE—The International Society for Optical Engineering, vol. 4855,

2003, pp. 1–18, Conference on Millimeter and Submillimeter Detectors for Astronomy, Waikoloa, HI, Aug 25–28, 2002.

- [11] A. Woodcraft, “Scuba-2: A 10000-pixel submillimetre camera for astronomy,” in *Infrared and Millimeter Waves, 2007, and the 2007 15th International Conference on Terahertz Electronics. IRMMW-THz. Joint 32nd International Conference on*, Sep 2007, pp. 594–595.
- [12] P. Day, H. LeDuc, B. Mazin, A. Vayonakis, and J. Zmuidzinas, “A broadband superconducting detector suitable for use in large arrays,” *Nature*, vol. 425, no. 6960, pp. 817–821, Oct 2003.
- [13] J. Zmuidzinas, “Superconducting microresonators: Physics and applications,” *Annual Review of Condensed Matter Physics*, vol. 3, no. 1, pp. 169–214, 2012. [Online]. Available: <http://www.annualreviews.org/doi/abs/10.1146/annurev-conmatphys-020911-125022>
- [14] S. McHugh, B. A. Mazin, B. Serfass, S. Meeker, K. O’Brien, R. Duan, R. Raffanti, and D. Werthimer, “A readout for large arrays of microwave kinetic inductance detectors,” *Review of Scientific Instruments*, vol. 83, no. 4, p. 044702, 2012. [Online]. Available: <http://link.aip.org/link/?RSI/83/044702/1>
- [15] B. Mazin, P. Day, K. Irwin, C. Reintsema, and J. Zmuidzinas, “Digital readouts for large microwave low-temperature detector arrays,” *Nuclear Instruments and Methods in Physics Research Section A: Accelerators, Spectrometers, Detectors and Associated Equipment*, vol. 559, no. 2, pp. 799–801, Apr 2006, 11th International Workshop on Low-Temperature Detectors, Univ Tokyo, Tokyo, Japan, Jul 31–Aug 05, 2005.
- [16] S. Weinreb, J. Bardin, H. Mani, and G. Jones, “Matched wideband low-noise amplifiers for radio astronomy,” *Review of Scientific Instruments*, vol. 80, no. 4, p. 044702, 2009. [Online]. Available: <http://link.aip.org/link/?RSI/80/044702/1>

- [17] P. R. Maloney, N. G. Czakon, P. K. Day, T. P. Downes, R. Duan, J. Gao, J. Glenn, S. R. Golwala, M. I. Hollister, H. G. LeDuc, B. A. Mazin, S. G. McHugh, O. Noroozian, H. T. Nguyen, J. Sayers, J. A. Schlaerth, S. Siegel, J. E. Vaillancourt, A. Vayonakis, P. Wilson, and J. Zmuidzinas, “MUSIC for sub/millimeter astrophysics,” in *Millimeter, Submillimeter, and Far-infrared Detectors and Instrumentation for Astronomy V*, ser. Proceedings of SPIE—The International Society for Optical Engineering, vol. 7741, 2010, Conference on Millimeter, Submillimeter, and Far-Infrared Detectors and Instrumentation for Astronomy V, San Diego, CA, Jun 29–Jul 02, 2010.
- [18] J. A. Schlaerth, N. G. Czakon, P. K. Day, T. P. Downes, R. Duan, J. Gao, J. Glenn, S. R. Golwala, M. I. Hollister, H. G. LeDuc, B. A. Mazin, P. R. Maloney, O. Noroozian, H. T. Nguyen, J. Sayers, S. Siegel, J. E. Vaillancourt, A. Vayonakis, P. R. Wilson, and J. Zmuidzinas, “MKID multicolor array status and results from DemoCam,” in *Millimeter, Submillimeter, and Far-infrared Detectors and Instrumentation for Astronomy V*, ser. Proceedings of SPIE—The International Society for Optical Engineering, vol. 7741, 2010, Conference on Millimeter, Submillimeter, and Far-Infrared Detectors and Instrumentation for Astronomy V, San Diego, CA, Jun 29–Jul 02, 2010.
- [19] B. A. Mazin, K. O’Brien, S. McHugh, B. Bumble, D. Moore, S. Golwala, and J. Zmuidzinas, “ARCONS: A highly multiplexed superconducting optical to near-IR camera,” in *Ground-based and Airborne Instrumentation for Astronomy III*, ser. Proceedings of SPIE—The International Society for Optical Engineering, vol. 7735, 2010, Conference on Ground-based and Airborne Instrumentation for Astronomy III, San Diego, CA, Jun 27–Jul 02, 2010.
- [20] A. Monfardini, A. Benoit, A. Bidaud, L. Swenson, A. Cruciani, P. Camus, C. Hoffmann, F. X. Dsert, S. Doyle, P. Ade, P. Mauskopf, C. Tucker, M. Roesch, S. Leclercq, K. F. Schuster, A. Endo, A. Baryshev, J. J. A. Baselmans, L. Ferrari, S. J. C. Yates, O. Bourrion, J. Macias-Perez, C. Vescovi, M. Calvo, and C. Giordano, “A dual-band millimeter-wave

- kinetic inductance camera for the iram 30 m telescope,” *The Astrophysical Journal Supplement Series*, vol. 194, no. 2, p. 24, 2011. [Online]. Available: <http://stacks.iop.org/0067-0049/194/i=2/a=24>
- [21] J. B. Hertzberg, T. Rocheleau, T. Ndukum, M. Savva, A. A. Clerk, and K. C. Schwab, “Back-action-evading measurements of nanomechanical motion,” *Nature Physics*, vol. 6, no. 3, pp. 213–217, Mar 2010.
- [22] J. Koch, A. A. Houck, K. L. Hur, and S. M. Girvin, “Time-reversal-symmetry breaking in circuit-qed-based photon lattices,” *Phys. Rev. A*, vol. 82, p. 043811, Oct 2010. [Online]. Available: <http://link.aps.org/doi/10.1103/PhysRevA.82.043811>
- [23] C. M. Wilson, T. Duty, M. Sandberg, F. Persson, V. Shumeiko, and P. Delsing, “Photon generation in an electromagnetic cavity with a time-dependent boundary,” *Phys. Rev. Lett.*, vol. 105, p. 233907, Dec 2010. [Online]. Available: <http://link.aps.org/doi/10.1103/PhysRevLett.105.233907>
- [24] J. A. B. Mates, G. C. Hilton, K. D. Irwin, L. R. Vale, and K. W. Lehnert, “Demonstration of a multiplexer of dissipationless superconducting quantum interference devices,” *Applied Physics Letters*, vol. 92, no. 2, p. 023514, 2008. [Online]. Available: <http://link.aip.org/link/?APL/92/023514/1>
- [25] E. A. Tholén, A. Ergül, E. M. Doherty, F. M. Weber, F. Grégis, and D. B. Haviland, “Nonlinearities and parametric amplification in superconducting coplanar waveguide resonators,” *Applied Physics Letters*, vol. 90, no. 25, p. 253509, 2007. [Online]. Available: <http://link.aip.org/link/?APL/90/253509/1>
- [26] J. Bardeen, L. N. Cooper, and J. R. Schrieffer, “Theory of superconductivity,” *Phys. Rev.*, vol. 108, pp. 1175–1204, Dec 1957. [Online]. Available: <http://link.aps.org/doi/10.1103/PhysRev.108.1175>

- [27] D. Mattis and J. Bardeen, “Theory of the Anomalous Skin Effect in Normal and Superconducting Metals,” *Physical Review*, vol. 111, no. 2, pp. 412–417, 1958.
- [28] J. Gao, “The physics of superconducting microwave resonators,” Ph.D. dissertation, California Institute of Technology, 2008.
- [29] R. Barends, J. J. A. Baselmans, S. J. C. Yates, J. R. Gao, J. N. Hovenier, and T. M. Klapwijk, “Quasiparticle relaxation in optically excited high- $q$  superconducting resonators,” *Phys. Rev. Lett.*, vol. 100, p. 257002, Jun 2008. [Online]. Available: <http://link.aps.org/doi/10.1103/PhysRevLett.100.257002>
- [30] R. Barends, S. van Vliet, J. J. A. Baselmans, S. J. C. Yates, J. R. Gao, and T. M. Klapwijk, “Enhancement of quasiparticle recombination in ta and al superconductors by implantation of magnetic and nonmagnetic atoms,” *Phys. Rev. B*, vol. 79, p. 020509, Jan 2009. [Online]. Available: <http://link.aps.org/doi/10.1103/PhysRevB.79.020509>
- [31] A. G. Kozorezov, A. A. Golubov, J. K. Wigmore, D. Martin, P. Verhoeve, R. A. Hijmering, and I. Jerjen, “Inelastic scattering of quasiparticles in a superconductor with magnetic impurities,” *Phys. Rev. B*, vol. 78, p. 174501, Nov 2008. [Online]. Available: <http://link.aps.org/doi/10.1103/PhysRevB.78.174501>
- [32] S. B. Kaplan, C. C. Chi, D. N. Langenberg, J. J. Chang, S. Jafarey, and D. J. Scalapino, “Quasiparticle and phonon lifetimes in superconductors,” *Phys. Rev. B*, vol. 14, pp. 4854–4873, Dec 1976. [Online]. Available: <http://link.aps.org/doi/10.1103/PhysRevB.14.4854>
- [33] B. Mazin, “Microwave kinetic inductance detectors,” Ph.D. dissertation, California Institute of Technology, 2004.
- [34] A. Wallraff, D. Schuster, A. Blais, L. Frunzio, R. Huang, J. Majer, S. Kumar, S. Girvin, and R. Schoelkopf, “Strong coupling of a single photon to a super-

- conducting qubit using circuit quantum electrodynamics,” *Nature*, vol. 431, no. 7005, pp. 162–167, Sep 2004.
- [35] O. Noroozian, J. Gao, J. Zmuidzinas, H. G. LeDuc, and B. A. Mazin, “Two-level system noise reduction for Microwave Kinetic Inductance Detectors,” in *Low Temperature Detectors LTD 13*, ser. AIP Conference Proceedings, vol. 1185, 2009, pp. 148–151, 13th International Workshop on Low Temperature Detectors, Stanford, CA, Jul 20–24, 2009. [Online]. Available: <http://link.aip.org/link/?APC/1185/148/1>
- [36] J. Gao, M. Daal, J. M. Martinis, A. Vayonakis, J. Zmuidzinas, B. Sadoulet, B. A. Mazin, P. K. Day, and H. G. Leduc, “A semiempirical model for two-level system noise in superconducting microresonators,” *Applied Physics Letters*, vol. 92, no. 21, May 2008.
- [37] W. A. Phillips, “Tunneling states in amorphous solids,” *Journal of Low Temperature Physics*, vol. 7, pp. 351–360, 1972, 10.1007/BF00660072. [Online]. Available: <http://dx.doi.org/10.1007/BF00660072>
- [38] P. Anderson, B. Halperin, and C. Varma, “Anomalous Low-Temperature Thermal Properties of Glasses and Spin Glasses,” *Philosophical Magazine*, vol. 25, no. 1, pp. 1–9, 1972.
- [39] J. Martinis, K. Cooper, R. McDermott, M. Steffen, M. Ansmann, K. Osborn, K. Cicak, S. Oh, D. Pappas, R. Simmonds, and C. Yu, “Decoherence in Josephson qubits from dielectric loss,” *Physical Review Letters*, vol. 95, no. 21, Nov 2005.
- [40] D. P. Pappas, M. R. Vissers, D. S. Wisbey, J. S. Kline, and J. Gao, “Two Level System Loss in Superconducting Microwave Resonators,” *IEEE Transactions on Applied Superconductivity*, vol. 21, no. 3, part 1, pp. 871–874, Jun 2011.
- [41] K. Shwetank, “Submillimeter wave camera using a novel photon detector technology,” Ph.D. dissertation, California Institute of Technology, 2008.

- [42] S. Kumar, J. Gao, J. Zmuidzinas, B. A. Mazin, H. G. LeDuc, and P. K. Day, “Temperature dependence of the frequency and noise of superconducting coplanar waveguide resonators,” *Applied Physics Letters*, vol. 92, no. 12, Mar 2008.
- [43] W. A. Phillips, “Two-level states in glasses,” *Reports on Progress in Physics*, vol. 50, no. 12, p. 1657, 1987. [Online]. Available: <http://stacks.iop.org/0034-4885/50/i=12/a=003>
- [44] M. V. Schickfus and S. Hunklinger, “Saturation of the dielectric absorption of vitreous silica at low temperatures,” *Physics Letters A*, vol. 64, no. 1, pp. 144–146, 1977. [Online]. Available: <http://www.sciencedirect.com/science/article/pii/0375960177905588>
- [45] A. D. O’Connell, M. Ansmann, R. C. Bialczak, M. Hofheinz, N. Katz, E. Lucero, C. McKenney, M. Neeley, H. Wang, E. M. Weig, A. N. Cleland, and J. M. Martinis, “Microwave dielectric loss at single photon energies and millikelvin temperatures,” *Applied Physics Letters*, vol. 92, no. 11, Mar 2008.
- [46] J. Gao, M. Daal, A. Vayonakis, S. Kumar, J. Zmuidzinas, B. Sadoulet, B. A. Mazin, P. K. Day, and H. G. Leduc, “Experimental evidence for a surface distribution of two-level systems in superconducting lithographed microwave resonators,” *Applied Physics Letters*, vol. 92, no. 15, Apr 2008.
- [47] R. Barends, N. Vercruyssen, A. Endo, P. J. de Visser, T. Zijlstra, T. M. Klapwijk, P. Diener, S. J. C. Yates, and J. J. A. Baselmans, “Minimal resonator loss for circuit quantum electrodynamics,” *Applied Physics Letters*, vol. 97, no. 2, Jul 2010.
- [48] J. Gao, J. Zmuidzinas, B. A. Mazin, H. G. LeDuc, and P. K. Day, “Noise properties of superconducting coplanar waveguide microwave resonators,” *Applied Physics Letters*, vol. 90, no. 10, Mar 2007.
- [49] J. Gao, L. R. Vale, J. A. B. Mates, D. R. Schmidt, G. C. Hilton, K. D. Irwin, F. Mallet, M. A. Castellanos-Beltran, K. W. Lehnert, J. Zmuidzinas, and

- H. G. Leduc, “Strongly quadrature-dependent noise in superconducting microresonators measured at the vacuum-noise limit,” *Applied Physics Letters*, vol. 98, no. 23, Jun 2011.
- [50] P. R. Maloney, N. G. Czakon, P. K. Day, R. Duan, J. Gao, J. Glenn, S. Golwala, M. Hollister, H. G. LeDuc, B. Mazin, O. Noroozian, H. T. Nguyen, J. Sayers, J. Schlaerth, J. E. Vaillancourt, A. Vayonakis, P. Wilson, and J. Zmuidzinas, “The MKID Camera,” in *Low Temperature Detectors LTD 13*, ser. AIP Conference Proceedings, vol. 1185, 2009, pp. 176–179, 13th International Workshop on Low Temperature Detectors, Stanford, CA, Jul 20–24, 2009.
- [51] J. E. Healey, T. Lindstrom, M. S. Colclough, C. M. Muirhead, and A. Y. Tzalenchuk, “Magnetic field tuning of coplanar waveguide resonators,” *Applied Physics Letters*, vol. 93, no. 4, p. 043513, Jul 2008.
- [52] Sonnet Software Inc., [Online]: <http://www.sonnetusa.com/>.
- [53] S. J. Weber, K. W. Murch, D. H. Slichter, R. Vijay, and I. Siddiqi, “Single crystal silicon capacitors with low microwave loss in the single photon regime,” *Applied Physics Letters*, vol. 98, no. 17, p. 172510, 2011. [Online]. Available: <http://link.aip.org/link/?APL/98/172510/1>
- [54] G. Ponchak, J. Papapolymerou, and M. Tentzeris, “Excitation of coupled slot-line mode in finite-ground cpw with unequal ground-plane widths,” *Microwave Theory and Techniques, IEEE Transactions on*, vol. 53, no. 2, pp. 713–717, Feb 2005.
- [55] J. Schlaerth, “Microwave kinetic inductance detector camera development for millimeter-wave astrophysics,” Ph.D. dissertation, University of Colorado, Boulder, 2010.
- [56] P. J. de Visser, S. Withington, and D. J. Goldie, “Readout-power heating and hysteretic switching between thermal quasiparticle states in kinetic inductance

- detectors,” *Journal of Applied Physics*, vol. 108, no. 11, p. 114504, 2010. [Online]. Available: <http://link.aip.org/link/?JAP/108/114504/1>
- [57] K. Wiesenfeld and B. McNamara, “Small-signal amplification in bifurcating dynamical systems,” *Phys. Rev. A*, vol. 33, pp. 629–642, Jan 1986. [Online]. Available: <http://link.aps.org/doi/10.1103/PhysRevA.33.629>
- [58] H. G. Leduc, B. Bumble, P. K. Day, B. H. Eom, J. Gao, S. Golwala, B. A. Mazin, S. McHugh, A. Merrill, D. C. Moore, O. Noroozian, A. D. Turner, and J. Zmuidzinas, “Titanium nitride films for ultrasensitive microresonator detectors,” *Applied Physics Letters*, vol. 97, no. 10, Sept 2010.
- [59] B. A. Mazin, D. Sank, S. McHugh, E. A. Lucero, A. Merrill, J. Gao, D. Pappas, D. Moore, and J. Zmuidzinas, “Thin film dielectric microstrip kinetic inductance detectors,” *Applied Physics Letters*, vol. 96, no. 10, p. 102504, Mar 2010.
- [60] R. Barends, N. Vercruyssen, A. Endo, P. J. de Visser, T. Zijlstra, T. M. Klapwijk, and J. J. A. Baselmans, “Reduced frequency noise in superconducting resonators,” *Applied Physics Letters*, vol. 97, no. 3, p. 033507, 2010. [Online]. Available: <http://link.aip.org/link/?APL/97/033507/1>
- [61] R. Barends, H. L. Hortensius, T. Zijlstra, J. J. A. Baselmans, S. J. C. Yates, J. R. Gao, and T. M. Klapwijk, “Contribution of dielectrics to frequency and noise of nbtin superconducting resonators,” *Applied Physics Letters*, vol. 92, no. 22, p. 223502, 2008. [Online]. Available: <http://link.aip.org/link/?APL/92/223502/1>
- [62] J. Schlaerth, N. Czakon, P. Day, T. Downes, R. Duan, J. Glenn, S. Golwala, M. Hollister, H. LeDuc, P. Maloney, B. Mazin, H. Nguyen, O. Noroozian, J. Sayers, S. Siegel, and J. Zmuidzinas, “The status of music: A multicolor sub/millimeter mkid instrument,” *Journal of Low Temperature Physics*, pp. 1–7. [Online]. Available: <http://dx.doi.org/10.1007/s10909-012-0541-7>

- [63] N. G. Czakon, J. A. Schlaerth, P. K. Day, T. P. Downes, R. P. Duan, J. Gao, J. Glenn, S. R. Golwala, M. I. Hollister, H. G. LeDuc, B. A. Mazin, P. R. Maloney, O. Noroozian, H. T. Nguyen, J. Sayers, S. Siegel, J. E. Vaillancourt, A. Vayonakis, P. R. Wilson, and J. Zmuidzinas, “Optimization of MKID Noise Performance Via Readout Technique for Astronomical Applications,” in *Millimeter, Submillimeter, and Far-infrared Detectors and Instrumentation for Astronomy V*, ser. Proceedings of SPIE—The International Society for Optical Engineering, vol. 7741, 2010, Conference on Millimeter, Submillimeter, and Far-Infrared Detectors and Instrumentation for Astronomy V, San Diego, CA, Jun 29–Jul 02, 2010.
- [64] M. I. Hollister, N. G. Czakon, P. K. Day, T. P. Downes, R. Duan, J. Gao, J. Glenn, S. R. Golwala, H. G. LeDuc, P. R. Maloney, B. A. Mazin, H. T. Nguyen, O. Noroozian, J. Sayers, J. Schlaerth, S. Siegel, J. E. Vaillancourt, A. Vayonakis, P. Wilson, and J. Zmuidzinas, “The cryomechanical design of MUSIC — A novel imaging instrument for millimeter-wave astrophysics at the Caltech Submillimeter Observatory,” in *Millimeter, Submillimeter, and Far-infrared Detectors and Instrumentation for Astronomy V*, ser. Proceedings of SPIE, vol. 7741, 2010, Conference on Millimeter, Submillimeter, and Far-Infrared Detectors and Instrumentation for Astronomy V, San Diego, CA, Jun 29–Jul 02, 2010.
- [65] J. Sayers, N. G. Czakon, P. K. Day, T. P. Downes, R. P. Duan, J. Gao, J. Glenn, S. R. Golwala, M. I. Hollister, H. G. LeDuc, B. A. Mazin, P. R. Maloney, O. Noroozian, H. T. Nguyen, J. A. Schlaerth, S. Siegel, J. E. Vaillancourt, A. Vayonakis, P. R. Wilson, and J. Zmuidzinas, “Optics for MUSIC: a New (Sub)millimeter Camera for the Caltech Submillimeter Observatory,” in *Millimeter, Submillimeter, and Far-infrared Detectors and Instrumentation for Astronomy V*, ser. Proceedings of SPIE—The International Society for Optical Engineering, vol. 7741, 2010, Conference on Millimeter, Submillimeter, and

Far-Infrared Detectors and Instrumentation for Astronomy V, San Diego, CA, Jun 29–Jul 02, 2010.

- [66] N. G. Czakon, A. Vayonakis, J. Schlaerth, M. I. Hollister, S. Golwala, P. K. Day, J. S. Gao, J. Glenn, H. LeDuc, P. R. Maloney, B. Mazin, O. Noroozian, H. T. Nguyen, J. Sayers, J. E. Vaillancourt, and J. Zmuidzinas, “Microwave Kinetic Inductance Detector (MKID) Camera Testing for Submillimeter Astronomy,” in *Low Temperature Detectors LTD 13*, ser. AIP Conference Proceedings, vol. 1185, 2009, pp. 172–175, 13th International Workshop on Low Temperature Detectors, Stanford, CA, Jul 20–24, 2009.
- [67] S. Doyle, P. Mauskopf, J. Naylon, A. Porch, and C. Duncombe, “Lumped element kinetic inductance detectors,” *Journal of Low Temperature Physics*, vol. 151, pp. 530–536, 2008. [Online]. Available: <http://dx.doi.org/10.1007/s10909-007-9685-2>
- [68] J. Glenn, P. K. Day, M. Ferry, J. Gao, S. R. Golwala, S. Kumar, H. G. LeDuc, P. R. Maloney, B. A. Mazin, H. Nguyen, O. Noroozian, J. Sayers, J. Schlaerth, J. E. Vaillancourt, A. Vayokanis, and J. Zmuidzinas, “A microwave kinetic inductance camera for sub/millimeter astrophysics,” in *Millimeter, Submillimeter, and Far-infrared Detectors and Instrumentation for Astronomy IV*, ser. Proceedings of SPIE—The International Society for Optical Engineering, vol. 7020, 2008, Conference on Millimeter and Submillimeter Detectors and Instrumentation for Astronomy IV, Marseille, France, Jun 26–28, 2008.
- [69] A. Goldin, J. J. Bock, C. Hunt, A. E. Lange, H. LeDuc, A. Vayonakis, and J. Zmuidzinas, “Samba: Superconducting antenna-coupled, multi-frequency, bolometric array,” *AIP Conference Proceedings*, vol. 605, no. 1, pp. 251–254, 2002. [Online]. Available: <http://link.aip.org/link/?APC/605/251/1>
- [70] A. Goldin, J. Bock, C. Hunt, A. Lange, H. LeDuc, A. Vayonakis, and J. Zmuidzinas, “Design of broadband filters and antennas for SAMBA,” in *Millimeter and*

*Ssubmillimeter Detectors for Astronomy*, ser. Proceedings of SPIE—The International Society for Optical Engineering, vol. 4855, 2003, pp. 163–171, Conference on Millimeter and Submillimeter Detectors for Astronomy, Waikoloa, HI, Aug 25–28, 2002.

- [71] J. Schlaerth, A. Vayonakis, P. Day, J. Glenn, J. Gao, S. Golwala, S. Kumar, H. LeDuc, B. Mazin, J. Vaillancourt, and J. Zmuidzinas, “A millimeter and submillimeter kinetic inductance detector camera,” *Journal of Low Temperature Physics*, vol. 151, pp. 684–689, 2008, 10.1007/s10909-008-9728-3. [Online]. Available: <http://dx.doi.org/10.1007/s10909-008-9728-3>
- [72] S. J. C. Yates, J. J. A. Baselmans, A. Endo, R. M. J. Janssen, L. Ferrari, P. Diener, and A. M. Baryshev, “Photon noise limited radiation detection with lens-antenna coupled microwave kinetic inductance detectors,” *Applied Physics Letters*, vol. 99, no. 7, p. 073505, 2011. [Online]. Available: <http://link.aip.org/link/?APL/99/073505/1>
- [73] S. Doyle, “Lumped element kinetic inductance detectors,” Ph.D. dissertation, Cardiff University, 2008.
- [74] A. Monfardini, A. Benoit, A. Bideaud, L. Swenson, A. Cruciani, P. Camus, C. Hoffmann, F. X. Dsert, S. Doyle, P. Ade, P. Mauskopf, C. Tucker, M. Roesch, S. Leclercq, K. F. Schuster, A. Endo, A. Baryshev, J. J. A. Baselmans, L. Ferrari, S. J. C. Yates, O. Bourrion, J. Macias-Perez, C. Vescovi, M. Calvo, and C. Giordano, “A dual-band millimeter-wave kinetic inductance camera for the iram 30 m telescope,” *The Astrophysical Journal Supplement Series*, vol. 194, no. 2, p. 24, 2011. [Online]. Available: <http://stacks.iop.org/0067-0049/194/i=2/a=24>
- [75] A.-D. Brown, W.-T. Hsieh, S. H. Moseley, T. R. Stevenson, K. U-yen, and E. J. Wollack, “Fabrication of an Absorber-Coupled MKID Detector and Readout for Sub-Millimeter and Far-Infrared Astronomy,” in *Millimeter, Submillimeter, and Far-Infrared Detectors and Instrumentation for Astronomy V*, ser. Proceedings

of SPIE—The International Society for Optical Engineering, vol. 7741, 2010, Conference on Millimeter, Submillimeter, and Far-Infrared Detectors and Instrumentation for Astronomy V, San Diego, CA, Jun 29–Jul 02, 2010.

- [76] P. D. Mauskopf, J. J. Bock, H. D. Castillo, W. L. Holzapfel, and A. E. Lange, “Composite infrared bolometers with  $\text{Si}_3\text{N}_4$  micromesh absorbers,” *Appl. Opt.*, vol. 36, no. 4, pp. 765–771, Feb 1997. [Online]. Available: <http://ao.osa.org/abstract.cfm?URI=ao-36-4-765>
- [77] R. Ulrich, “Far-infrared properties of metallic mesh and its complementary structure,” *Infrared Physics*, vol. 7, no. 1, pp. 37–55, 1967. [Online]. Available: <http://www.sciencedirect.com/science/article/pii/0020089167900280>
- [78] J. Clarke, G. I. Hoffer, P. L. Richards, and N. H. Yeh, “Superconductive bolometers for submillimeter wavelengths,” *Journal of Applied Physics*, vol. 48, no. 12, pp. 4865–4879, 1977. [Online]. Available: <http://link.aip.org/link/?JAP/48/4865/1>
- [79] S. Doyle, P. Mauskopf, J. Zhang, S. Withington, D. Goldie, D. Glowacka, A. Monfardini, L. Swenson, and M. Roesch, “Optimisation of lumped element kinetic inductance detectors for use in ground based mm and sub-mm arrays,” *AIP Conference Proceedings*, vol. 1185, no. 1, pp. 156–159, 2009. [Online]. Available: <http://link.aip.org/link/?APC/1185/156/1>
- [80] R. Ulrich, K. Renk, and L. Genzel, “Tunable submillimeter interferometers of the fabry-perot type,” *Microwave Theory and Techniques, IEEE Transactions on*, vol. 11, no. 5, pp. 363–371, Sep 1963.
- [81] H. Engan, “Excitation of elastic surface waves by spatial harmonics of interdigital transducers,” *Electron Devices, IEEE Transactions on*, vol. 16, no. 12, pp. 1014–1017, Dec 1969.
- [82] Jonas Zmuidzinis, Internal report, California Institute of Technology, Mar 2009.

- [83] J. Lamb, “Miscellaneous data on materials for millimetre and submillimetre optics,” *International Journal of Infrared and Millimeter Waves*, vol. 17, no. 12, pp. 1997–2034, Dec 1996.
- [84] S. Padin, M. Hollister, S. Radford, J. Sayers, D. Woody, J. Zmuidzinas, G. Cortes-Medellin, T. Sebring, and G. Stacey, “CCAT Optics,” in *Ground-based and Airborne Telescopes III*, ser. Proceedings of SPIE-The International Society for Optical Engineering, vol. 7733. SPIE, 2010, Conference on Ground-Based and Airborne Telescopes III, San Diego, CA, Jun 27–Jul 02, 2010.
- [85] V. Trifunovic and B. Jokanovic, “Four decade bandwidth uniplanar balun,” *Electronics Letters*, vol. 28, no. 6, pp. 534–535, Mar 1992.
- [86] A. Kolsrud, M.-Y. Li, and K. Chang, “Dual-frequency electronically tunable cpw-fed cps dipole antenna,” *Electronics Letters*, vol. 34, no. 7, pp. 609–611, Apr 1998.
- [87] A. Vasylichenko, L. Wang, Z. Ma, W. De Raedt, and G. A. E. Vandenbosch, “A very compact CPW-to-CPS Balun for UWB antenna feeding,” ser. IEEE Convention of Electrical and Electronics Engineers in Israel, Dec 2008, pp. 446–449.
- [88] J. Mates, “The microwave squid multiplexer,” Ph.D. dissertation, University of Colorado, Boulder, 2011.
- [89] O. Noroozian, P. Day, B. H. Eom, H. Leduc, and J. Zmuidzinas, “Crosstalk reduction for superconducting microwave resonator arrays,” *Microwave Theory and Techniques, IEEE Transactions on*, vol. 60, no. 5, pp. 1235–1243, May 2012. [Online]. Available: <http://dx.doi.org/10.1109/TMTT.2012.2187538>
- [90] Nuria Llombardt, 2011, Private communication.
- [91] Peter K. Day, 2010, Private communication.

- [92] B. Sacépé, C. Chapelier, T. I. Baturina, V. M. Vinokur, M. R. Baklanov, and M. Sanquer, “Disorder-induced inhomogeneities of the superconducting state close to the superconductor-insulator transition,” *Phys. Rev. Lett.*, vol. 101, p. 157006, Oct 2008. [Online]. Available: <http://link.aps.org/doi/10.1103/PhysRevLett.101.157006>
- [93] S. J. C. Yates, J. J. A. Baselmans, A. M. Baryshev, A. Neto, G. Gerini, R. Barends, and Y. J. Y. Lankwarden, “Antenna coupled kinetic inductance arrays for space and ground based imaging arrays,” *AIP Conference Proceedings*, vol. 1185, no. 1, pp. 144–147, 2009. [Online]. Available: <http://link.aip.org/link/?APC/1185/144/1>
- [94] P. J. de Visser, J. J. A. Baselmans, P. Diener, S. J. C. Yates, A. Endo, and T. M. Klapwijk, “Number fluctuations of sparse quasiparticles in a superconductor,” *Phys. Rev. Lett.*, vol. 106, p. 167004, Apr 2011. [Online]. Available: <http://link.aps.org/doi/10.1103/PhysRevLett.106.167004>
- [95] P. de Visser, J. Baselmans, P. Diener, S. Yates, A. Endo, and T. Klapwijk, “Generation-recombination noise: The fundamental sensitivity limit for kinetic inductance detectors,” *Journal of Low Temperature Physics*, pp. 1–6, 10.1007/s10909-012-0519-5. [Online]. Available: <http://dx.doi.org/10.1007/s10909-012-0519-5>
- [96] W. Spengler, R. Kaiser, A. N. Christensen, and G. Müller-Vogt, “Raman scattering, superconductivity, and phonon density of states of stoichiometric and nonstoichiometric tin,” *Phys. Rev. B*, vol. 17, pp. 1095–1101, Feb 1978. [Online]. Available: <http://link.aps.org/doi/10.1103/PhysRevB.17.1095>
- [97] M. R. Vissers, J. Gao, D. S. Wisbey, D. A. Hite, C. C. Tsuei, A. D. Corcoles, M. Steffen, and D. P. Pappas, “Low loss superconducting titanium nitride coplanar waveguide resonators,” *Applied Physics Letters*, vol. 97, no. 23, p. 232509, 2010. [Online]. Available: <http://link.aip.org/link/?APL/97/232509/1>

- [98] J.-E. Sundgren, B.-O. Johansson, S.-E. Karlsson, and H. Hentzell, “Mechanisms of reactive sputtering of titanium nitride and titanium carbide ii: Morphology and structure,” *Thin Solid Films*, vol. 105, no. 4, pp. 367–384, 1983. [Online]. Available: <http://www.sciencedirect.com/science/article/pii/004060908390319X>
- [99] W. Escoffier, C. Chapelier, N. Hadacek, and J.-C. Villégier, “Anomalous proximity effect in an inhomogeneous disordered superconductor,” *Phys. Rev. Lett.*, vol. 93, p. 217005, Nov 2004. [Online]. Available: <http://link.aps.org/doi/10.1103/PhysRevLett.93.217005>
- [100] P. Diener, H. Leduc, S. Yates, Y. Lankwarden, and J. Baselmans, “Design and testing of kinetic inductance detectors made of titanium nitride,” *Journal of Low Temperature Physics*, pp. 1–6. [Online]. Available: <http://dx.doi.org/10.1007/s10909-012-0484-z>
- [101] J. J. A. Baselmans and S. J. C. Yates, “Long quasiparticle lifetime in aluminum microwave kinetic inductance detectors using coaxial stray light filters,” *AIP Conference Proceedings*, vol. 1185, no. 1, pp. 160–163, 2009. [Online]. Available: <http://link.aip.org/link/?APC/1185/160/1>
- [102] Z. Dridi, B. Bouhafs, P. Ruterana, and H. Aourag, “First-principles calculations of vacancy effects on structural and electronic properties of  $\text{TiC}_x$  and  $\text{TiN}_x$ ,” *Journal of Physics: Condensed Matter*, vol. 14, no. 43, p. 10237, 2002. [Online]. Available: <http://stacks.iop.org/0953-8984/14/i=43/a=320>
- [103] H. Allmaier, L. Chioncel, and E. Arrigoni, “Titanium nitride: A correlated metal at the threshold of a Mott transition,” *Physical Review B*, vol. 79, no. 23, Jun 2009.
- [104] O. Noroozian, P. K. Day, B. H. Eom, H. G. LeDuc, and J. Zmuidzinas, “Microwave Crosstalk in Lumped Element Far-IR MKIDs,” in *35Th International Conference on Infrared, Millimeter, and Terahertz Waves (IRMMW-THZ*

2010), 2010, 35th International Conference on International Conference on Infrared, Millimeter and Terahertz Waves, Rome, Italy, Sep 5–10, 2010.

- [105] J. von Neumann and E. Wigner, “Concerning the behaviour of eigenvalues in adiabatic processes.” *Physikalische Zeitschrift*, vol. 30, pp. 467–470, 1929.
- [106] P. D. Lax, *Linear algebra and its applications*. Wiley-Interscience, 2007.
- [107] T. Dahm and D. J. Scalapino, “Theory of intermodulation in a superconducting microstrip resonator,” *Journal of Applied Physics*, vol. 81, no. 4, pp. 2002–2009, Feb 1997.